IMPROVED GROWTH, ORDERING, AND CHARACTERIZATION OF SIDEWALL EPITAXIAL GRAPHENE NANORIBBONS

A Thesis
Presented to
The Academic Faculty

by

Meredith Swegan Nevius

In Partial Fulfillment
of the Requirements for the Degree
Doctor of Philosophy in the
School of Physics

Georgia Institute of Technology
August 2016

IMPROVED GROWTH, ORDERING, AND CHARACTERIZATION OF SIDEWALL EPITAXIAL GRAPHENE NANORIBBONS

Approved by:

Edward H. Conrad, Advisor
School of Physics
Georgia Institute of Technology

Dr. Zhigang Jiang
School of Physics
Georgia Institute of Technology

Dr. Walter de Heer
School of Physics
Georgia Institute of Technology

Dr. Nazanin Bassiri-Gharb
School of Mechanical Engineering
Georgia Institute of Technology

Dr. Phillip First
School of Physics
Georgia Institute of Technology

Date Approved: May 18th, 2016

To Justin and Logan

ACKNOWLEDGEMENTS

I would like to begin by thanking my advisor, Dr. Edward Conrad, for his direction, encouragement, and support. Without his providential guidance from the beginning, I might not have studied Condensed Matter Physics. I would also like to thank my committee for their time, assistance, and feedback.

For countless discussions concerning research efforts, I would like to thank Dr. Claire Berger, Dr. Walt de Heer, Dr. Phillip First, and Dr. Zhigang Jiang. For immeasurable help and collaboration, I heartily thank Dr. Amina Taleb-Ibrahimi, Dr. Antonio Tejeda, and the rest of the Casiopée beamline at the Synchrotron SOLEIL. I would also like to thank Arlensiú Celis, Dr. Maya Narayanan-Nair, and Dr. Irene Palacio Rodriguez. Collaboration among graduate students in the School of Physics is exceptional. I would like to thank the following students for their discussion and insights throughout my graduate school tenure: Matthew Conrad, Zach Dromsky, Dr. Zelei Guo, Dr. John Hankinson, Dr. Jeremy Hicks, Dr. Yike Hu, Dr. Yuntao Li, Dr. James Palmer, Owen Vail, and Dr. Feng Wang. For his indispensable help and attention to detail, I would like to thank Andrei Savu. I would also like to thank Devin Brown and the exceptional IEN Cleanroom staff for their tireless efforts to keep Cleanroom users safe, productive, and well-informed.

Because graduate students must first start their educational career in elementary, middle, and high school, I would like to thank all the teachers who contributed to my education. In particular, without the enthusiasm and dedication of Dr. Jonathan Crymes and Melodee Lackey, I might not have pursued my graduate education.

My husband Justin Nevius has been more supportive than I could have ever asked. I would also like to acknowledge the constant support and encouragement of my

parents, Bill and Dianne Swegan, without whom I would not be the woman I am today. Finally, I would also like to acknowledge my two-year-old son Logan, who is a joy. I hope my journey inspires him to pursue his dreams.

Research presented in this work was supported by the NSF under Grants No. DMR-1401193 and No. DMR-1005880. I would also like to acknowledge support from the NSF PREM program under Grant No. DMR-0934142. Part of the work was funded by the French Research Agency under contract ANR Corigraph. Additional support came from the Partner University Fund from the French Embassy and the Keck foundation.

TABLE OF CONTENTS

LIST OF TABLES

LIST OF FIGURES

SUMMARY

One material that has drawn much attention as a viable supplementary material to silicon is graphene, an atom-thick sheet of carbon in a hexagonal lattice. Graphene has many desirable qualities, including massless Dirac fermion charge carriers and an intrinsically two-dimensional structure. However, graphene is a semi-metal; it lacks a bandgap. Therefore, the purpose of this work is to explore a structured graphene geometry that is shown to produce a new form of semiconducting graphene seamlessly connected to metallic graphene nanoribbons. Nanoribbons are patterned and grown on silicon carbide with a combined top-down/bottom-up fabrication method that is compatible with current lithographic technology. Surface characterization measurements, including angle-resolved photoemission spectroscopy (ARPES), low-energy electron microscopy (LEEM), and photoemission electron microscopy (PEEM), are used to characterize ribbon samples and verify semiconducting and metallic properties of the structured graphene.

CHAPTER I

BACKGROUND

1.1 Graphene Overview

Initial interest in graphene arose because of its structural similarity to unrolled carbon nanotubes (CNTs) and subsequently increased due to its many exciting properties, including linear dispersion (implying massless Dirac fermion charge carriers) [1], room temperature ballistic transport [2, 3, 4], and high mobilities [2, 5]. Since the initial excitement concerning graphene's electronic properties, many other widely-varying applications have been found, including use in chemical sensors [6, 7, 8], drug delivery [9], solar cells [10, 11, 12], and enhancement of mechanical properties in composites [13, 14]. It is possible that graphene may one day prove to be vital to these efforts. However, due to the unique suitability of graphene's properties for next generation nanotechnology, the research presented in this work will focus on the fabrication, engineering, and characterization of graphene as a material for nano-electronics purposes.

In this Chapter, we will review the physical and electronic properties of ideal graphene, describe the common methods of fabricating graphene, address the fundamental problem of creating a semiconducting form of graphene, and quickly review a few useful characterization techniques for analyzing graphene samples.

1.2 Structure of Graphene

In structure, graphene is an atomically-thin layer of sp^2-bonded carbon atoms arranged in a hexagonal lattice. Each carbon atom forms a strong sigma bond with three neighboring carbon atoms. The strong sigma bonds contribute to the chemical

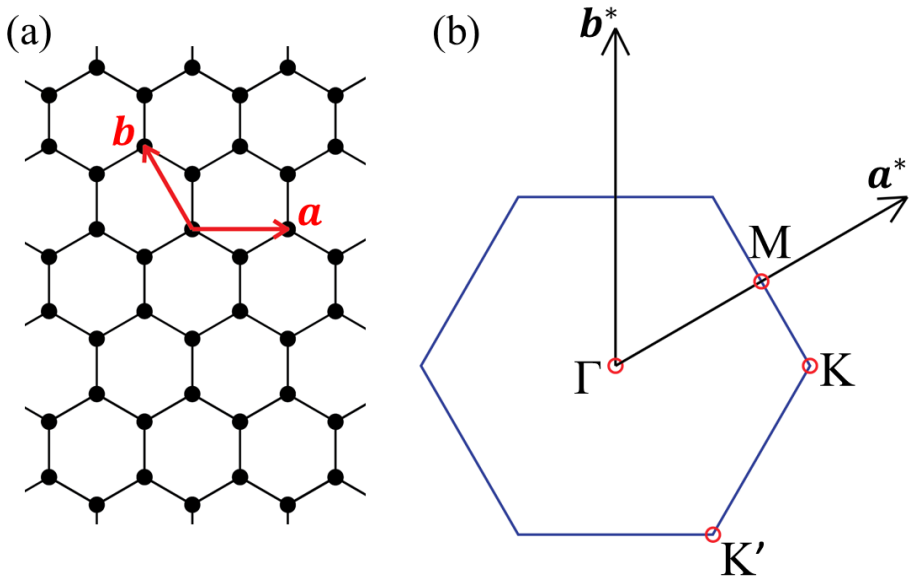

Figure 1.1: (a) Graphene lattice, with lattice vectors. (b) Reciprocal space Brillouin Zone for graphene, with reciprocal lattice vectors. High symmetry points Γ, K, and M are shown.

inertness and mechanical strength of graphene. A p_z orbital perpendicular to the plane of the lattice is associated with the fourth valence electron from each atom. When the p_z orbital remains isolated, it contributes to electrical conduction, and the associated electron is very mobile.

In real space, the hexagonal graphene lattice has lattice vectors that are 120° apart and have magnitudes $|a| = |b| = 2.450$ Å (see Fig. 1.1(a)) [15]. In reciprocal space, the Brillouin zone for graphene is also hexagonal. See Fig. 1.1(b) for the location of high symmetry points Γ, K, and M in reciprocal space. Reciprocal lattice vectors have magnitude $|a^*| = |b^*| = 2.961$ Å^{-1}, which means that the distance between points Γ and K is $k_{\Gamma-K} = 1.710$ Å^{-1}.

One of the most unique features of graphene is that it exhibits linear dispersion near the K point. Since the energy-momentum relationship for photons ($E = \hbar ck$) is also linear, it can be said that the charge carriers in graphene respond to the periodic crystal potential in such a way as to externally appear as if they are massless. It was this potential for "massless" charge carriers, combined with the material's intrinsic

two-dimensional nature, that drew much attention to graphene as a prospect for future device development.

1.3 Graphene Fabrication Methods

While general interest in graphene as a contender for post-CMOS electronics is widespread, a number of divergent paths for the production of the material have emerged. Some current production methods include mechanical exfoliation of graphite, chemical vapor deposition, reduction of graphene oxide, self-assembly, and epitaxially grown graphene on surfaces of silicon carbide (SiC), called Epitaxial graphene (EG).

1.3.1 Mechanically Exfoliated Graphene

Graphite contains sheets of graphene that are Bernal stacked. Some of the earliest electronic measurements of graphene were done on pieces of graphene that were mechanically exfoliated from highly ordered pyrolytic graphite (HOPG) [16]. Mechanically exfoliated graphene is created by the repeated peeling of graphite until the preferred number of layers is obtained. The layers are then deposited onto a desirable substrate. Exfoliated graphene has thus far been useful in the measurement and confirmation of electronic properties of graphene. However, there exist a number of significant drawbacks to its long-term use: determination of material thickness is generally limited to optical verification, a slow and undesirable process [17]; samples are necessarily limited in size and irregular in shape, which is incompatible with large-scale production of electronics [16, 17]; and many defects are incurred in the peeling and transfer process (e.g., presence of adsorbates, degradation by ripping, tearing, folding, etc.)[16, 18].

1.3.2 CVD Graphene

It has long been known that hydrocarbons can form on the surface of certain metals [19, 20]. Recently, a method has been developed for forming graphene layers on metal

substrates, commonly nickel, copper, or ruthenium [21]. A metal film is heated in the presence of a carbon-containing gas mixture (e.g. methane or ethylene with argon). The reaction gas deposits carbon on and into the metal by reaction or dissociation. Rapid cooling can then result in the formation of only a few layers of graphene on the metal's surface [22, 23].

Due to the insolubility of carbon in copper at the appropriate growth temperatures and pressures, graphene films as thin as a monolayer have been obtained [23]. The dimensions of the graphene sheet are limited only by the size of the metal film. In this way, large sheets of graphene can be formed. However, graphene domain size is limited by both the distance between nucleation sites and the crystalline domains of the metal substrate; therefore, most CVD graphene samples contain many domains, decreasing the material's conductivity [24, 25, 26]. Also, graphene that is directly adsorbed onto a metallic substrate is inadequate for the purposes of creating an electronic device. Thus, the few layers of graphene created on the metal film must be subsequently transferred to another substrate. Common metal etchants like iron (III) chloride are known to intercalate between sheets of graphene [27]. Necessarily, then, CVD graphene that has been transferred to an appropriate substrate contains rips, tears, wrinkles, and other structural defects from the transfer process [22, 23]; possesses many graphene domains [22, 23]; and may be exceptionally difficult to clean due to intercalants and adsorbates [27].

1.3.3 Reduced Graphene Oxide

Since graphene is a semi-metal and does not have a bandgap, some researchers are pursuing an alternative to pristine graphene by studying the production of reduced graphene oxide (rGO). Intercalated graphite and graphite oxide have been produced in the lab for over 100 years [28]. Due to the exceptional hydrophilic nature of graphite oxide, a sample can be put into water and sonicated to completely dissociate

into sheets of graphite oxide (alternatively called graphene oxide, GO) [29]. Thus, an abundance of GO can be fabricated at one time.

GO is an insulating material [30, 31]; therefore, for use in traditional electronic devices, the sheets of GO need to be selectively reduced. The amount of reduction that occurs on the GO layers determines whether the rGO will be insulating/semiconducting or approaching semi-metallic. However, because GO intrinsically contains defects [32], the structure of rGO is not equivalent to pristine graphene even after reduction [32, 30, 29, 31]: defects abound, samples contain many wrinkles, some functional groups remain, and conductivities are very low (varying from 0.5-2 S/cm [33] to highest reported values of $\approx$ 300 S/cm [34], considerably less than that of pristine graphite, $2 - 3 \times 10^5$ S/cm [35]). Sheet resistances of both GO and rGO are extremely sensitive to ambient conditions and reduction temperature used [29, 31, 36]. Also, the problem remains that GO is not thermally stable; thermal reduction spontaneously begins around 100°C [29]. Therefore, until sufficient solutions to these problems can be found, rGO is not a viable option for graphene-based electronics.

1.3.4 Self-Assembly of Graphene

There exists another class of graphene fabrication methods that boast the descriptor of "self-assembled". Many such methods generally begin with GO and then use chemical reactions to stack and reduce layers, sometimes with chemical additives included in the final structure for specific purposes [37, 38]. While these paths to graphene formation may present opportunities for graphene-based solar cells, composites, or energy storage materials, these methods also produce graphene and heterostructures with severely limited electrical conductivities, preventing them from being preferred for graphene-based electronic nano-devices.

An additional sub-class of "self-assembled" production methods includes the formation of graphene nanoribbons from carbon-containing precursors. Carbon in sp^2-bonded hexagonal rings is a very common component of many organic and polymeric materials. It is not surprising, therefore, that researchers would attempt to perfect methods for fabricating graphene from organic monomer precursors. In one such typical process [39], monomer precursors are thermally sublimated onto a solid substrate, during which the halogen components of the monomers are removed. The remaining components of the monomers are then thermally activated to undergo addition reactions, forming linear polymer chains. Finally, a surface-assisted cyclodehydrogenation process creates the final graphene ribbon product.

Unfortunately, while the described method creates graphene nanoribbons with very specific edge structures and widths, metallic substrates are required (e.g. gold or silver) [39]. For use in a nano-scale device, the graphene would need to be transferred to a different substrate. Also, the final location and orientation of the nanoribbons with respect to the formation substrate are relatively unconstrained. Locating the ribbons for transfer would necessitate an additional step in the device fabrication process. Therefore, creating graphene nanoribbons via self-assembly on metal substrates is useful for characterization of graphene nanoribbon systems but would require processing modifications to be compatible with large-scale electronics fabrication.

1.3.5 Epitaxial Graphene

In addition to the previously discussed approaches for fabricating graphene, another production method remains that deserves consideration. It has been well demonstrated that when SiC is heated to sufficient temperatures, thermal decomposition of the surface leads to the formation of graphene as the surface silicon atoms sublimate at a faster rate than the surface carbon atoms [40, 41]. The two polar faces of SiC form graphene differently: on the SiC(0001) face (also called the Si-face), graphene

forms epitaxially and slowly; and on the SiC$(000\bar{1})$ face (called the C-face), graphene forms comparatively quickly and exhibits non-Bernal stacking.

Epitaxial graphene, grown on SiC, has many beneficial qualities compared to the other types previously discussed. First and foremost, SiC is a readily-available wide-bandgap substrate already being produced by and used in the semiconductor industry; thus, graphene formed on SiC does not need to be transferred to a secondary substrate, unlike exfoliated and CVD graphene. All defects and adsorbates associated with the transfer process are avoided. Because graphene grows epitaxially, large sheets of graphene formed on SiC can be grown with known thickness and orientation. Monolayer graphene on the Si-face behaves like a sheet of isolated graphene, except with lower mobilities. Even multiple layers on the C-face act like isolated graphene sheets because of their stacking [5, 42]. Additionally, both EG and SiC are compatible with current lithographic techniques [2, 43, 44], so features can be patterned at desired positions on the wafer. It is also important to note that the number of layers of graphene formed on SiC surfaces can be chosen based on growth time and temperature. Therefore, production and lithographic processing of EG is the most practical and the most promising route to large-scale graphene-based electronics.

1.4 Epitaxial Graphene Growth on Surfaces of Silicon Carbide

Silicon carbide (SiC) exists in many different crystalline forms, including both cubic and hexagonal polytypes. Of the structures used in the exploration of EG formation, the hexagonal 4H- and 6H- polytypes have been primarily studied. For a nH-SiC structure, there exist n bilayers per unit cell. A bilayer contains one plane each of silicon and carbon atoms. Stacking of the bilayers varies based on the polytype: 4H-SiC is stacked ABCB, while 6H-SiC is stacked ABCACB. Thermal decomposition of both polytypes has been shown to form graphene [45, 46].

There exist a number of techniques for growing graphene from SiC by varying

the combination of heating method and pressure during growth. SiC can be heated resistively, with an electron beam, or in a furnace to form graphene on exposed surfaces [47, 48, 46]. Pressure conditions during growth greatly affect the long-range order and homogeneity of the EG sample: heating SiC under ultra-high vacuum (UHV) tends to produce graphene that contains an increased degree of disorder [49, 50, 51] since the growth process occurs quickly and far from equilibrium. With the relationship between these growth conditions and the quality of produced graphene being taken into account, the method that will be used for preparation of samples in this work is referred to as confinement controlled sublimation of SiC [46].

1.4.1 Confinement Controlled Sublimation Growth

In confinement controlled sublimation (CCS), SiC samples are placed in a graphite crucible and heated via rf-induction under high vacuum. Figure 1.2 depicts a typical CCS furnace like the one used to grow graphene samples throughout this work. For more detailed information concerning CCS furnaces, see Ref. [52]. As a sample is heated, silicon sublimates and is contained within the crucible, creating an atmosphere of silicon vapor. The existence of silicon vapor pressure above the sample slows the rate at which further silicon sublimates from the surface. Having a slower sublimation rate equates to slower overall graphene growth. A slower growth rate enables the creation of films that are better ordered and more uniform than samples grown in UHV. Also, slower growth means that samples can be grown at higher temperatures over longer times while still achieving thin film thicknesses. As a result, growth of graphene in a CCS furnace is more uniform and exhibits better control of film thickness than graphene growth in UHV.

If a SiC sample were heated within a tightly enclosed crucible, the silicon vapor pressure would continue to increase and would eventually slow silicon sublimation to the point of stopping further graphene growth all together. Consequently, a hole of

pre-determined size is often put in the crucible to enable a leak of silicon vapor. With a constant leak rate, an equilibrium is reached such that the silicon sublimating from the surface is roughly equivalent to the silicon leaking from the crucible. This equilibrium allows continued, controlled growth without the drawback of inhibiting the formation of more graphene. The magnitude of the silicon leak can be macroscopically controlled by changing the size of the hole in the crucible as necessary.

For consistent growth of samples over long-term use of a crucible, several additional factors need to be considered. First, some of the silicon that sublimates from SiC during growth is adsorbed onto the walls of the graphite crucible. If a crucible is used to grow only one type of sample (e.g. only monolayer graphene samples), then a somewhat steady-state is achieved for the silicon content in that crucible. However, if several types of samples are interchangeably grown in the crucible over time, then there might be some inconsistencies in growth results if care is not taken. For example, if a monolayer layer sample is grown, followed by the growth of a sidewall ribbon (which typically involves higher growth temperatures than monolayer samples), and then another sample that is desired to be monolayer is grown, it is possible that the last "monolayer" sample will be over-grown compared to the first sample due to a decrease in silicon content in the crucible from the high-temperature ribbon sample recipe. Knowing such effects can occur, it might be considered preferable for separate crucibles to be used for high- and low-temperature recipes if long-term consistency in growth is desired. Second, considering the adsorption of silicon onto the walls of the graphite crucible, certain steps are required for the establishment of the appropriate amount of silicon in the crucible before consistent results can be achieved, and an occasional maintenance step might be required. For additional information concerning seasoning and maintenance of crucibles, see Appendix B.

For any nano-scale material, surface characteristics become increasingly important compared to bulk contributions. Thus, it is understandable that the condition of

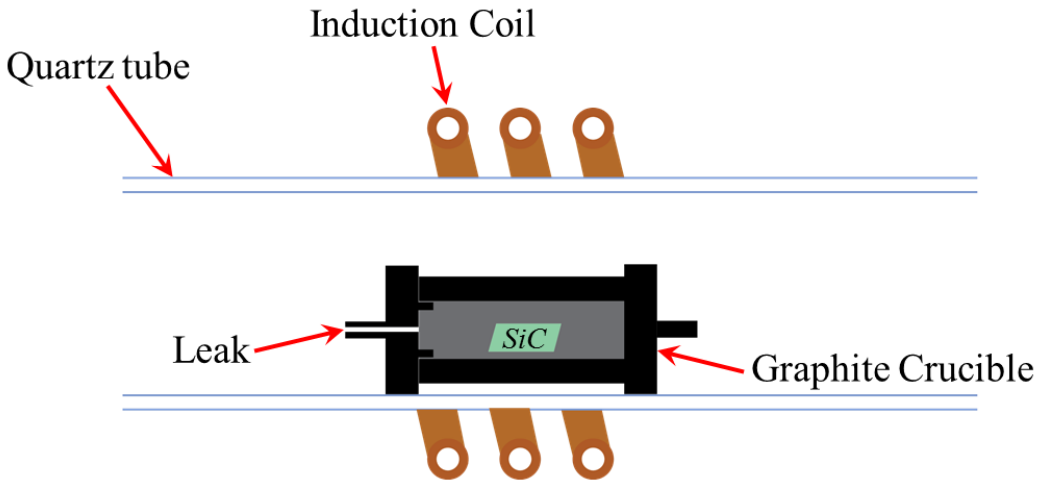

Figure 1.2: Depiction of one type of Confinement-Controlled Sublimation furnace. A graphite crucible is composed of the body of the crucible plus the lid. The lid typically has a 1 mm-diameter hole to allow a leak of Si vapor. The crucible is contained within a quartz tube, and the system is pumped down to high vacuum pressures via a turbomolecular pump. The *rf*-induction antenna (composed of hollow copper tubing filled with flowing water for cooling) goes around the quartz tube and is centered on the crucible. An oscillating electric field resistively heats the graphite crucible, thus heating the SiC sample as well. For more detailed information about CCS furnaces, see Ref. [52].

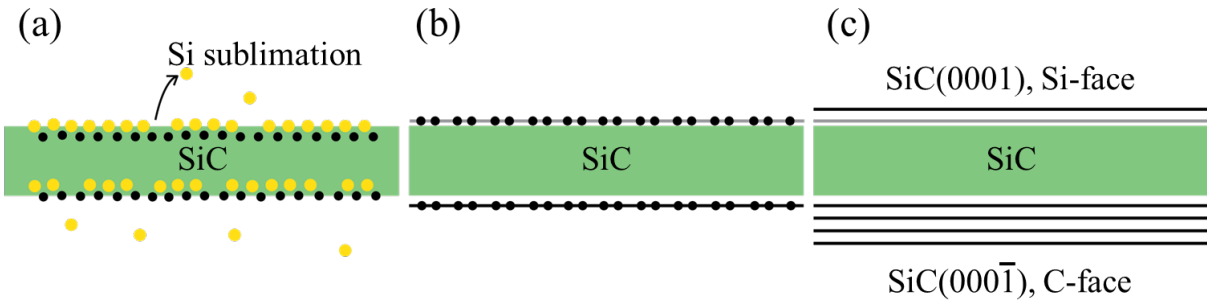

Figure 1.3: (a) A SiC crystal is heated inside a graphite crucible via *rf*-induction. Si atoms sublimate from the exposed facets faster than C atoms. (b) Excess carbon remaining on the SiC facets recrystallizes to form graphene. (c) Different crystallographic facets of SiC form graphene at different rates and with varying stacking and substrate interactions. The Si-face forms graphene much more slowly than the C-face.

the SiC surfaces helps to determine the quality of the graphene formed. Surface treatments such as chemically and mechanically polishing (cmp) and hydrogen etching (H-etching) can greatly improve the structural characteristics of the EG grown on the treated surfaces. For example, it has been shown that cmp-treated SiC wafers produce graphene that is not as rough and is more uniform than graphene samples on unpolished surfaces, as determined by AFM [46, 53, 54]. H-etching has also been used to form well-ordered unit cell step heights across SiC surfaces [49, 55]. As a substrate, therefore, surface treated SiC is ideal for producing industrial-quality graphene.

1.4.2 C-Face Graphene

It has been known for decades that graphene grows very differently on the two polar faces of SiC [40, 41]; see Fig. 1.3. First, many layers of graphene can be grown very quickly on the C-face [40] in the same time as only 1-2 layers of growth in the Si-face. In fact, it can be difficult to find the appropriate growth parameters to obtain single- to few-layer C-face graphene [50, 51, 56]. Second, multilayer C-face graphene persists in showing characteristics of nearly ideal, isolated graphene sheets in transport and ARPES measurements [5, 57, 1] while multilayer Si-face graphene does not. To determine why sheets of multilayer C-face graphene behave like single sheets, LEED, ARPES, and surface x-ray diffraction (SXRD) measurements have been taken [42, 1]. LEED shows graphene diffraction spots rotated 30° from the SiC spots but also azimuthal streaking centered at 0° [42]. The diffraction spots rotated 30° from SiC suggest that at least some of the graphene layers are oriented consistent with a $(6\sqrt{3}\times 6\sqrt{3})$R30° reconstruction (in SiC units). XRD azimuthal scans indicate that other layers are oriented ±2°, accounting for the azimuthal streaking [42]. ARPES data also support both conclusions [1, 51]. The rotational variance of 30° and ±2° cause the p_z orbitals of most of the carbon atoms in a sheet to remain isolated. Thus, graphene layers formed on the C-face can act as isolated sheets. ARPES again

confirms this by showing that the band structure for all observable layers remains linear near the K-point; the stacking of multilayer C-face graphene does not change the linear dispersion [1, 51].

1.4.3 Si-Face Graphene

Growth of graphene on the Si-face is very different from that on the C-face. First and foremost, it is crucial to note that the first layer of graphene that forms on the Si-face of SiC, while structurally like that of electronic graphene, actually bonds to the surface; consequently, the first layer lacks the characteristic linear dispersion of isolated graphene [58]. Henceforth, this layer will be called the buffer layer (depicted by the light gray layer in Fig. 1.3(b) and (c)), and any reference to monolayer or bilayer Si-face graphene shall be in terms of the number of graphene layers above the buffer layer. Growth of C-face graphene lacks any such graphitic layer that highly interacts with the substrate [59]. The cause of this asymmetry of substrate interaction on the polar faces has been attributed to differences in structure at the interface [58]. For more information concerning the electronic band structure of the Si-face buffer layer, see Chapter 2. While ARPES data show that the Si-face buffer layer lacks a Dirac cone [58], monolayer graphene above the buffer layer does show linear dispersion, indicating that the monolayer graphene and buffer layer do not strongly interact [58]. It can now be shown that this weak interaction between the buffer layer and monolayer is due to an incommensurate structure; for more information about this structure, see Ref. [60].

In addition to structural differences at the interface and, subsequently, disparate first layer/substrate interactions, the polar faces of SiC also greatly vary in their growth rate of graphene. While 4-5 layers of graphene can be formed at 1420°C in 6 minutes on the C-face [61], growth at temperatures in excess of 1500°C for 20 minutes under the same furnace conditions can form only bilayer graphene on the

Si-face. Films can reach a thickness of 60 layers on the C-face, but it is difficult to obtain even 3-4 layers on the Si-face [59]. It is therefore apparent that differences between the interface structures on the polar faces affect the rate at which silicon sublimates from the bulk [59].

The stacking of graphene layers is also different on the Si-face. LEED and ARPES data indicate that Si-face graphene grows epitaxially, rotated 30° from the SiC substrate [2, 51]. In contrast to multilayer C-face graphene samples (which show layers rotated 30° and ±2° from SiC), bilayer graphene on Si-face shows AB stacking (Bernal stacking) [62, 63, 64].

1.4.4 Growth on Other Facets

Since it has been clearly demonstrated that graphene grown on the two polar faces of SiC are characteristically different in growth rate, substrate interactions, and stacking of layers, it is reasonable to assume that growth on other facets of SiC also varies based on SiC interface structure. Attempts to pattern topographical structures on the Si-face have shown that, depending on patterning and growth conditions, certain SiC facets are more thermodynamically stable than others. Reference [46] shows that when circular pillars are patterned on the Si-face they facet into "armchair" facets SiC$\{1\bar{1}0n\}$ during growth, which are apparently thermodynamically and energetically preferred. Not only are certain facets more stable, different facets also exhibit disparate growth rates. As a specific example, armchair facets have been shown to grow monolayer graphene faster than the Si-face [43, 44]; monolayer graphene on SiC$\{1\bar{1}0n\}$ facets is observed while, simultaneously, buffer layer and bare SiC are observed on the Si-face [65]. Thus, because of the differences exhibited in graphene growth rates and substrate interactions for graphene on the C-face, Si-face, and various facets on the Si-face, it should **not** be assumed that graphene formed on different facets should interact equivalently with the SiC substrate.

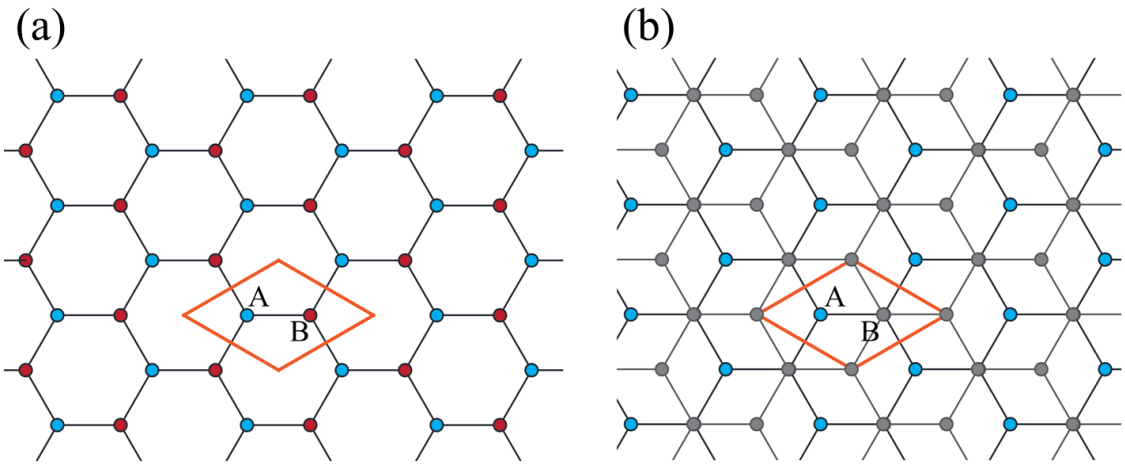

Figure 1.4: (a) Monolayer Graphene lattice. Sublattices are depicted by red and blue atoms. (b) Bilayer Graphene, Bernal stacked (as is observed for bilayer Si-face graphene). The top layer is depicted by the gray lattice. Because of the stacking geometry, the two sublattices are no longer equivalent.

1.5 Methods for Creating Semiconducting Graphene

The goal of studying graphene is to determine a way to leverage graphene's intrinsically useful properties to improve upon the state of modern electronics, because silicon-based transistors will not be able to be scaled down indefinitely. Graphene is an ideal candidate for next generation nanotechnology because of its two-dimensional nature, linear dispersion implying "massless" charge carriers [1], high mobilities [2, 5], and ballistic transport capabilities [2, 3, 4]. However, graphene is a semi-metal; it lacks a bandgap. Therefore, if graphene is to be used in conventional digital electronics, a method must be found that can selectively open a room temperature bandgap in graphene while also being consistent with large-scale electronics production, thus utilizing graphene's exciting properties to the fullest extent. A number of such methods have been theoretically proposed and subsequently researched; the advantages and disadvantages of each will be briefly discussed here.

1.5.1 Bilayer Graphene

Bilayer graphene on the Si-face is Bernal stacked, also known as AB-stacked. AB-stacked graphene has nonlinear dispersion near the K point due to sublattice symmetry breaking [66]. While AA stacking of graphene layers (A atoms directly above A atoms, B atoms directly above B atoms) preserves sublattice symmetry, AB stacking does not. In AB stacking, the A atom has no corresponding carbon atom above it (as is the case in ideal monolayer graphene), but the B atom is positioned directly below and weakly bonds to another B atom in the layer above it. The two sublattices can no longer be considered equivalent. Figure 1.4 depicts this sublattice symmetry breaking. Sublattices are depicted by red and blue atoms in Fig. 1.4(a). The top layer of bilayer graphene is depicted by the gray lattice in Fig. 1.4(b). Observing that only A sublattice atoms remain uncovered by carbon atoms in the graphene sheet above, it becomes obvious that AB-stacking breaks the sublattice symmetry by making the A and B atoms unequivalent.

The asymmetry in the bonding between AB-stacked sheets has been shown to destroy the linear dispersion near the K point and to open a bandgap [66]. Two nearly parallel conduction bands exist above two nearly parallel valence bands. See Ref. [66] for ARPES images showing the band structure of bilayer Si-face graphene. Without doping or an applied voltage to render the two graphene sheets unequivalent, the highest valence band and lowest conduction band touch for zero bandgap. However, experiment verifies that when either a voltage is applied across the layers or doping adsorbates are evaporated onto the surface of one of the layers, the highest valence band and lowest conduction band split, creating a bandgap due to the asymmetry between the two graphene sheets [66]. Applying a voltage has been shown to create a tunable bandgap in bilayer graphene as large as 250 meV [67]. Epitaxial bilayer Si-face graphene exhibits a bandgap without an applied voltage due to unequivalent charge transfer from the substrate [66]. Unfortunately, this bandgap is only 0.1 eV,

too small to be useful for digital electronics. For bilayer graphene to be of use as a semiconductor in conventional digital electronics, a bandgap more like that of silicon, germanium, or gallium arsenide would be required (1.1, 0.67, and 1.4 eV, respectively) [68].

1.5.2 Strain

Another method that has been predicted to open a bandgap at the K point of graphene is strain. Theoretical calculations made by various researchers suggest disparate requirements for a strain-induced, sizable bandgap in graphene; while some first principles calculations have suggested gaps as large as 300 meV for a lattice with 1% strain [69], others calculate no bandgap formation for uniaxial strains as large as 10-20% [70]. It has also been theorized that a combination of shear and uniaxial strain could be used to open a bandgap as large as 0.9 eV [71]. Despite the existence of copious theoretical calculations, experimental verification of graphene with a significant bandgap due to strain is sorely lacking, perhaps in part because producing well-ordered local strain patterns is difficult at best [72, 73]. Perhaps future fabrication and characterization experiments will prove to rectify this problem; however, it is more likely that other methods that have already been demonstrated to open a useable bandgap will be more successful in the development of graphene-based electronics.

1.5.3 Quantum Confinement

Similar to CNTs, theory has consistently predicted that graphene nanoribbons (GNRs) should have a bandgap due to quantum confinement [74, 75]. Unfortunately, both the exact parameters necessary for opening a bandgap as well as the size of the resulting bandgap are debated among theoretical calculations. All popular theories agree, however, that the gap should depend on exact edge structure [74, 76, 77]. Commonly cited is the calculation that relates bandgap size with ribbon width, suggesting that the size of the gap is inversely proportional to the ribbon width [78], with a 1 nm

nanoribbon possessing a ≈ 1 eV bandgap.

A bandgap created by confinement effects in graphene nanoribbons remains, as yet, undemonstrated due to problems with lithographic constraints. When patterning flat graphene sheets into ribbons, realistic lithographic resolutions of ≈ 20 nm lead to extremely disordered edges. Thus, confirmation of a quantum confinement-induced bandgap cannot be reasonably expected from lithographically patterned ribbons. For the creation of nanoribbons with atomically well-ordered edges, a different approach is needed (see Chapter 3 on Sidewall Graphene Nanoribbons).

1.5.4 Chemical Functionalization

Chemical functionalization of graphene presents a myriad of possible methods for opening a bandgap in graphene. Similar to the case of AB-stacked bilayer graphene, if a graphene sheet can be made to bond to a chemical species (e.g., functional groups) in a well-ordered way such that the A and B sublattices are no longer equivalent, then a bandgap may open in the graphene band structure.

Many attempts have been made to create functionalized graphene with a useable bandgap. Fabrication and subsequent reduction of graphene oxide (GO) to form reduced graphene oxide (rGO) creates a semiconducting material. However, rGO is not structurally or electronically equivalent to graphene, possessing inferior conductance due to residual functional groups and structural defects [32, 30, 29, 31]. Other forms of chemically modified graphene, like graphane (graphene with hydrogen atoms used to rehybridize some of the material's π electrons) [79, 80] and fluorographene (graphene with fluorine atoms) [81, 82], have been demonstrated to possess bandgaps, but none are larger than 450 meV. It is critical to point out that none of the mentioned forms of chemically modified graphene are stable above 400°C: GO starts to spontaneously reduce above 100°C [25]; fluorographene reduced at 500-600°C still exhibits resistances 100 times higher than that of pristine graphene [81]; and annealing

above 450°C reduces graphane back to metallic graphene [79].

1.5.5 Functionalization through Substrate Interactions

In addition to modifying graphene by bonding with functional groups, a well-ordered substrate interaction could break sublattice symmetry and, thus, create a bandgap. Because graphene by itself is only a single-atom-thick sheet, it intrinsically has a large surface area-to-volume ratio. It is understandable that a material with such considerable surface area would have material properties that are greatly affected by its underlying substrate.

Graphene must always be put on an underlying substrate or else suspended between two points of contact. Therefore, it is of vital importance to consider any effects that may be induced by interactions with the substrate. For graphene that has been transferred from its original fabrication source to a secondary substrate, there will be inherent disorder, rotational uncertainty, adsorbates, and induced defects (rips, tears, wrinkles, etc). However, if highly ordered graphene can be fabricated on a substrate without needing to be transferred (i.e. epitaxial graphene), then a well-ordered interaction between the graphene and the substrate could form a bandgap in graphene's band structure by breaking the sublattice symmetry. In Chapter 2, one such type of substrate interaction will be discussed that, for the first time, creates a semiconducting form of graphene with a bandgap useable for digital electronics.

1.6 Surface Analysis Techniques

In order to determine the structure and properties of fabricated graphene samples, a number of characterization techniques have been utilized and will be presented in this work. Therefore, an overview of the theory and purpose of applicable surface analysis techniques is both necessary and practical.

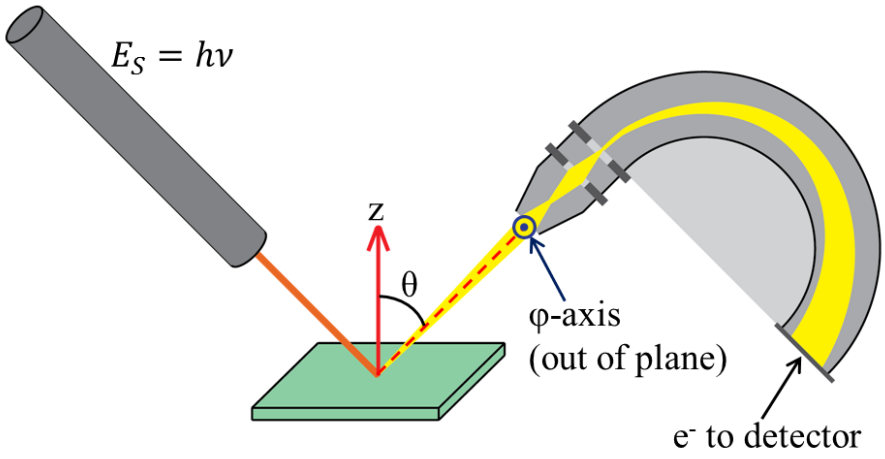

Figure 1.5: ARPES geometry for a slit detector. A light source ($E_S = h\nu$) is incident on the sample with energy sufficient to produce photoelectrons. The detector measures the kinetic energies of the electrons as well as their outgoing angles, θ and ϕ. The electron's origin in the material's band structure can be determined from the measurement of angles θ and ϕ for each electron.

1.6.1 ARPES

Angle-resolved photoemission spectroscopy (ARPES) is useful for the direct measurement of a material's band structure. Generally, a synchrotron light source is used. Photons are chosen with an energy sufficient to cause photoelectrons to be ejected from the surface of the material. Both the kinetic energy and the outgoing angle of the ejected electrons are measured. Thus, from the relations

$$E_{KE} = E_S - E_{BE} - \Phi \tag{1.1}$$

$$k_{total} = \frac{\sqrt{2mE_{KE}}}{\hbar} \tag{1.2}$$

we can ascertain where the photoelectron came from in the material's k-space band structure. Here, E_{KE} is the electron's kinetic energy after being ejected from the surface, $E_S = h\nu$ is the source energy, E_{BE} is the electron's binding energy, and Φ is the material work function.

The vector $\mathbf{k_{total}}$ can be broken into a perpendicular component k_z and two in-plane components, k_x and k_y. For two-dimensional materials like graphene, the band

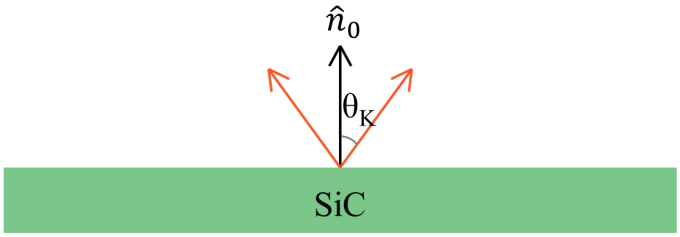

Figure 1.6: In ARPES, the angle θ_K needed to reach the K point is determined by the source energy, $h\nu$. For $h\nu = 36$ eV, $\theta_K \approx 36°$.

structure has no dependence on k_z. The exact relationships between k_x, k_y, and the independent angles θ and ϕ depend on the detector geometry. See Appendix C for further details. For the experimental set-up at the Cassiopée Beamline of the Synchrotron SOLEIL, a slit detector is used (Fig. 1.5), and we find the relations

$$k_x \approx 0.512\sqrt{E_{KE}}\sin\theta\cos\phi \tag{1.3}$$

$$k_y \approx 0.512\sqrt{E_{KE}}\sin\phi \tag{1.4}$$

Counting a large enough number of electrons to be statistically relevant gives images that are cuts of k-space (k_x, k_y, and energy), depicting electronic bands via measured intensity.

Because the origins of the photoelectrons from the material's k-space band structure are determined by angles θ and ϕ, it is important to point out a few practical consequences for analysis of characterization data. First, for the graphene Brillouin zone (Fig. 1.1(b)), the distance between Γ and a K point is $k_{\Gamma-K} = 1.710$ Å^{-1}. So, $(k_x, k_y) = (1.710$ Å$^{-1}, 0$ Å$^{-1})$ would be the location of one K point. Thus, from equations 1.3 and 1.4, for a source energy of $h\nu = 36$ eV, we would expect to measure a Dirac cone at $\theta_K \approx 36°$ and $\phi_K = 0°$. Figure 1.6 depicts the measurement of θ_K relative to the surface normal.

Second, the correlation between a location in k-space and how it is measured (via angle) also implies that if a surface is not completely flat, e.g., contains roughness or patterned topographical features, then the bands that are measured might overlap

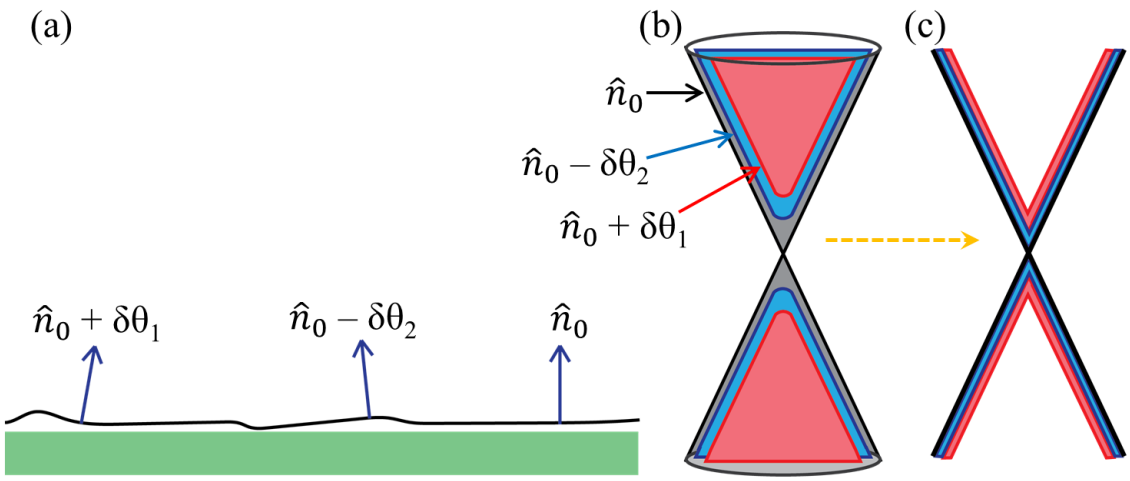

Figure 1.7: (a) A surface that is rough (has a range of surface normals) affects ARPES images from the surface by broadening the measured bands. (b) Several conic sections are shown from the varying surface normals in (a). (c) A broadening of the measured ARPES band structure would result from the variation in surface normal.

each other in angle. That is to say, if a graphene monolayer is rough (has a range of surface normals), then a Dirac cone measured at θ_K might appear broadened by additional intensity from conic sections that originate from parts of the surface with slightly different surface normals. Figure 1.7 depicts such a situation. Also, if a surface has a patterned trench or facet with graphene on it, the bands from the faceted surface would be tilted by the facet angle. Brillouin zones measured by ARPES are necessarily parallel to the surface from which they originate. Bands from these topographic features are not observed as a projection onto the SiC(0001) Brillouin zone but instead are observed with additive angular components; see Chapter 3 for more information on this geometry. Consequently, bands from different crystallographic facets (disparate physical origins) could appear in an overlapping angular range. See Chapter 3 for more information about such samples.

Figure 1.8(a) depicts a typical ARPES image obtained from the K point of monolayer Si-face EG. Note the direct observation of graphene's linear dispersion. Figure 1.8(b) shows a constant energy (Fermi surface) image. The conical shape of the

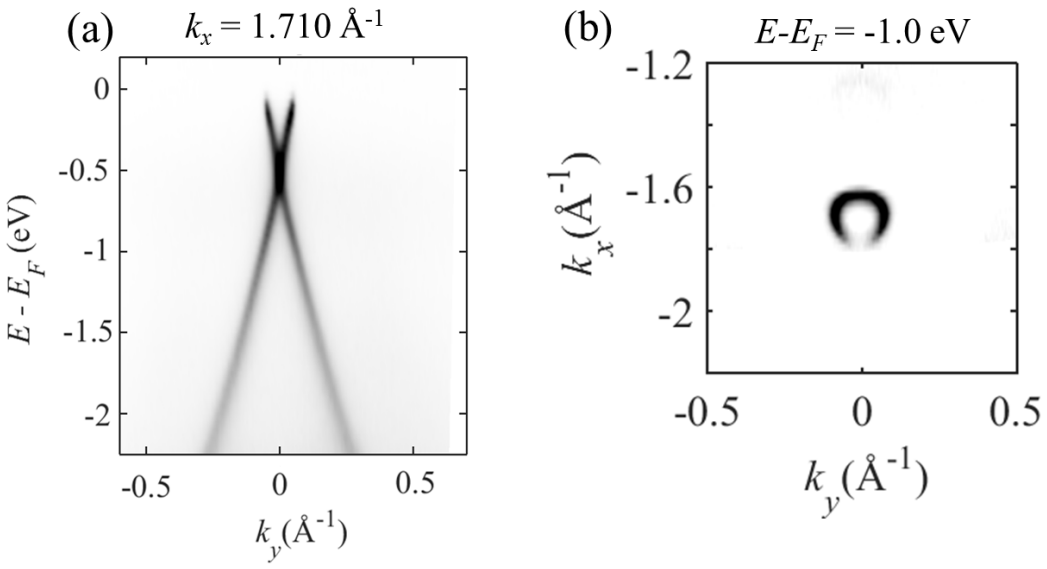

Figure 1.8: (a) ARPES of monolayer Si-face graphene. The linear dispersion near the K-point ($k_x = 1.710$ Å^{-1}) of graphene is evident. (b) A constant energy (Fermi surface) ARPES image showing the conical cross-section of the Dirac cone. For both ARPES images, $h\nu = 36$ eV.

graphene Dirac cone is observed. While the photon source is incident on the sample, many photoelectrons come out of the material. Therefore, particle interactions cannot be neglected. Matrix element effects can cause parts of electronic bands to have low or zero detected intensity within certain angular ranges [83]. Consequently, extracting the real band structure from the experimentally measured band structure is non-trivial. One such example of this matrix element effect can be noted in Fig. 1.8(b); intensity is missing from part of the circular conic section. Given the experimental set-up used for images in this work, ARPES cuts of the Dirac cone that are taken perpendicular to the Γ-K direction (along k_y, as in 1.8(a)) show both sides of the cone. However, ARPES cuts taken parallel to Γ-K (along k_x) show only one side of the cone because the matrix element effect diminishes all intensity from the other side of the cone. For an example of such images, see Ref. [58].

1.6.2 LEEM

Low-energy electron microscopy (LEEM) uses an electron microscope to image surfaces. High energy electrons are sent from an electron gun toward the sample surface of interest. The sample is held at a potential close to that of the electron gun, consequently slowing down the incoming electrons. The lowest energy (most surface sensitive) electrons can then be measured. A number of imaging modes exist. Bright Field-LEEM (BF-LEEM) makes use of the fact that electrons coming from different heights on the surface have different phases; steps on the surface are then imaged with varying contrast. Dark-Field LEEM (DF-LEEM, or diffraction contrast LEEM) utilizes a contrast aperture to obtain intensity from only one diffraction spot. The resulting image gives a measurement of the physical locations on the surface from which the intensity of the diffraction spot of interest originates. Also, images can be taken in so-called reflectivity mode. Reflectivity mode can be used to image regions on a surface of different composition. In particular, LEEM reflectivity mode can be used to determine the number of epitaxial graphene layers on different regions of a sample [84]. With access to all of these imaging modes, LEEM is a very useful technique for characterizing epitaxial graphene samples.

1.6.3 XPEEM

X-ray photoemission electron microscopy (XPEEM) utilizes x-rays to eject electrons from the surface of a sample. The kinetic energies of the ejected electrons are measured and, knowing the source energy, the binding energies of the electrons can be calculated from Eqn 1.1. Then, using optical elements, the real space topography of the sample can be imaged as a function of electron binding energy. Also, an aperture can be put in place to discriminate electrons that come out of the sample with a specific angle. The correlations between angle and $k_{\|}$ components, k_x and k_y, are found in Eqns 1.3 and 1.4. Thus, an image of a sample can be taken such that all

intensity comes from electrons ejected from a specific place in the reciprocal space band structure of the sample's surface; such images are called dark field-XPEEM (DF-XPEEM) images.

CHAPTER II

THE SIC(0001) BUFFER LAYER AS A SEMICONDUCTING FORM OF GRAPHENE

2.1 Introduction to the Buffer Layer as a Functionalized Graphene System

Realization of the goal to create graphene-based electronic devices requires the development of semiconducting graphene. One theoretical method for opening a bandgap in graphene is to periodically bond to all atoms in one sublattice (see Fig. 2.1), consequently breaking graphene's chiral symmetry; this is referred to as graphene functionalization. Many different approaches have been taken to develop a useful semiconducting form of functionalized graphene that is compatible with industrial-scale fabrication of electronics. However, up to this point no workable form of semiconducting graphene has been developed because the functionalization methods being utilized introduce disorder during the growth and functionalization processes [85, 86, 87]. In fact, the lack of timely success in efforts to create semiconducting graphene was the motivation for research to shift to metal dichalcogenides, despite the inability to grow such materials at the level of purity and ordering necessary for industrial-scale electronics.

It has been well established that the first layer of graphene to grow on the SiC(0001) (Si-face) is not electronic graphene [62, 58, 88]. That is to say, the first layer of graphene on the Si-face, hereafter called the "buffer" layer, does not exhibit the typical linearly dispersing Dirac cone at the K point of graphene [58]. Unlike the first layer of graphene that grows on the SiC($000\bar{1}$) C-face, which exhibits a Dirac cone, the Si-face buffer layer interacts and bonds in some fashion to the substrate,

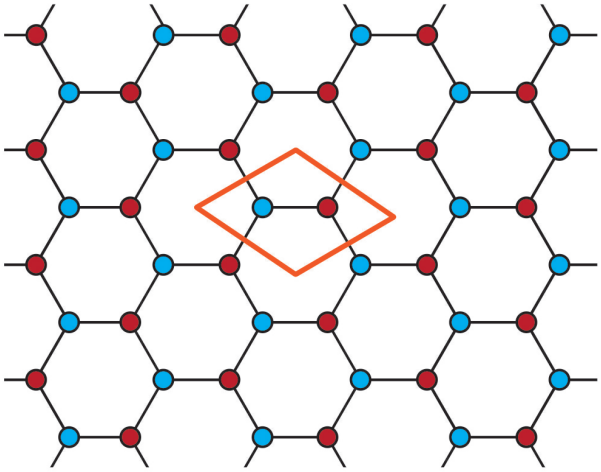

Figure 2.1: A hexagonal lattice can also be represented as a triangular lattice with a two atom basis. In this figure, the two sublattices of graphene are depicted by blue and red carbon atoms. Each of the two atoms in the graphene unit cell belongs to one of the two sublattices. Breaking the symmetry between the sublattices (e.g., via chemical functionalization) makes the two atoms unequivalent and can open a bandgap in graphene's band structure.

modifying the π-bands. If a well-ordered interaction could be created between the buffer layer and the SiC bilayers beneath it, then the buffer layer would be a phenomenal example of a functionalized graphene system and would be of extreme interest and usefulness in the pursuit of graphene electronics. Thus, the exact nature of the buffer layer band structure has been of much interest to researchers.

Early studies of the buffer layer primarily involved samples grown in ultra-high vacuum (UHV). ARPES measurements of these early samples showed two non-dispersing states, called g_1 and g_2. These two states were the only band structure features observed between the SiC valence band maximum and the Fermi level [58] and were interpreted to be Mott-Hubbard states from the hybridized SiC dangling bonds at the surface. Figure 2.2 shows g_1 and g_2, measured at $E - E_F = -0.5$ eV and -1.6 eV, respectively. It is now known that sub-nanometer disorder in these UHV-grown buffer samples prevented the required symmetry breaking necessary to open a bandgap. Therefore, to create an ordered substrate interaction capable of opening a dispersing and gapped band, improvements to fabrication of the buffer layer was necessary.

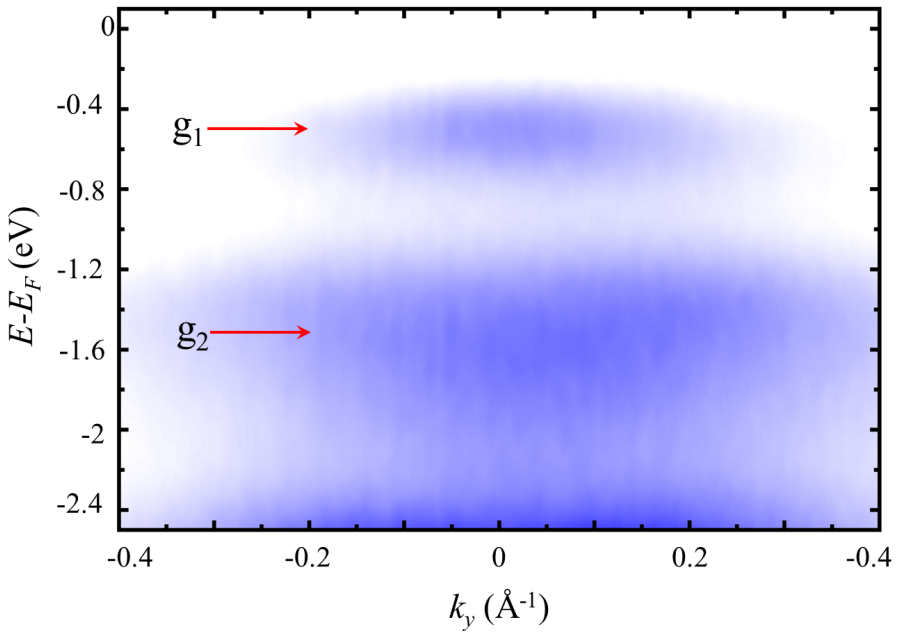

Figure 2.2: ARPES image taken at the K point of graphene for a sub-buffer sample. k_y is in the direction perpendicular to Γ-K. The SiC non-dispersing surface states g_1 and g_2 are found at $E - E_F = -0.5$ eV and -1.6 eV, respectively. The same surface states are seen in UHV-grown buffer layer samples [58]. For this ARPES image, $h\nu = 36$ eV.

2.2 The Buffer Layer as a Semiconducting Form of Graphene

Through improved ordering due to advances in growth processes, we now show that a well-ordered buffer layer is, in fact, semiconducting. Previous attempts to obtain any meaningful data concerning the buffer layer band structure were thwarted by an inability to grow a well-ordered buffer layer. We show that our optimized growth parameters create highly ordered buffer films with two measurable dispersing bands not previously observed in samples grown by other methods. Figure 2.3 shows ARPES images of the two semiconducting buffer bands now observed in numerous samples. The first band, called ε_1, is observed at the K point of graphene. The second band, called ε_2, is observed in three lobes around the graphene K point, with orientation of the lobes along the Γ-K direction (see Fig. 2.3(c)). Each band has a bandgap ≥ 0.5 eV.

In this work, we use confinement-controlled sublimation (CCS) [46] growth of graphene at low vacuum pressures (10^{-6} torr). The presence of Si vapor pressure in the crucible, with a fixed leak rate through a hole in the crucible lid, causes growth to be slower and more easily controlled than in UHV. First attempts to grow well-ordered buffer layer in this way utilized recipes which had been formulated for sidewall graphene nanoribbon growth (see Chapter 3 for details on temperatures and times for sidewall ribbon-type recipes). These high temperature/short time recipes had been developed to form monolayer graphene on sidewalls of steps (either on natural steps or patterned sidewalls), and to minimize monolayer graphene growth on flat areas of the Si-face. The consequence of these temperature and time parameters is that the flat SiC(0001) surfaces between step edges contain a combination of buffer layer and bare SiC, with some partial monolayer coverage close to step edges where growth is seeded the fastest. Such recipes were successful in creating highly ordered buffer layer films and resulted in the first measurements of the semiconducting buffer graphene bands.

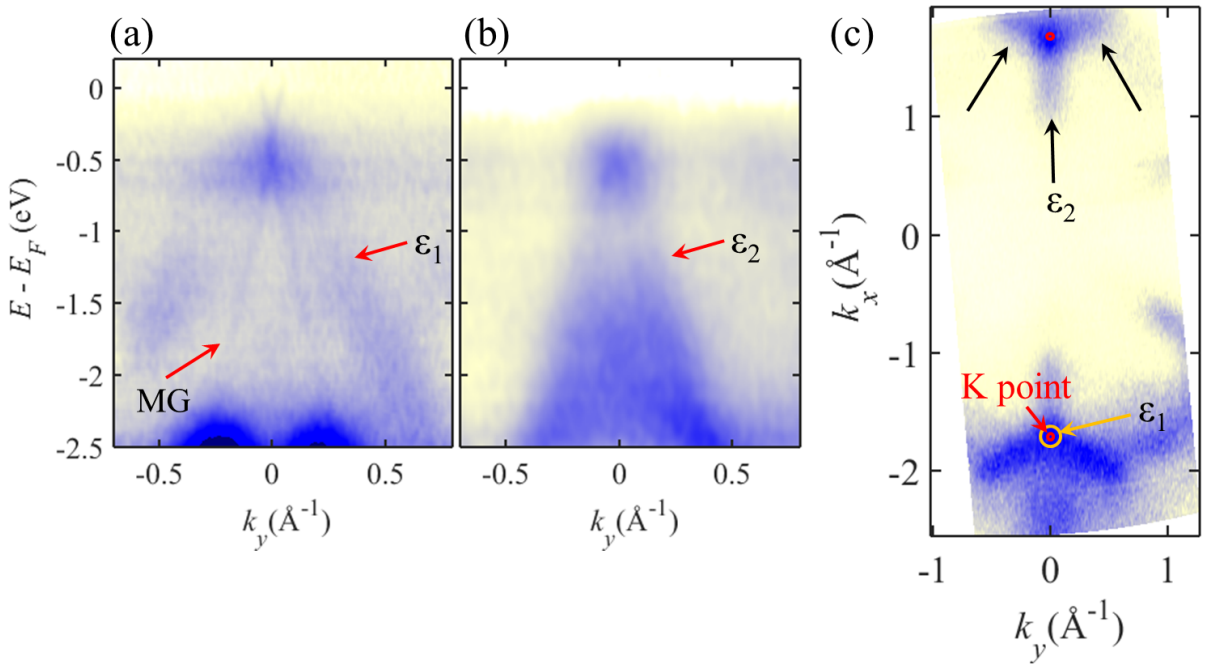

Figure 2.3: ARPES images of semiconducting buffer bands ε_1 and ε_2 from a buffer sample grown with a sidewall ribbon-type recipe. For both bands, $E - E_F \approx -0.5$ eV. For all images, k_y is perpendicular to Γ-K. (a) ε_1 is observed at the graphene K point. A small coverage ($\sim 2\%$) of monolayer graphene (MG) near natural step edges contributes to a weak Dirac cone. (b) ε_2 is observed in three lobes around the K point. (c) Fermi surface ARPES image taken at $E - E_F = -0.6$ eV. Two K points are seen, with intensity from ε_1 around the K point. ε_2 is observed as a three-fold symmetric band, with three lobes extending along the Γ-K direction. Here, Γ is located at $(k_x, k_y) = (0\ \text{Å}^{-1}, 0\ \text{Å}^{-1})$. For all images, $h\nu = 70$ eV.

In fact, it is important to note that Hicks et al in Reference [44] were actually the first to record an observation of the semiconducting ε_2 band from the buffer layer grown on a sidewall ribbon sample. Hicks et al measured an array of armchair-oriented sidewall ribbons with ARPES (see Chapter 4 for more information on armchair sidewall ribbon samples). They discovered a gapped band with $E - E_F = -0.5$ eV in an angular region which corresponded well with the range of surface normals between the SiC(0001) trench tops and the measured facet angle. Thus, it was concluded that the gapped band should come from graphene in or near the bend region between the SiC(0001) and the faceted sidewall. The exact cause of the bandgap could not be determined via ARPES. It is now known that the samples measured in Ref. [44] actually contained a significant amount of buffer layer on the SiC(0001) trench tops, and the gapped band which Hicks et al measured was, in fact, ε_2 from the buffer layer near the bend region on the trench tops. The angular correlation of the bend region/trench top surface normal transition and the angular region near K where ε_2 is observed is coincidental; for further discussion about this geometry, see Section 4.3.2.

Re-evaluation of the data from Ref. [44] also reveals the ε_1 band at the K point of graphene on the SiC(0001) trench tops, though it is broadened compared to ε_1 observed from flat buffer samples due to some angular disorder. ε_2 from Ref. [44] also has noticeable inner intensity compared to buffer from flat samples due to angular disorder on the trench tops. As discussed in Section 1.6.1 and shown in Fig. 1.7, any variation in surface normal across a sample directly affects where a band is measured in θ and can, therefore, cause band broadening and additional intensity inside the bands. Figure 2.4 shows a comparison of the gapped band reported in Ref. [44] versus ε_2 from a buffer sample, grown with a sidewall ribbon-type recipe.

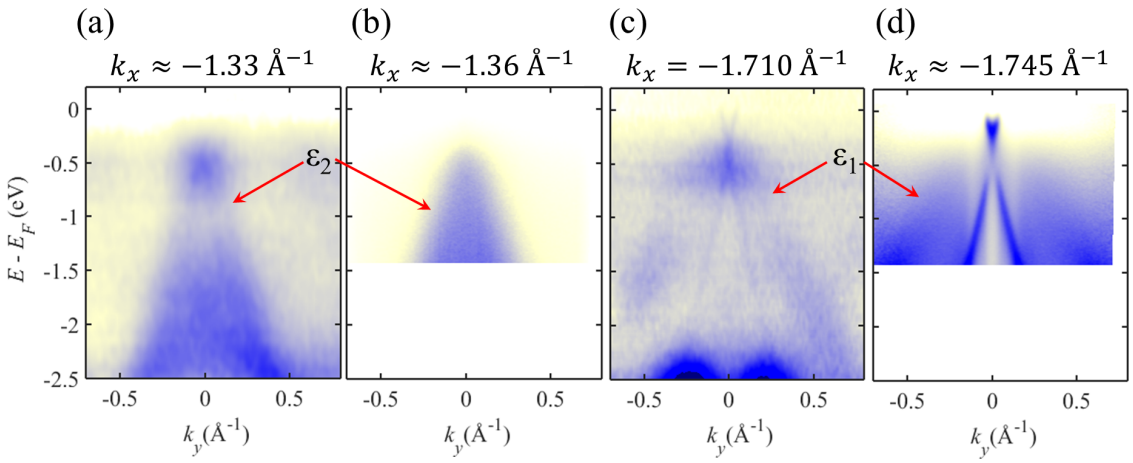

Figure 2.4: Comparison of semiconducting buffer bands with gapped band discovered by Hicks et al [44]. (a) and (b) Buffer band ε_2 from flat buffer and from Ref. [44], respectively. (b) is the gapped band published in Ref. [44]. Some angular disorder associated with the topographical features in the patterned ribbon sample contribute to additional intensity inside the ε_2 band in (b). (c) and (d) Buffer band ε_1 from flat buffer and from the sample in Ref. [44], respectively. The ARPES cut in (d) has been incidentally measured slightly off from the K point, $k_x \approx -1.745$ Å^{-1} instead of -1.710 Å^{-1}, which changes the appearance of the conic section of the Dirac cone. Comparatively large monolayer coverage on the SiC(0001) trench tops of the sidewall sample is evidenced by the high intensity of the monolayer graphene Dirac cone. For (a) and (c), the photon energy is $h\nu = 70$ eV, and for (b) and (d), $h\nu = 36$ eV.

2.2.1 Proof of Highly Ordered Samples

In a first attempt to deliberately measure the band structure of the buffer layer, before it was discovered that the ε_2 band from buffer had unknowingly been observed on ribbon trench tops [44], a similar sidewall ribbon-type recipe was used on flat (unpatterned) samples. Without the added complexity of sidewall trench topographical features, ε_1 and ε_2 from buffer were both observed and noted for the first time. It can be seen from measurements of these samples that the buffer layer and partial monolayer graphene films are very well ordered. A strong indication of the improved sample order is the consistent observation of both first- and second- order replica cones from umklapp processes.

In flat buffer samples grown with sidewall ribbon recipes, there exists some small amount of monolayer above the buffer layer near natural step edges. Thus, a Dirac cone is observable at the K point of graphene. The buffer and monolayer films have such a high degree of order that many replica cones are observed. All replica cones from the K^{th} K-point can be indexed using reciprocal lattice vectors of the SiC 6×6 unit cell: $\mathbf{G}_K(m,n) = m\mathbf{s}_1 + n\mathbf{s}_2$, where $|\mathbf{s}_1| = |\mathbf{s}_2| = \frac{1}{6}|\mathbf{a}^*_{SiC}|$. Figure 2.5 shows locations and indices m, n of replica cones which have been observed. Replica cones are clearly seen from both 1^{st}-order 6×6 ($m, n = 1$) and 1^{st}-order 1×1 (a SiC $\mathbf{G}$ vector, ($m, n = 6$), e.g., the $\mathbf{G}_{01}(0,\bar{6})$ and $\mathbf{G}_{\bar{1}1}(6,\bar{6})$) as well as from multiple scattering processes involving 1^{st}-order $(\mathbf{s}_1, \mathbf{s}_2)$ plus a SiC $\mathbf{G}$ vector (e.g., the $\mathbf{G}_{01}(0,\bar{7})$ and $\mathbf{G}_{1\bar{1}}(7,\bar{7})$). Early UHV grown samples only showed 1^{st}-order 6×6 replicas ($m, n=1$) [89]. The fact that so many ARPES replica bands are observed in these films (in addition to 6th order x-ray diffraction rods observed in other experiments [60]) testifies to the improved order of the films. Figure 2.6 shows an ARPES Fermi surface cut with a number of observable replica cones.

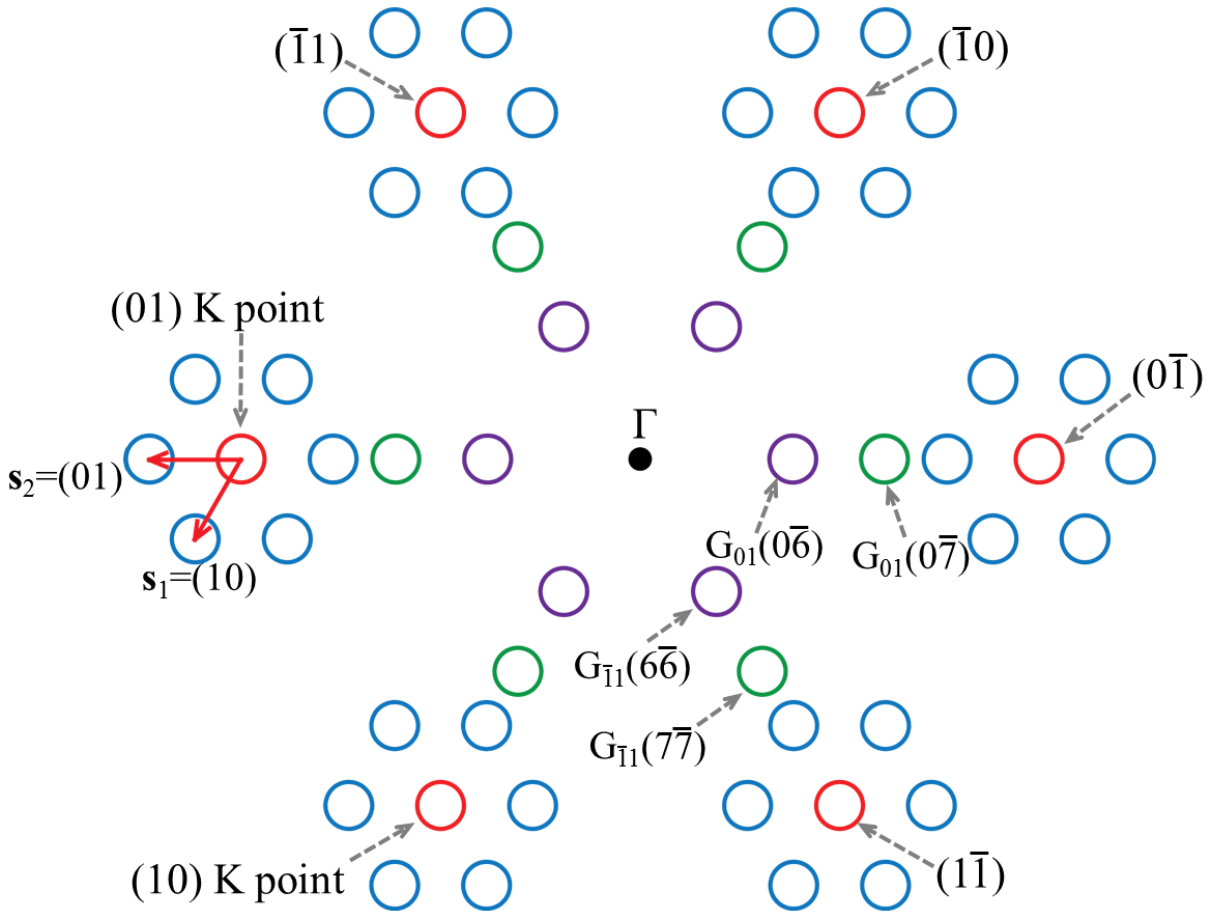

Figure 2.5: Locations of replica cones observed in ARPES due to high degree of ordering in graphene films. The magnitudes of $\mathbf{s}_1$ and $\mathbf{s}_2$ are equivalent to 1/6 the SiC reciprocal lattice vector, $|\mathbf{s}_{1,2}| = \frac{1}{6}|\mathbf{a}^*_{SiC}|$. Replica cones observed include cones which have $(m,n) = 1$ (i.e. 6×6), $(m,n) = 6$ (i.e. $\mathbf{G_K} = |\mathbf{a}^*_{SiC}| = 6|\mathbf{s}_{1,2}|$), and $(m,n) = 7$ (i.e. $\mathbf{G_K} = |\mathbf{a}^*_{SiC}| + \frac{1}{6}|\mathbf{a}^*_{SiC}| = \frac{7}{6}|\mathbf{a}^*_{SiC}|$).

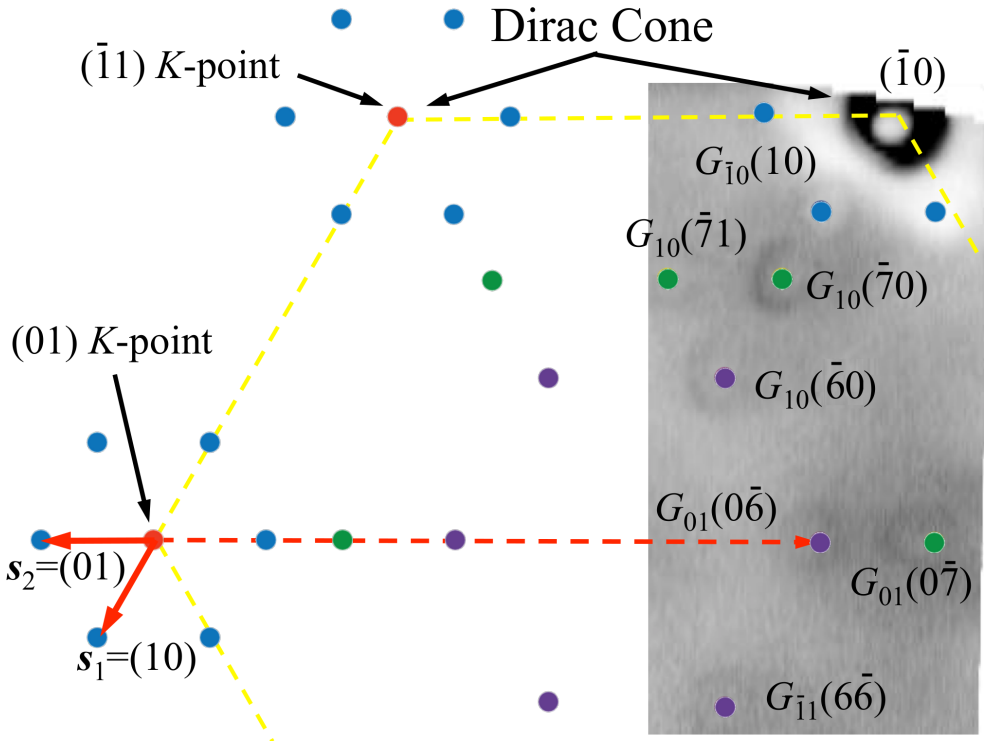

Figure 2.6: ARPES Fermi surface cut showing replica cones due to high degree of ordering in graphene films. For this image, $E - E_F = -1$ eV, $h\nu = 36$ eV.

2.2.2 Lower-Temperature Recipes for Buffer Growth

While recipes developed for sidewall graphene successfully grow highly-ordered buffer layer films, the high temperatures and short growth times can result in more monolayer growth at natural step edges than would be seen for lower temperature recipes. Thus, a lower temperature/longer time recipe was developed and optimized to create a complete, well-ordered buffer layer with consistently minimal monolayer graphene coverage. With this lower temperature recipe, any monolayer graphene observed in ARPES is small in coverage, $< 2\%$.

With the current crucible geometry and growth configuration, it is known that the low temperature buffer layer recipe forms buffer within the range of 1350 °C $\pm$10 °C , while a monolayer forms above the buffer layer at 1520 °C in 20 min. Growth $\approx$ 20 °C below the buffer growth temperature results in the formation of a "sub-buffer" layer. This sub-buffer layer will exhibit a $(6\sqrt{3}\times6\sqrt{3})$R30° LEED pattern but will not show

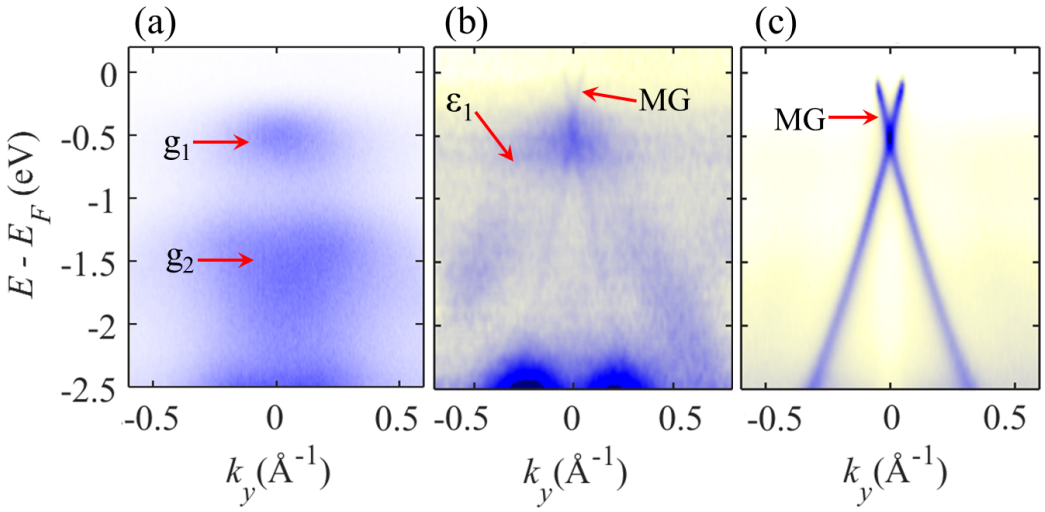

Figure 2.7: ARPES Images depicting the progression of graphene growth on the Si-face as a function of growth temperature. (a) K point of a sub-buffer sample, as in Fig. 2.2. The sample was grown ≈ 20 °C below the low temperature-recipe buffer layer. (b) ε_1 at the K point of a buffer layer. (c) Monolayer graphene. An intense Dirac cone is observed at the K point, without any observable ε_1, g_1, or g_2 bands. For (a) and (c), $h\nu = 36$ eV, and for (b), $h\nu = 70$ eV.

ε_1 or ε_2. Instead, the two non-dispersing SiC surface states g_1 and g_2 are observed; ARPES of a sub-buffer sample is shown in Figs. 2.2 and 2.7(a). Figure 2.7 shows the evolution of growth from sub-buffer to complete buffer (with a small amount of monolayer graphene near step edges, contributing to a Dirac cone at the K point) to monolayer.

2.2.3 Dispersion of ε_1 and ε_2

For the first time, these two types of CCS recipes created a buffer layer which was well-ordered enough to measure coherent dispersing bands, confirming that when the buffer/SiC substrate interaction is well-ordered, the buffer layer is indeed semiconducting. Further discussion of the details concerning the dispersion of these two semiconducting bands is of interest.

As previously discussed, ARPES measurements from these improved samples show two semiconducting π-bands, ε_1 and ε_2. Figure 2.8 summarizes the dispersion of

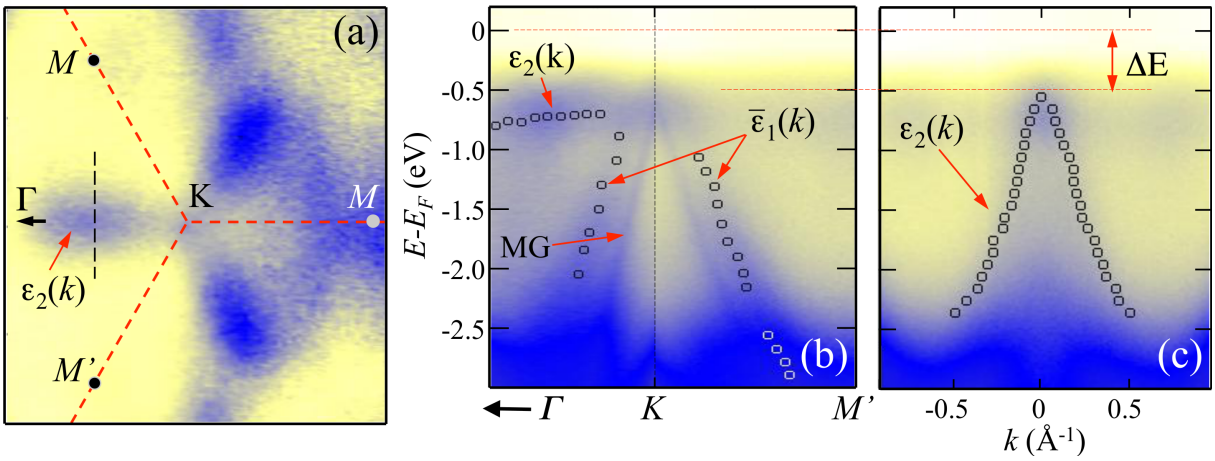

Figure 2.8: ARPES images of buffer layer semiconducting bands. The buffer sample depicted here was grown with a low temperature recipe. (a) ARPES Fermi surface cut showing ε_2, a three-fold symmetric band occurring in lobes around the graphene K point. Lobes are oriented along the Γ-K direction. For this image, $E-E_F = -0.41$ eV. (b) A composite ARPES image showing the Γ-K-M' direction. A weak Dirac cone from monolayer graphene (MG) can be seen at the K point. $\bar{\varepsilon}_1(k)$ is shown, with circles at peak positions for the average dispersion. (c) An ARPES image showing $\varepsilon_2(k)$, taken perpendicular to Γ-K. Circles depict the edge positions of the band. For all images, $h\nu = 70$ eV.

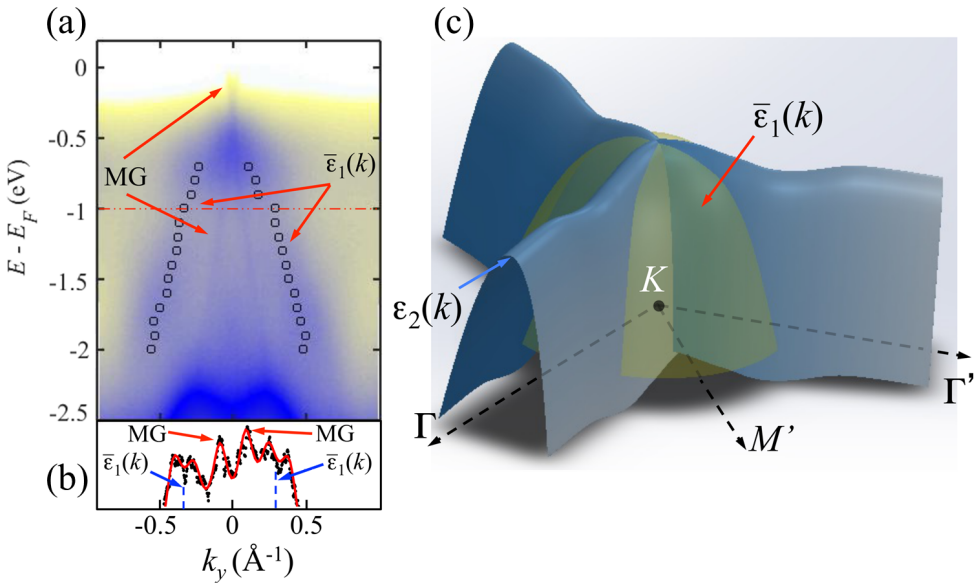

Figure 2.9: (a) ARPES image at the graphene K point. $\bar{\varepsilon}_1$ from buffer can be seen, in addition to a weak Dirac cone from partial monolayer graphene (MG). (b) MDC cut of the ARPES image at $E - E_F = -1.0$ eV, depicted with a dashed red line in (a). The splitting in $\bar{\varepsilon}_1$ can be seen. (c) Schematic of $\bar{\varepsilon}_1$ and ε_2 near the K point. For the ARPES image in (a), $h\nu = 70$ eV.

ε_1 and ε_2 in three ARPES cuts. Figure 2.8(a) shows a Fermi surface (constant energy) ARPES cut through part of the Brillouin zone of a graphene buffer layer near the ε_1 band maximum. Three lobes are visible; these lobes represent the three-fold symmetric ε_2 band, which extends along Γ-K and disperses perpendicular to Γ-K. Figure 2.8(b) is an ARPES image in the Γ- K-M' direction. ε_1 and ε_2 are seen, in addition to a Dirac cone from a small amount of monolayer. Figure 2.8(c) shows a cut perpendicular to Γ-K through the ε_2 lobe, as indicated by the dashed line in Fig. 2.8(a).

The ε_1 band disperses slower perpendicular to Γ-K than along either Γ-K or K-M. The linear part of ε_1 has a velocity v that is significantly lower than the Fermi velocity v_F, reducing to nearly half v_F perpendicular to Γ-K (see Table 2.1). As a result, ε_1 has an effective mass (m^*) that ranges from 0.55 to $1.5m_e$. Similarly, ε_2 is a light band perpendicular to Γ-K but has a smaller dispersion (larger m^*) along Γ-K. The band velocity of ε_2 perpendicular to Γ-K is nearly the same as monolayer graphene (see Table 2.1). A schematic of the two bands is shown in Fig. 2.9(c).

Figure 2.9(a) is an ARPES cut at the graphene K point. Taking a momentum distribution curve (MDC) through the K point, seen in Fig. 2.9(b), actually reveals that ε_1 is split into two bands. In the MDC, three sets of bands are observed: one set from the partial monolayer, and another set from the split pair of bands recognized as $\varepsilon_1(k)$. Even though the split bands have a Δk width that is only 12% wider than the monolayer graphene bands, their splitting (< 0.13 Å^{-1}) and the background level make them difficult to resolve. Therefore, in this work, we will now refer to these bands by their average dispersion $\bar{\varepsilon}_1(k)$.

The two bands $\bar{\varepsilon}_1$ and ε_2 are independent of the perpendicular momentum $k_\perp(E)$. Therefore, the bands must originate from a two-dimensional system and cannot be due to bulk bands. As previously mentioned, the tops of both bands lie $E - E_F \sim -0.5$ eV. Because ARPES does not measure unfilled states, the energy of the conduction band

minimum is not yet known. However, the full bandgap for the buffer layer must be at least $\Delta E = 0.5$ eV, indicating that the buffer layer is a semiconducting form graphene with a bandgap suitable for real electronics applications.

Table 2.1: Band velocity and effective mass (m^*) near the π-band maximum. m^* is estimated assuming parabolic bands.

Band	v/v_F	m^*/m_e
ML Dirac cone	1.0	-
$\bar{\varepsilon}_1$ ($\perp \Gamma K$)	0.55 ± 0.01	1.00 ± 0.02
$\bar{\varepsilon}_1$ (ΓK)	0.63 ± 0.1	1.5 ± 0.5
$\bar{\varepsilon}_1$ (KM)	0.80 ± 0.1	0.55 ± 0.05
ε_2 ($\perp \Gamma K$)	0.98 ± 0.07	0.25 ± 0.02
ε_2 (ΓK)	$\gtrsim 10^{-3}$	1.5 ± 0.1

While any periodic potential that breaks the sublattice symmetry in graphene can open a bandgap at the K point (e.g., through bonding, chemical modification, strain fields, or finite size effects), it is unlikely that the bandgaps observed in the buffer layer band structure originate from anything but a well-ordered substrate interaction. Experiments that show H-passivation reversibly creating metallic graphene from buffer layer by saturating bonds to the SiC support the idea that the buffer layer bandgap is created by a substrate interaction [90, 91]. Recent x-ray diffraction measurements and tight binding calculations also support this conclusion [60]. Therefore, periodic bonding of the buffer layer to the underlying substrate remains the most likely source of the chiral symmetry breaking.

2.3 Theoretical Calculations of Buffer Layer Band Structure

The buffer layer exhibits a $(6\sqrt{3}\times 6\sqrt{3})$R30° pattern in LEED (henceforth abbreviated as $6\sqrt{3}$), in the same way that a monolayer Si-face epitaxial graphene film does. Thus, it has been believed until recently that the buffer layer must be commensurate with the substrate over the $6\sqrt{3}$ unit cell. Unfortunately, the size of the $6\sqrt{3}$ unit cell makes theoretical calculations for the band structure of buffer computationally difficult.

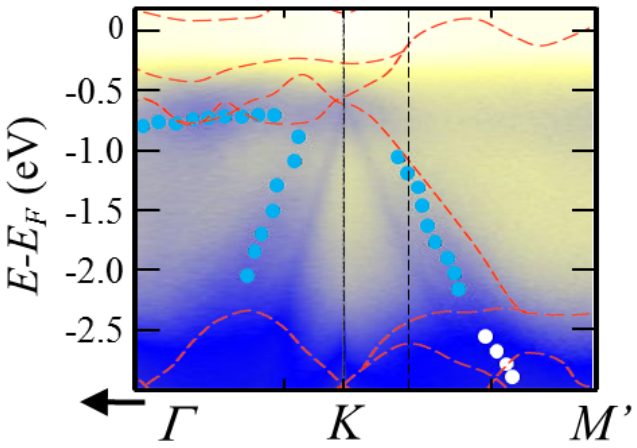

Figure 2.10: Overlay of the theoretical buffer band structure (shown with dashed red lines), as calculated in Ref. [94], with an ARPES image of the buffer layer band structure along the Γ-K-M' direction. Circles represent the location of the experimentally measured buffer layer bands, as determined by fits to MDCs. While the calculated band structure is not semiconducting, the dispersion predicted in the K-M' direction is comparatively similar to the measured band structure. For the ARPES image, $h\nu = 70$ eV.

Several early attempts to predict the band structure of the buffer layer utilized a strained $\sqrt{3}\times\sqrt{3}$ R30 SiC reconstruction to make calculations more tractable; these predicted the buffer layer would only possess weakly-dispersing states near the Fermi level [92, 93]. Only one *ab initio* calculation utilized a full $6\sqrt{3}$ unit cell, with bulk terminated SiC beneath the buffer layer [94]. This calculation did not predict any gapped bands either [94], but it did show a band with dispersion similar to ε_1 between K and M. Figure 2.10 shows an overlay of the predicted band structure from Ref. [94] with the measured band structure of the buffer layer along the Γ-K-M′ direction.

Recently, it has been shown that the buffer layer is actually incommensurate with the substrate [60], and that the SiC bilayers directly beneath the buffer layer are not structurally equivalent to bulk SiC [95, 60]. Therefore, calculations performed using truncated, commensurate unit cells and bulk-terminated SiC are insufficient to fully predict the buffer layer band structure. Recent calculations that take into account the incommensurate structure correctly predict semiconducting buffer bands [60].

CHAPTER III

AN INTRODUCTION TO SIDEWALL GRAPHENE NANORIBBONS

3.1 Graphene Nanoribbons as a Form of Semiconducting Graphene

As previously discussed, isolated graphene is a semi-metal; it has no bandgap. If the goal to develop graphene-based electronics is to be fulfilled, a method for selectively creating a bandgap in graphene must be found. It has recently been confirmed that the buffer layer is a semiconducting form of graphene (see Ch. 2 for more information), with the top of the valence band at $E-E_F = -0.5$ eV, so the buffer layer is a promising candidate for use in graphene electronics development. However, if the conduction band near the K point lies just above the Fermi level E_F, then the total buffer layer bandgap would be 0.5 eV, which is small compared to that of currently used semiconducting materials (1.1 eV for Si, 0.67 eV for Ge, and 1.4 eV for GaAs [68]). Graphene nanoribbons (GNRs) are theorized to have quantum confinement-induced bandgaps dependent on edge structure and ribbon width [74, 76, 77]. Because the width of the ribbon is predicted to determine the size of the bandgap [74], GNRs would have a tunable bandgap determined by ribbon width, which would make them useful as a semiconducting material for graphene-based devices. Thus, much research has already been completed toward finding a feasible method for reproducibly fabricating graphene nanoribbons with specific edge structure and width.

3.2 Fabrication of Graphene Nanoribbons

Current fabrication methods for GNRs include self-assembled GNRs from molecular precursors; flat, lithographically patterned GNRs from EG, exfoliated, and CVD

graphene; and sidewall epitaxial GNRs. As previously discussed in Chapter 1, self-assembled GNRs can be created with very specific edge structures and widths from carbon-containing monomers [39], but metallic substrates are required. Thus, for use in a device, the nanoribbons would need to be transferred to a different substrate. Also, the location and orientation of the self-assembled nanoribbons with respect to the formation substrate are both generally unconstrained. Locating the ribbons for transfer would require further steps in the device fabrication process and would result in additional orientational uncertainty upon transfer to the final desired substrate. Therefore, considerable processing modifications would be required to make such fabrication methods compatible with industrial-scale electronics production, a research effort that has not proven successful over the past two decades. Current fabrication methods for GNRs include self-assembled GNRs from molecular precursors; flat, lithographically patterned GNRs from EG, exfoliated, and CVD graphene; and sidewall epitaxial GNRs. As previously discussed in Chapter 1, self-assembled GNRs can be created with very specific edge structures and widths from carbon-containing monomers [39], but metallic substrates are required. Thus, for use in a device, the nanoribbons would need to be transferred to a different substrate. Also, the location and orientation of the self-assembled nanoribbons with respect to the formation substrate are both generally unconstrained. Locating the ribbons for transfer would require further steps in the device fabrication process and would result in additional orientational uncertainty upon transfer to the final desired substrate. Therefore, considerable processing modifications would be required to make such fabrication methods compatible with industrial-scale electronics production, a research effort that has not proven successful over the past two decades.

Flat graphene sheets can be fabricated through a number of methods, including mechanical exfoliation of graphite, chemical vapor deposition, and thermal decomposition of SiC. Subsequent lithographic steps can then be taken to pattern the flat

graphene into GNRs. However, lithographic patterning of GNRs from flat graphene presents many processing problems. With current technology, lithographic resolutions prevent ribbons from being patterned with widths less than $\sim 10 - 20$nm[1]. Edges in such ribbons are extremely disordered, very far from being atomically precise [97]; and much smaller widths are required by theory to open a bandgap comparable to that of silicon[2] [78].

Also, for graphene fabrication methods that require transfer from the original substrate to a final desired substrate (e.g., exfoliated or CVD graphene), the transfer process necessarily results in orientational uncertainty as well as copious structural defects. Because precise orientation of the graphene sheet is critical for patterning ribbons with specific edge structure, such rotational uncertainty would render atomically specific edge structures unobtainable, even if lithographic resolutions were not an issue. Epitaxial graphene grown on the Si-face of SiC does not need to be transferred and always forms with a known orientation, thus reducing many sources of disorder and structural uncertainty in the GNR fabrication process. Nevertheless, GNRs patterned from flat sheets of EG still suffer from lithographic resolution limits. Therefore, for the viable creation of reproducible, atomically precise, narrow GNRs, another method for production must be used.

In this Chapter, it will be presented that sidewall graphene nanoribbons on SiC provide the most reliable method for fabricating well-ordered GNRs with known location and orientation on a substrate compatible with device fabrication (no transfer necessary). The remainder of the Chapter will then discuss the sidewall nanoribbon fabrication process, describe the geometry of sidewall GNRs, demonstrate the

[1] $\sim$ 10nm features can now be patterned, but patterning such small features requires isolation from all other lithographic features [96].

[2] Experimental data suggests that when bandgaps are observed in flat, lithographically-patterned GNRs, the gap results from edge roughness instead of quantum confinement [97] and would therefore not be repeatable enough for large scale production.

implications of sidewall GNR geometry on characterization measurements, and discuss the fundamental structural differences between the two primary types of sidewall nanoribbons.

3.3 Sidewall Graphene Nanoribbons

While lithographic patterning of flat graphene cannot produce ribbons with atomically-ordered edges, reactive ion etching (RIE) of SiC can be performed consistently with depths < 5nm and overall roughness on the order of ~ 1 nm across a macroscopically large pattern [43, 44]. Because it has been shown that graphene can form on many facets of SiC [98, 43, 44, 65], GNRs can be grown on sidewalls of trenches etched into the SiC. Such GNRs have widths determined by etch depth, not dependent on lithographic resolutions but only on plasma etching parameters. Consequently, the width of the sidewall ribbon can be specified as desired. Narrow ribbons with widths less than that of the smallest lithographically patterned ribbons can be created by etching shallow trenches, without edge roughness due to lithographic resolutions (although other difficulties are discovered in trying to grow epitaxial graphene on shallow trenches; see Chapter 4 for more information). The only pattern feature affected by the lithographic resolution is the maximum areal density of sidewall trenches.

Graphene grown on the Si-face of SiC has a known crystalligraphic orientation with respect to the substrate, which removes the orientational uncertainty associated with other ribbon patterning methods. Also, graphene growth has been observed to be continuous (maintain crystallographic orientation) over steps [43, 98, 65, 4, 99, 100]. Consequently, GNRs can be formed on the sidewalls of trenches with known atomic edge structure. All of these factors are extremely important, implying that well-ordered GNRs can be patterned on a substrate from which transfer is not necessary, in the desired final location, using processing techniques that are compatible with large-scale electronics production. Therefore, due to the abundantly enumerated

factors, sidewall GNRs are a viable option for graphene-based electronics.

3.3.1 Patterning and Growth of Sidewall Graphene Nanoribbons

The patterning process which creates sidewall graphene nanoribbons is straightforward and compatible with current lithographic processes used in industry. Figure 3.1 depicts the steps of the patterning process. First, a SiC sample is cleaned and, if necessary, H-etched to form a well-ordered SiC(0001) surface. Then, spin-coating a uniform layer of resist prepares the sample for lithography. Two types of resist exist and are chosen based on the desired pattern parameters: positive resists (e.g., ZEP520a and PMMA) and negative resists (e.g., HSQ). Exposing and developing the resist creates the desired pattern on the SiC, dependent on which type of resist is used; during development, positive resist is removed from the substrate where it has been exposed, while negative resist remains on the substrate where it has been exposed. A positive resist would be used if the surface areas needing to be etched are small compared to the size of the sample, whereas a negative resist would be used if the surface areas needing to be etched are large. Finally, etching with a SF_6-O_2-Ar plasma forms trenches with the intended orientation and location on the substrate. Any remnants of the resist are removed prior to heating the sample for graphene growth. Specific details concerning the processing used for samples presented in this work can be found in Appendix A, and further specifications about post-patterning growth steps will be discussed in detail in Chapters 4 and 5.

3.3.2 Geometry of Sidewall Graphene Nanoribbons

There are two primary graphene crystal directions, the armchair and zigzag directions. Correspondingly, GNRs with edges along the primary directions are called armchair and zigzag nanoribbons, respectively, depicted in Fig. 3.2 (b) and (c). Knowing the orientation of graphene grown on the Si-face of SiC, Fig. 3.2(a) shows the graphene primary directions with respect to SiC crystallographic directions. Depending on

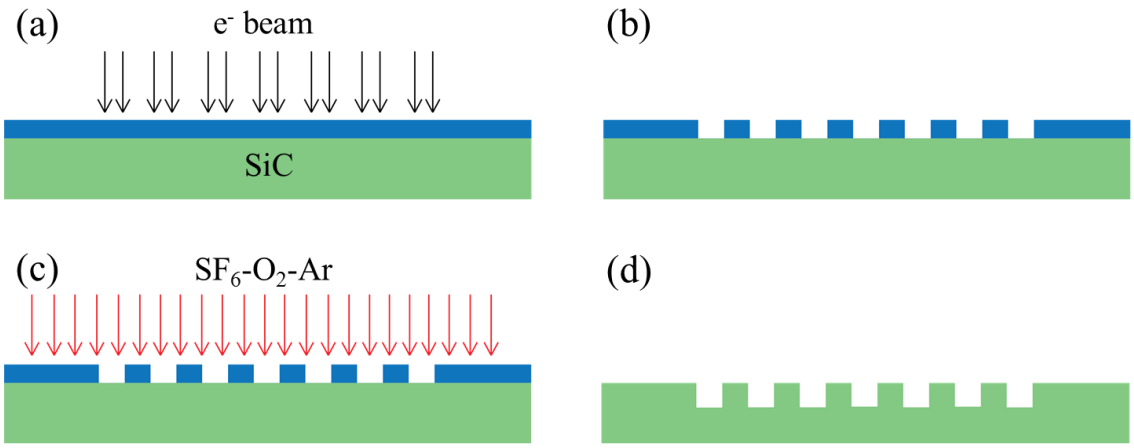

Figure 3.1: (a) e-beam resist is spin-coated onto a clean, well-ordered Si-face sample. The resist is then exposed with electrons, with features oriented along the intended crystal direction and in the desired location on the substrate. (b) After exposure, the resist is developed. (c) A SF_6-O_2-Ar plasma is used to etch trenches into the SiC, with a desired depth. (d) Any remaining resist is removed from the sample prior to graphene growth.

the desired graphene ribbon edge structure, trenches can be etched along one of the two graphene crystal directions to create sidewall graphene with either armchair- or zigzag-edges. Shown in Fig. 3.3, the $\{1\bar{1}00\}$ family of facets are armchair facets (creating armchair-edge sidewall graphene), while the $\{11\bar{2}0\}$ family of facets are zigzag facets (creating zigzag-edge sidewall graphene).

Upon initial heating, it is known that both armchair and zigzag trench walls facet outward. As a result, the facet angle changes from $\theta_F \sim 90°$ to an angle $\theta_F \neq 90°$. That is to say, the $(1\bar{1}00)$ and $(11\bar{2}0)$ facets become $(1\bar{1}0n)$ and $(11\bar{2}m)$ respectively, with $n, m \neq 0$. As an additional result of this faceting, a small shrinkage in the patterned width of the trench top is observed due to mass diffusion as the vertical facet walls transform into more stable, angled crystal facets. Figure 3.4 depicts both aspects of this transformation.

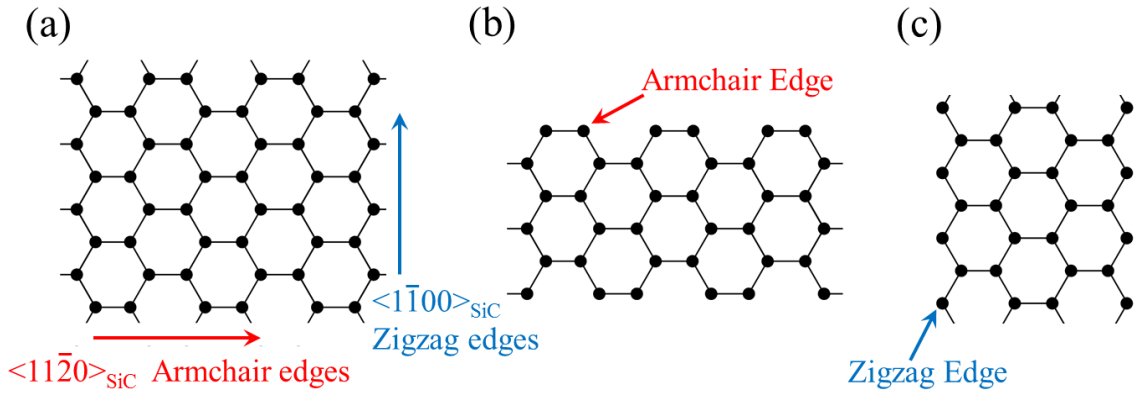

Figure 3.2: (a) Graphene lattice, with SiC directions indicated for orientation of graphene on Si-face. The $<1\bar{1}00>_{SiC}$ direction corresponds to the zigzag graphene edge, and the $<11\bar{2}0>_{SiC}$ direction corresponds to the armchair graphene edge. (b) Graphene armchair ribbon, with armchair edge indicated. (c) Graphene zigzag ribbon, with zigzag edge indicated.

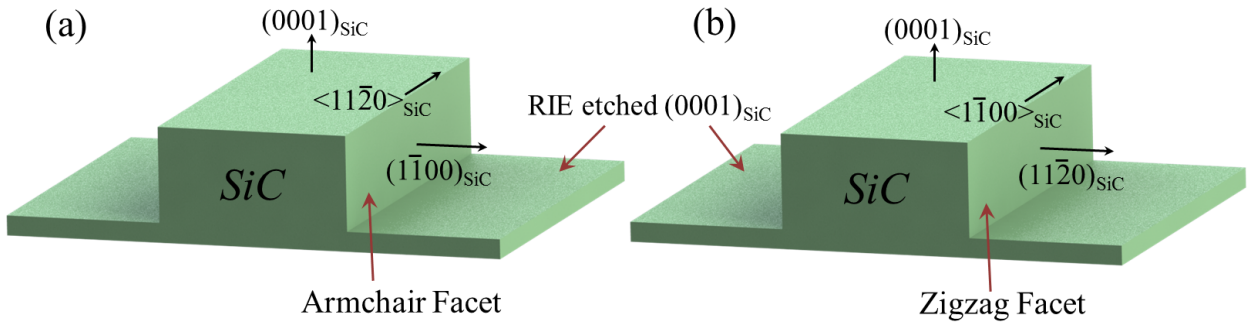

Figure 3.3: (a) An armchair trench after patterning. The trench tops and trench bottoms are SiC(0001). The trenches are etched such that the edge runs along the armchair direction, $<11\bar{2}0>_{SiC}$. The as-patterned trench wall is SiC($1\bar{1}00$). (b) A zigzag trench after patterning. Likewise, the trench tops and trench bottoms are SiC(0001). The trenches are etched such that the edge runs along the zigzag direction, $<1\bar{1}00>_{SiC}$. The as-patterned trench wall is SiC($11\bar{2}0$).

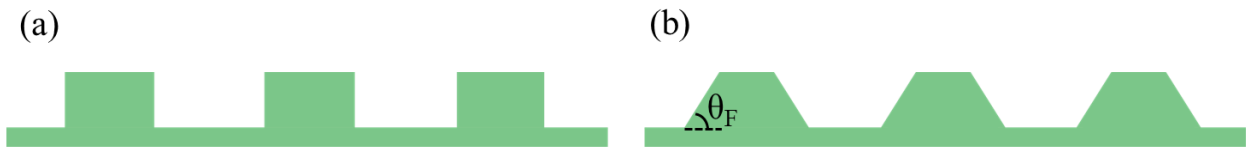

Figure 3.4: (a) SiC trenches, as patterned. (b) SiC facets after growth. $\theta_F \neq 90°$.

3.3.3 Reciprocal Space/Real Space Geometry Correlations

The surface characterization techniques ARPES and LEED measure properties of a material's reciprocal space structure. Note that surface sensitive material characterization techniques only allow for the measurement of the portions of a Brillouin zone which are parallel to the surface being probed. Samples that are flat and uniform in composition/structure show only one Brillouin zone (BZ), observed in a plane parallel to the surface. However, as soon as a material exhibits a non-trivial topography, measurements of bands or diffraction rods become convoluted with their topographical angle, showing Brillouin zones parallel to each tilted surface. Sidewall ribbon samples contain several topographical features of interest. First, trench tops and trench bottoms, for on-axis samples, are SiC(0001) and have a Brillouin zone parallel to the (0001) surface. Second, sidewalls with facet angles $\theta_{\mathrm{F}} \neq 90^{\circ}$ have Brillouin zones which are tilted by θ_{F} compared to the (0001) surface normal. An illustration of this effect is shown in Figs. 3.5 and 3.6. It is important to note that there are no distortions to the sidewall graphene Brillouin zone as a result of the surface being tilted compared to the macroscopic surface normal; the Γ-K and Γ-M distances remain the same.

Understanding that faceted surfaces have tilted Brillouin zones leads to several conclusions for surface characterization techniques. In LEED, diffraction rods from sidewall graphene are tilted by facet angle θ_{F} relative to the rods from SiC and graphene on the SiC(0001). In ARPES, for all sample surfaces, the sample is sufficiently far away from the detector for the illuminated portion of the sample to be considered a point source. Therefore, all bands are measured using angles θ and ϕ relative to the macroscopic surface normal $\hat{\mathbf{n}}_0$, where $\hat{\mathbf{n}}_0$ is the surface normal for the SiC(0001). See Section 1.6.1 for a diagram showing the θ and ϕ axes. The bands at the SiC(0001) Γ point are measured at $(\theta, \phi) = (0^{\circ}, 0^{\circ})$. The angle needed to measure the Dirac cone at the Si-face graphene K point can be determined by Eqns. 1.3 and

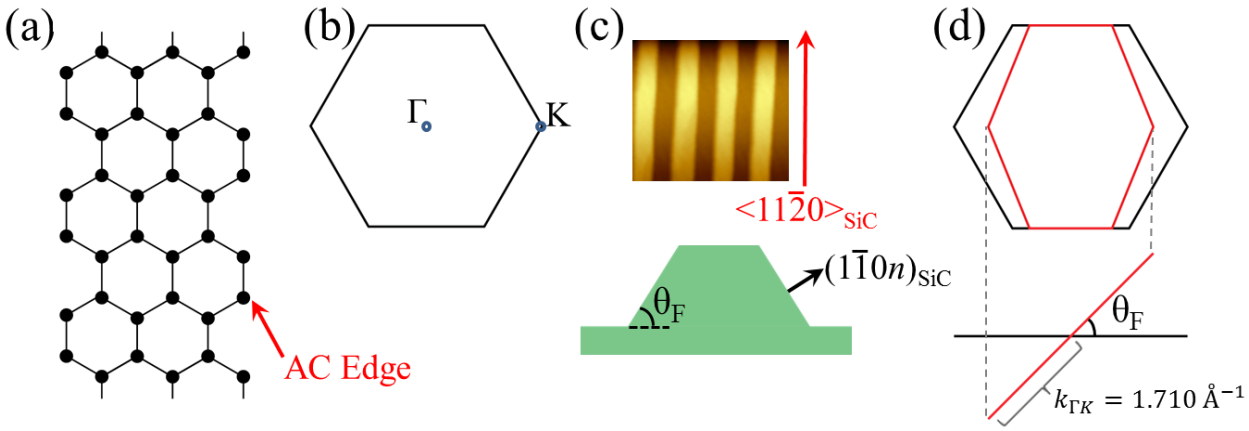

Figure 3.5: (a) Lattice for an armchair nanoribbon. (b) Brillouin zone for flat graphene, with the appropriate orientation to be consistent with the lattice orientation in (a). (c) Upper- AFM image depicting the trench orientation necessary to create armchair sidewall graphene nanoribbons, assuming the orientation of graphene on the SiC(0001) is the same as that in (a). Lower- Diagram showing the armchair facet $(1\bar{1}0n)$, with facet angle θ_{F}. (d) The two Brillouin zones for a sidewall ribbon sample with graphene on both trench tops and sidewalls. The black Brillouin zone is for graphene on the SiC(0001), whereas the red Brillouin zone is depicted for graphene on the sidewall, tilted by an angle θ_{F} compared to the flat Brillouin zone.

1.4, with $k_x = 1.710\text{Å}^{-1}$ and $k_y = 0$. Thus,

$$\theta_{\mathrm{K}} \approx \arcsin\left(\frac{1.710}{0.512\sqrt{E_S - E_F - \Phi}}\right) \tag{3.1}$$

where 0.512 comes from the physical constants $\frac{\sqrt{2m_e}}{\hbar}$. The Fermi level E_F and work function Φ are constants. So, then, θ_{K} for graphene is only determined by the photon energy, $E_S = h\nu$. This angle θ_{K} is the same between both the SiC(0001) Γ and K points and between the facet normal and the K point for the tilted graphene Brillouin zone (see Fig. 3.7(a)). Because the sample can be considered a point source, the experimentally measured angle for a graphene Dirac cone from a tilted surface is not observed as a projection onto the SiC(0001) Brillouin zone but is instead observed with additive angular components,

$$\theta_{\mathrm{meas}} = \pm|\theta_{\mathrm{F}}| \pm |\theta_{\mathrm{K}}| \tag{3.2}$$

Here, θ_{meas} is the angle where the facet cone is observed by the detector, measured relative to the macroscopic surface normal $\hat{\mathbf{n}}_0$; θ_{F} is the facet angle; and θ_{K} is

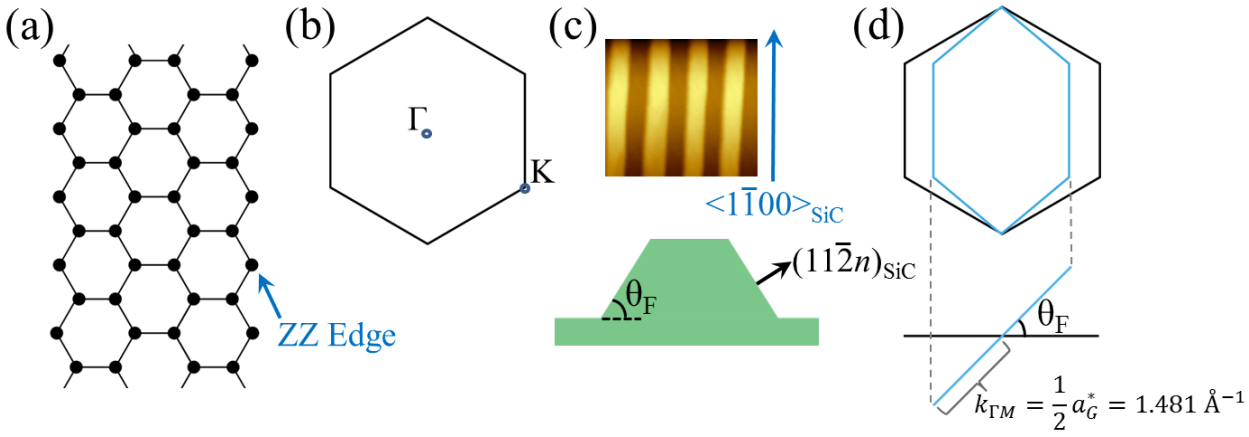

Figure 3.6: (a) Lattice for a zigzag nanoribbon. (b) Brillouin zone for flat graphene, with the appropriate orientation to be consistent with the lattice orientation in (a). (c) Upper- AFM image depicting the trench orientation necessary to create zigzag sidewall graphene nanoribbons, assuming the orientation of graphene on the SiC(0001) is the same as that in (a). Lower- Diagram showing the zigzag facet (11$\bar{2}n$), with facet angle θ_F. (d) The two Brillouin zones for a sidewall ribbon sample with graphene on both trench tops and sidewalls. The black Brillouin zone is for graphene on the SiC(0001), whereas the blue Brillouin zone is depicted for graphene on the sidewall, tilted by an angle θ_F compared to the flat Brillouin zone.

determined by Eqn. 3.1. Figure 3.7(c) illustrates the additive nature of the angular measurements. For the particular K point being measured, K_{F+-}, $\theta_{meas} = \theta_F - \theta_K$. The choice of signs in Eqn. 3.2 (upper or lower) depends on which facet and K point are being measured.

In order to correctly analyze characterization data, the complications which arise from having both tilted and flat Brillouin zones need to be considered. First, it is important to note that the crystallographic direction of the etched trench, relative to the orientation of the Brillouin zone for graphene on the (0001), directly affects the reciprocal space rotation axis for the tilted Brillouin zone. Thus, the crystallographic trench direction changes the reciprocal space direction where facet cones are expected. Expounding upon Figs. 3.5(d) and 3.6(d), which show the tilted Brillouin zones for armchair and zigzag facets, Fig. 3.8 illustrates that armchair facet cones are expected along the K_{+0}-Γ-K_{0-} direction (Fig. 3.8(a)), while zigzag facet cones are expected

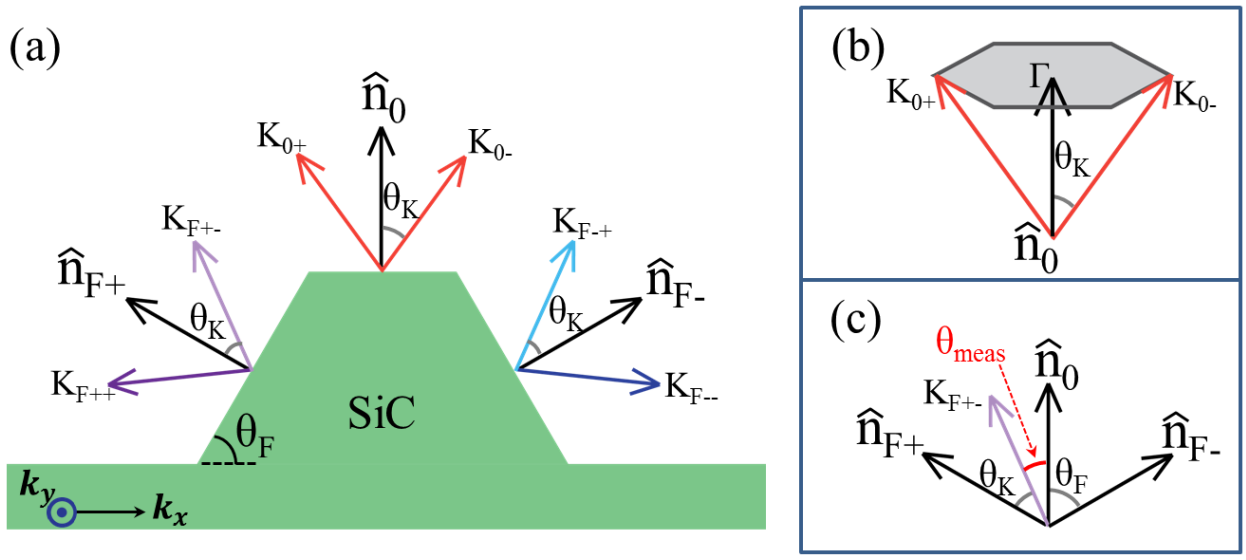

Figure 3.7: (a) Depiction of a sidewall ribbon sample, assuming only one type of facet. The macroscopic surface normal is $\hat{\mathbf{n}}_0$, the normal for the SiC(0001). Dirac cones for graphene on the trench tops would be measured at $\pm\theta_K$; the exact value of θ_K is determined by the photon energy. Two facets are shown, with surface normals $\hat{\mathbf{n}}_{\mathbf{F}-}$ and $\hat{\mathbf{n}}_{\mathbf{F}+}$. The angle required to measure the Dirac cones at the K points of the tilted Brillouin zones is still θ_K, relative to the facet normals. (b) Depiction of the origin of θ_K . $\theta = 0°$ is the angle where the Γ point is measured, and θ_K is the angle where the K point is measured. (c) Depiction of the experimental measurement of sidewall graphene Dirac cones. The sample is far enough away from the detector to be a point source. Thus, the experimental measurement of a Dirac cone from the sidewall is determined relative to the macroscopic surface normal $\hat{\mathbf{n}}_0$. The facet cone being measured (K_{F+-} in (a)) is observed at angle $\theta_{meas} = \theta_F - \theta_K$.

along the K'_{0+}-K'_{0-} direction (Fig. 3.8(b)).

Because the k-space location of a band is measured strictly as a function of angle, there is a disconnect between reciprocal space measurements and real space translational features; two different crystal surfaces (separated in physical space and possessing different surface normals) may have electronic bands which overlap in θ- and ϕ-space over some angular range, even though they are structurally unrelated and completely independent features. In a generalized example, a photon energy is chosen in ARPES such that the Dirac cone at the K point for flat graphene on the SiC(0001) is observed at θ_K, while a band from a tilted crystal surface is observed at an angle $\theta_{meas} = |\theta_{band}| - |\theta_F|$ for the same photon energy. Here, θ_{meas} is the angle

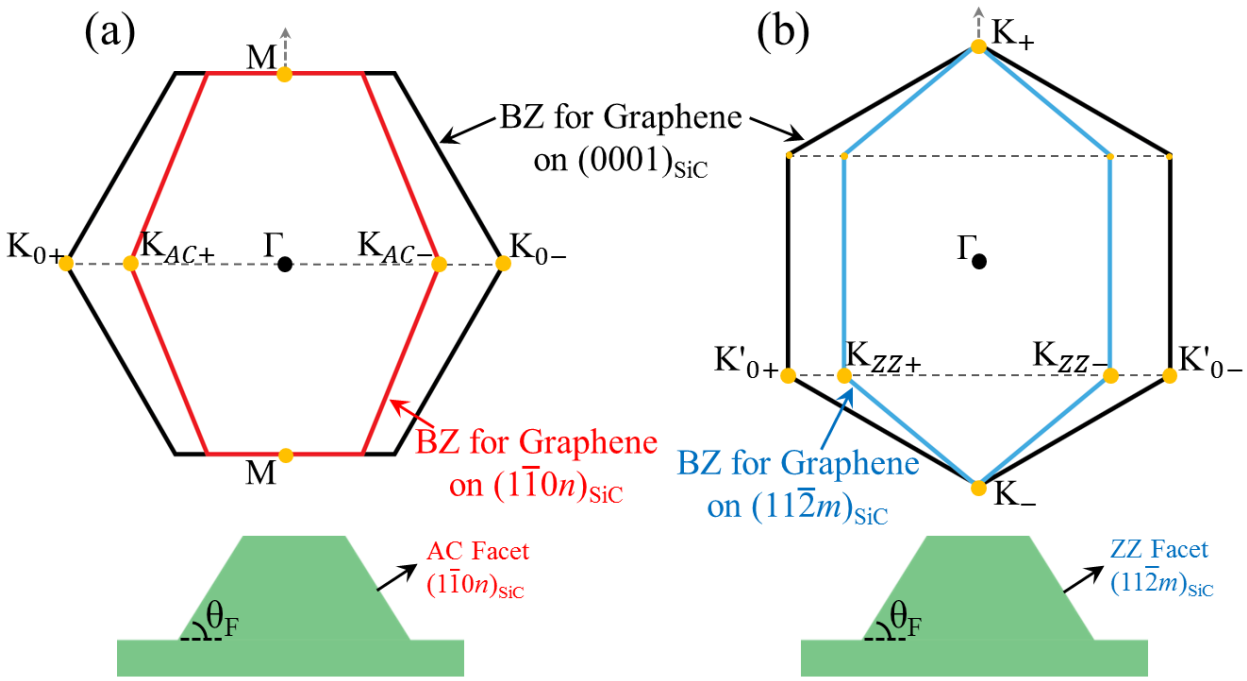

Figure 3.8: (a) Depiction of the Brillouin zones for an armchair sidewall graphene sample. The black Brillouin zone is for graphene on the SiC(0001), and the tilted red Brillouin zone is for graphene on the armchair sidewall. Because of the orientation of the trenches, the sidewall Brillouin zone is tilted with a rotation axis along the M-Γ-M direction. Thus, armchair graphene facet cones would be expected to be observed along the K_{0+}-Γ-K_{0-} direction, as shown. (b) Depiction of the Brillouin zones for a zigzag sidewall graphene sample. The black Brillouin zone is for graphene on the SiC(0001), and the tilted blue Brillouin zone is for graphene on the zigzag sidewall. Because of the orientation of the trenches, the sidewall Brillouin zone is tilted with a rotation axis along the K_{+}-Γ-K_{-} direction. Thus, zigzag graphene facet cones would be expected to be observed along the K'_{0+}-K'_{0-} direction, as shown.

where the facet band is measured by the detector relative to the macroscopic surface normal $\hat{\mathbf{n}}_0$; θ_{F} is the angle of the crystal facet relative to $\hat{\mathbf{n}}_0$; and θ_{band} is determined by the photon energy and the reciprocal space location (k_x, k_y) of the band in the tilted Brillouin zone (with the Γ point of the tilted Brillouin zone at $(k_x, k_y) = (0, 0)$. See Fig. 3.9(b). For most cases being considered, facet bands are expected to have $\phi_{\mathrm{band}} = 0°$, so θ_{band} would then be determined by Eqn. 1.3, which leads to

$$\theta_{\mathrm{band}} \approx \arcsin\left(\frac{k_x}{0.512\sqrt{E_S - E_F - \Phi}}\right) \tag{3.3}$$

Figure 3.9 can be used to illustrate this general example. It is possible for θ_{F} and θ_{band} to be angular values such that $\theta_{meas} = \theta_{\mathrm{K}}$; if so, both the band from the tilted surface and the Dirac cone from graphene on the SiC(0001) would be measured in the same ARPES θ-cut, even though the bands are structurally unrelated. An experimental way to determine if two bands measured at the same angle θ are related to the same physical surface is to change the photon energy and take a new measurement at the appropriate angle, as determined by Eqn. 3.3 for the new source energy. Specifically, choosing a different photon energy would change the values of θ_{K} and θ_{band} via Eqns. 3.1 and 3.3. If the bands both originate from the same surface, then the k-space distance between them $(\Delta k_x, \Delta k_y)$ would be maintained. However, if the bands originate from different surfaces, then the new angular locations of the bands would be unrelated to each other and only determined by the k_x and k_y values for each band in reference of their surface's Brillouin zone.

3.4 Preliminary Comparison of Growth on Armchair- and Zigzag-Oriented Facets

Characterization measurements used to directly compare the two primary types of sidewall graphene nanoribbons suggest that armchair and zigzag sidewall graphene nanoribbons are not structurally or electronically equivalent. Just as the Si-face and

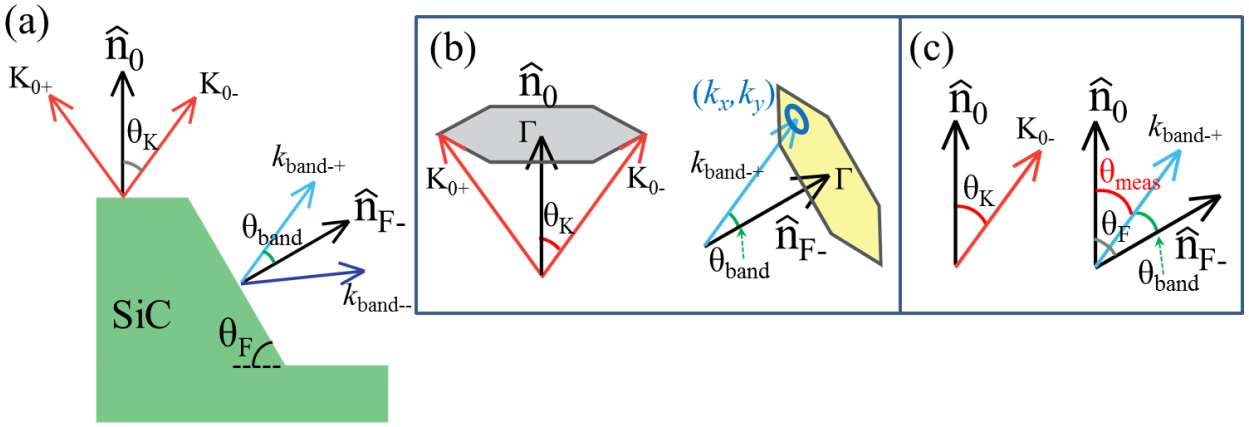

Figure 3.9: (a) Depiction of a sidewall ribbon sample. The macroscopic surface normal is $\hat{\mathbf{n}}_0$, the normal for the SiC(0001). Dirac cones for graphene on the trench tops would be measured at $\pm\theta_K$; the exact value of θ_K is determined by the photon energy. One facet is shown, with surface normal $\hat{\mathbf{n}}_{F-}$. The angle for a band originating from the sidewall, relative to the facet surface normal $\hat{\mathbf{n}}_{F-}$, is θ_{band}. (b) Depiction of the origin of the angles θ_K and θ_{band}. The hypothetical sidewall band of interest is located (k_x, k_y) away from the Γ point of the sidewall Brillouin zone. The angle θ_{band} is determined by (k_x, k_y) and the photon energy. (c) Depiction of the experimental measurement of the bands. The sample is far enough away from the detector to be able to assume a point source. Thus, the experimental measurement of the hypothetical band from the sidewall is determined relative to the macroscopic surface normal $\hat{\mathbf{n}}_0$. The sidewall band from either facet would be measured at angle $\theta_{meas} = \pm|\theta_{band}|\pm|\theta_F|$. The specific facet and band location shown ($\hat{\mathbf{n}}_{F-}$ and k_{band-+}) would give $\theta_{meas} = |\theta_{band}| - |\theta_F|$.

C-face of SiC exhibit extremely different growth characteristics and substrate interactions, the armchair- and zigzag-oriented facets possess different sidewall graphene growth properties. The exact details of the differences as well as the characteristics known about each type of sidewall nanoribbon will be the topic of the next two Chapters of this work. However, an overview of the initially recognized differences between the two types of sidewall ribbons will now be given.

LEEM, PEEM, μ-ARPES, and μ-LEED measurements of armchair and zigzag sidewall ribbon samples suggest that the two ribbon types are not the same. In a specific experiment, armchair and zigzag trenches were patterned on the same sample and, consequently, were grown under identical conditions. Microscopy images (LEEM and PEEM) confirmed that the trenches were perpendicular to each other and oriented along the armchair and zigzag crystallographic directions appropriately. For the armchair sidewall ribbons, μ-ARPES measurements revealed a set of metallic Dirac cones at a k-space location appropriate for an armchair facet with $\theta_{\mathrm{F}} \approx 30^{\circ}$ (Fig. 3.10(b)).

Alternatively, the zigzag sidewall ribbons showed no metallic Dirac cone for any zigzag facet angle along the expected direction (K'_{0+}-K'_{0-}, Fig. 3.10(c)). Instead, μ-ARPES measurements of the zigzag trenches showed Dirac cone intensity along K_{0+}-Γ-K_{0-} (Fig. 3.10(d)), which is the direction expected for armchair facet cones (Fig. 3.10(a)). μ-LEED measurements also showed two sets of armchair diffraction rods, identified as rods from $(01\bar{1}n)$ and $(10\bar{1}n)$ armchair facets (see Fig. 5.6). Because microscopy images undeniably show that the zigzag trenches were etched along the zigzag direction, the conclusion reached from these μ-ARPES and μ-LEED measurements is that armchair nano-facets existed somewhere along the zigzag trench. This conclusion is not unreasonable considering that it has been previously shown that armchair facets appear to be thermodynamically preferred to zizag facets: miscut SiC samples as well as large circular islands patterned in SiC show a preference for

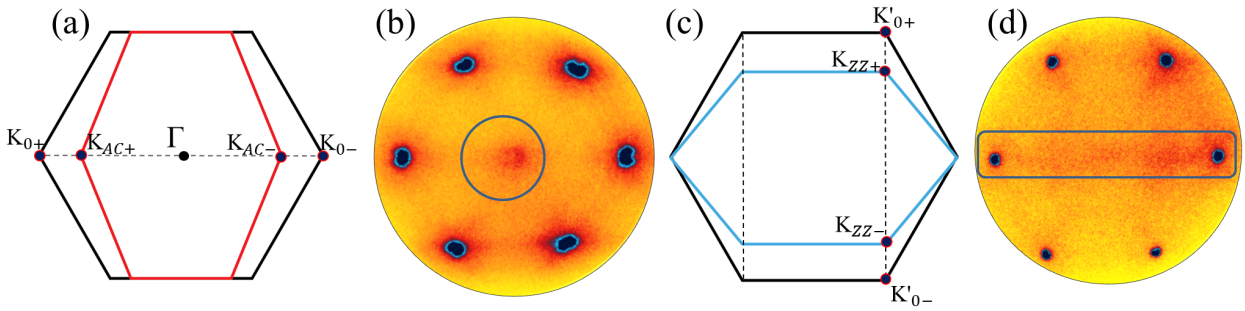

Figure 3.10: Preliminary comparison of armchair and zigzag structural differences. (a) Due to the tilting of the sidewall Brillouin zone, the metallic armchair facet cones would be expected along the dashed line, which is the K_{0+}-Γ-K_{0-} direction. (b) μ-ARPES image of the armchair sidewall sample ($E = 38$ eV, $h\nu = 44$ eV). Facet cone intensity is observed near Γ (inside the blue circle), consistent with an armchair facet angle of $\theta_F \approx 30°$. (c) Theoretically, the tilting of the zigzag facet Brillouin zone would give zigzag facet cones along the K'_{0+}-K'_{0-} directions, indicated by the dashed lines. (d) μ-ARPES image of the zigzag sidewall sample ($E = 37$ eV, $h\nu = 44$ eV). Instead of seeing zigzag facet cone intensity, weak facet cones are detected along the K_{0+}-Γ-K_{0-} direction, as would be expected for armchair facets (see (a)).

armchair facets [101, 55, 46]. It is probable that any small, local variation from the zigzag direction along the trench wall due to lithographic roughness resulted in nano-armchair facet formation and, therefore, a measurable coverage of armchair nano-facet metallic graphene.

The fact that armchair facets show metallic sidewall graphene while zigzag facets, grown under identical conditions, do not show any zigzag facet metallic graphene leads to one of two possible conclusions. Either zigzag facets require higher temperatures/longer times to grow metallic sidewall graphene compared to armchair facets, or the first layer of structural graphene on the zigzag facets is not electronic graphene, bonding to the substrate in a manner analogous to buffer layer on SiC(0001). It is important to note that even extremely disordered, corrugated exfoliated graphene produces a Dirac cone measurable by μ-ARPES [102]. Thus, if there were any metallic graphene present on the zigzag facets grown with these temperature and time parameters, a zigzag facet Dirac cone would have been observed. Further analysis of the μ-ARPES and μ-LEED data presented here, as well as additional LEEM, PEEM,

and ARPES measurements, will now be presented for armchair sidewall ribbons in Chapter 4, and for zigzag sidewall ribbons in Chapter 5.

CHAPTER IV

SIDEWALL GRAPHENE NANORIBBONS ON SIC$(1\bar{1}0N)$ FACETS: ARMCHAIR GRAPHENE NANORIBBONS

4.1 Creation of the First Armchair Sidewall Graphene Nanoribbons

Initial progress toward atomically-ordered graphene nanoribbons (GNRs) began with efforts to grow graphene on sidewalls of trenches etched into SiC. Graphene on the Si-face of SiC always grows with a known orientation, and growth has been shown to be continuous over steps [43, 98, 65, 4, 99, 100]. Thus, it was concluded that graphene nanoribbons should be able to grow on sidewalls of trenches etched into the Si-face with known orientation and atomically-ordered edge structure. Step bunching [55, 103, 104] and patterned circular pillars [46] on the Si-face show a predilection toward armchair facets. Research suggests that the propensity for the Si-face to create armchair facets could be due to surface energy minimization for such crystal faces [55, 105]. Also, early tight binding calculations [74] predicted that armchair GNRs with specific widths would be semiconducting while zigzag GNRs would not. Later calculations suggested that zigzag GNRs could also be semiconducting [76], but it was decided to begin work on sidewall GNRs by studying armchair-oriented patterned trenches.

While graphene grows on both the C-face and Si-face of SiC, it should not be taken for granted that graphene should grow in a well-ordered manner on all other facets as well. Even graphene growth on the two polar faces is considerably different in ultimate film thickness, growth rate, and substrate interactions: many layers can be grown quickly on the C-face with even the first layer showing linear dispersion characteristic

of ideal graphene; on the other hand, only a few layers can easily be grown on the Si-face, and the first layer closest to the substrate does not display the linear dispersion characteristic of ideal graphene (this "buffer" layer is, in fact, semiconducting; see Chapter 2). It was not known for certain whether graphene would grow on sidewalls etched into SiC in a controlled way, but because sidewall GNRs presented a promising opportunity for well-ordered graphene nanoribbons with atomically specific edges, research proceeded in efforts to determine if sidewall graphene could actually be formed.

Fortuitously, characterization measurements of the first armchair samples strongly suggested the existence of graphene on the sidewalls. Sprinkle et al [43] showed Raman spectroscopy mapping of a known graphene peak (the 2D peak) with significant intensity on the sidewalls, as well as cross-sectional TEM that indicated carbon layers. It was also observed that the sidewall had not remained $\sim 90^\circ$ but had faceted outward. The angle of the armchair facet was measured to be $\approx 24^\circ$, leading to the conclusion that it was a $(1\bar{1}0n)$ facet, with $n \approx 8$. However, Sprinkle et al suggested that the exact crystal facet structure achieved during growth might depend on processing and growth parameters [43].

After the promising initial indications that sidewall graphene could be created, further research efforts were spent in determining the structure and electronic properties of these armchair sidewall nanoribbons for future device development and fabrication. The remainder of this Chapter will review what was previously thought as well as what is now known about armchair graphene ribbon samples in light of further characterization experiments. New research will be presented, focusing on the improved fabrication, growth, and characterization of armchair sidewall GNRs. Details concerning the optimization of the growth recipe as well as experimental verification of the improved quality of the recipe will be discussed. A re-evaluation of initial data will then be given. Finally, an in-depth discussion of how improved growth techniques

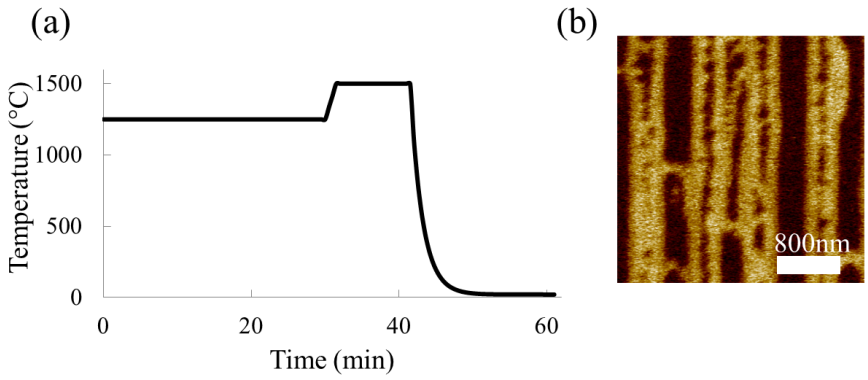

Figure 4.1: (a) Depiction of the preliminary recipe developed for armchair sidewall nanoribbons, A_{Sp}. The graph presents the recipe as macroscopically measured crucible temperature as a function of time. (b) EFM image of a sample grown with a recipe similar to that in (a). Growth time was 10min. The ribbons are not straight, and there is an indication of a significant amount of graphene on the sidewalls and trench tops. Scale bar is 800nm.

led to the discovery of a new form of semiconducting graphene will be presented.

4.2 Growth Methods Used to Create the First Armchair Sidewall Graphene Nanoribbons

All sidewall graphene samples discussed in this work were grown using Confinement Controlled Sublimation (CCS) to create epitaxial graphene nanoribbons on SiC. Sprinkle et al in Ref. [43] describe the growth procedure used at that time to fabricate sidewall graphene nanoribbons. After patterning trenches via lithography and RIE etching the SiC substrate (see Fig. 3.1 for a diagram of this process), two growth steps were used. First, samples were annealed at $T \approx 1200$ °C $- 1300$ °C for 30min. Then, the temperature was raised over the course of 1.5 min to reach the growth temperature, $T > 1450$ °C . Samples were grown at this temperature for ~ 10 min before being allowed to cool at a natural rate. This preliminary temperature and time recipe will now be referred to as the A_{Sp} recipe. Figure 4.1 depicts A_{Sp}, as well as electrostatic force microscopy (EFM) of a sample grown similarly.

The earliest samples grown with the recipe A_{Sp} contained > 2 graphene layers on the sidewall. TEM of an armchair sidewall in Ref. [43] shows many graphene layers

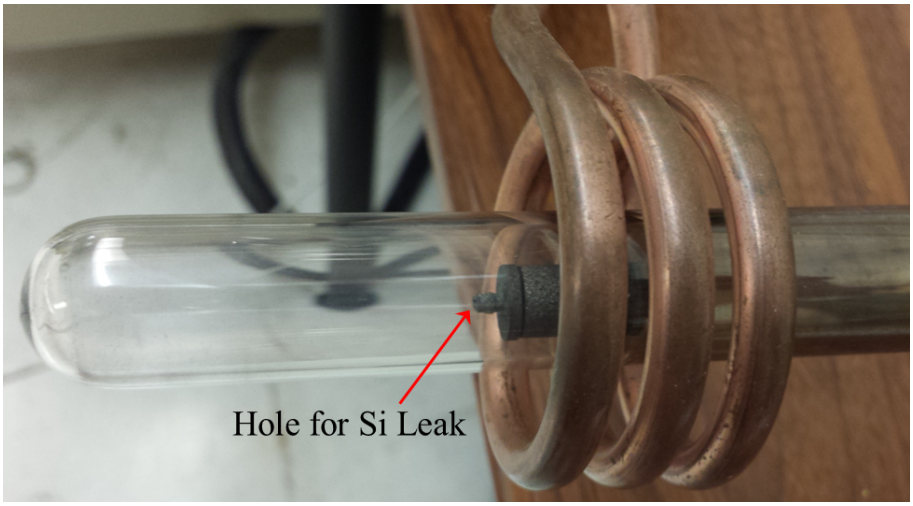

Figure 4.2: Picture of a CCS Furnace with the new, smaller crucible design. The crucible is ~ 1 cm in diameter and can be heated and cooled very quickly. The hole in the lid which allows for a leak of Si vapor pressure is indicated. Reference [52] contains further details about this type of furnace.

on the facet. These samples were grown in comparatively large crucibles ($\sim 2-3$ cm in diameter) inside an alumina susceptor; due to the size of the system being heated, this type of furnace took a non-trivial amount of time to reach the desired growth temperature. Development of a furnace with a smaller crucible (~ 1 cm in diameter) without a susceptor enabled quick variations in temperature. Such a furnace geometry is depicted in Fig. 4.2; see also Fig. 1.2. Reference [52] contains further details. Using this type of quick-heat/quick-cool furnace, a shorter and higher temperature recipe (henceforth called B_H) was tested for growth of dense arrays of trenches for ARPES experiments. The experiment in Ref. [44] by Hicks et al used samples grown with recipe B_H.

4.3 The First ARPES Band Structure Measurements of Armchair Sidewall GNRs

The first successful direct measurement of the band structure of sidewall graphene is seen in work by Hicks et al [44], which showed metallic Dirac cones that could have only come from graphene on the sidewall. Surprising to researchers at that time, more

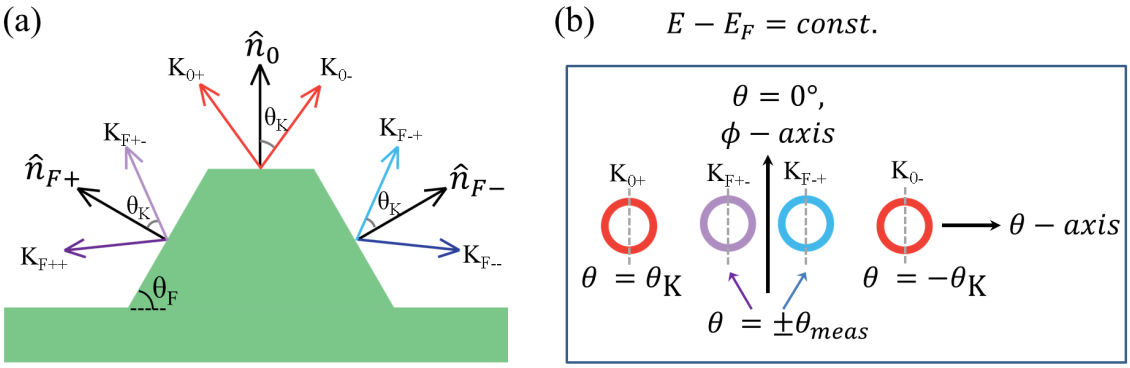

Figure 4.3: (a) Schematic of a sidewall sample with only one crystallographic facet (with angle θ_F). θ_K is the angle needed to reach the K point from the surface normal (either the trench top surface normal or the facet normals). (b) Depiction of an ideal Fermi surface (constant energy) with axes corresponding to θ and ϕ measured by the detector. The two K points from the trench tops K_{0+} and K_{0-} are shown by orange circles, measured at angles $\pm\theta_K$. The purple and blue circles represent facet cones from the K_{F+-} and K_{F-+} facet K points, respectively. K_{F+-} would be measured at angle $\theta_{meas} = |\theta_F - \theta_K|$, and K_{F-+} would be measured at $\theta_{meas} = -|\theta_F - \theta_K|$. $\theta_{meas} = 0°$ coincides with the trench top surface normal, $\hat{n}_0$.

Dirac cones were observed than would be expected for a single facet. Figure 4.3 shows a diagram for what would be expected to be measured in ARPES if only one type of crystallographic sidewall facet was present. The angle needed to reach the K point for graphene on the SiC(0001) trench tops, θ_K, is the same angle needed to reach the K point of the sidewall facets (relative to the facet surface normal); this is shown in Fig. 4.3(a). Figure 4.3(b) depicts an idealized Fermi surface with the locations of the facet cones in θ and ϕ. The circles represent constant energy cross sections of the Dirac cones. In ARPES experiments, the sample is sufficiently far from the detector to be treated as a point source. Thus, the macroscopically measured angles are additive. Facet cones would be expected to be measured at $\theta_{meas} = \pm|\theta_K| \pm |\theta_F|$, where θ_F is the facet angle. The two facet cones K_{F+-} and K_{F-+} experimentally observed between the two trench-top K points (K_{0+} and K_{0-}) at this photon energy would be measured at angles $\theta_{meas} = \pm|\theta_F - \theta_K|$.

Figure 4.4(a) shows a constant energy (Fermi surface) ARPES image of the data measured by Hicks et al. It is observed that there are two sets of angles measured for

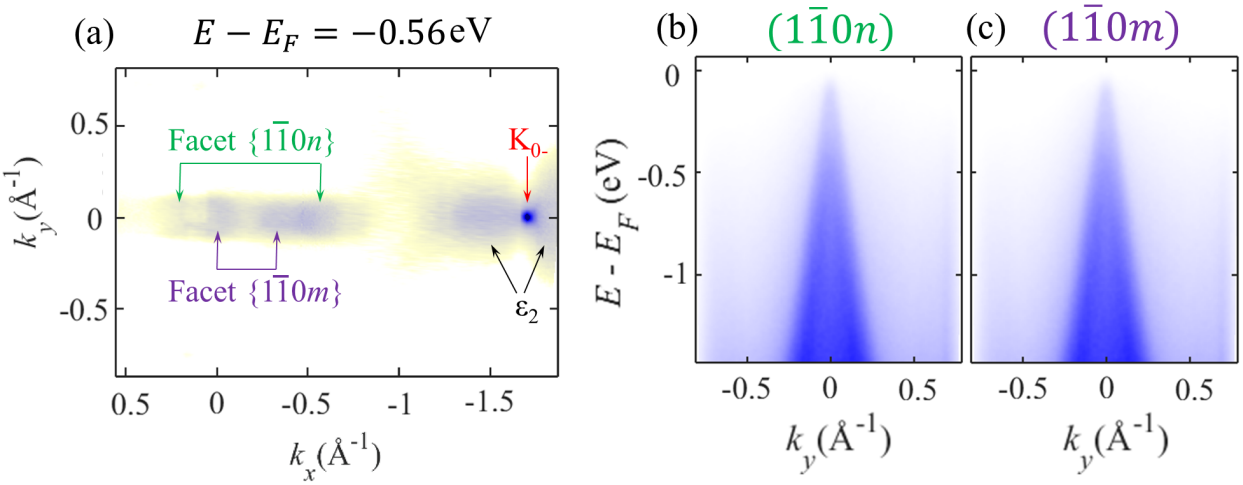

Figure 4.4: (a) ARPES Fermi surface ($E - E_F = -0.56$ eV) of a sample from Hicks et al [44], grown with recipe B_H. One K point from the trench top is measured, K_{0-}. ε_2 from buffer layer on the trench tops is observed in three lobes around K_{0-}. Two sets of facet cones are observed instead of only one, with measured angles $\pm\theta_{\mathrm{meas},n}$ and $\pm\theta_{\mathrm{meas},m}$. Because both $\theta_{\mathrm{meas},n}$ and $\theta_{\mathrm{meas},m}$ cannot be explained by a single crystallographic facet, they must necessarily originate from two different facets with indices $(1\bar{1}0n)$ and $(1\bar{1}0m)$. (b) ARPES k_x cut ($\theta_{\mathrm{meas}} \approx -7°$) of a $(1\bar{1}0n)$ facet cone. (c) ARPES k_x cut ($\theta_{\mathrm{meas}} \approx -1°$) of a $(1\bar{1}0m)$ facet cone. For all ARPES images, $h\nu = 36$ eV.

the facet cones, $\pm\theta_{\mathrm{meas},n}$ and $\pm\theta_{\mathrm{meas},m}$. Because there is no single armchair facet with facet angle θ_{F} that could produce cones at both sets of measured angles $\pm\theta_{\mathrm{meas},n}$ and $\pm\theta_{\mathrm{meas},m}$, it is necessary for there to be two unique crystallographic facets with facet angles, $\theta_{\mathrm{F},n}$ and $\theta_{\mathrm{F},m}$, consistently present in the sidewall structure.

For ARPES experiments, arrays of trenches are patterned with a typical pitch of $\sim$ 400 nm. Because the ARPES spot size is $\sim$ 50 μm, the intensity measured by the detector is consequently an average over hundreds of ribbons. Thus, the observation of facet cones of roughly equal intensity with two different facet angles indicates that two types of structural facets exist consistently across hundreds of sidewall structures. This new observation of two different facet angles is in agreement with the prediction by Sprinkle et al [43] that processing and growth parameters might affect the equilibrium sidewall facet structure. Given that samples measured by Hicks et al were grown with a significantly different recipe (B_H) than previous experiments

(A_{Sp}), it is unsurprising that the characterization measurements discovered a different structure.

While ARPES measurements clearly show the existence of two separate crystallographic facets, it is not immediately obvious from ARPES how the two facets coexist in real space. Two possibilities emerge: either the sidewalls switch between the two facets laterally along the lengths of the trenches, or else the two different facets both exist down the sidewall itself. Section 4.6 will discuss what we now know about the structure of these facets and where they are located.

4.3.1 Identification of Facet Angles from Samples with Angular Broadening due to Disorder

Initial analysis of the data led to the conclusion that the facets being measured by Hicks et al were $(2\bar{2}07)$ and $(1\bar{1}03)$ facets; however, angular broadening from B_H, an unoptimized recipe, meant that a small range of θ_{meas} values were observed for each facet. Being unable to accurately determine the appropriate center (θ_{meas}) of the broadened angular range for each facet made strict identification of the correct facet angles $\theta_{\text{F},n}$ and $\theta_{\text{F},m}$ understandably difficult. Table 4.1 illustrates this difficulty. For armchair facets $(1\bar{1}0n)$, the angles where the facet cones would be measured are given by $\theta_{\text{meas,-}} = \pm|\theta_{\text{F}} - \theta_{\text{K}}|$ and $\theta_{\text{meas,+}} = \pm|\theta_{\text{F}} + \theta_{\text{K}}|$. For the values in Table 4.1, it is assumed that $h\nu = 36$ eV and, therefore, $\theta_{\text{K}} \approx 36°$. It should be noted that for certain facet indices, the angles where facet cones would be measured are not unique, even without the complication of angular broadening: both $(1\bar{1}03)$ and $(1\bar{1}0\ 10)$ would be measured at $\theta_{\text{meas}} \approx 15°$, while both $(1\bar{1}04)$ and $(1\bar{1}07)$ would be measured at $\theta_{\text{meas}} \approx 7°$. When also considering the effects of angular broadening, which prevent strict determination of θ_{meas}, it is of interest to note that $(1\bar{1}05)$ and $(1\bar{1}06)$ are measured at $\theta_{\text{meas}} \approx 1°$ and $\theta_{\text{meas}} \approx 4°$, respectively – well within the range of being indistinguishable due to angular broadening. Also, $(1\bar{1}03)$ and higher order facets $(1\bar{1}0n)$, with $n = 10$ to 13, are all measured within the range of $\sim 15°$ to $18°$.

Thus, when sidewall structures become disordered due to unoptimized patterning or growth, identification of facet angles is exceptionally difficult without the assistance of corroborative characterization techniques. It is now known from TEM and re-analysis of the data that the facets were not initially identified correctly due to the complications described; the facets were in fact $(1\bar{1}05)$ and $(1\bar{1}07)$. Importantly, the TEM-determined facet indices are consistent with all ARPES measurements. More will be discussed about the experiment by Hicks et al and what has been learned from TEM in Section 4.6.

Table 4.1: Facet angle θ_F for each armchair facet $(1\bar{1}0n)$, relative to the SiC(0001) surface normal. θ_{meas} is the angle where a facet cone from each facet would be measured, assuming $h\nu = 36$ eV and, thus, $\theta_{\text{K}} \approx 36.0°$. All θ_{meas} values can be positive or negative.

n	θ_{F}	$\pm\theta_{\text{meas,-}}$	$\pm\theta_{\text{meas,+}}$
0	90°	54.0°	126.0°
1	75.2°	39.2°	111.2°
2	62.1°	26.1°	98.1°
3	51.6°	15.5°	87.6°
4	43.4°	7.4°	79.4°
5	37.1°	1.1°	73.1°
6	32.2°	3.8°	68.2°
7	28.4°	7.7°	64.4°
8	25.3°	10.7°	61.3°
9	22.8°	13.2°	58.8°
10	20.7°	15.3°	56.7°
11	19.0°	17.1°	55.0°
12	17.5°	18.5°	53.5°

4.3.2 Additional Analysis of Data from Hicks et al

The ARPES Fermi surface from data in Ref. [44] (Fig. 4.4(a)) shows several features in addition to the two sets of facet cones. Note that the k-values given on the axes in Fig. 4.4(a) are in reference to the monolayer Si-face graphene Brillouin zone. A Dirac cone for epitaxial graphene on the SiC(0001) can be seen at the K point, $(k_x, k_y) = (-1.710, 0)$ Å^{-1}, as expected. A semiconducting band with $E_{gap} \geq 0.5$

eV can also be seen around the K point. Due to the angular location of the gapped band, it was initially thought to originate from graphene that bends between the trench tops and the sidewall. It is now known that this band is actually the gapped buffer layer band ε_2. The cause for the initial incorrect attribution of the band requires clarification.

It was originally believed that the semiconducting band measured by Hicks et al [44] near the Si-face graphene K point was a gapped band from graphene bent over the step edge from the SiC(0001) trench tops to the sidewall facet $(1\bar{1}0n)$. At the time, the band structure of buffer layer was unknown. The reason the gapped band was attributed to the bend region was because of the largely overlapping expected angular range.

Later measurements of a flat buffer layer would reveal ε_2 in three lobes around the K point (with the lobes pointing along the Γ-K directions), extending from the K point $(k_x, k_y) = (1.710, 0)\text{Å}^{-1}$ to an approximate location $(k_x, k_y) \approx (1.00, 0)\text{Å}^{-1}$. Figure 4.5 depicts this range of values for ε_2. If a photon energy $h\nu = 36$ eV is used, the angular observation range for ε_2 is $\theta_{\varepsilon_2} = [\theta_{\max}, \theta_{\text{K}}] = [\sim 20°, \sim 36°]$, shown in Fig. 4.5. For sidewall graphene on a facet with angle $\theta_{\text{F}} \approx 30°$ (the approximate angle macroscopically observed by AFM scans), the K point for the facet would be measured at $\theta_{\text{meas}} = 6°$. Thus, for graphene grown on a SiC region near the trench step edge, which transitions from SiC(0001) to a $(1\bar{1}0n)$ facet with angle $\theta_{\text{F}} = 30°$, the K point for the graphene in the bend region would, in theory, continuously span the angular range $\theta_{\text{meas}} = [6°, 36°]$. While this theoretical range is larger than the observed range for the gapped band measured by Hicks et al, graphene in the bend region was the most reasonable explanation for the gapped band, given what was known about the structure of sidewall samples at the time. Upon the analysis of band structure data from well-ordered, flat buffer samples, it became obvious that the gapped band from Ref. [44] was, in fact, ε_2 from buffer layer on the trench tops

of the ribbon sample.

4.3.3 Sidewall Facet Cones from Recipe $\mathbf{B}_H$

Upon viewing ARPES k_x cuts of the facet cones (Fig. 4.4(b) and (c)), it is evident that the facet cones measured by Hicks et al are metallic, though intensities drop off near E_F somewhat faster than might be expected, and the k-widths appear to be larger than desirable. Figure 4.6 shows a comparison of the k-widths of these facet cones with the k-width of the Dirac cone from monolayer graphene on the Si-face trench tops. Fits of the momentum distribution curves (MDCs) in Fig. 4.6 show that the full k-widths of the facet cones are 0.137 ± 0.004 Å^{-1} for the $(1\bar{1}0n)$ facet and 0.118 ± 0.003 Å^{-1} for the $(1\bar{1}0m)$ facet at $E - E_D \sim -0.5$ eV. Contrastingly, the full k-width of the cone from graphene on the SiC(0001) trench tops is 0.0696 ± 0.0010 Å^{-1} at $E - E_D = -0.5$ eV, approximately half the width of the facet cone bands. The doping for monolayer Si-face graphene is determined to be $E_D - E_F \approx -0.45$ eV for these samples, while the doping of the facet cones appears to be $E_D - E_F \approx 0$ eV. Note that the ARPES cuts in Fig. 4.6(c) and (d) are taken on either side of the K point, K$\pm\delta k$, which causes the maximum intensity to appear below (Fig. 4.6(c)) and above (Fig. 4.6(d)) the Dirac point instead of exactly at the Dirac point, $E_D - E_F \sim -0.45$eV.

Because it appears that there is only a single band for each facet, it was deduced that the sample had monolayer graphene on the sidewall. Consequently, it was extrapolated that monolayer armchair sidewall graphene is essentially charge neutral ($E_D - E_F \approx 0$). It was not yet known at the time that this deduction was incorrect, due to the fact that the sample measured by Hicks et al [44] actually contained two sidewall graphene layers; because of broadening from disorder, the k widths of the bilayer bands were not able to be individually resolved. An in-depth discussion about how it is known that this sample contained two sidewall graphene layers can be found

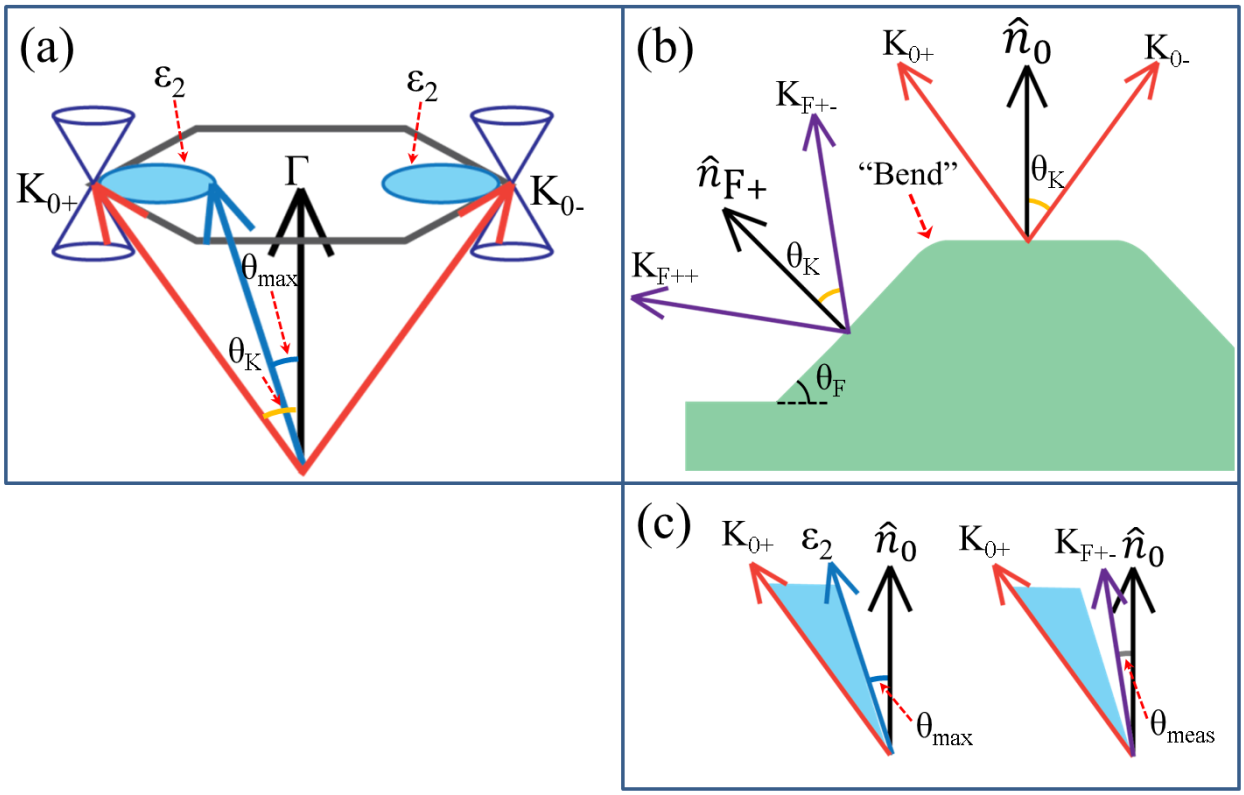

Figure 4.5: Illustration of how ε_2 could be mistaken for a band coming from the bend region. (a) Depiction of the buffer layer Brillouin zone. It is assumed that a minimal amount of monolayer contributes to weak Dirac cones at the K points, for reference. The ε_2 band is visible from the K point ($k_x = 1.710\text{Å}^{-1}$) to a point along the Γ-K direction ($k_x \approx 1.00\text{Å}^{-1}$). Thus, the buffer band ε_2 can be observed in ARPES throughout the angular range $[\theta_{\text{max}}, \theta_{\text{K}}]$ spanning from the K point (measured at angle θ_{K}) to some maximum angle θ_{max}. Also, ε_2 would be measured on the other side of the Γ point in an angular range $[-\theta_{\text{max}}, -\theta_{\text{K}}]$. (b) Depiction of a sidewall facet system with facet angle θ_{F}. The "bend" region that transitions between SiC(0001) and the armchair facet is indicated. (c) Graphic summary of the angular region where ε_2 is measured (left) and the angular region for the K point of graphene going over the bend (right). It becomes obvious that the angular regions are similar.

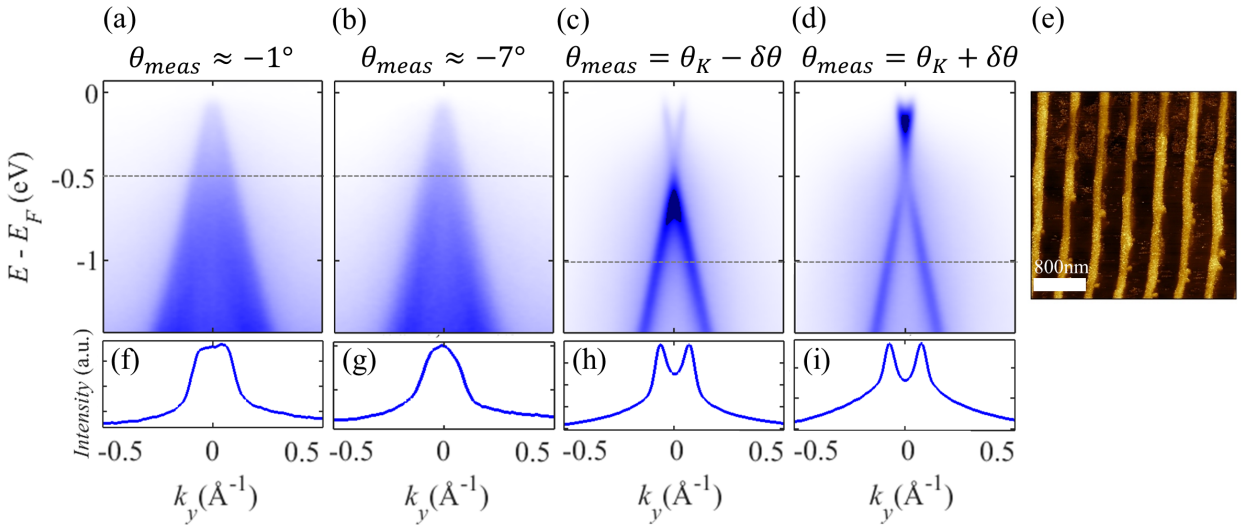

Figure 4.6: (a)-(d) ARPES k_x cuts of facet cones, in(a) and (b), and the SiC(0001) K point (K_{0-}), in (c) and (d). It appears that the widths of the facet cones are much broader than the K_{0-} cone, and there is much more intensity inside the facet cones than inside the K_{0-} cone. Note that (c) and (d) are taken slightly off from the K point ($\theta_{\text{meas}} = \theta_{\text{K}} \pm \delta\theta$, or k= K $\pm\delta k$), which is why greater intensity is seen below and above $E = E_D$, respectively. (e) NC-AFM of the sample from Ref. [44]. Scale bar is 800nm. Trenches are not as straight as would be ideal, which contributes to the ϕ-disorder that gives rise to broadened facet cones in (a) and (b); see Fig. 4.9 for a depiction of how non-straight trenches create ϕ-broadening. (f)-(i) MDC cuts of the ARPES images in (a)-(d), taken at $E \approx E_D - 0.5$ eV for each cone, shown by the dashed lines. Fits of the MDCs show FWHM (Δk) values of (f) 0.118 ± 0.003 Å^{-1}, (g) 0.137 ± 0.004 Å^{-1}, (h) 0.0724 ± 0.0008 Å^{-1}, and (i) 0.0668 ± 0.0011 Å^{-1}. Note that for (a) and (b) $E_D \approx E_F$, while for (c) and (d) $E_D = E_F - 0.45$ eV. For all ARPES images, $h\nu = 36$ eV.

in Section 4.6.2.

4.4 Additional Structural Information from Complementary Characterization Techniques

Also in the early stages of armchair sidewall nanoribbon characterization, LEEM and PEEM measurements were used to confirm several sidewall structural features [106]. Samples were grown with unoptimized high temperature/short time recipes similar, though not identical, to B_H.

Bright field LEEM (BF-LEEM) images show a well-ordered array of trenches oriented along the SiC$\langle 11\bar{2}0\rangle$ (Fig. 4.8(a)). μ-LEED in Fig. 4.7 shows graphene and SiC diffraction rods consistent with the trench tops, as well as a set of tilted diffraction rods for graphene on the facet walls. When utilizing a LEEM system, low-energy diffraction rods are independent of $k_\perp$ when the electrons interact with macroscopically flat surfaces. Therefore, any tilted diffraction rods (LEED spots that appear to move with changing energy) must originate from a surface that is angled compared to the macroscopic surface normal. Figures 4.7(a) and (b) show how the tilted graphene diffraction rods from the facet wall are observed as moving spots in LEED.

Dark field LEEM (DF-LEEM, or contrast aperture LEEM) confirms that the tilted diffraction rod intensity does, in fact, originate from the sidewalls. Figure 4.7(c) shows a composite image of DF-LEEM from a graphene $(0\bar{1})_G$ diffraction spot from the SiC(0001) trench tops (intensity in red) with a DF-LEEM image from a $(\bar{1}0)_{FG}$ facet graphene diffraction rod (intensity in blue; rod indicated in Fig. 4.7(b)). It is evident that the diffraction intensity from graphene with a surface normal parallel the macroscopic surface normal does, in fact, originate from the trench tops, while the intensity from the tilted diffraction rods originates from the sidewalls. Only one tilted diffraction rod was within the aperture when creating the DF-LEEM image (blue intensity in Fig. 4.7(c)), so intensity is only observed from trenches on one side. If a diffraction rod tilted symmetrically in the other direction had been used (e.g.,

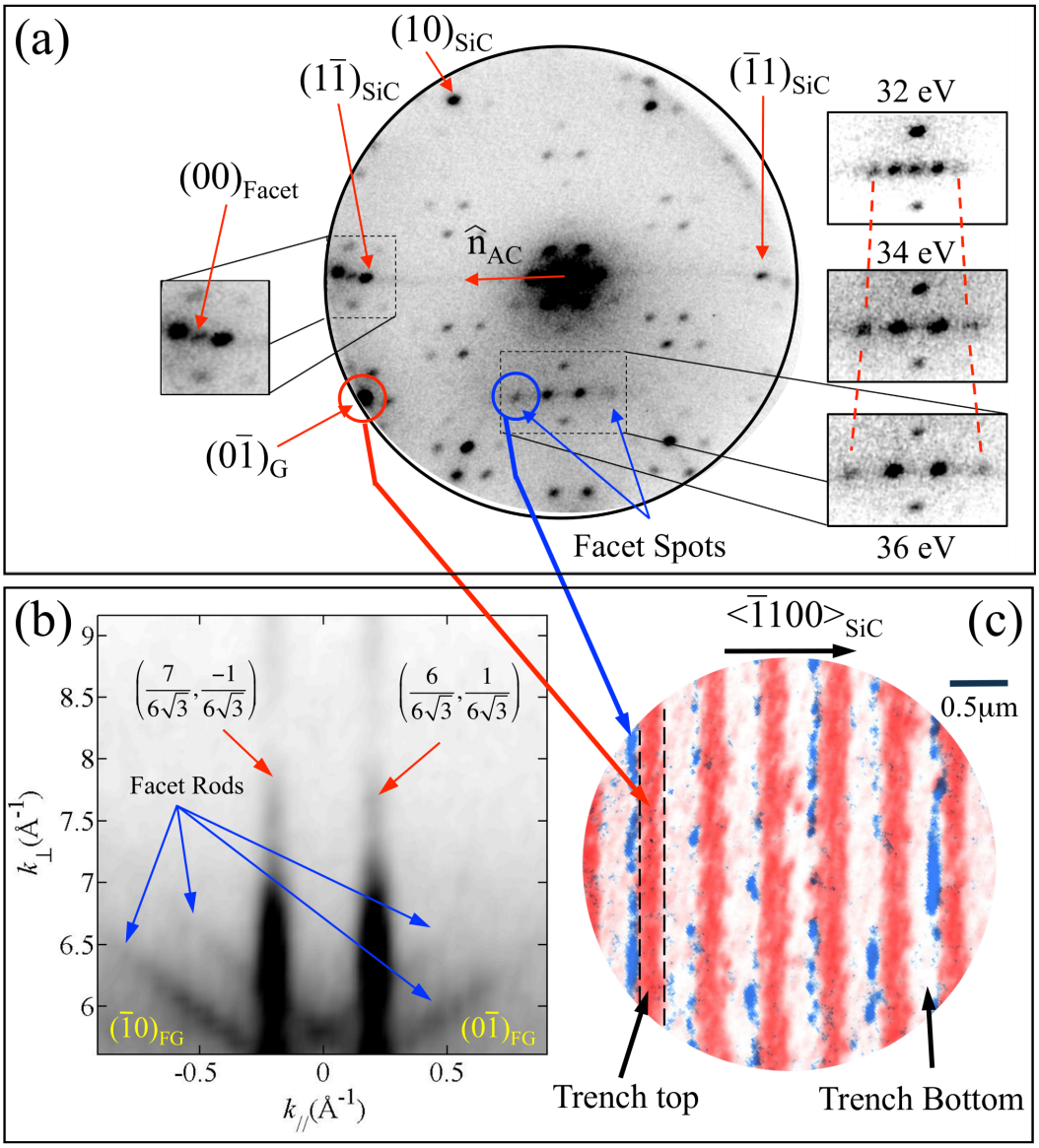

Figure 4.7: (a) μ-LEED of armchair sidewall ribbons, with the facet normal direction $\hat{n}_{AC}$ shown. The graphene facet rods are tilted along the armchair facet direction, as expected. Right Insets- The graphene facet rods are tilted by the facet angle and, thus, appear as moving spots in μ-LEED images as energy is changed. (b) $k_{||}$ and $k_\perp$ cut through graphene diffraction rods (the rods that are shown in the center of the dashed box in (a)). The rods that are independent of $k_\perp$ are from graphene on the trench tops. The set of tilted rods labeled $(\bar{1}0)_{FG}$ and $(0\bar{1})_{FG}$ are from graphene on the armchair facet walls. (c) A composite DF-LEEM image. Intensity in red was measured when the contrast aperture was placed over a Si-face graphene diffraction spot (red circle in (a)). Intensity in blue was measured when the contrast aperture was placed over a facet diffraction spot (blue circle in (a)). It is evident from DF-LEEM that the tilted rod intensity does, in fact, originate from the armchair sidewalls.

the $(0\bar{1})_{\mathrm{FG}}$ rod in Fig. 4.7(b) instead of the $(\bar{1}0)_{\mathrm{FG}}$), DF-LEEM would have measured intensity on the other side of the trench tops. A composite image of Bright field LEEM (BF-LEEM), which shows topography, and DF-LEEM of the facet diffraction rod intensity also confirms that the facet rods come from the sidewalls; see Fig. 4.8(a).

While LEED and LEEM suggest a graphene-like structure on the surface of the sidewalls, these two characterization techniques cannot discriminate between metallic graphene (with linear dispersion) and a material that is structurally identical to graphene but does not possess the characteristic linear dispersion of graphene due to a substrate interaction. Therefore, μ-ARPES was also used to characterize the armchair sidewalls. μ-ARPES measurements show Dirac cones from graphene on the trench tops as well as a set of metallic Dirac facet cones along the k-space direction expected for armchair facets (Γ-K). The energy resolution of the μ-ARPES performed is not sufficient to unequivocally determine the doping of the facet cones, though a qualitative comparison shows that the cones from the trench tops are at least slightly more n-doped than the facet cones (see Fig. 4.8(c)-(e)). It is clear from all of the corroborative characterization techniques that graphene can be grown on the sidewalls of armchair trenches etched into the Si-face of SiC.

4.5 Efforts to Improve Sidewall Graphene Growth Methods

4.5.1 Motivation

Samples experimentally measured by Hicks et al in Ref. [44] were grown with the higher temperature/shorter growth time recipe B_H, having the overall goal of creating well-ordered sidewall graphene samples with fewer sidewall layers than were previously seen in TEM from recipe A_{Sp} [43]. While initial ARPES measurements of these B_H recipe samples were successful, it became obvious that the sidewall graphene recipe could be further optimized for several reasons. First, recipe B_H yielded trenches which were not terribly straight, as viewed from AFM (Fig. 4.6(e)). Not having

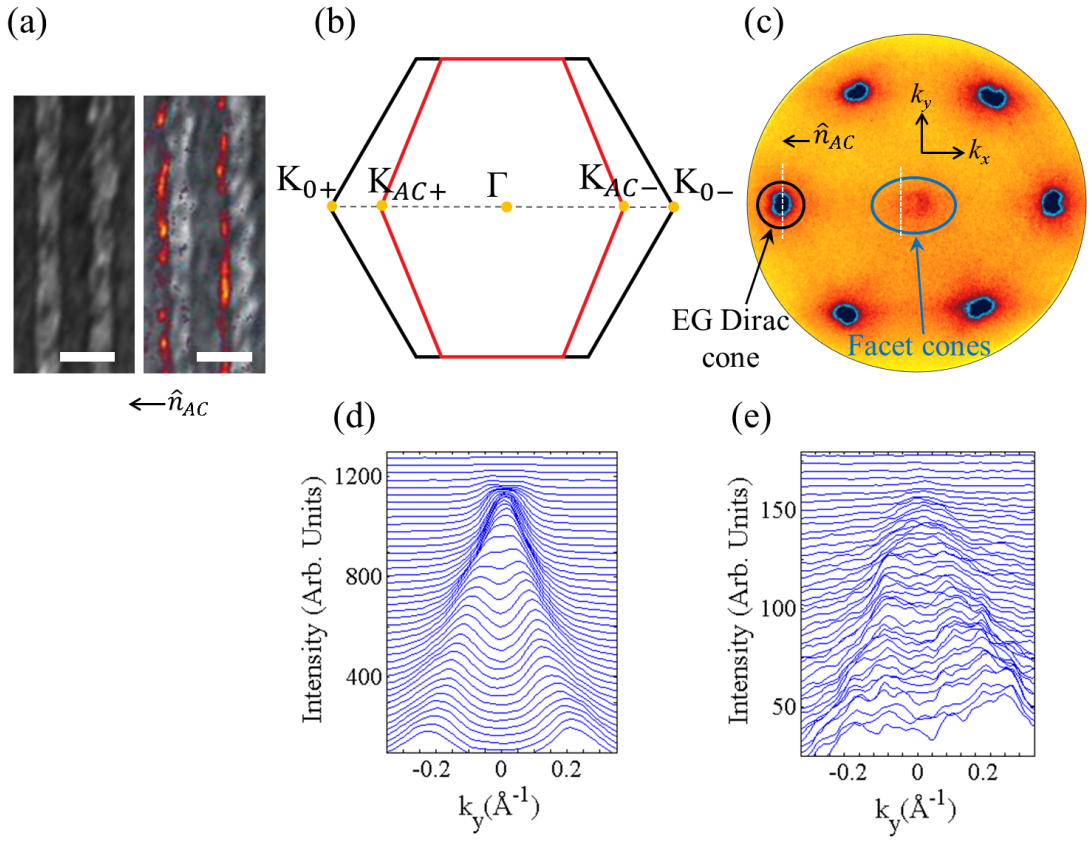

Figure 4.8: (a) Left- BF-LEEM of an armchair sidewall sample. Right- Overlay of the same BF-LEEM image (gray) with DF-LEEM intensity from the tilted diffraction rod (red/orange). It is evident that the tilted diffraction rod originates from the sidewall. Scale bars are 400nm. (b) Depiction of the graphene Brillouin zone from Si-face graphene (black hexagon) and armchair facet sidewall graphene (red hexagon, tilted). Armchair facet cones would be expected somewhere along the K_{0+}-Γ-K_{0-} direction; the exact location of the facet cones along K_{0+}-Γ-K_{0-} depends on the facet angle. (c) μ-ARPES image taken on an armchair sidewall nanoribbon sample ($E = 38$ eV, $h\nu = 44$ eV). Six Dirac cones are seen from monolayer graphene on the trench tops. Two facet cones are observed near Γ, with measured angles consistent with $(1\bar{1}07)$ armchair facets. (d) Constant k_x cut through a Dirac cone from the trench tops, indicated by the dashed line through the black circle in (c), with MDCs periodically spaced in energy to show intensities. The cone appears as expected for monolayer epitaxial graphene. (e) Constant k_x cut through a facet cone, indicated by the dashed line through the blue oval in (c), with MDCs periodically spaced in energy to show intensities. Intensities and energy resolution are insufficient to accurately determine cone doping, though the facet cone appears to be metallic and less n-doped than the cone in (d).

straight trenches is a problem because the trenches do not perfectly maintain the crystallographic orientation desired. Also, when trenches possess wandering step edge normals, an increased k_y-broadening is observed in ARPES measurements, making it difficult to resolve band structure features (depicted in Fig. 4.9). Measurements of the facet cones in Ref. [44] did, in fact, appear to be quite broad in k_y compared to the width of the Dirac cone from graphene on the trench tops (see Fig. 4.6), which motivated improvements to the recipe. Second, recipe B_H used by Hicks et al in Ref. [44] was developed with the goal of growing monolayer graphene on trench tops. It was believed at the time that buffer layer + monolayer on trench tops would yield a "sidewall buffer" layer + a metallic graphene layer on the sidewalls. However, it was not known if the first layer on the armchair sidewall would be a "sidewall buffer" layer or not, bonding to the facet like buffer layer on the SiC(0001). In fact, recent TEM images of sidewall samples show that the first sidewall layer actually does not bond to the facet like a buffer layer, so no "sidewall buffer" layer exists for armchair facets; see Section 4.6.1. Therefore, growth of a second sidewall graphene layer is unnecessary. Also, having metallic monolayer graphene on the Si-face trench tops is not necessarily desirable either from the point of view of performing transport on the sidewall GNRs, or potentially for the creation of a GNR-based device. All of these factors being considered, the development of a recipe that grows one well-ordered graphene layer on the sidewall and a smaller amount of monolayer graphene on trench tops was desired.

Efforts to improve the growth of armchair sidewall nanoribbons began with fine-tuning the recipe parameters. Many samples were patterned and grown with varying trench depth and growth parameters, and it soon became obvious that "shallow" armchair ribbon samples (trench depths < 15 nm) do not behave the same as "deep" armchair ribbon samples (trench depths 15 nm). In equilibrium, the SiC surface would prefer to melt all trenches and regain the SiC(0001) surface, so growth must

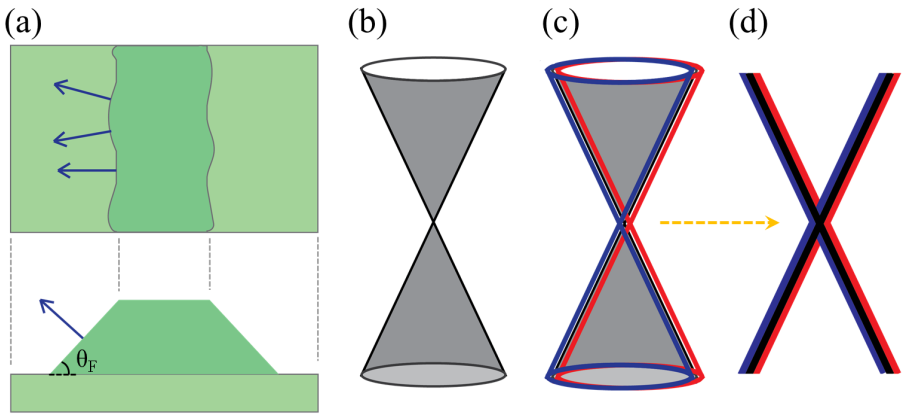

Figure 4.9: When trenches are not straight, broadening of measured ARPES bands can result. (a) Depiction of sidewall trenches which are not straight, wandering away from the SiC$\langle 11\bar{2}0\rangle$ direction at the step edge. Local step edge surface normals vary. (b) A Dirac cone from ideal sidewalls with only one surface normal. (c) A Dirac cone from the macroscopic surface normals is shown (gray), in addition to two other Dirac cones from local variations in the surface normal (blue and red). The cones that are from locally varying surface normals have Dirac points which are shifted in ϕ. (d) A broadened ARPES Dirac cone, with k-width enlarged by broadening due to step wandering.

be done far from thermodynamic equilibrium in order to maintain patterned features. Hence, high temperature/short growth time recipes that are able to achieve monolayer sidewall graphene growth are preferred to long growth time recipes, because shorter growth steps minimize the amount of time during which mass movement can cause disordering or melting of features. However, it is still observed that shallower trenches ($<$ 15nm) have a greater tendency to melt than deeper trenches, with all other processing and growth parameters the same. The remainder of this section will discuss the optimization of growth parameters for samples with trench depths $>$ 15 nm; growth of shallow trenches will be discussed in Section 4.7.

Any amount of disorder created during the patterning process prior to growth, as determined by AFM or SEM, should be avoided for successful growth of ordered sidewall graphene. Non-uniform and disordered etches have been observed to be extremely detrimental to sidewall graphene growth. Given a good etch and processing, the most overgrown samples created using a high temperature/short growth time

recipe exhibit 1-2 sidewall layers and yet only show buffer and some coverage of monolayer graphene on the trench tops, as determined by ARPES. However, if a sample with a disordered etch is grown with a recipe that should only create one layer on the sidewall and buffer/monolayer on the trench tops, it is instead observed that the sample forms a very disordered 1-2 layers on the sidewall and monolayer + bilayer on the trench tops near the step edges; such a sample is shown in Fig. 4.10.

AFM in Fig. 4.10(d-Top) shows a sample with a poor quality etch, yet the post-growth AFM (d-Bottom) does not look terribly disordered. It might be casually concluded that no lasting damage was done to growth on the sidewalls. However, ARPES shows that there exists monolayer + some bilayer on the trench tops, and a disordered 1-2 layers on the sidewall. The facet cone in Fig. 4.10(e)-(f) shows disorder-induced low-quality statistics, yielding a poor second derivative image. It is still apparent, however, that there are two sets of bands. Comparison with higher quality bilayer sidewall samples suggests that the second band could be from a small amount of bilayer sidewall coverage in the disordered sample. Alternatively, it is also possible that disorder from the bad etch led to inconsistent doping levels across the sample, causing a "secondary" cone to be seen, shifted in energy. If that is the case, the shifted Dirac point is coincidentally the same as is seen in bilayer sidewall samples. Further discussion about what is currently known concerning the band structure of bilayer sidewall graphene can be found in Section 4.6.2. With good pre-growth processing, bilayer graphene on the trench tops is never observed from recipes that create 1-2 sidewalls layers. It is believed that pre-growth disorder induced by a poor quality etch can create additional sites for Si atoms to sublimate, leading to faster, more disordered growth than would otherwise be observed. Consequently, it is necessary to take great care in pre-growth processing of samples.

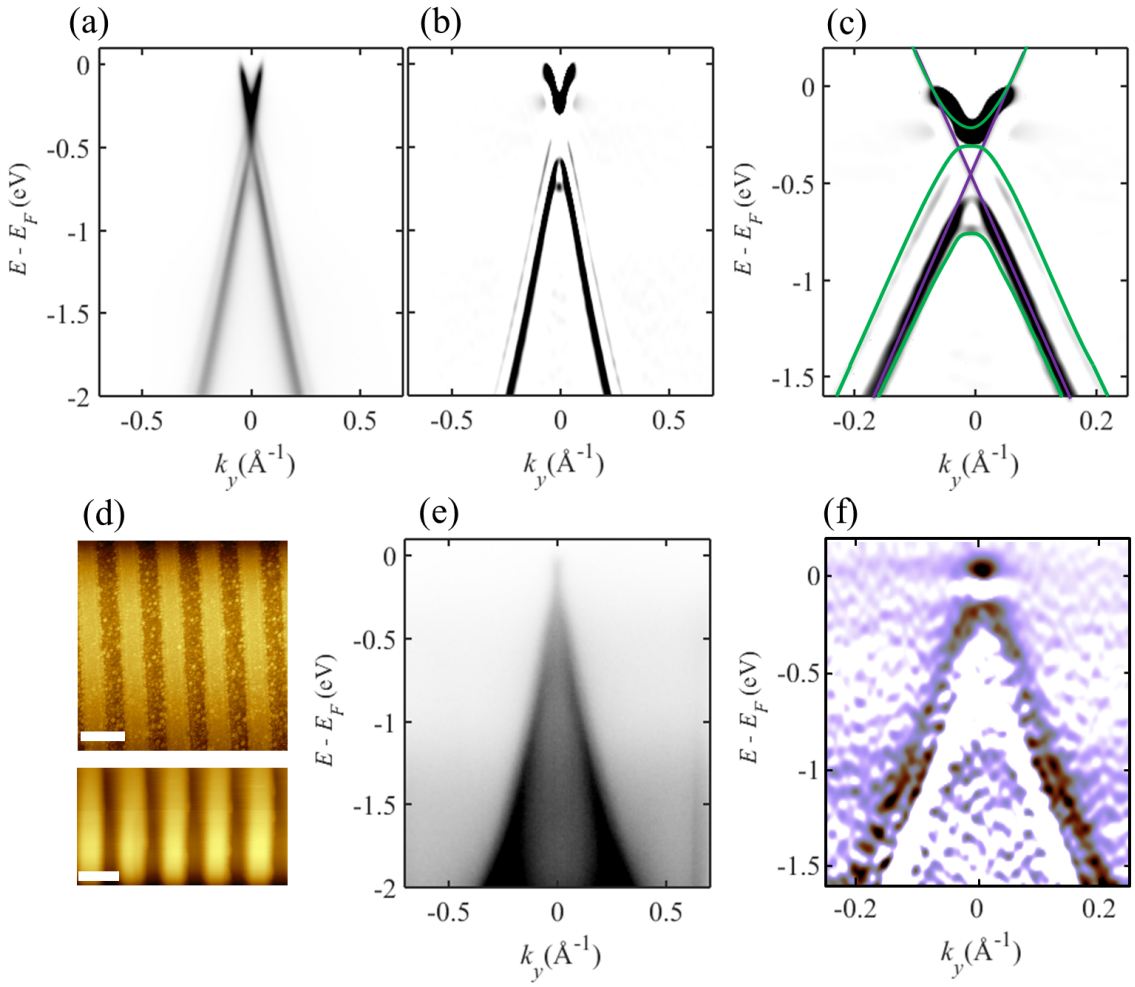

Figure 4.10: Illustration of how poor etch quality can affect armchair sidewall nanoribbon structure and properties. (a) ARPES at the K point for graphene on the Si-face trench tops. More than just a monolayer band is observed. (b) Negative second derivative of the ARPES image in (a). In addition to monolayer, there is also some bilayer graphene on the trench tops. (c) Same derivative image as in (b) with an overlay of tight-binding calculations from Ref. [62] for monolayer (purple) and bilayer (green) epitaxial graphene. (d) Top- Pre-growth AFM of a sample after a poor-quality etch; the sample is the same as that measured with ARPES in (a)-(c), (e), and (f). The etch did not create clean trench features. Bottom- Post-growth AFM, which appears to show straight, well-ordered trenches. Sample was grown with recipe $C_N^{(d)}$; see Section 4.5.3. Both- Scale bars 800nm. (e) Facet cone from a $(1\bar{1}05)$ armchair facet. Faint intensity outside the monolayer band suggests a second band or disorder in either ϕ or doping level. (f) Negative second derivative of the facet cone in (e). Two bands are seen, suggesting more than ϕ-broadening. Correlation of this band structure with intentionally-grown multilayer sidewall samples shows the second band most likely originates from small bilayer sidewall coverage in addition to monolayer coverage. See Section 4.6.2 for further discussion about multilayer sidewall graphene. Overall, even if post-growth AFM appears well-ordered, poor quality pre-growth processing leads to disordered graphene growth as well as the formation of more graphene layers than would otherwise be observed for the same recipe. For all ARPES images, $h\nu = 36$ eV.

4.5.2 Effectiveness of an Annealing Step

It was discovered early on that an annealing step at ~ 1150 °C , performed before the growth step, not only stabilized the surface to help prevent trenches from melting during growth but also improved the wandering of the step edge away from the SiC$\langle 11\bar{2}0\rangle$ direction. Hicks shows in Ref. [107] that, given identically patterned trenches (same pitch and trench depth), a pattern can melt without the annealing step and not melt when heated with the annealing step prior to growth. The robustness of this annealing step in preventing pattern melting under extreme conditions (e.g., small pitch and excessively high growth temperatures) has not yet been tested; however, the step has been shown to be effective in preventing melting of all patterned features under the growth conditions necessary to form 1-2 sidewall graphene layers.

4.5.3 Optimization of Growth Parameters and Indications of Improvement

While including an annealing step helps stabilize the surfaces by preventing trenches from melting during growth procedures, the growth temperature parameters must next be optimized to create well-ordered sidewall monolayers without growing additional sidewall layers. A number of samples were fabricated with growth times and temperatures chosen within a certain range. It was determined that a growth time of 1 min at temperatures > 1500 °C was necessary to create any significant monolayer graphene coverage on the sidewalls. Growing samples between 1 and 1.5 min at temperatures 1530-1565 °C consistently yields monolayer graphene facet cones, as seen in ARPES, given good pre-growth processing. This range of temperature and time parameters will now be referred to as recipe $\mathrm{C}_N^{(d)}$.

A correlation of the $\mathrm{C}_N^{(d)}$ recipe with various characterization measurements reveals a number of important things. First, TEM images of samples grown with $\mathrm{C}_N^{(d)}$ show a single layer on the sidewalls; see Fig. 4.19 in Section 4.6. Also, it is obvious that short growth times yield samples that are straighter over larger areas than samples

grown with either A_{Sp} or B_H. AFM images of $C_N^{(d)}$ samples (Fig. 4.11(c)) show better-ordered, more parallel trenches. ARPES of $C_N^{(d)}$ samples reveals facet cones with k-widths that appear to be significantly narrower than those first observed by Hicks et al [44]. Samples grown with the $C_N^{(d)}$ recipe have average k-widths of $\Delta k = 0.075 \pm 0.010 \text{Å}^{-1}$ at $E - E_D = -0.5$ eV, approaching instrument resolution for the experimental parameters used. Contrastingly, fits of facet cone MDC curves from B_H samples show widths on the order of $\Delta k = 0.127 \pm 0.003 \text{Å}^{-1}$ at $E - E_D = -0.5$ eV. However, it is now known that this k-width includes a monolayer sidewall cone as well as bilayer sidewall bands; see Section 4.6.2. Regardless, the monolayer and bilayer bands from B_H samples are too wide in k to be individually resolved. k-widths of these magnitudes suggest long-range order on the length scale $\frac{2\pi}{\Delta k} = L \approx 8.4$ nm for samples grown with $C_N^{(d)}$, compared to $L \approx 4.9$ nm for samples grown with B_H.

Figures 4.12 and 4.13 show the obvious improvement in quality of facet cones for samples grown with recipe $C_N^{(d)}$, as observed by ARPES measurements. Note that the doping of the monolayer sidewall facet cones from these $C_N^{(d)}$ samples (trench depth > 15 nm) is $E_D - E_F \approx -0.24 \pm 0.02$ eV, while the facet cones from B_H-grown samples in Ref. [44] appear to be approximately charge neutral ($E_D \approx E_F$); this is because the B_H sample actually possessed bilayer sidewall bands in addition to a monolayer facet cone, and it can be observed from better resolved samples that the bilayer bands have a Dirac point that is within -0.1 eV of the Fermi level. See Section 4.6.2 for further discussion of how this doping level change is consistent with Si-face graphene, which shows decreasing doping (approaching charge neutral) with increasing number of layers [62]. While $C_N^{(d)}$ facet cone intensities do persist up to the Fermi level, it is apparent that intensities drop off more quickly than might be expected, starting at $\sim (E - E_F) \approx -0.4$ eV. There is currently no explanation for this observation. Second derivative images confirm that the doping level is $E_D - E_F \approx -0.24$ eV and that the cones do continue up to the Fermi level, despite the decreasing intensity.

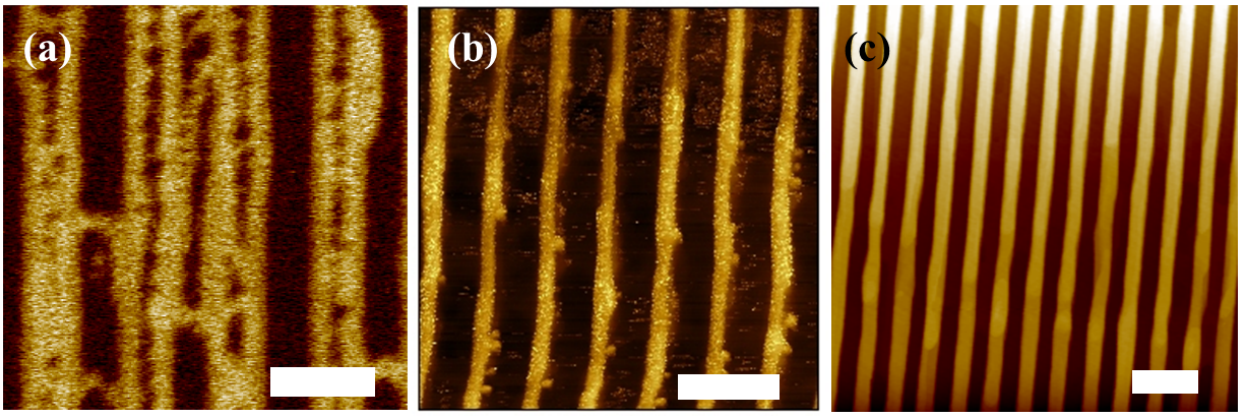

Figure 4.11: (a) EFM of a sample grown with a recipe similar to A_{Sp}. Growth time was 10 min. There appears to be a significant amount of graphene as well as step edge wandering. (b) NC-AFM of a sample grown with B_H. Again, trench edges are not straight. (c) NC-AFM of a sample after growth with a $C_N^{(d)}$ recipe. In all figures, the scale bar is 800nm.

4.5.4 Consistency of Recipes Between Different CCS Furnaces

While exact conditions inside a CCS crucible during growth might vary slightly from crucible to crucible (e.g., the amount of Si adsorbed onto the inner graphite walls), it is reasonable to assume that monolayer sidewall growth can be expected under the conditions described for $C_N^{(d)}$ recipes for any reasonably prepared CCS furnace. Graphene growth on the Si-face has been found to be primarily activated by temperature [108]: while ARPES of buffer layer grown for 20min at 1360 °C might show a weak Dirac cone from monolayer graphene near step edges ($< 2\%$ coverage), monolayer graphene has not been found to grow in earnest until $\sim$ 1520 °C [108]. Similarly, monolayer sidewall graphene does not appear to grow with consistent coverages until $\geq$ 1500 °C . Thus, if a CCS crucible can grow a well-ordered monolayer film in $\sim$ 20 min at 1520 °C , it should also be expected that the same crucible would grow monolayer armchair sidewall graphene using recipe $C_N^{(d)}$.

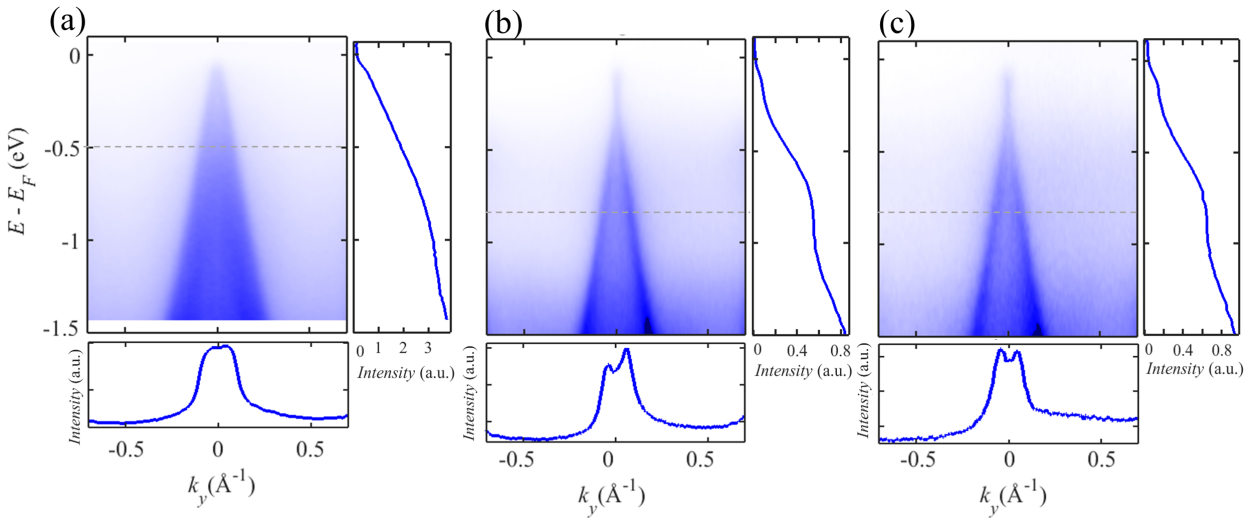

Figure 4.12: Comparison of a facet cone from recipe B_H with facet cones from the improved recipe $C_N^{(d)}$. (a) ARPES at the K point of a $(1\bar{1}07)$ facet cone, from a sample grown with B_H. Right- EDC through the center of the cone, $k_y = 0$ Å^{-1}. Intensity goes up to the Fermi level, indicating the cone is metallic. Bottom- MDC through $E - E_D \approx -0.5$ eV. The k-width at $E - E_D = -0.5$ eV is 0.118(3)Å^{-1}. (b) ARPES at the K point of a $(1\bar{1}07)$ facet, from a sample grown with $C_N^{(d)}$. Right- EDC through the center of the cone, $k_y = 0$ Å^{-1}. Intensity drops off unexpectedly quickly near the Fermi level, but intensity does go up to the Fermi level, indicating the cone is metallic. Bottom- MDC through $E - E_D = 0.5$ eV, with a k-width determined to be 0.084(4)Å^{-1}. (c) ARPES at the K point of a $(1\bar{1}05)$ facet cone, from a sample grown with $C_N^{(d)}$. Right- EDC through the center of the cone, $k_y = 0$ Å^{-1}. Intensity drops off unexpectedly quickly near the Fermi level, but intensity does go up to the Fermi level, indicating the cone is metallic. Bottom- MDC through $E - E_D = -0.5$ eV, with a k-width determined to be 0.062(2)Å^{-1}. Note that for (a) the apparent doping of the facet cone is $E_D - E_F \approx 0$ eV, while the apparent doping of the facet cones in (b) and (c) is $E_D - E_F \approx -0.24$ eV. See Section 4.6.2 for the explanation of this difference. For all ARPES images, $h\nu = 36$ eV.

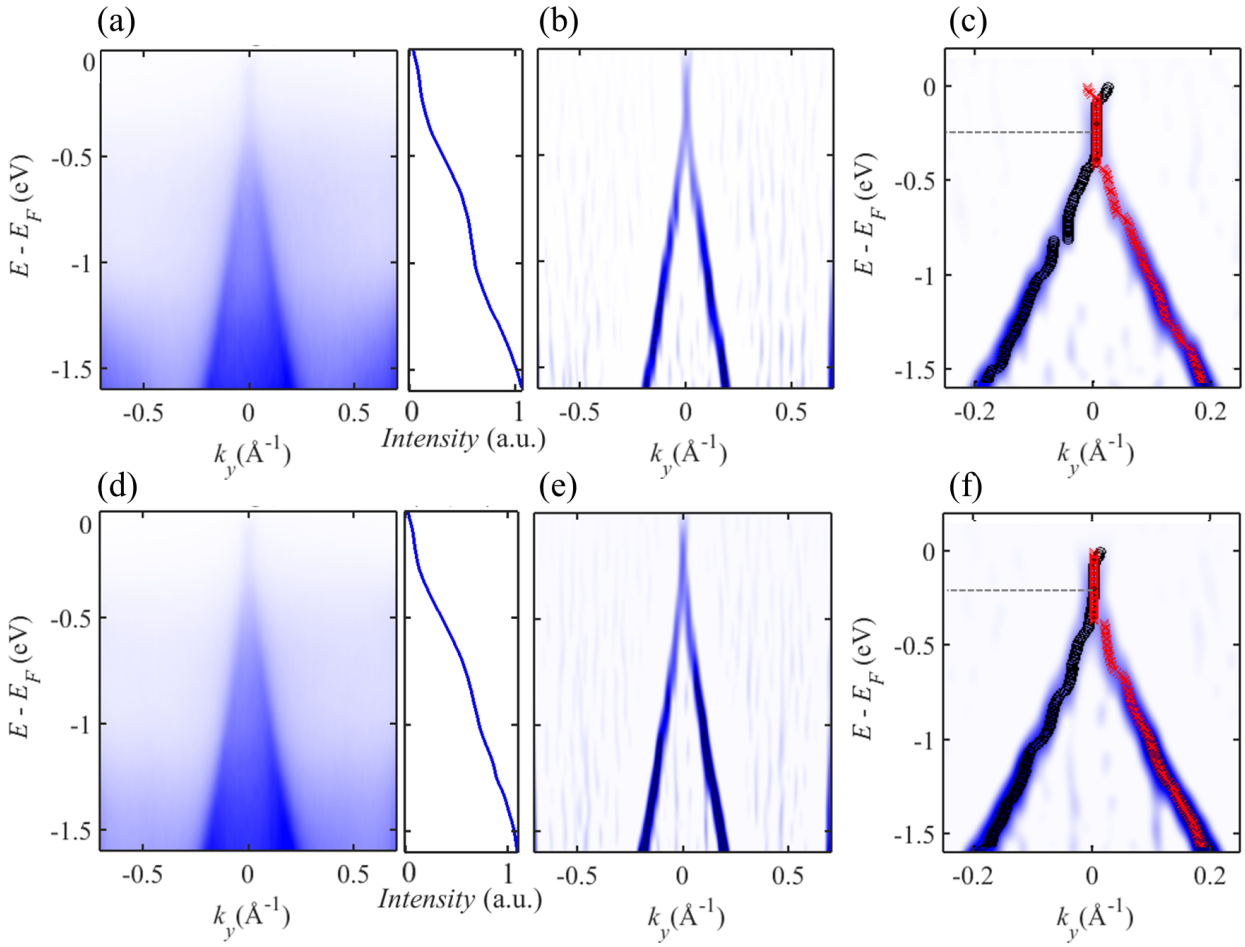

Figure 4.13: Overview of the facet cones measured by ARPES for samples grown with $C_N^{(d)}$. (a) Left- A facet cone from a $(1\bar{1}05)$ facet. Right- EDC from the facet cone, taken at $k_y = 0$ Å^{-1}. It is evident that, while intensity drops off unexpectedly quickly, intensity from the facet cone does go up to the Fermi level. (b) Negative second derivative of the facet cone in (a), which more obviously shows the structure of the cone near the Fermi level. (c) Same derivative as in (b), zoomed in and overlayed with fits to the bands to show the doping level is $E_D - E_F \approx -0.25$ eV. (d) Left- A facet cone from a $(1\bar{1}07)$ facet. Right- EDC from the facet cone, taken at $k_y = 0$ Å^{-1}. It is evident that, while intensity drops off unexpectedly quickly, intensity from the facet cone does go up to the Fermi level. (e) Negative second derivative of the facet cone in (d), which more obviously shows the structure of the cone near the Fermi level. (f) Same derivative as in (e), zoomed in and overlayed with fits to the bands to show the doping level is $E_D - E_F \approx -0.25$ eV. For all ARPES images, $h\nu = 36$ eV.

4.5.5 Additional Indications of Improved Order

In addition to straighter trenches and facet cones with narrower k-widths, samples grown with the recipe $C_N^{(d)}$ also show improved ordering through the observation of replica cones. For the first time, both first- and second-order replica cones created from umklapp processes are measured and observed consistently. Figure 4.14 shows ARPES cuts of replica cones from samples grown with $C_N^{(d)}$. Using the same convention as seen in Chapter 2, replica cones from the K^{th} K-point can be indexed using reciprocal lattice vectors of the SiC 6×6 unit cell: $\mathbf{G}_K(m,n)=m\mathbf{s}_1+n\mathbf{s}_2$, where $|\mathbf{s}_1| = |\mathbf{s}_2| = \frac{1}{6}|\mathbf{a}^*_{SiC}|$. Depicted in Fig. 4.14 are ARPES images of: (a) $\mathbf{G}_{10}(\bar{6}0)$ and $\mathbf{G}_{\bar{1}1}(6\bar{6})$, (b) $\mathbf{G}_{01}(0\bar{7})$, (c) $\mathbf{G}_{0\bar{1}}(\bar{1}1)$ and $\mathbf{G}_{0\bar{1}}(10)$, (d) $\mathbf{G}_{01}(0\bar{6})$, and (e) $\mathbf{G}_{0\bar{1}}(01)$. None of these replica cones were clearly observed in samples grown with B_H.

Many problems hamper a direct numerical comparison of integrated intensities for facet cones on different samples due to potential focusing issues, beamline intensities, etc, especially when experimental data is taken months or years apart. Also, directly comparing k-widths of facet cones from samples grown and measured at different times is troublesome. However, the observation of replica cones does indicate slight differences in the degree of ordering based on temperature and time of growth. Samples with growth temperatures above $\sim$ 1560 °C display all replica cones identified in Fig. 4.14, while samples with temperatures below $\sim$ 1550 °C show all first order replicas but are usually missing 1-3 of the higher order replicas (typically $\mathbf{G}_{10}(\bar{6}0)$,$\mathbf{G}_{\bar{1}1}(6\bar{6})$, or $\mathbf{G}_{01}(0\bar{7})$). Therefore, if no other method can statistically compare recipes with any satisfaction, the observation of replica cones indicates that the best $C_N^{(d)}$ recipes are those with growth temperatures T = 1560-1565 °C and growth time t = 90 sec.

At this point, it is important to note that all growth temperatures given for $C_N^{(d)}$ recipes refer to the highest temperature reached before the end of the growth step. The CCS furnace used to grow samples in this work utilizes a control system that does not specifically control temperatures via feedback but instead uses

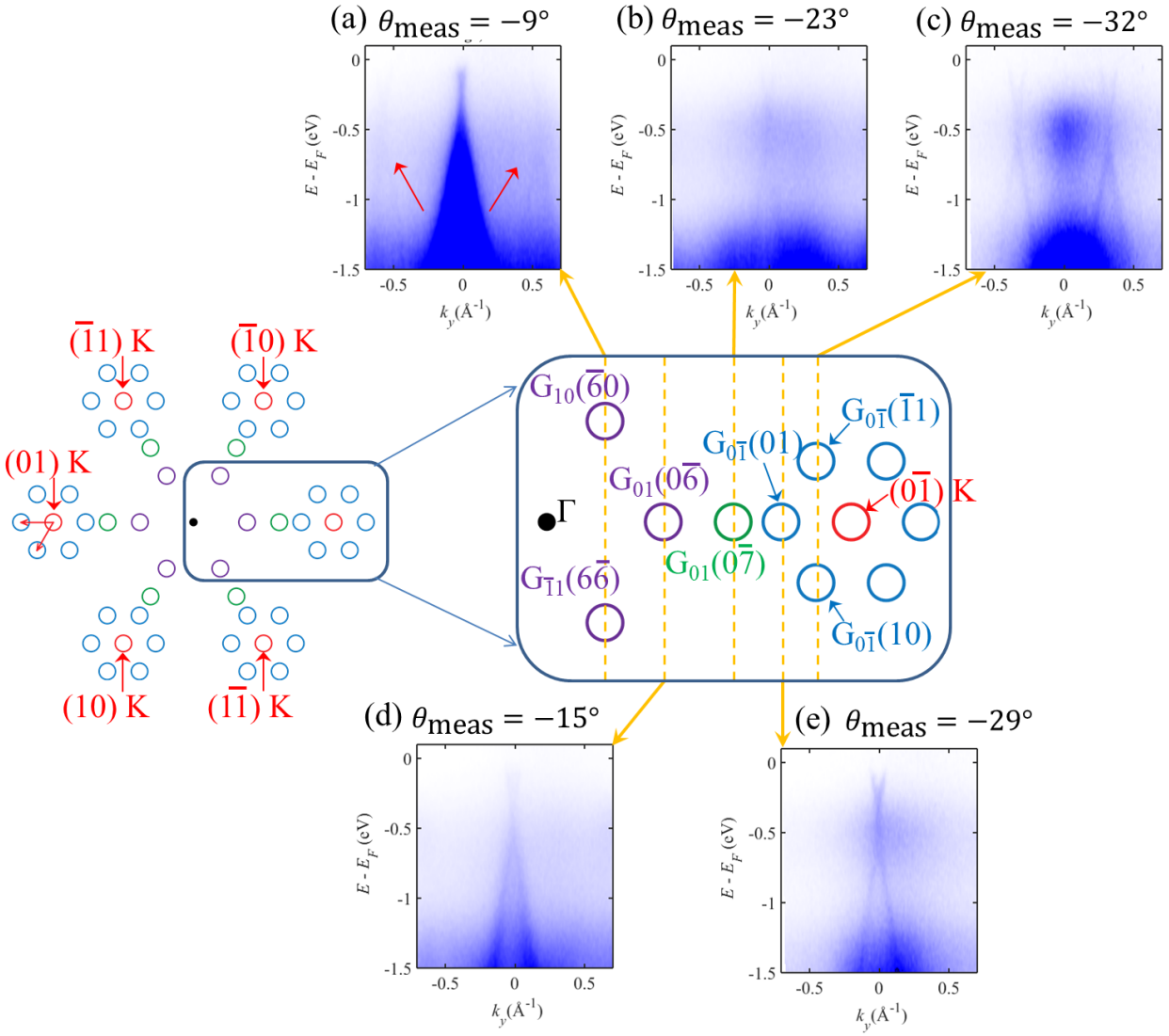

Figure 4.14: Samples grown with recipe $C_N^{(d)}$ show many indications of improved order, including the observation of first- and second-order replica cones. Replica cone locations can be indexed by multiples of SiC 6×6 unit vectors. As expected, replica cones show the same doping as the monolayer EG Dirac cone from the Si-face trench tops, $E_D - E_F = -0.45$ eV. (a) ARPES showing a $(1\bar{1}07)$ facet cone (center) as well as the $\mathbf{G}_{10}(\bar{6}0)$ and $\mathbf{G}_{\bar{1}1}(6\bar{6})$ replica cones (faint), indicated by arrows. (b) ARPES showing a $\mathbf{G}_{01}(0\bar{7})$ replica cone. (c) ARPES showing two of the 6×6 replica cones surrounding the $(0\bar{1})$ K point, indexed as the $\mathbf{G}_{0\bar{1}}(\bar{1}1)$ and $\mathbf{G}_{0\bar{1}}(10)$ replica cones. (d) ARPES showing the $\mathbf{G}_{01}(0\bar{6})$ replica cone, which is superimposed on a $(1\bar{1}07)$ facet cone, near the end of the angular range where the $(1\bar{1}07)$ facet cones are observed. (e) ARPES of another 6×6 replica cone surrounding the $(0\bar{1})$ K point, indexed as the $\mathbf{G}_{0\bar{1}}(01)$ replica cone. Intensity can also be seen from the non-dispersing SiC surface state g_1 at $E - E_F = -0.5$ eV in (b), (c), and (e). For all ARPES images, $h\nu = 36$ eV.

applied voltages as inputs. Voltages were consistently correlated with peak temperatures via a digital pyrometer aligned with the crucible during the growth process. Consequently, the furnace does not reach its peak temperature until ~ 40 sec in to the growth step. Growth times stated for all recipes incorporate this temperature-ramping phase. As an example, for a $C_N^{(d)}$ recipe that is stated to have an annealing step at ~ 1150 °C followed by a growth temperature of 1560 °C with a growth time of 90 sec, then the first $\sim 30-40$ sec of the growth time would include ramping from 1150 °C to 1560 °C . High temperatures are reached fairly quickly, with the crucible attaining temperatures ≥ 1500 °C within the first 10-15 sec. The growth step would end after 90 sec, therefore including up to 60 sec at or near 1560 °C .

Table 4.2: Correlation of $C_N^{(d)}$ recipe parameters (peak growth temperature and total growth time) with k-widths and replica cones as a measurement of ordering. The percentage of replica cones is out of the total number of replica cones observed within the typical ARPES Fermi surface parameters. Δk width values are for monolayer Si-face graphene Dirac cones from graphene on trench tops; values were determined by fitting MDCs ($E - E_F = -0.3$ eV) with Lorentzian peaks.

Growth Temp. (°C)	Growth Time (sec)	% Replicas Observed	Δk (Å^{-1})
1535°	90	57%	0.0370(6)
1540-1545°	70	71%	0.0313(6)
1540-1545°	90	71%	0.0286(4)
1555-1560°	90	100%	0.0254(4)
1560-1565°	60[1]	43%	0.0332(4)
1560-1565°	90	100%	0.0261(4)
1575°[2]	50	100%	0.0316(6)

One additional indication of improvement in $C_N^{(d)}$ samples compared to B_H samples is an increased ability to individually resolve facets. Intensities from facets are more obviously separate, indicating a lower degree of angular disorder. This decreased angular disorder enables more successful determination facet angle and, thus, facet

[1] Extremely weak facet cones
[2] Multiple sidewall layers grown.

indices. A numerical way of representing the improved angular ordering of the measured facet cones is seen by taking momentum distribution curves (MDCs) at the same energy for each angle in a range of ARPES cuts containing the facet cones. In particular, the Dirac point energy is usually chosen ($E = E_D$). Plotting the maximum in MDC intensity for each angle then gives a picture of the angular location of the facets. Figures 4.15, 4.16, and 4.17 show how this particular type of graph helps determine the facet angles being measured. Because ARPES θ-cuts actually measure conic sections of the Dirac cone, the angle for measuring exactly at the K point of graphene on the facet ($\theta_{\text{meas}} = \pm|\theta_{\text{K}}| \pm |\theta_{\text{F}}|$) is where the most intensity would be expected to be measured for MDCs taken at the Dirac point energy. In an ideal case, if the facet cones were infinitesimally thin ($\Delta k \to 0$), then the graph of maximum MDC intensity as a function of theta would be observed to have a delta function at the angle which represents the K point for the facet ($\theta = \theta_{\text{meas}}$) with zero intensity at all other angles (Fig. 4.15). However, it is observed that all bands have finite k-widths. Therefore, a peak which is less sharp than a delta function is expected, centered around the appropriate K point angle (Fig. 4.16). When multiple crystallographic facets exist, a peak would be expected at θ_{meas} for each facet angle (see Fig. 4.17 for an illustration with three theoretical facets; also, see Table 4.1 for the θ_{meas} values for each facet $(1\bar{1}0n)$). For samples with disorder-induced angular broadening, peaks depicting individual facets would not be able to be resolved. Figure 4.18 shows data from a sample grown with a $\text{C}_N^{(d)}$ recipe. Facets consistent with TEM-determined indices ($n = 5, 7$) are easily observed.

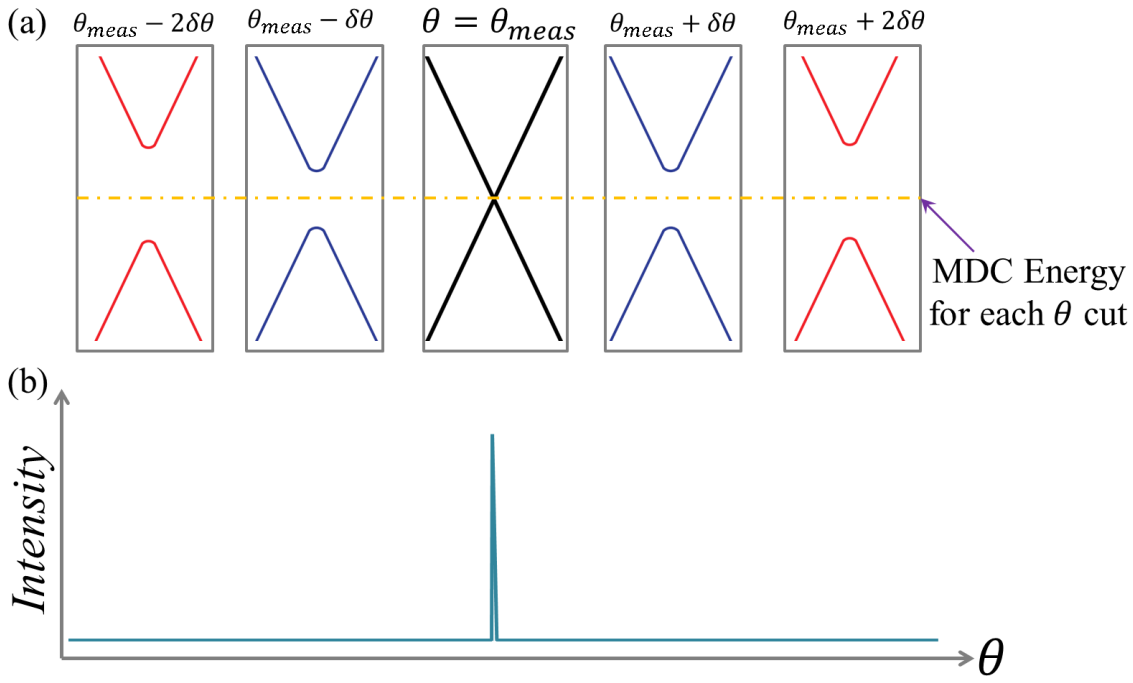

Figure 4.15: Graphic representation of the usefulness of the MDC max intensity plot as a function of θ. (a) ARPES constant θ cuts (each gray box) near a Dirac cone measure conic sections of the Dirac cone. MDC cuts for each angle θ would then be taken, measuring intensity of the bands at the chosen energy, usually $E - E_F = E_D$ (shown by the yellow line). (b) For infinitely thin bands ($\Delta k \to 0$), the graph of maximum MDC intensity as a function of θ would, ideally, look like a delta function at the angle for the K point of the Dirac cone, $\theta_{\text{meas}} = \pm|\theta_{\text{K}}| \pm |\theta_{\text{F}}|$.

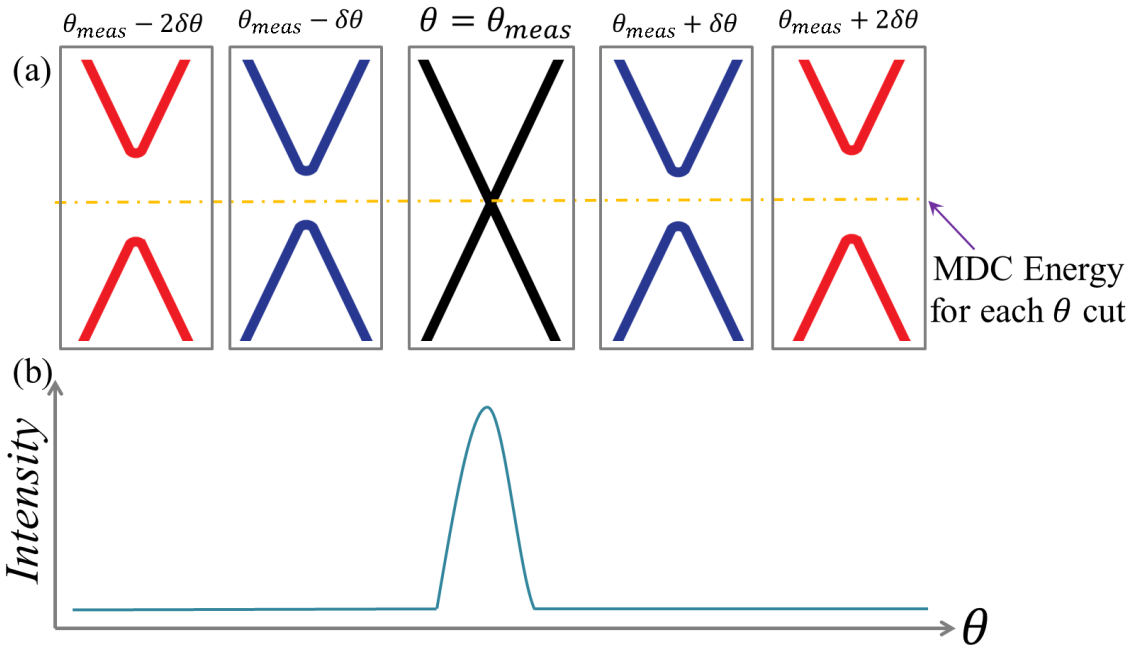

Figure 4.16: Graphic representation of the usefulness of the MDC max intensity plot as a function of θ. (a) ARPES constant θ cuts (each gray box) near a Dirac cone measure conic sections of the Dirac cone. MDC cuts for each angle θ would then be taken, measuring intensity of the bands at the chosen energy, usually $E - E_F = E_D$ (shown by the yellow line). (b) For bands with finite k-widths ($\Delta k \neq 0$), the graph of maximum MDC intensity as a function of θ would be broader than the delta function observed for infinitesimally thin bands. The peak should still be centered around the appropriate K point angle, $\theta_{\text{meas}} = \pm|\theta_{\text{K}}| \pm |\theta_{\text{F}}|$.

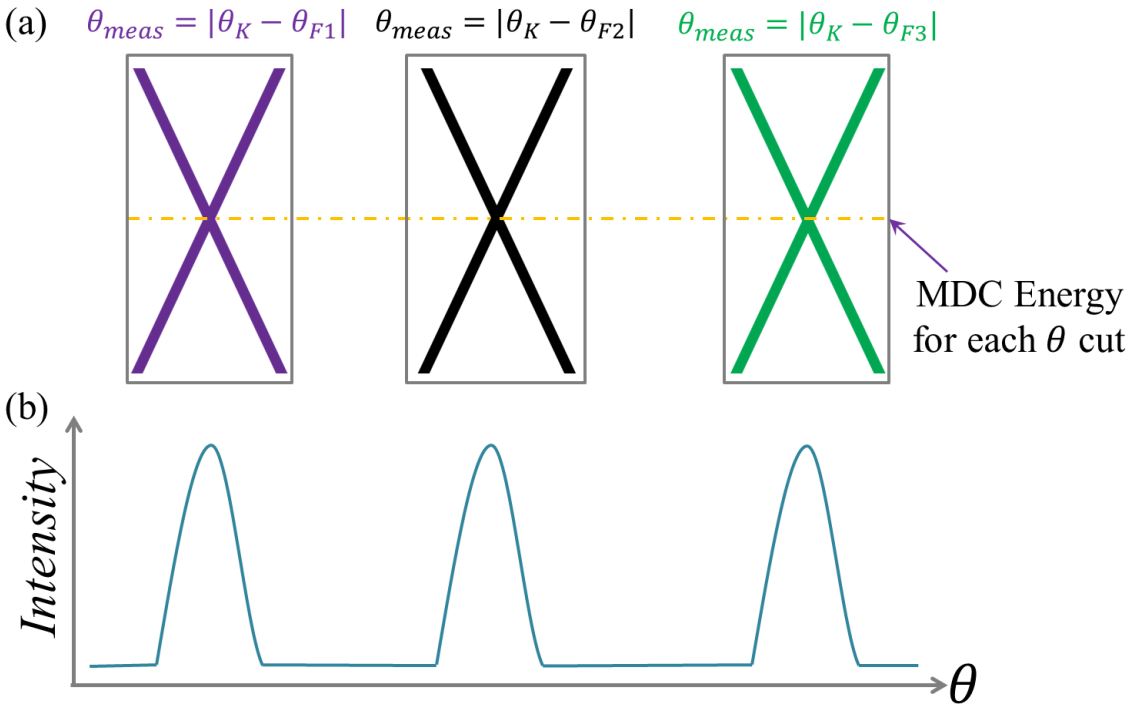

Figure 4.17: Graphic representation of the usefulness of the MDC max intensity plot as a function of θ for determining facet angles. (a) ARPES constant θ cuts (each gray box) near several Dirac cones, one shown for each unique facet angle. MDC cuts for each angle θ would then be taken, measuring intensity of the bands at the chosen energy, usually $E - E_F = E_D$ (shown by the yellow line). (b) For multiple K points caused by the presence of multiple crystallographic facets, it would be expected for a peak to occur for each facet at angles $\theta_{\text{meas}} = \pm|\theta_{\text{K}}| \pm |\theta_{\text{F},n}|$, with $\theta_{\text{F},n}$ determined by the facet indices.

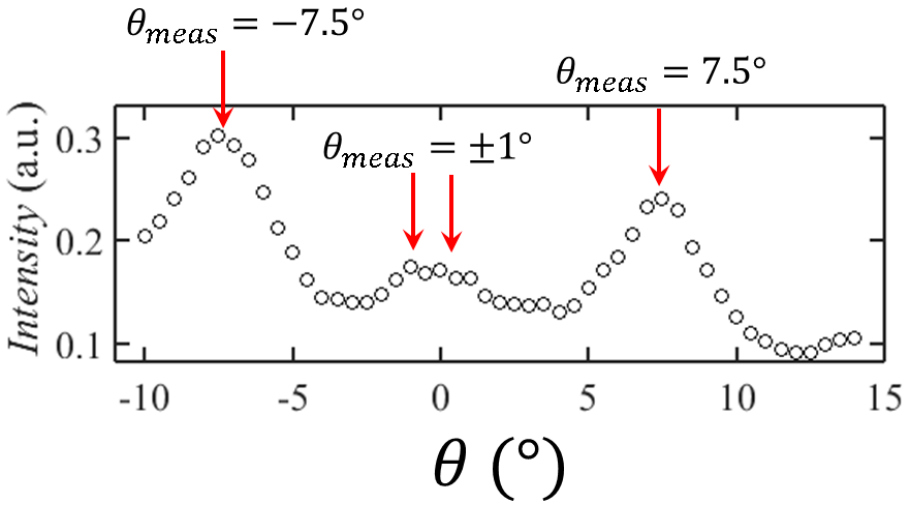

Figure 4.18: A graph of maximum MDC intensity for each θ ARPES cut, with MDCs taken at $E_F \approx E_D$. The sample was grown with recipe $C_N^{(d)}$. Three peaks in intensity are observed at angles $\theta_{\text{meas}} = \pm 7.5°$ and $\theta_{\text{meas}} \approx 0°$. The cone near 0°spreads out into $\theta_{\text{meas}} = \pm 1°$, consistent with the expected angle for a $(1\bar{1}05)$ facet. Likewise, the peaks at ±7.5°are consistent with the expected angle for a $(1\bar{1}07)$ facet. It is known from TEM that samples like the one represented here possess $(1\bar{1}05)$ and $(1\bar{1}07)$ facets; thus, this type of graph is a helpful indicator of facet angles for ARPES of sidewall GNRs.

4.6 Corroboration of Structure and Improved Growth with Other Characterization Techniques

TEM images of samples (performed by collaborators; see Ref. [65][3]) grown with recipe $C_N^{(d)}$ consistently show one sidewall layer, with a direct observation of the two facets previously measured by Hicks et al [44]. Instead of having a combination of $(1\bar{1}0n)$ and $(1\bar{1}0m)$ facets alternating laterally along the length of trenches, TEM images reveal that there are nano-scale $(1\bar{1}05)$ facets at the trench top and bottom ($\sim$ 2 nm wide each), with a larger $(1\bar{1}07)$ facet composing the majority of the sidewall (hereafter referred to as the "primary" facet). See Fig. 4.19 for an image showing these structural features. The angles where $(1\bar{1}07)$ and $(1\bar{1}05)$ facet cones would be observed in ARPES are consistent with the data taken in Ref. [44] as well as with all ARPES data of samples grown with recipe $C_N^{(d)}$; see Table 4.1. In fact, growth

[3]Also, Supporting Information for Ref. [65]

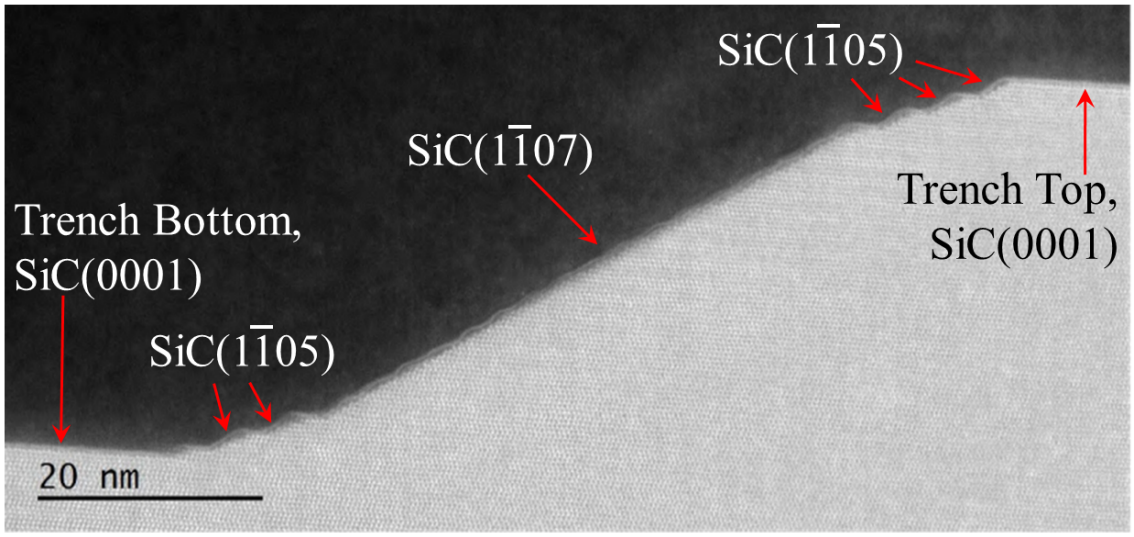

Figure 4.19: TEM of an armchair sidewall nanoribbon sample grown with $C_N^{(d)}$. The SiC(0001) trench top and bottom are indicated, for reference. It is obvious that the sidewall faceted outward, with 1-2 nm-wide (1$\bar{1}$05) nano-facets near the trench top and bottom. Separating each (1$\bar{1}$05) nano-facet are 1-2 nm-wide SiC(0001) terraces, referred to as nano-terraces. In between the groups of nano-facets is a large (1$\bar{1}$07) facet, taking up most of the sidewall. This (1$\bar{1}$07) facet is often referred to as the primary facet. All TEM images of samples grown with $C_N^{(d)}$ are structurally consistent with the image shown here. Image courtesy of Palacio et al (Ref. [65], Supporting Info.).

models for epitaxial graphene on SiC facets (Ref. [109]) suggest that it is reasonable to expect the formation of nano-facets.

It is evident from numerous TEM images of these improved samples grown with recipe $C_N^{(d)}$ that sidewalls are very well ordered and are structurally consistent from sample to sample. All TEM images of $C_N^{(d)}$ samples sow the same structure (that is, (1$\bar{1}$05) nano-facets at top and bottom of the sidewall with (1$\bar{1}$07) in between). In agreement with ARPES measurements that suggest improved sample quality, the high degree of order observed by TEM is evident in the resolution with which the graphene layers are imaged; any disorder along the length of the trenches (the direction into the plane of the image) would cause the graphene sheet to appear somewhat blurred. Such disorder-induced effects are not observed for $C_N^{(d)}$ samples.

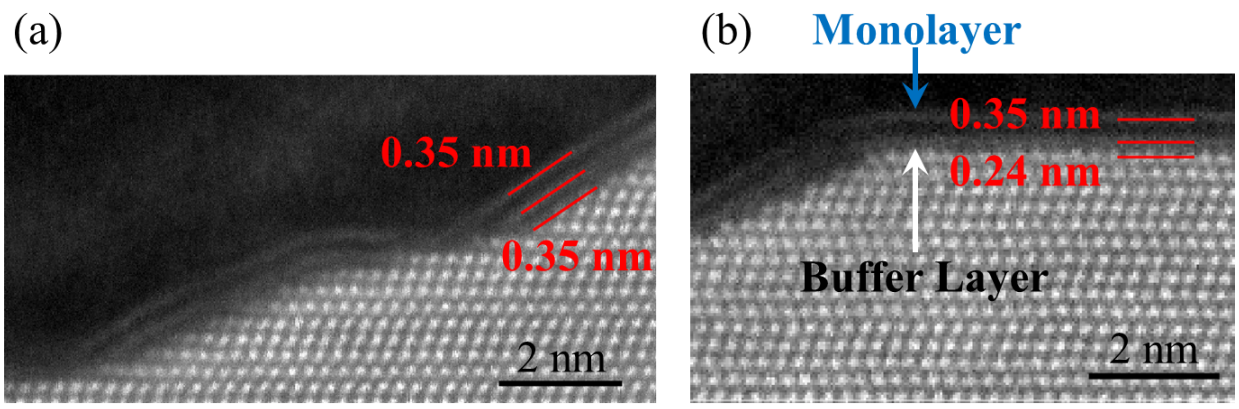

Figure 4.20: TEM images of a sample grown with recipe B_H. Two sidewall layers are evident, as well as buffer + monolayer on the trench top. (a) TEM image on the sidewall. A disordered nano-facet is seen near the trench bottom. $(1\bar{1}05)$ nano-facets are more disordered for B_H samples than for $C_N^{(d)}$ samples. The distance between the first sidewall layer and the $(1\bar{1}07)$ facet is 0.35 nm. The distance between the first and second sidewall layers on the $(1\bar{1}07)$ facet is also 0.35 nm. (b) TEM image near the trench top of a B_H sample. Buffer layer is seen to be 0.24 nm above the SiC, indicative of a substrate interaction. The monolayer rests 0.35 nm above the buffer layer. Thus, these observations are highly suggestive that the first layer of graphene on the $(1\bar{1}07)$ facet is metallic. Images courtesy of Palacio et al (Ref. [65], Supporting Info.).

4.6.1 Lack of a "Sidewall Buffer" Layer

We now also know from TEM measurements of improved samples that the first layer of graphene that grows on an armchair sidewall is metallic; there is no existence of an armchair "sidewall buffer" layer. The distance between buffer layer on the SiC(0001) and the SiC beneath it has been observed to be 0.24 nm (Fig. 4.20(b)), indicative of a substrate interaction and consistent with the semiconducting nature of the buffer layer, as measured by ARPES. On the other hand, monolayer graphene on the Si-face is observed to be distance of 0.35 nm above the buffer layer, consistent with the metallic nature of monolayer graphene. In TEM images of the armchair sidewall, it is evident that the first layer of graphene on the sidewall is a distance 0.35 nm from the underlying facet wall; see Fig. 4.20(a). This graphene-substrate distance is consistent with metallic graphene that is not bound or strongly interacting with the facet wall.

When a second layer is grown on the sidewall as well, the distance between the two graphene layers is observed to be 0.35 nm.

When ARPES measurements and TEM images were both taken on the same sample, if the sample showed monolayer sidewall graphene on the $(1\bar{1}05)$ and $(1\bar{1}07)$ facets in TEM, then a monolayer Dirac cone was also observed at angles appropriate for $(1\bar{1}05)$ and $(1\bar{1}07)$ facets. Necessarily, then, the single sidewall layer observed in TEM must be the source of the monolayer facet cones. EELS measurements performed on the armchair sidewall samples are also consistent with the first sidewall graphene layer being metallic graphene [65]. Thus, only metallic graphene forms on the armchair facets created with processing and growth methods presented here. The specific substrate interaction between the buffer layer and the top-most SiC bilayers on the SiC(0001) must result from the substrate geometry and graphene formation mechanism on the SiC(0001) facet. It is possible that a similar substrate interaction could be observed on other facets of SiC, but there is assuredly no "buffer" layer on the armchair sidewalls; even the first layer of graphene on the sidewalls is metallic and exhibits a graphene Dirac cone.

4.6.2 Bilayer Sidewall Graphene

While TEM images of samples grown with $C_N^{(d)}$ are enlightening as to the structure of the improved samples, TEM of the sample measured by Hicks et al in Ref. [44] (grown with B_H) is extremely impactful for the reinterpretation of ARPES data in Ref. [44]. Notably, the facet cones that were initially identified as $(2\bar{2}07)$ and $(1\bar{1}03)$ are observed in TEM to actually be $(1\bar{1}05)$ and $(1\bar{1}07)$; the corresponding facet angles ($\theta_{n=7} \approx 28^\circ$ and $\theta_{n=5} \approx 37^\circ$) are consistent with the facet cones observed in Ref. [44]. Compared to $C_N^{(d)}$ samples, TEM reveals that the $(1\bar{1}05)$ facets from the B_H sample appear to be somewhat larger, fewer in number, and more disordered in structure. Clearly, the optimized $C_N^{(d)}$ recipe did, in fact, improve the structure and ordering

of the $(1\bar{1}05)$ nano-facets. Also of great impact, TEM images of the sample from Ref. [44] show many of the sidewalls in the patterned array possessing two sidewall graphene layers. It is evident that the preliminary high temperature/short growth time recipe B_H did create fewer sidewall layers than recipe A_{Sp} (Ref. [43]); however, instead of one sidewall layer, B_H led to the formation of two sidewall layers.

Before TEM of the B_H sample revealed two sidewall layers, it had been deduced that there was only one sidewall layer because only one facet cone band could be resolved, albeit a band with an undesirably large k-width. It is now recognized that the "band" being measured in Ref. [44] was actually a monolayer band + a broadened bilayer band structure, with k-widths too large to be individually resolved due to angular broadening and unoptimized growth. TEM of this sample can be seen in Fig. 4.21, which shows two layers going across all $(1\bar{1}05)$ and $(1\bar{1}07)$ facets. Additional TEM images of this sample sometimes show partial second layers at the top and/or bottom of the sidewall, with monolayer sidewall coverage in between. Hence, both monolayer and bilayer bands would be observed if their k-widths did not make them indistinguishable. For more information and additional TEM images, see Palacio et al [65].

Improved fabrication of bilayer sidewall samples using a recipe similar to $C_N^{(d)}$ but with a higher peak growth temperature ($T \sim 1575$ °C ; this recipe will now be referred to as $C_N^{(BL)}$ for convenience) reveals three resolved bands, one from monolayer sidewall graphene and two from bilayer sidewall graphene. Figure 4.22 shows the band structure of the bilayer sidewall sample fabricated with the improved recipe: (b) is the raw data ARPES image, while (c) is a negative second derivative of the image in (b), used to highlight the location of the three visible bands. For comparison, Fig. 4.22(a) shows a monolayer sidewall facet cone (negative second derivative) with fits to the maxima in band intensities. The monolayer fit is then overlayed in Fig. 4.22(c) to show that the innermost band observed for the multilayer sample, which is the most

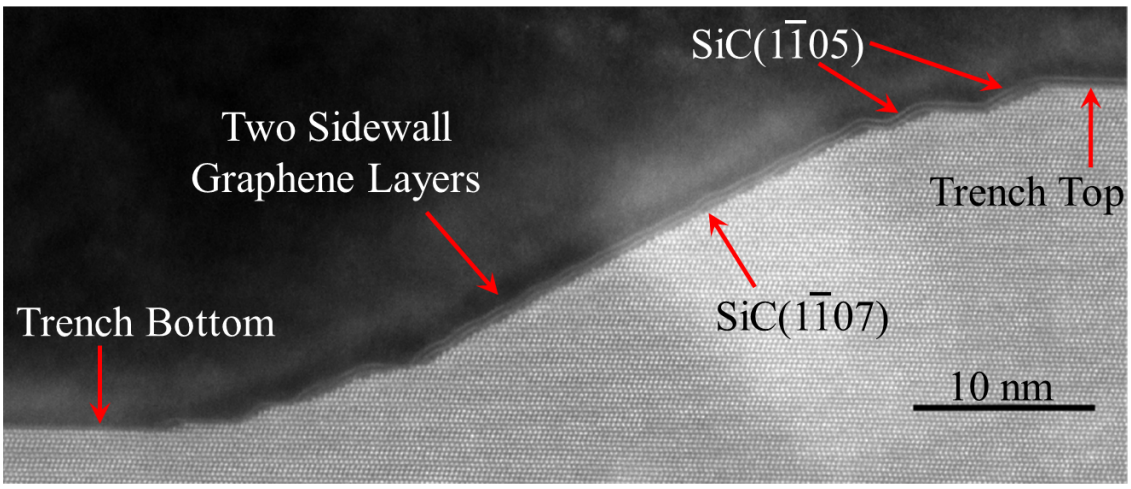

Figure 4.21: TEM image of a sample grown with B_H; this sample was used for ARPES measurements by Hicks et al in Ref. [44]. It is apparent that there are two sidewall layers going across all facets, seamlessly connected to buffer + monolayer on the trench top. (1$\bar{1}$05) and (1$\bar{1}$07) facets exist, as with samples grown with $C_N^{(d)}$. However, direct comparison of TEM images of both times of samples show that the (1$\bar{1}$05) facets are more disordered on samples grown with B_H. The fact that the sample from Hicks et al shows two sidewall layers his highly impactful for re-analysis of initial ARPES data [44]. Image courtesy of Palacio et al (Ref. [65], Supporting Info.).

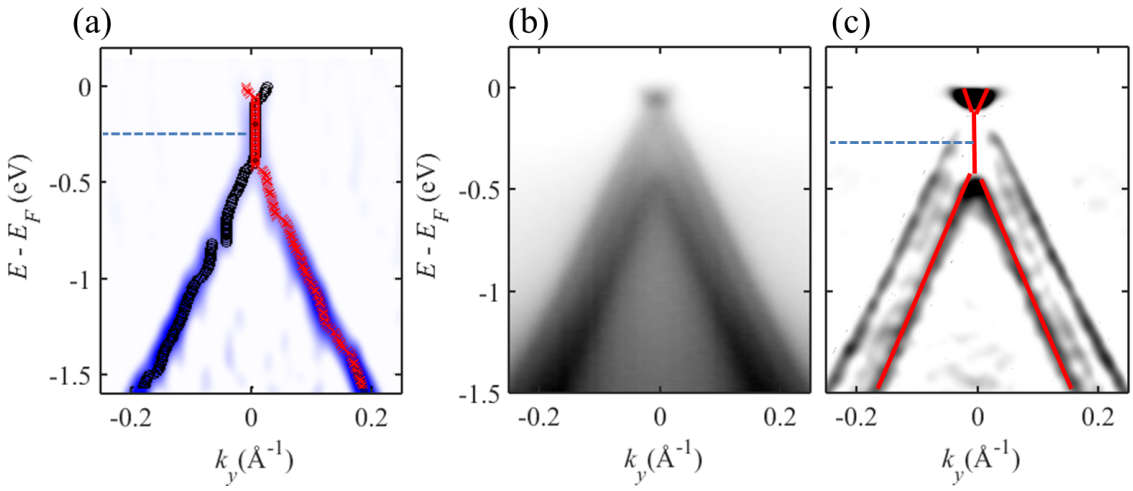

Figure 4.22: (a) Negative second derivative image of a monolayer sidewall graphene cone, for reference. The sample was grown with a $C_N^{(d)}$ recipe, and the facet cone is representative of all facet cones observed for such samples. The maxima in intensities were fit to show the center of the bands (red/black circles). (b) Band structure for a sidewall facet, grown with recipe $C_N^{(BL)}$ (a modified $C_N^{(d)}$ recipe). Three bands are observed. (c) Negative second derivative image of the facet cone in (b). The locations of the three bands can more easily be seen. The red lines exactly represent the fits to the monolayer sidewall facet cone in (a). It appears that the innermost band from the multilayer sidewall sample originates from some amount of coverage of monolayer sidewall graphene; the doping level and Fermi velocities are identical.

intense of the three bands, is from monolayer sidewall graphene. The upper two bands originate from some coverage of bilayer on the sidewalls. Note that for the bilayer bands, the Dirac point appears to be roughly 0.1 eV below the Fermi level.

It can be shown that the band structure from this more highly ordered multilayer sidewall sample is consistent with the unresolvable band structure from Hicks et al. Figure 4.23 is useful in showing the similarities between the band structures. Figures 4.23(a)-(c) shows the band structure of the $C_N^{(BL)}$ sample; (a) is, again, the ARPES k_x cut while (b) and (c) are negative second derivatives of the same image. The monolayer fit overlayed in (c) shows that the innermost band is consistent with a monolayer facet cone with doping $E - E_F \approx 0.24$ eV, the same as is typically observed. Figures 4.23(d)-(f) show a facet cone from Hicks et al [44]. It can be seen in the raw data k_x cut in (d) that there appears to be greater intensity inside the cone

where the monolayer band would be expected. Figure 4.23(e) shows an overlay of the sample from Ref. [44] (blue) with the second derivative image from (b) (black/red for contrast). It is apparent that the band structures look remarkably similar. At most, there might be a doping difference of < 0.05 eV between the two samples, which is not an unreasonable variation between two samples patterned and grown with different parameters. Figure (f) shows the same cone in (d) with the overlay of the fit from a monolayer facet cone. The location of the monolayer cone aligns well with the area of increased intensity inside the band structure in (d). Figures 4.23(g) and (h) show MDCs and EDCs for the modified-$C_N^{(d)}$ sample and the B_H sample, respectively. MDCs are taken at $E - E_F = -0.8$ eV, and the EDCs are taken at $k_y = 0$ Å^{-1}. Fitting the MDCs for each cone shows that the total k-spacing for the three resolved bands (MDC in (g), $\Delta k \approx 0.128 \pm 0.003$ Å^{-1}) is approximately equal to the total k-width of the "band" observed in the B_H sample (MDC in (h), $\Delta k \approx 0.118 \pm 0.022$ Å^{-1}). It can be seen that the two band structures are qualitatively similar, though the B_H sample exhibits greater inner intensities from θ-disorder and larger k-widths from ϕ-disorder. Since it is known that the B_H sample contained 1-2 sidewall layers, it can be extrapolated that the well-ordered sample contains 1-2 layers that are better ordered and, therefore, possess more easily resolved bands. Improved growth from the $C_N^{(BL)}$ recipe clearly made the band structure of 1-2 sidewall layers observable.

It should now be noted that while the innermost cone observed in Fig. 4.23 seems to originate from monolayer sidewall graphene and can easily be fit to the known monolayer facet Dirac cone, the two outermost bands do not seem to be explained by tight-binding calculations for AB-stacked bilayer. Even though graphene on the Si-face is known to exhibit AB-stacking, it is not surprising that the sidewall graphene does not maintain AB-stacking down the sidewall. Calculations for two graphene sheets that are slipped relative to each other [110] show widely varying bilayer band structures based on the slip vector magnitude and direction, even for small slip

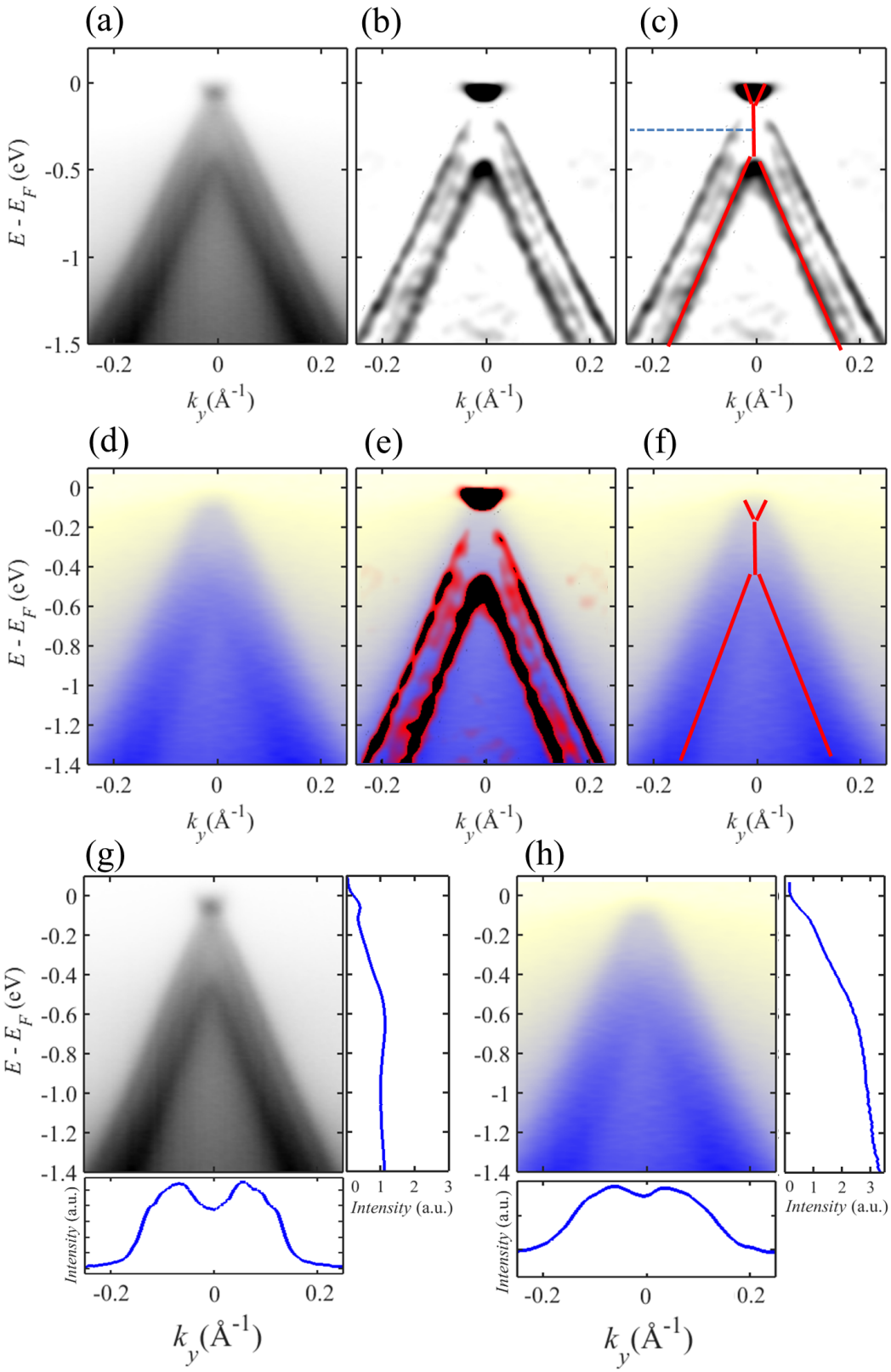

Figure 4.23: Summary of what is known about the band structure of multilayer sidewall graphene. (a)-(c) Band structure of a sample grown with recipe $C_N^{(BL)}$. (d)-(f) Band structure of a B_H sample (measured with ARPES by Hicks et al [44]). For all ARPES images, $h\nu = 36$ eV.

amounts. No calculations have yet been done to fit the bilayer bands observed in Fig. 4.23; further experiments will be required.

One additional explanation for the three $C_N^{(BL)}$ bands remains and should be addressed. It is possible that the $C_N^{(BL)}$ band structure is actually representative of sidewall trilayer. If so, then it is a coincidence that the innermost band corresponds well with the Dirac point and Fermi velocity of the known monolayer sidewall cone. However, there are several reasons why this trilayer explanation seems less likely than the monolayer + bilayer explanation. Primarily, the Dirac point of the "trilayer" band structure would necessarily be the same as the B_H sample, which was known from TEM to have monolayer + bilayer. On the Si-face, it is known that each additional graphene layer tends to have a Dirac point that is shifted ~ 0.1 eV above the Dirac point for the system with one less graphene layer; Ohta et al found Dirac points of $E_D - E_F = -0.44$ eV for monolayer graphene, $E_D - E_F = -0.30$ eV for bilayer graphene, $E_D - E_F = -0.21$ eV for trilayer graphene, and $E_D - E_F = -0.15$ eV for quadlayer graphene [62]. It would seem unlikely for both bilayer and trilayer sidewall graphene to have the same Dirac point. Additionally, if the innermost band does not originate from monolayer graphene on some percentage of the sidewalls, then almost all of the ~ 200 ribbons being measured by the $\sim 50\mu m$ beam must necessarily contain an entire three layers, else bilayer and monolayer band structures would also be observed in ARPES measurements. Given that the peak growth temperature was ~ 10 °C higher than a recipe known to grow only monolayer sidewall graphene (and, in fact, the growth time used in $C_N^{(BL)}$ was 50 sec, shorter than all $C_N^{(d)}$ recipes), it seems highly improbable that the sidewalls would have grown three complete layers.

Thus, if it can be assumed that the innermost band originates from monolayer sidewall graphene, then it can be observed that the two outermost bands from the $C_N^{(BL)}$ sample do not appear to be from AB-stacked graphene. Figure 4.24(b) shows tight-binding calculations from Ref. [62] for AB-stacked bilayer graphene near the

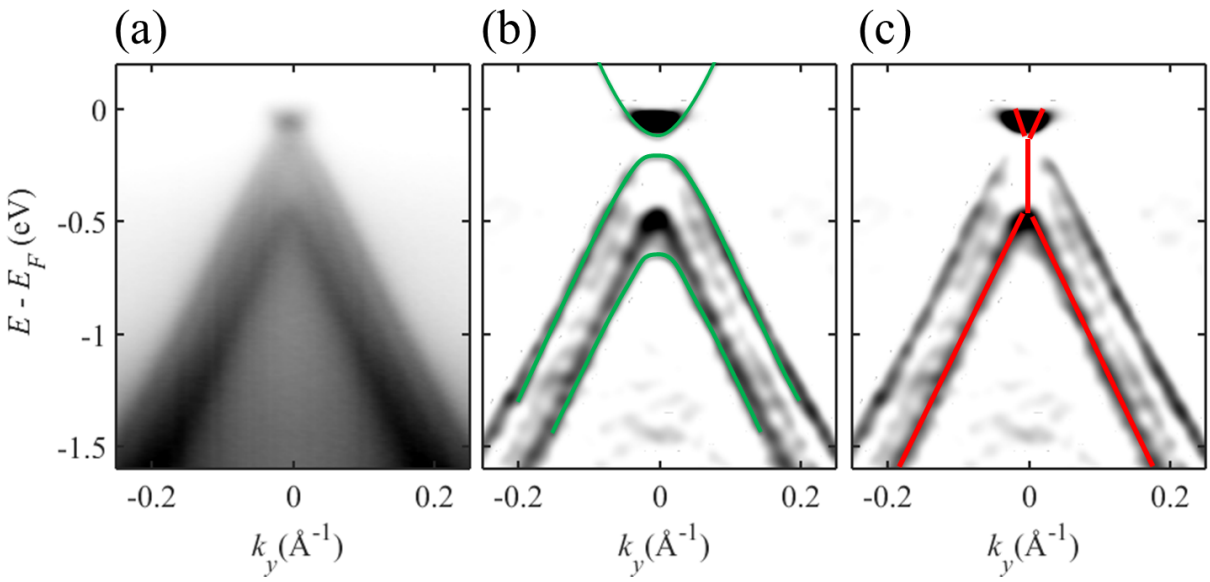

Figure 4.24: (a) ARPES of the $C_N^{(BL)}$ facet cone band structure. Three bands are observed. (b) Overlay of the negative second derivative of the image in (a) with tight-binding bands calculated for AB-stacked graphene. While the calculated bands seem to fit well for the innermost and outermost $C_N^{(BL)}$ bands, the middle band is not explained at all. Also, it is most probable that the innermost band actually originates from monolayer sidewall graphene; (c) The fit for monolayer sidewall facet cones is a good fit with the innermost $C_N^{(BL)}$ band. Thus, it is deduced that AB-stacking does not sufficiently explain the band structure observed for the $C_N^{(BL)}$ sample. For all ARPES images, $h\nu = 36$ eV.

Fermi level. The lowest tight-binding bilayer band shown is similar to the band that appears to necessarily originate from a sidewall monolayer. The outermost $C_N^{(BL)}$ band is well approximated by the nearest tight-binding bilayer band. However, the middle band from $C_N^{(BL)}$ is not explainable by either tight-binding band, nor could it be explained by monolayer sidewall graphene without a shift in the monolayer Dirac point. The $C_N^{(BL)}$ band structure does not fit well with tight-binding calculations for ABA- or ABC-stacked trilayer, either, though it is unlikely that the sample contains trilayer anyway, as previously discussed.

4.6.3 Perceived Inconsistency in Doping Level Between B_H Samples and $C_N^{(d)}$ Samples

Regardless of the explanation for the three bands measured from $C_N^{(BL)}$, it is known from TEM that the B_H sample from Hicks et al [44] contained monolayer + bilayer sidewall coverage, while TEM images of $C_N^{(d)}$ samples show only monolayer sidewall graphene. Thus, the perceived inconsistency between the doping level of the facet cones in Hicks et al ($E_D - E_F \approx 0$) and the doping of all measured $C_N^{(d)}$ facet cones is easily resolved. It is expected for the Dirac point of bilayer epitaxial graphene to be closer to the Fermi level than that of monolayer graphene. In Ref. [62], Ohta et al measure a similar difference in the Dirac points of monolayer and bilayer graphene on the SiC(0001), as determined by ARPES [62]. They find that the Dirac point for monolayer Si-face graphene is $E_D - E_F = -0.44$ eV, while the Dirac point for bilayer EG is $E_D - E_F = -0.30$ eV. In the same way, the Dirac point for monolayer sidewall graphene is $E_D - E_F = -0.24$ eV while the bilayer bands appear to have a Dirac point $E_D - E_F \approx -0.1$ to 0 eV.

4.6.4 Speculations on the Evolution of Armchair Facet Structure

It has been noted that TEM of samples grown with $C_N^{(d)}$ recipes show well-ordered, regular arrays of $(1\bar{1}05)$ nano-facets at the tops and bottoms of sidewalls, with a large $(1\bar{1}07)$ in between. TEM images of samples that contain full or partial bilayers on the sidewall tend to show fewer $(1\bar{1}05)$ facets at the top and bottom of the trench, with larger SiC(0001)-nano-terraces in between them; this difference is observed when comparing Fig. 4.19 with Fig. 4.21. Additionally, TEM seen in Sprinkle et al [43] of the sample grown with the A_{Sp} recipe (10min growth time at temperatures > 1450 °C) shows only one main facet, with minimal indication that there may have been a nano-facet near the top which disappeared at some point before the end of the growth process. From all of this information, it can be speculated that the $(1\bar{1}05)$ nano-facets form early on in the faceting and graphene growth process. Then,

as graphene growth continues, the nano-facets merge and slowly disappear with the creation of further graphene layers and the sublimation of Si away from the sample. Such a trend would be consistent with growth models by Ming et al [109, 111]. Nevertheless, it is also possible that processing differences between initial samples grown with A_{Sp} and more recent samples are primarily responsible for the lack of $(1\bar{1}05)$ nano-terraces in Ref. [43], rather than growth correlations. Experiments correlating growth, processing, and the evolution of the nano-facets via TEM would be required to confirm either explanation.

4.7 Growth of Armchair Sidewalls with Shallow Trench Depths

As previously mentioned, armchair samples with trench depths < 15 nm exhibit an increased tendency toward disorder and melting than samples etched ~ 20 nm or more. AFM clearly shows this in Fig. 4.25; samples in both (a) and (b) were grown with identical recipes, yet the shallow sample in (b) (~ 10 nm trench depth) has trenches that are much less straight after growth than the deeper sample in (a) (~ 20 nm trench depth).

In efforts to remedy the structural differences between deep and shallow trenches, a modification to the $C_N^{(d)}$ recipe was tested in hopes of producing straighter shallow trenches. Typical $C_N^{(d)}$ recipes contain a < 700 °C outgassing step, a ~ 1150 °C annealing step, and the growth step (< 1500 °C). It was conjectured that an additional annealing step at ~ 1350 °C (the buffer growth temperature) before the growth step might cause buffer layer to form on trench tops and decrease the amount of mass movement during growth. However, it was instead found that the features melted away entirely when this annealing step was used. Clearly, proceeding straight from the new anneal temperature ~ 1350 °C to the growth temperature > 1500 °C actually induced greater mass movement.

Subsequently, the recipe shown in Fig. 4.26(c) was tested. This new recipe, which

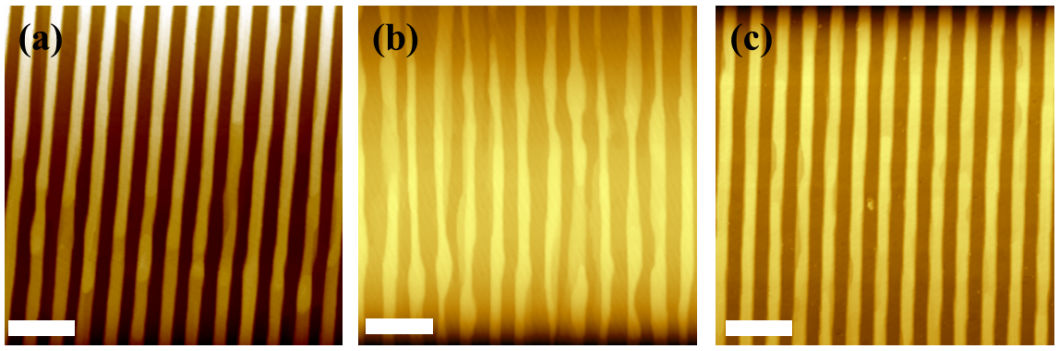

Figure 4.25: NC-AFM images of samples after growth. (a) AFM of a $\sim$ 20 nm-deep sample after growth with recipe $C_N^{(d)}$. (b) AFM of a $\sim$ 10 nm-deep after growth with recipe $C_N^{(d)}$. Trenches are significantly less straight than the sample in (a), showing significant wandering from the patterned step edge, despite the fact that all processing and growth parameters were identical except for etch depth. (c) AFM of a $\sim$ 10 nm-deep sample after growth with the $C_N^{(s)}$ recipe, described in the text. It is evident that the shallow trenches are greatly improved compared to the sample in (b). All scale bars are $1\mu m$.

will now be referred to as $C_N^{(s)}$, begins identically to $C_N^{(d)}$: an outgassing step < 700 °C is followed by a $\sim$ 1150 °C annealing step. Then, the temperature is increased to $\sim$ 1250 °C for 5 min before being allowed to cool back down to $\sim$ 1150 °C for 15-20 min. This second $\sim$ 1150 °C step is proceeded by the growth step, using the same desired parameters as would be used for a deep sample with recipe $C_N^{(d)}$ (1530-1565 °C for 1-1.5 min). Figure 4.26 shows the evolution from recipe $C_N^{(d)}$ to recipe $C_N^{(s)}$, with corresponding AFM for each modification to the recipe.

After growth with $C_N^{(s)}$, not only did shallow trenches not melt, they appear to be significantly improved. AFM clearly shows the improvement to the quality of the shallow trench step edges after growth with $C_N^{(s)}$. Figure 4.25 directly compares a deep sample grown with $C_N^{(d)}$, a shallow sample grown with $C_N^{(d)}$, and a shallow sample grown with $C_N^{(s)}$. The trenches grown with $C_N^{(s)}$ in (c) are at least as straight as the deep sample in (a); no qualitative difference can be observed between them.

ARPES measurements of shallow sidewalls grown with $C_N^{(s)}$ (Fig. 4.27) reveal a structure similar to that of deep samples: both $(1\bar{1}05)$ and $(1\bar{1}07)$ facets are still

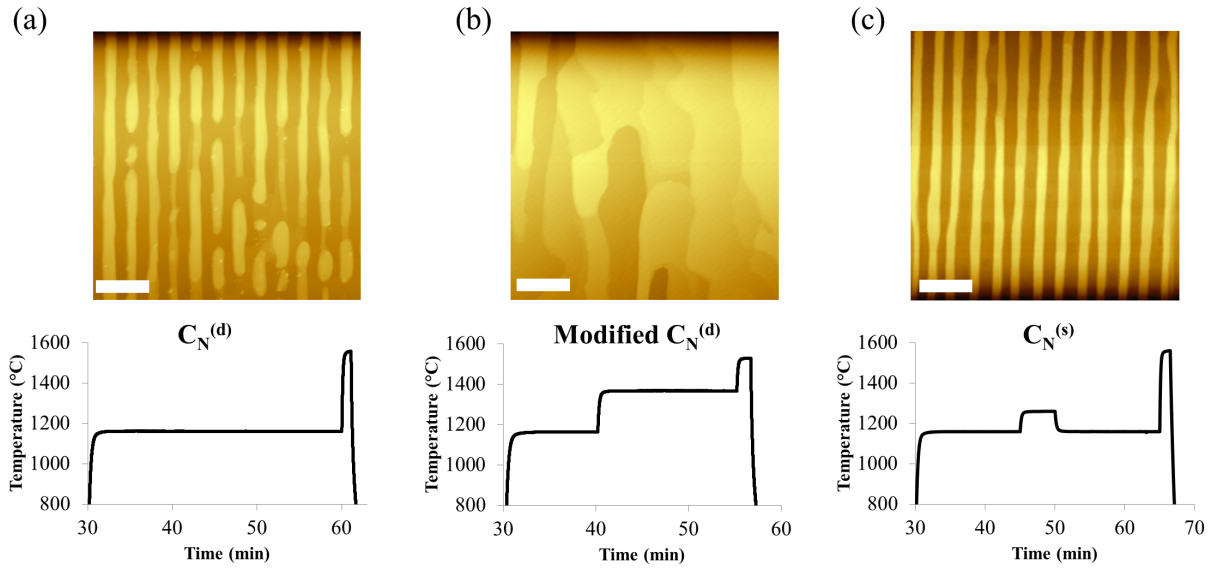

Figure 4.26: Evolution of the recipes developed for sidewall samples, based on trench depth. All images are NC-AFM. (a) Top- AFM of a shallow sample ($\sim$ 9nm trench depth) grown with $C_N^{(d)}$. In addition to step edge wandering away from the patterned trench direction, it is evident that some features also began to melt during growth. Bottom- Graph of the $C_N^{(d)}$ recipe, starting after the < 700 °C outgassing step. (b) Top- AFM image of a shallow sample ($\sim$ 10nm trench depth) grown with a modified $C_N^{(d)}$ recipe. An additional annealing step at $\sim$ 1350 °C was included before the growth step. It is apparent that this recipe caused all features to melt. Bottom- Recipe used to grow the AFM image above it; the graph begins after the < 700 °C outgassing step. (c) Top- AFM of a shallow sample ($\sim$ 10nm trench depth) grown with newly developed recipe $C_N^{(s)}$. Features did not melt, and step edges wander much less than shallow samples grown with $C_N^{(d)}$; this is helpful for minimizing ϕ-broadening in ARPES. Scale bars in all images are $1\mu m$.

clearly observed in shallow samples (Fig. 4.28), with metallic facet cones (Fig. 4.27). In fact, facet angles are often more clearly resolved than for deep samples grown with $C_N^{(d)}$. Perhaps it should be attempted to grow deep trenches with recipe $C_N^{(s)}$ as well. There appears to be only one notable difference between the band structures of the shallow ribbons compared to the deep ribbons: the shallow sample facet cones for both the $(1\bar{1}07)$ and $(1\bar{1}05)$ facets are doped $E_D - E_F = -0.33 \pm 0.03$ eV, compared to the doping of $E_D - E_F = -0.24$ eV for deep samples. To date, no TEM has been performed on shallow sidewall samples grown with the described methods, so it is currently unclear why there might be a doping level difference between shallow samples and deep samples.

In light of the structural information gained from TEM of deep trenches, it is likely that the shallow sidewall samples have $(1\bar{1}07)$ facets that are smaller in width than their deep trench counterparts, causing the $(1\bar{1}05)$ nano-facets to be closer together. It is not clear how this could affect the difference in doping levels, if at all. Two speculative explanations are: that the graphene monolayer going over the shallow trenches is more closely approximated by a continuous graphene sheet than for deeper samples, causing the doping of the sidewall graphene to more closely align with that of monolayer Si-face graphene ($E_D - E_F = -0.45$ eV); or that a work function difference on the shallow sidewalls, compared to the deep sidewall geometry, is responsible for the measured difference in doping. Further characterization experiments on shallow samples would be enlightening.

Independent of the doping level difference, shallow samples grown with $C_N^{(s)}$ show as many indications of being well-ordered as the deep $C_N^{(d)}$ samples. Δk-widths are observed to be statistically similar to those in Table 4.2 for deep samples. Also, many of the replica cones are observed, with all replica cones shown in Fig. 4.14 being observed for growth temperatures > 1555 °C . Therefore, it is evident that recipe $C_N^{(s)}$ creates shallow sidewall ribbons samples that are highly ordered, though it has

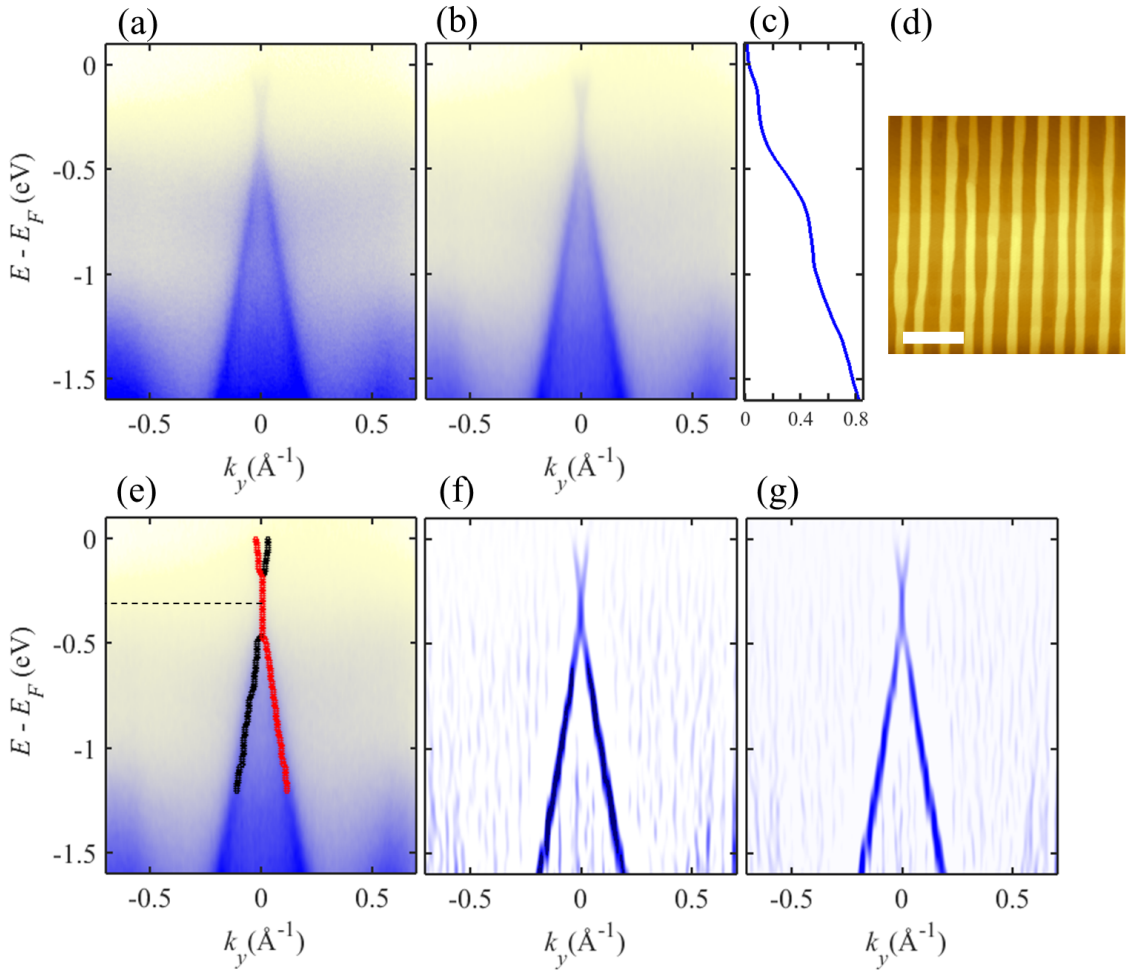

Figure 4.27: ARPES of a shallow ribbon sample ($\sim$ 10 nm trench depth) grown with recipe $C_N^{(s)}$. Shallow samples are observed in ARPES to have a similar structure to deep ($>$ 15 nm) samples, in that they show $(1\bar{1}05)$ and $(1\bar{1}07)$ facet cones, measured in (a) and (b) respectively. (c) An EDC of the cone in (b), at $k_y = 0$ Å^{-1}; intensity goes up to the Fermi level, indicating that the cone is metallic. (d) NC-AFM image of the sample measured with ARPES in the rest of the Figure. Scale bar is $1\mu m$. The sample was grown with $C_N^{(s)}$; the trenches are much straighter than shallow samples grown with recipe $C_N^{(d)}$. The lack of step edge wandering leads to the small Δk widths observed in all ARPES images. (e) Fits to the band peaks in the ARPES image in (b) show that the doping level is $E - E_F \approx -0.33$ eV. In a similar manner to deep samples, intensity drops off near the Fermi level faster than might be expected. However, EDCs (c) and negative second derivative images (f)-(g) show that facet cone intensity does, in fact, go up to the Fermi level; the cones appear to be metallic. For all ARPES images, $h\nu = 36$ eV.

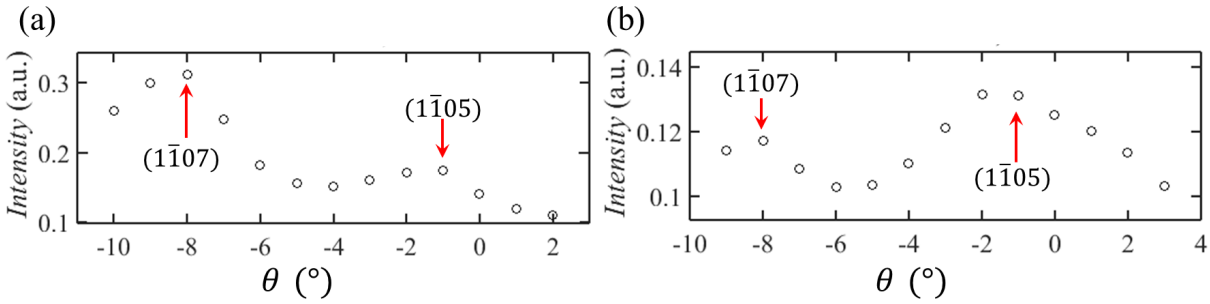

Figure 4.28: Analogous to Fig. 4.18, (a) and (b) show maximum MDC intensity as a function of measured angle θ_{meas}. It is obvious that the shallow samples still show $(1\bar{1}05)$ and $(1\bar{1}07)$ facets. While for deep samples, $(1\bar{1}07)$ facets tend to show higher intensities than $(1\bar{1}05)$ facets (on the same sample), the trend is not identical for shallow samples. Clearly, the $(1\bar{1}07)$ facet is more intense than the $(1\bar{1}05)$ facet in (a), but the opposite is true in (b). Both samples were ~ 10 nm deep and grown with $C_N^{(s)}$ recipes. However, the sample in (a) was grown with a peak temperature $\sim 10°$ higher than the sample in (b), which suggests that for shallow samples (and possibly also for deep samples), growth is seeded on the $(1\bar{1}05)$ nano-facets before growth on the $(1\bar{1}07)$ facets. Also, since the shallow sample trench depths are less, it is likely that the $(1\bar{1}07)$ facets have surface areas much more equivalent to the $(1\bar{1}05)$ facets than for deep samples, where $(1\bar{1}07)$ facets are significantly larger.

not yet been determined why the modification to the $C_N^{(d)}$ recipe was able to improve step edge wandering so significantly.

To date, no TEM has been performed on shallow sidewall samples. However, in light of the structural information revealed by TEM of deeper sidewall samples, it is likely that the $(1\bar{1}07)$ primary facets on shallow samples are much smaller, causing the $(1\bar{1}05)$ nano-facets at the top and bottom of trenches to be close together. Having nanometer-sized facets extremely close together during the heating and graphene growth process would, understandably, increase the likelihood that facet walls would become structurally more disordered, wandering away from the SiC$<11\bar{2}0>$ direction and sometimes melting entirely. Figure 4.25 shows AFM of a deep sample (etch depth $\sim$ 20nm compared to AFM of a shallow sample (etch depth $\sim$ 10nm). Both samples were grown with identical recipe parameters. The deeper trenches are much straighter than the shallow trenches, which wander away from the SiC$\langle 11\bar{2}0\rangle$ direction.

In efforts to remedy the structural differences between shallow and deep samples,

an additional annealing step (after the preliminary annealing step, $\sim$ 1150 °C) before the growth step was tested. This secondary annealing step was chosen to go up to the temperature at which buffer layer forms, in the hope that buffer layer would begin to grow on the SiC(0001) and, consequently, pin the trenches and prevent them from melting. Initially, when the secondary annealing step was tested and continued straight to the growth temperature step (T$>$ 1530 °C), the patterned features melted away. However, when the secondary annealing step was terminated and the sample was allowed to go back down to the primary annealing step temperature for $>$ 5min before going back up to the growth temperature, the features did not melt; in fact, not only did the features not melt, the trenches were much straighter than they would otherwise have been without the addition of this secondary annealing temperature. It has now been shown through ARPES measurements of samples grown with this recipe that the samples are extremely well-ordered (exhibiting replica cones and good k widths, comparable to those in Table 4.2 for deeper trenches) and still contain only monolayer graphene on the sidewalls. Thus, a separate optimized recipe has been developed for armchair trenches with etch depths $<$ 15nm.

4.8 Semiconducting Graphene Nanoribbons from Highly Ordered Substrate Interactions

Initial interest in researching sidewall graphene nanoribbons was motivated by the theoretical ability to create a semiconducting form of graphene for use in graphene-based devices. It has been predicted that graphene nanoribbons would have quantum confinement-induced bandgaps dependent on ribbon edge structure and width [74, 76, 77]. Because the width of the ribbon is predicted to determine the size of the bandgap [74], GNRs would theoretically have a tunable bandgap determined by ribbon width, which would make GNRs useful as a semiconducting material for graphene-based devices. However, to date all ARPES measurements of sidewall ribbons have shown metallic graphene on $(1\bar{1}05)$ and $(1\bar{1}07)$ facets; no sidewall graphene

nanoribbon bandgap has been measured.

It is possible that none of the sidewall ribbons measured thus far have been of an appropriate width for opening a gap, in which case further experiments will be needed utilizing shallower trench depths and recipe $C_N^{(s)}$. Another possible explanation for the lack of an observed bandgap exists. Many of the calculations that predict confinement-induced bandgaps also assume isolated ribbons (no substrate effects) and, typically, H-passivated ribbon edges [74, 76]. Unlike lithographically patterned GNRs, sidewall ribbons possess atomically ordered edges; however, sidewall ribbons are shown to seamlessly connect to a graphene buffer layer on the trench tops. It is possible that, because of edge bonding effects, sidewall GNRs do not fulfill the idealized boundary conditions assumed for many of the calculations that predict bandgaps. Whichever the case may be, sidewall graphene nanoribbon systems to date have not produced evidence of semiconducting graphene nanoribbons.

While such a result may be disappointing for research efforts desiring to create semiconducting GNRs, a gapped graphene band has emerged and now been identified, deriving its band structure from the highly ordered substrate interactions that result from the optimized growth parameters developed and discussed at length in this Chapter. We now present the experimental measurements of the gapped graphene band and discuss how the structural origin of the band it has been determined.

4.8.1 Details of Sidewall Graphene Structure

ARPES measurements [44] and TEM images [65] of sidewall nanoribbons have been very instructive as to the structure and electronic nature of sidewall ribbon samples. Figure 4.29 shows a TEM image with the typical nanoribbon structure after growth. While trenches are initially etched straight down into the SiC (creating SiC$\{1\bar{1}00\}$ facets), the growth process causes the SiC trenches to facet outward. For samples with an initial etch depth of $>$ 20nm, the equilibrium growth geometry consists of

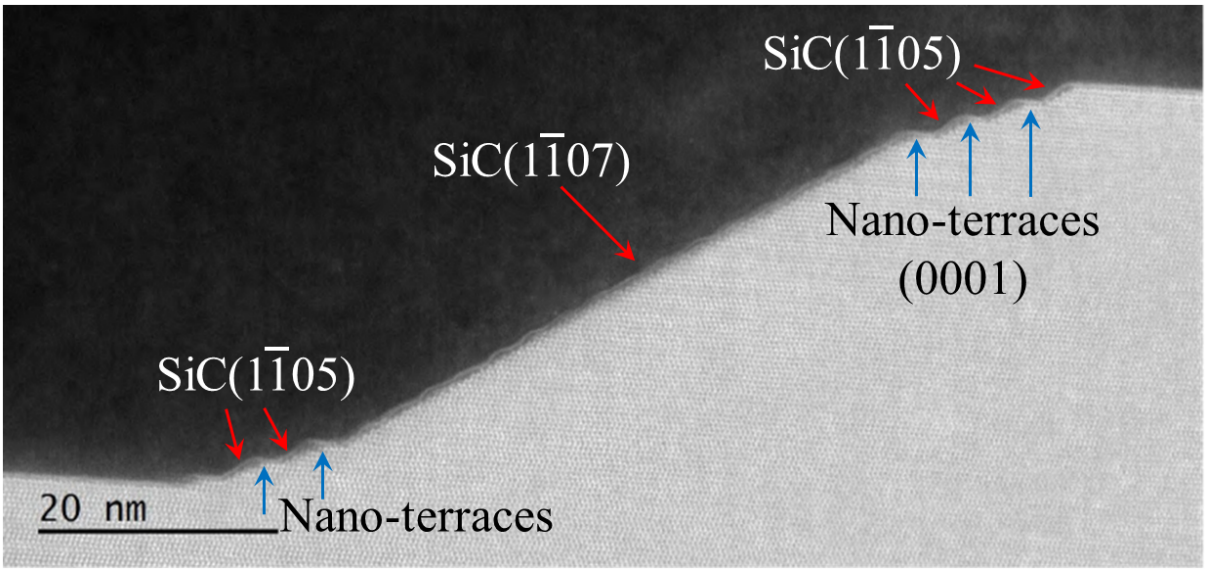

Figure 4.29: TEM image of a typical armchair sidewall sample, grown with $C_N^{(d)}$. The SiC(1$\bar{1}$05) nano-facets at the top and bottom of the sidewall are separated by SiC(0001) nano-terraces that are 1-2 nm wide. The distance between graphene on the nano-terraces and the SiC is measured to be 0.23 nm, slightly smaller than the distance between Si-face buffer layer and the underlying SiC (0.24 nm) [65]. Image courtesy of Palacio et al (Ref.[65], Supporting Info.).

nanometer-scale (1$\bar{1}$05) facets near the top and bottom of the trench, with a $\sim$ 20 nm-wide SiC(1$\bar{1}$07) facet in between, hereafter called the primary facet. In between each (1$\bar{1}$05) nano-facet, there exist nanometer-scale SiC(0001) terraces.

ARPES [44], TEM and EELS [65] data show that the graphene layer on the primary (1$\bar{1}$07) facet and (1$\bar{1}$05) nano-facets is metallic. ARPES measurements of samples exhibit n-doped Dirac cones at the appropriate angles for the known sidewall facets. EELS spectra for graphene on the (1$\bar{1}$05) and (1$\bar{1}$07) facets are consistent with metallic monolayer graphene. Also, TEM shows that the distance between the SiC facet and the sidewall graphene layer (0.35 nm) is the same as the distance between Si-face buffer layer and monolayer (0.35 nm; monolayer Si-face graphene is metallic). In fact, a direct correlation of various characterization techniques reveals that samples showing monolayer facet cones for each facet via ARPES also show a single sidewall layer on the (1$\bar{1}$07) and (1$\bar{1}$05) facets in TEM. Thus, the first layer of sidewall graphene

on these facets is metallic. However, TEM images show that graphene on the (0001) nano-terraces is even more closely bound to the SiC substrate than buffer on the SiC(0001) trench tops [65]: the distance between graphene on the nano-terraces and the underlying SiC is 0.23 nm, compared to 0.24 nm between regular Si-face buffer and the underlying SiC bilayers. This observed distance is highly indicative that the graphene on the nano-terraces is bound to the substrate and not metallic, in the same way that the Si-face buffer layer is not metallic. EELS data also show a spectral component consistent with a bandgap for graphene on the nano-terraces [65].

4.8.2 $\varepsilon_{\mathbf{ter}}$ as a Gapped Graphene Band

ARPES measurements of samples grown with improved processing and growth parameters (recipes $C_N^{(d)}$ and $C_N^{(s)}$) consistently show a gapped band, ε_{ter}, in a finite region of k-space. Samples that show ε_{ter} also exhibit many first- and second-order replica cones, and facet cones have small k-widths (approaching instrument resolution limits for the appropriate experimental parameters), indicating the high level of ordering achieved by improved growth methods. This ε_{ter} band was not observed in previous samples grown with unoptimized recipe B_H[4]. Because of the order created by optimized fabrication and growth parameters, ε_{ter} has now been observed consistently in numerous samples. Figure 4.30(d) shows a cut of the band in k_x, perpendicular to the Γ-K direction. It is evident that ε_{ter} has an observable bandgap between the Fermi level and the top of the valence band of $E - E_F \approx -1.5$ eV. Because ARPES does not measure unfilled states, the bottom of the conduction band has not yet been measured; thus, the full size of the bandgap is currently unknown. Note that the SiC non-dispersing surface state g_1 can be seen in Figs. 4.30(b) and (d); this surface state originates from any bare SiC that is being simultaneously measured with the graphene on the trench tops and sidewalls and is structurally unrelated to any band

[4]No ARPES has been performed on samples grown with recipe A_{Sp}.

features originating from graphene or buffer layer.

Isolating the band structure features from graphene on each of the surfaces known to structurally exist on sidewall samples (Fig. 4.29) requires care in order to separate real space and reciprocal space. The diagram in Fig. 4.31 depicts all of the structural features present on sidewall samples fabricated with described methods, including all local surface normals. For correct interpretation of ARPES data from samples with more than one crystallographic surface, it is necessary to remember that ARPES measures bands via $E(k_{\|})$, where $k_{\|}(\theta)$ is the parallel momentum of the photoelectron ejected at an angle θ relative to the local surface normal. Correspondingly, a disconnect exists between the angle where a band is measured and the topographical location from which the band originates.

The ARPES spot size ($\sim 50\mu m$) is large enough such that hundreds of sidewall ribbons are measured simultaneously, each with a number of topographical features. Facets are tilted by corresponding angles θ_{F} determined by the facet indices $(1\bar{1}0n)$; see Table 4.1. Bands originating from tilted facets ($\theta_{\mathrm{F}} \neq 0^{\circ}$) are measured at an angle that is convoluted with their facet angle, $\theta_{\mathrm{meas}} = \pm|\theta_{band}| \pm |\theta_{\mathrm{F}}|$, with θ_{band} determined from the band's k_x and k_y location in the tilted facet Brillouin zone (via Eqns. 1.3 and 1.4). With all of this being taken into account, it becomes obvious that when a band with unknown origin is measured, which high symmetry Brillouin zone point the band likely originates from as well which faceted surface the band originates from must be determined.

As an example of this convolution of facet angle and band location, if a band is discovered with $\theta_{\mathrm{meas}} = [-1^{\circ}, 1^{\circ}]$ for $h\nu = 36$ eV, then the band would likely originate from one of two structural locations. The K point of a $(1\bar{1}05)$ facet would be measured at $\pm 1^{\circ}$, because $\theta_{\mathrm{K}} \approx 36^{\circ}$ for $h\nu = 36$ eV, and $\theta_{\mathrm{F}} \approx 37^{\circ}$ for $(1\bar{1}05)$. Otherwise, the Γ point of the (0001) surface would also be measured in this angular range, since $\theta_{\Gamma} = 0^{\circ}$ and $\theta_{\mathrm{F}} = 0^{\circ}$ for SiC(0001).

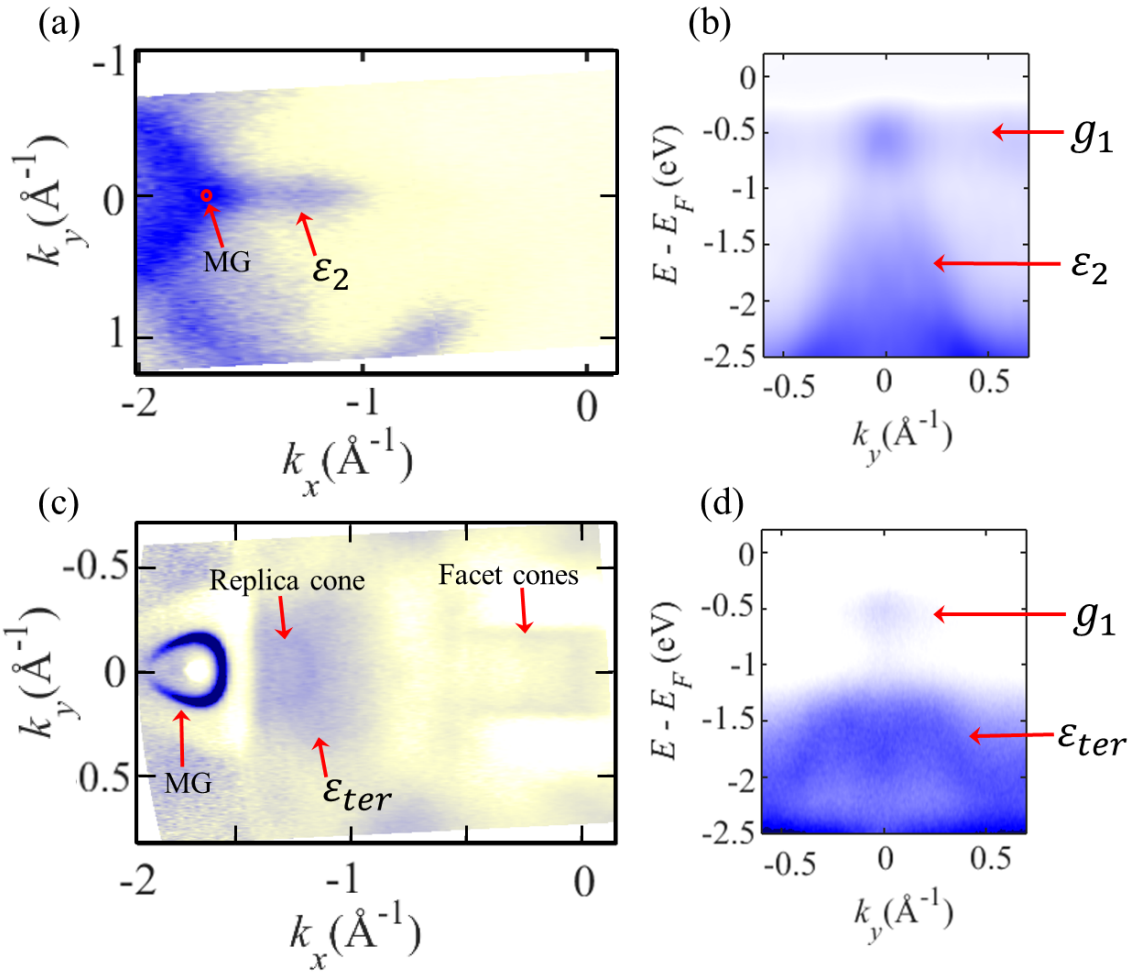

Figure 4.30: (a) ARPES Fermi Surface ($E - E_F = -0.6$ eV) of a flat buffer sample. One K point for monolayer epitaxial graphene is measured (location indicated by red circle). The buffer band ε_2 is observed in three lobes around the K point, along the Γ-K directions. (b) A constant k_x cut through ε_2, taken at $k_x \approx -1.2$ Å^{-1}. In addition to ε_2, some intensity can be seen from the non-dispersing SiC state g_1. (c) ARPES Fermi Surface ($E - E_F = -1.55$ eV) of an armchair sidewall ribbon sample. One K point for monolayer epitaxial graphene on the trench tops is measured. Facet cones are visible between $k_x = 0$ and $k_x \approx -0.5$ Å^{-1}. The gapped band ε_{ter} is observed in the same angular range ($k_x = -1.710$ Å^{-1} to ~ -1.0 Å^{-1} from the reference of the Si-face graphene Brillouin zone) as ε_2 from buffer. Note that intensities around the monolayer K point are diminished due to a matrix element effect. Also, a 6×6 replica cone from the monolayer cone is often observed and happens to coincide with part of the ε_{ter} angular range. (d) A constant k_x cut through ε_{ter}, taken at $k_x \approx -1.1$ Å^{-1}. In addition to ε_{ter}, some intensity can be seen from the non-dispersing SiC state g_1. For (a) and (b), $h\nu = 70$ eV. For (c) and (d), $h\nu = 36$ eV.

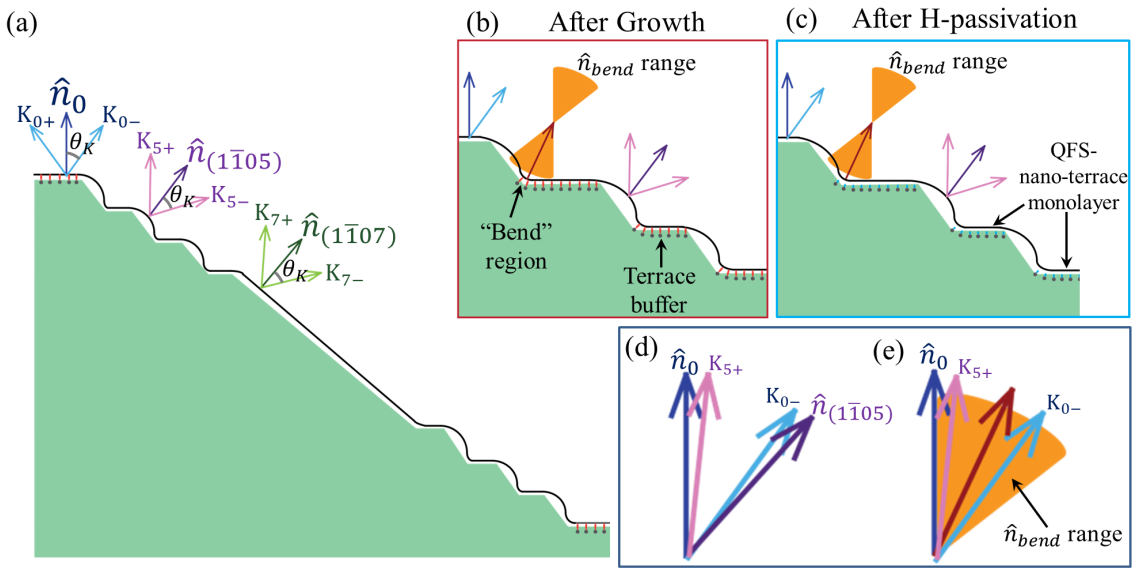

Figure 4.31: Diagram of the armchair sidewall for further explanation of the origins of the angular locations of bands measured for H-passivated sidewalls. (a) The surface normals and K points for the (0001), $(1\bar{1}05)$, and $(1\bar{1}07)$ facets are indicated. (b) Depiction of the nano-facet and nano-terrace geometry after growth. Characterization experiments indicate that graphene on the nano-terraces is bonded to the substrate, in a manner analogous to buffer layer on the Si-face; this nano-terrace buffer layer is hereafter called terrace buffer. In addition to the nano-terraces and $(1\bar{1}05)$ nano-facets, a bend region is seen to exist in TEM, with graphene that also appears to interact with and bond to the substrate. The bend region contains graphene with a large range of surface normals. (c) The same nano-terrace and nano-facet section is shown after H-passivation. The passivation process is known to de-couple buffer layer from the substrate, creating quasi-free-standing graphene. Passivation of the sidewall sample, therefore, is expected to de-couple the terrace buffer and, thus, lead to a metallic Dirac cone at the K point, which is also the K point for graphene on the Si-face. De-coupling of graphene in the bend region would produce metallic graphene with a large range of surface normals. (d) Illustration of the angular range for the transition from the (0001) K point to the $(1\bar{1}05)$ K point. (e) The range of surface normal K points overlaps with the angular range between the (0001) and $(1\bar{1}05)$ K points.

The gapped graphene band ε_{ter} is observed in the same angular range as the semiconducting ε_2 band from flat buffer. Because sidewall ribbon samples where ε_{ter} are observed have many topographical components, it would not be out of the question for ε_{ter} to originate from an angled surface with an appropriate surface normal; the coincidental angular overlap with ε_2 does not necessarily require a similar structural origin. ε_{ter} is measured continuously within the range $\theta_{\text{meas}} = [20°, 36°]$ for $\theta_{\text{K}} = 36$ eV; this angular range does not correspond with the K points for any $(1\bar{1}0n)$ facet which has been known from TEM and ARPES to exist on the sidewall samples. Table 4.1 reveals which facet indices would be expected for a K point within the angular range measured for ε_{ter}. If ε_{ter} originates from the K point of some angled surface, it would be structurally necessary for the facet to be $(1\bar{1}0n)$ with $n = 2$ or $n > 12$. Since ε_{ter} has been observed consistently in $C_N^{(d)}$ and $C_N^{(s)}$ samples and yet no TEM of $C_N^{(d)}$ samples have observed $n = 2$ or $n > 12$ facets, it is highly unlikely that ε_{ter} originates from graphene on any such surfaces. One additional possibility remains. The angular range where ε_{ter} exists also includes the Γ point for SiC$(1\bar{1}07)$ facets. However, the band from the SiC Γ point for $(1\bar{1}07)$ has been observed in extremely undergrown samples, and it does not disperse in any fashion similar to ε_{ter}.

As demonstrated, the k-space region near the Si-face EG K point where ε_{ter} is observed is quite unique; it does not correspond with any likely high symmetry points for any facets observed in TEM. Therefore, since ε_{ter} does possess the same angular range as ε_2 from flat buffer (see Fig. 4.30 (a) and (c)), it is most likely that ε_{ter} originates from a buffer-like layer with the same surface normal as the macroscopic SiC(0001) surface normal. If ε_{ter} originates from some type of buffer layer, then the question remains as to why the band structure is different from that of buffer layer measured previously on flat samples (Chapter 2). We will now discuss what can be deduced, based on the correlation of ARPES observations of ε_{ter} with TEM and EELS measurements of ribbon samples as well as XRD measurements of the buffer layer [60].

4.8.3 Structural Origin of $\varepsilon_{\mathbf{ter}}$

As previously discussed, it has been observed in TEM that the nano-(0001)-terraces contain a graphene layer which interacts with the substrate. The distance between the "terrace buffer" and the underlying SiC nano-terrace is 0.23 nm [65], 0.01 nm smaller than the observed distance between buffer on the trench tops and the underlying SiC bilayers; see Fig. 4.20. EELS spectra also suggest that the "terrace buffer" graphene possesses a bandgap [65]. Thus, graphene on the nano-terraces would be expected to have non-metallic bands. The nano-terraces have a surface normal which is parallel to the macroscopic surface normal for the Si-face. The correlated location of ε_{ter} with that of ε_2 from flat buffer is, then, consistent with the fact that the Brillouin zones for the nano-terraces are parallel and oriented the same as the Brillouin zone for Si-face buffer layer. The location of ε_{ter} in k-space is consistent with that of the buffer band ε_2, which is observed on all CCS-grown flat buffer layer samples grown with optimized parameters. Thus, the strips of terrace buffer layer on the (0001) nano-terraces appear to be the source of the ε_{ter} band and are, in essence, 1-2 nm-wide semiconducting GNRs; however, the measured bandgap appears to originate from substrate interactions instead of the quantum confinement-induced bandgap expected for isolated GNRs (which cannot be reasonably expected to apply to the terrace buffer).

The question remains as to why ε_{ter} is observed for the nano-terraces instead of the typical ε_2 buffer band. In answer to that question, recent XRD measurements on flat buffer layer samples are enlightening [60]. These diffraction measurements show that the Si-face buffer layer is actually incommensurate with the SiC, with a fundamental period of modulation $\lambda \approx 1.9$ nm [60]. This length scale is on the order of the widths of the nano-terraces, and sometimes larger. Thus, it would not be reasonabe to expect the substrate interaction between the graphene on the nano-terraces and the SiC beneath it to be identical to that of a macroscopically-ordered large buffer

sheet on the Si-face. In fact, step relaxation effects would be expected. The fact that TEM shows a different graphene/substrate distance for the nano-terraces than for buffer on the Si-face is supportive of the fact that a different bonding configuration is occurring. It is likely that the individual bond strengths are comparable between regular buffer and terrace buffer; most likely, it is the location and number of bonds as well as the periodic distances between them that is different. More experiments would be necessary to determine the exact bonding involved.

A band with similar k_y dispersion to ε_{ter} has been observed below the ε_2 buffer band on flat buffer samples. For buffer samples, the top of this similarly dispersing band reaches only up to $E - E_F \sim -2.5$ eV. Most likely, the change in bonding configuration for buffer on the nano-terraces destroys buffer's ε_2 band (or pushes it above the Fermi level) and shifts this similar band from ~ 2.5 eV below E_F up to 1.5 eV. This picture is consistent with a well-ordered terrace buffer layer that interacts and bonds to the substrate in a manner similar to but different from that of Si-face buffer. Figure 4.32 shows ε_{ter} and ε_2, with the band which resembles ε_{ter} observed below ε_2.

4.8.4 Corroboration of Origin of ε_{ter} with H-passivation Experiments

Another indication that ε_{ter} originates from a well-ordered substrate interaction is the fact that ε_{ter} disappears upon H-passivation of the sidewall sample. In similar experiments, it can be shown that a flat buffer layer does not possess a metallic Dirac cone until after H-passivation causes the buffer layer to no longer interact with the substrate. H-passivation of a sidewall sample shows metallic facet cones on the $(1\bar{1}05)$ and $(1\bar{1}07)$ facets with doping levels that are approximately charge neutral; this might be expected, because the sidewall graphene on those facets was already metallic, exhibiting minimal interaction with the substrate, and because quasi-free-standing monolayer graphene on the Si-face is also observed to be approximately

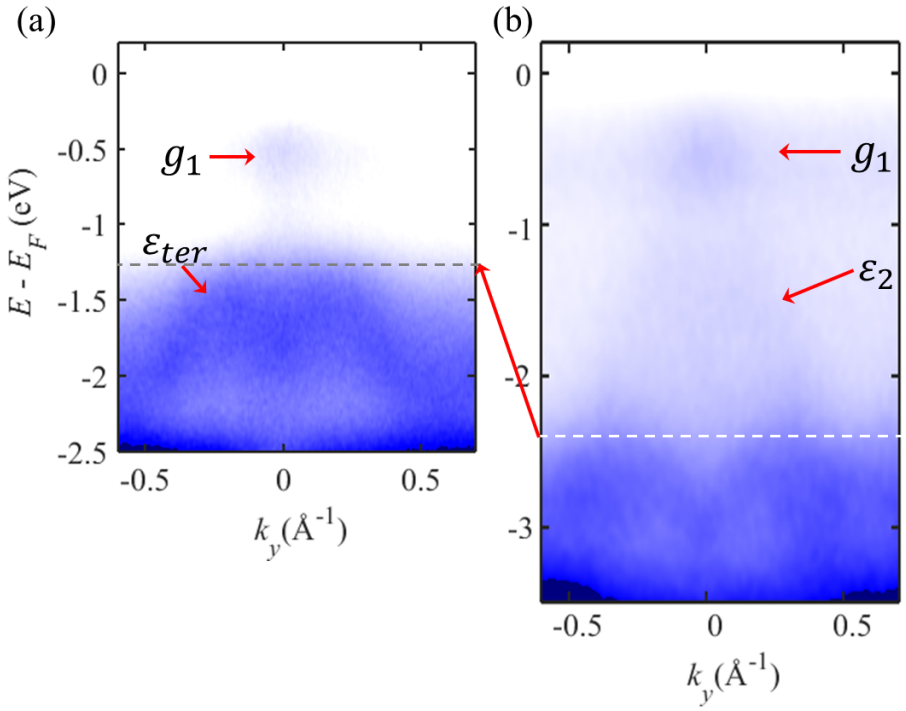

Figure 4.32: Comparison of ε_{ter} with a higher binding energy buffer layer band. (a) ARPES k_x cut through the ε_{ter} band. Some intensity from the non-dispersing SiC surface state g_1 is observed. $h\nu = 36$ eV. (b) ARPES k_x cut through the buffer layer band ε_2 at the same k_x value as in (a). A band that disperses similarly to ε_{ter} is observed below ε_2, with the top of the band at $E - E_F \approx -2.4$ eV. It is believed that the specific bonding geometry of the terrace buffer layer to the nano-terrace either destroys ε_2 or shifts it above the Fermi level. Then, the higher binding energy band in (b) could have also been shifted up to the binding energy where it is seen for terrace buffer, $E - E_F = -1.5$ eV. It is reasonable for a different bonding geometry to occur for the nano-terraces due to what is known about the incommensurate structure of the buffer layer on the Si-face (see Ref. [60] for more information). For (b), $h\nu = 70$ eV.

charge neutral. As previously stated, ε_{ter} disappears upon H-passivation.

If ε_{ter} does, in fact, originate from a buffer-like layer on the (0001) nano-terraces, then the nano-terrace buffer possess a Brillouin zone that is parallel to that of the Si-face graphene Brillouin zone. Thus, H-passivation would be expected to cause a Dirac cone from the passivated nano-terrace buffer at the same K point for Si-face graphene. In fact, H-passivation of a sidewall sample does show two Dirac cones at the Si-face graphene K point; Figure 4.33 shows this. The outer, more intense cone is consistent with H-passivated Si-face buffer layer (also called quasi-free-standing monolayer). However, the inner cone is neither consistent with quasi-free-standing monolayer nor the inner band expected for quasi-free-standing bilayer (that is, H-passivated buffer + monolayer). For ARPES measurements of H-passivated epitaxial graphene, see Ref. [90]. Therefore, the inner cone seen in Fig. 4.33(e) and (f) could be explained by H-passivated terrace buffer. It is important to note that this inner cone is not observed at the K point for graphene off the ribbon pattern; the cone is, then, associated with the pattern features.

Also of importance for the correct interpretation of the inner cone observed at the K-point of Si-face graphene for H-passivated ribbon samples is the fact that H-passivation experiments performed by Riedl et al show consistent doping levels for all quasi-free-standing graphene bands. When H-passivated samples are heated to reversibly remove the hydrogen, intensities from the quasi-free-standing bands diminishes until only the pre-passivation band structure is observed. No change in doping of the cones is observed during the hydrogen-removal process. Thus, the inner cone observed on the H-passivated ribbon sample, which has doping $E_D - E_F \approx -0.35$ eV, cannot be explained by either normal monolayer graphene or by a partially H-passivated buffer layer. It is not currently understood why H-passivated nano-terrace buffer would not be approximately charge neutral, like quas-free-standing-monolayer on the Si-face, instead of n-doped by ~ -0.35 eV.

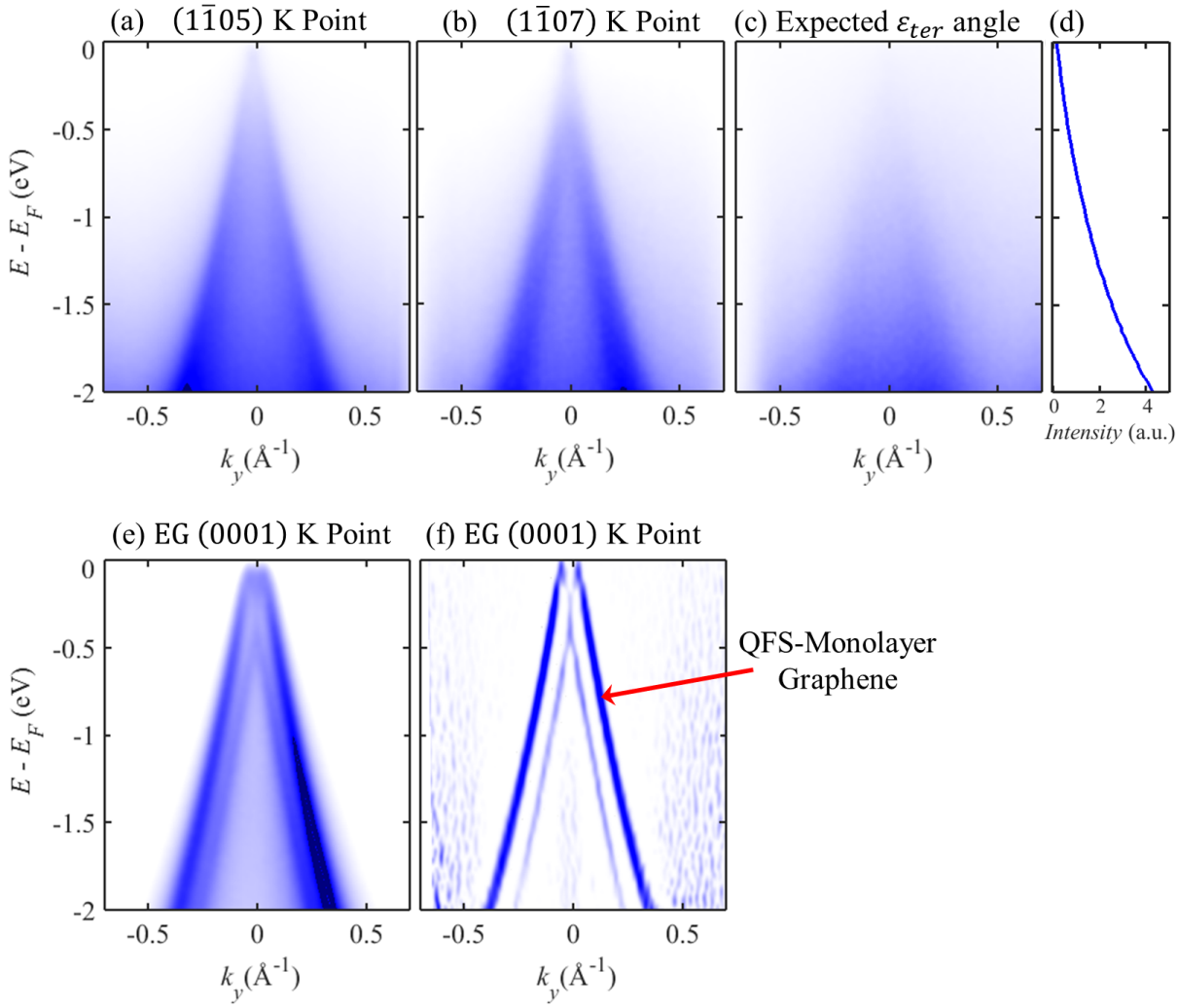

Figure 4.33: ARPES of an armchair sidewall nanoribbon sample. Metallic Dirac cones are observed at the K points for the (a) (1$\bar{1}$05) and (b) (1$\bar{1}$07) facets, as expected. (c) In the angular region where ε_{ter} would be expected for a non-H-passivated sample, there is instead a weak metallic Dirac cone (as shown by the EDC in (d)). See Fig. 4.31 and the related discussion for an explanation of why a weak Dirac cone might be expected in this angular range. (e) ARPES through the K point for EG on the Si-face. The outer, more intense cone is consistent with the cone expected for quasi-free-standing monolayer. It is believed that this cone originates from the passivated buffer layer on the trench tops. The inner cone cannot be explained by either quasi-free-standing monolayer or quasi-free-standing bilayer. (f) Negative Second derivative image of the cone in (e). It appears that the inner cone has a doping of ~ -0.35 eV. Note that this n-doped cone is not observed at the (0001) EG K point off the ribbon pattern; thus, the origins of this cone must be related to the ribbon features. For all ARPES images, $h\nu = 36$ eV.

As observed in Fig. 4.33, the $(1\bar{1}05)$ and $(1\bar{1}07)$ facet cones are relatively unperturbed by the H-passivation process except for an increased Δk_y-width. Cones from quasi-free-standing monolayer and quasi-free-standing graphene on the nano-terraces are observed at the K point of graphene with a surface normal parallel to the macroscopic SiC(0001) surface normal, as expected. ε_{ter} is removed after H-passivation, as would be expected for a material that interacts with the substrate.

One additional observation deserves comment. In the angular region where ε_{ter} would be expected to be measured, a weak metallic Dirac cone is instead observed. This weak cone would not otherwise be expected in this angular region, because it does not overlap with the finite K point angular regions for the $(1\bar{1}05)$ and $(1\bar{1}07)$ facets. Nevertheless, a reasonable explanation for the observation of this weak cone can be found. The diagram in Fig. 4.31 illustrates the fact that there are regions between the (0001) nano-terraces and the $(1\bar{1}05)$ nano-facets that possess graphene with varying local surface normals, ranging from the normal of the (0001) terraces to the normal of the $(1\bar{1}05)$ facets (denoted as the $\hat{n}_{bend}$ range in orange in Figs. 4.31(b), (c), and (e)). TEM images show that the distance between graphene in these "bend" regions is small, approximately the same as the distance between the nano-terrace buffer and the underlying SiC; this small distance is indicative of a substrate interaction between the graphene and the local SiC. EELS spectra [65] also indicate that graphene in these bend regions is not metallic; a component consistent with a bandgap can be seen both for the nano-terrace buffer as well as for the graphene in these bent regions. Therefore, it would be expected for H-passivation of sidewall samples to produce graphene that is no longer interacting with the substrate in these regions. The weak metallic cones (Fig. 4.33) are, in fact, observed in the angular range expected for K points transitioning between SiC(0001) and a sidewall facet. The full extent of the angular range where the H-passivation-created cones are observed is difficult due to their weak intensity.

4.8.5 A Second Potentially Semiconducting Graphene Band

The gapped band ε_{ter} is robustly observed on samples grown with optimized recipes $C_N^{(d)}$ and $C_N^{(s)}$ within the peak growth temperature range 1530-1575 °C . In addition to ε_{ter}, another gapped band has been observed in well-ordered samples grown with with $C_N^{(d)}$ recipes, though its observation is not as robust under varying growth conditions as that of ε_{ter}. Figure 4.34 depicts this band, which will now be referred to as $\varepsilon_{\text{bend}}$. The $\varepsilon_{\text{bend}}$ band is observed over a large angular range that encompasses both the $(1\bar{1}05)$ and $(1\bar{1}07)$ K points, and even overlaps with ε_{ter} for part of it's angular range– in total, an angular range encompassing $\theta_{\text{meas}} = [0°, \sim -28°]$. Over that angular range, the band does not disperse in k_y, the direction parallel to the trench step edges; this non-dispersion and large angular range is suggestive of a one-dimensional source. A splitting in $\varepsilon_{\text{bend}}$ can also be observed in the most undergrown samples where $\varepsilon_{\text{bend}}$ is measured. The splitting occurs such that an upper band ${\varepsilon_{\text{bend}}}^{(u)}$ is observed near the angular range for the K point of the $(1\bar{1}05)$ facets, and a lower band ${\varepsilon_{\text{bend}}}^{(l)}$ is observed near the angular range for the K point of the $(1\bar{1}07)$ facets. There is a certain angular range between the expected facet K points where both ${\varepsilon_{\text{bend}}}^{(u)}$ and ${\varepsilon_{\text{bend}}}^{(l)}$ are observed simultaneously (Fig. 4.34(b)). However, for less undergrown samples, the splitting in $\varepsilon_{\text{bend}}$is not observed; instead, $\varepsilon_{\text{bend}}$ appears broadened throughout the entire angular range where it is seen. Presumably, this broadening would be due to disorder in the structural origin of the band, but correlation with exact growth temperatures has been inconsistent.

At this point in time, it is impossible to conclude the exact source of $\varepsilon_{\text{bend}}$. TEM and observation of the geometry of the $(1\bar{1}05)$ and $(1\bar{1}07)$ SiC crystallographic facets suggest that there could be periodic, linear chains of bonds to the sidewall graphene layer along the $(1\bar{1}07)$ primary facet ($\sim$ 2 nm between bonding chains down the length of the facet) as well as one-dimensional bonding along the $(1\bar{1}05)$ nano-facet edges. Nevertheless, the correlation of $\varepsilon_{\text{bend}}$ with the $(1\bar{1}05)$ and $(1\bar{1}07)$ K points also suggests

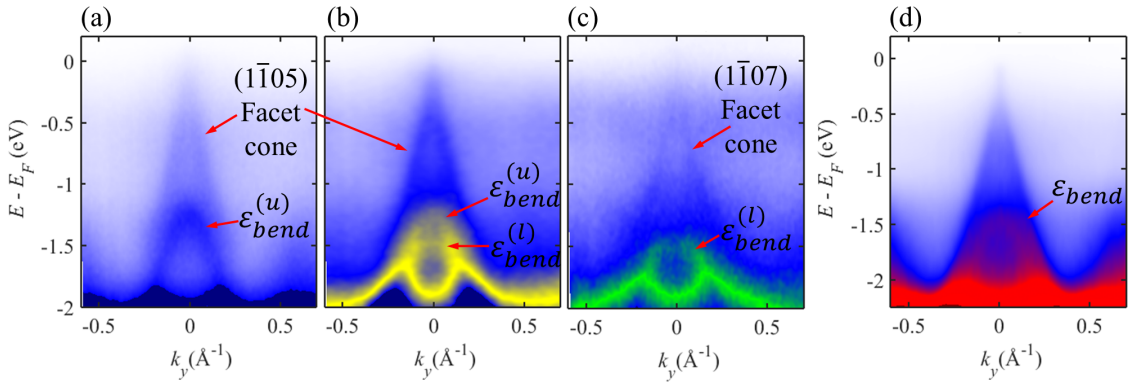

Figure 4.34: ARPES k_x cuts through the observed band $\varepsilon_{\text{bend}}$. (a) The upper splitting of the $\varepsilon_{\text{bend}}$ band, observed near the (1$\bar{1}$05) K point; a facet cone is observed above $\varepsilon_{\text{bend}}$. (b) In an angular range between the (1$\bar{1}$05) and (1$\bar{1}$07) K points, both the upper and lower $\varepsilon_{\text{bend}}$ bands are observed simultaneously. (c) At the end of the (1$\bar{1}$07) facet cone range, only the lower splitting of $\varepsilon_{\text{bend}}$ is observed. Images in (a)-(c) were taken on an "undergrown" sidewall sample; that is, the growth temperature and time were on the low end of the range for which monolayer graphene is observed, indicated by the weak facet cone intensities. (d) $\varepsilon_{\text{bend}}$, as measured on a sample that is not undergrown. The intensity from the two splittings in $\varepsilon_{\text{bend}}$ cannot be resolved, so the band appears much broader. For all ARPES images, $h\nu = 36$ eV.

that $\varepsilon_{\text{bend}}$ could be a sidewall graphene sub-band. Due to the large angular observation range and the inconsistency of exact growth conditions with which $\varepsilon_{\text{bend}}$ is observed, it is impossible to determine the exact source of $\varepsilon_{\text{bend}}$ at this point in time. Further experiments with varying temperature, growth time, and processing are required to attempt to measure the $\varepsilon_{\text{bend}}$ band more consistently.

4.9 Conclusions from Armchair Sidewall Nanoribbons

The armchair sidewall nanoribbon geometry is promising for future electronics purposes. Well-ordered graphene nanoribbons can be fabricated. The high level of order in the nanoribbons is evidenced by replica cones and k-widths approaching that of instrument resolution for the experimental parameters used.

Due to improved growth methods, a gapped graphene band was discovered, leading to the conclusion that there is a second type of semiconducting graphene in addition to Si-face buffer layer. "Terrace" buffer layers on nanometer-scale SiC(0001) terraces

formed on optimized ribbon samples show a gapped band which is much larger than that of the buffer layer (1.5 eV instead of 0.5 eV). It is possible that further structured substrate engineering and optimized growth efforts could produce graphene with a bandgap similar to that of Si, connecting metallic graphene nanoribbons for a useful future device geometry.

CHAPTER V

SIDEWALL GRAPHENE NANORIBBONS ON SIC$(11\bar{2}N)$ FACETS: ZIGZAG GRAPHENE NANORIBBONS

5.1 Introduction to Zigzag-Oriented Sidewalls

As previously discussed, graphene has two primary crystallographic directions: the armchair direction and the zigzag direction. Graphene on the Si-face grows consistently with a known orientation, so trenches can be etched into SiC along either of these graphene directions to create trenches that have armchair edge graphene or zigzag edge graphene on the trench tops. Graphene growth has been shown to maintain crystallographic orientation over steps [43, 65, 98, 4, 99, 100], so it has been assumed that graphene can form over step edges onto sidewalls of etched trenches to create graphene nanoribbons on the sides of facets with known edge structure. For sidewall graphene ribbons that are desired to have zigzag edges, trenches should be etched into SiC such that the initial facet is SiC$\{11\bar{2}0\}$.

Armchair sidewall nanoribbons have been studied extensively and discussed in Chapter 4. Likewise, zigzag-oriented trenches grown with confinement controlled sublimation (CCS) have also been studied; however, these "zigzag sidewall ribbons" have presented many unforeseen problems to researchers due to differences in growth kinetics and substrate interactions between armchair and zigzag SiC facets, as will now be described. It should not be surprising that the armchair and zigzag facets grow graphene at dissimilar rates and show substrate interactions that are different. In an analogous fashion, the Si-face grows graphene much more slowly than the C-face, and the first layer of graphene on the Si-face (the buffer layer) interacts and bonds to the substrate so that it is not metallic graphene. However, on the C-face, even the first

layer of graphene is metallic and shows a Dirac cone when measured with ARPES. Thus, it would be reasonable to discover that zigzag oriented facets do not behave identically to armchair facets in growth of sidewall graphene. The differences between the two types of facets as well as everything currently known about zigzag sidewall graphene will now be discussed.

5.2 Attempts to Develop a Recipe for Zigzag Sidewall Nanoribbon Samples

Growth of zigzag samples presented in this work began concurrently with attempts to improve armchair sidewall ribbon recipes ($C_N^{(d)}$ in Chapter 4). It was implicitly assumed that any recipe developed for armchair samples would be a good starting point for growing and studying zigzag ribbons as well. However, these zigzag samples proved to be troublesome. Unlike armchair facets, which readily produce metallic sidewall graphene with Dirac cones measurable in ARPES, CCS recipes that are known to grow monolayer sidewall graphene on armchair sidewalls (e.g., $C_N^{(d)}$) do not show any evidence of metallic sidewall graphene for zigzag sidewall samples. Interestingly, while metallic Dirac facet cones have not been measured for zigzag samples, neither have any semiconducting bands to within $E - E_F = -3$ eV. Thus, if there is metallic or semiconducting graphene on the sidewalls, it is either not well-ordered enough (grown at these temperatures) to produce bands that are coherent and measurable in ARPES, or the band gap is > 3 eV.

Historically, researchers have had difficulties growing zigzag samples because of patterned features melting during growth. The specific growth temperatures being used for early samples that led to frequent pattern melting are not known. Nevertheless, it was suggested during initial research efforts to grow zigzag samples for ARPES measurements that a buffer layer grown prior to patterning might stabilize features and prevent melting during growth. Many samples have been patterned and grown in this way.

The recipe that is typically used for zigzag samples in this work will be referred to as Z_N when a buffer layer was not grown on the sample prior to patterning trenches via lithography, while the recipe $Z_N^{(B)}$ will refer to samples that had a flat buffer layer grown on the Si-face, then were patterned via lithography, and finally were grown with a recipe like Z_N. Typical growth temperatures for Z_N and $Z_N^{(B)}$ recipes are approximately the same as those used with $C_N^{(d)}$ and $C_N^{(s)}$ recipes ($\sim$ 1530 $-$ 1570 °C); such recipes are known to form monolayer sidewall graphene on armchair facets. Growth times for Z_N and $Z_N^{(B)}$ recipes are typically longer than for $C_N^{(d)}$ and $C_N^{(s)}$ recipes.

Many of the samples that have been characterized within this work were grown with $Z_N^{(B)}$ recipes. Consequently, it is often observed in ARPES that a significant amount of monolayer as well as some bilayer exist on the trench tops. It should also be noted that no samples grown with either $Z_N^{(B)}$ or Z_N have been observed to melt. Thus, it is possible that the pre-patterning buffer growth step is unnecessary. Nevertheless, it is possible that growth temperatures used with Z_N recipes are not high enough to induce the pattern melting observed by previous researchers.

5.3 ARPES Measurements of Samples Grown with Z_N and $Z_N^{(B)}$

Zigzag sidewall samples grown with Z_N and $Z_N^{(B)}$ recipes do not show any metallic facet cones, as observed by ARPES. Figure 5.1 shows a Fermi surface of a sample grown with $Z_N^{(B)}$(peak growth temperature $\sim$ 1565 °C). It is evident that the graphene on the trench tops is extremely well-ordered, because a plethora of first- and second-order replica cones are observed. In fact, this Fermi surface shows more replica cones than are observed for armchair samples grown with either $C_N^{(d)}$ or $C_N^{(s)}$. Despite the presence of a well-ordered monolayer on the trench tops, no facet cones are observed along the direction required for zigzag facets; see Fig. 5.1(a). Because of the orientation of the zigzag facet normal relative to the Si-face graphene Brillouin zone, Dirac cones from

metallic graphene on zigzag facets should be seen along the $K_{(\bar{1}0)}$-$K_{(1\bar{1})}$ direction (as indicated by the dashed black lines in Fig. 5.1(a)). Only replica cones from monolayer graphene on the trench tops are observed near the $K_{(\bar{1}0)}$-$K_{(1\bar{1})}$ direction. Therefore, either graphene is not present on the sidewalls when trenches are grown with Z_N, the structure is too disordered to produce coherent bands measurable by ARPES, or any graphene/graphene-like layer present on the sidewalls is not metallic (does not possess a metallic Dirac cone).

ARPES k_x cuts through the observed replica cones confirm that they originate from umklapp processes. As expected, the doping of the replica cones is $E_D - E_F = -0.45$ eV, identical to that of monolayer graphene on the trench tops. Additionally, it is known that all observed cones are replica cones because they can be indexed with SiC 6×6 unit vectors from the monolayer K points. Figure 5.2 presents k_x cuts from the Fermi surface in Fig. 5.1, showing a few of the observed replicas: $\mathbf{G}_{10}(\bar{7}1)$, $\mathbf{G}_{10}(\bar{7}0)$, $\mathbf{G}_{01}(0\bar{6})$, $\mathbf{G}_{01}(0\bar{7})$, $\mathbf{G}_{1\bar{1}}(\bar{1}1)$, and $\mathbf{G}_{1\bar{1}}(\bar{1}0)$.

As previously stated, it is obvious that from the copious number of replica cones observed that the monolayer graphene on the trench tops is extremely well-ordered. However, it is observed in ARPES of these Z_N and $Z_N^{(B)}$ samples that there is often a diffuse background intensity, as seen in Figs. 5.2(a)-(c). Such a high intensity diffuse background is inconsistent with the observable high quality of the monolayer on the trench tops. It is also important to note that high intensity diffuse backgrounds are not typically observed for armchair samples grown with $C_N^{(d)}$ and $C_N^{(s)}$. As a result, it is possible (if not probable) that the diffuse intensity observed from Z_N and $Z_N^{(B)}$ samples originates from the zigzag facets, which do not possess well-ordered metallic graphene since no facet cones are observed.

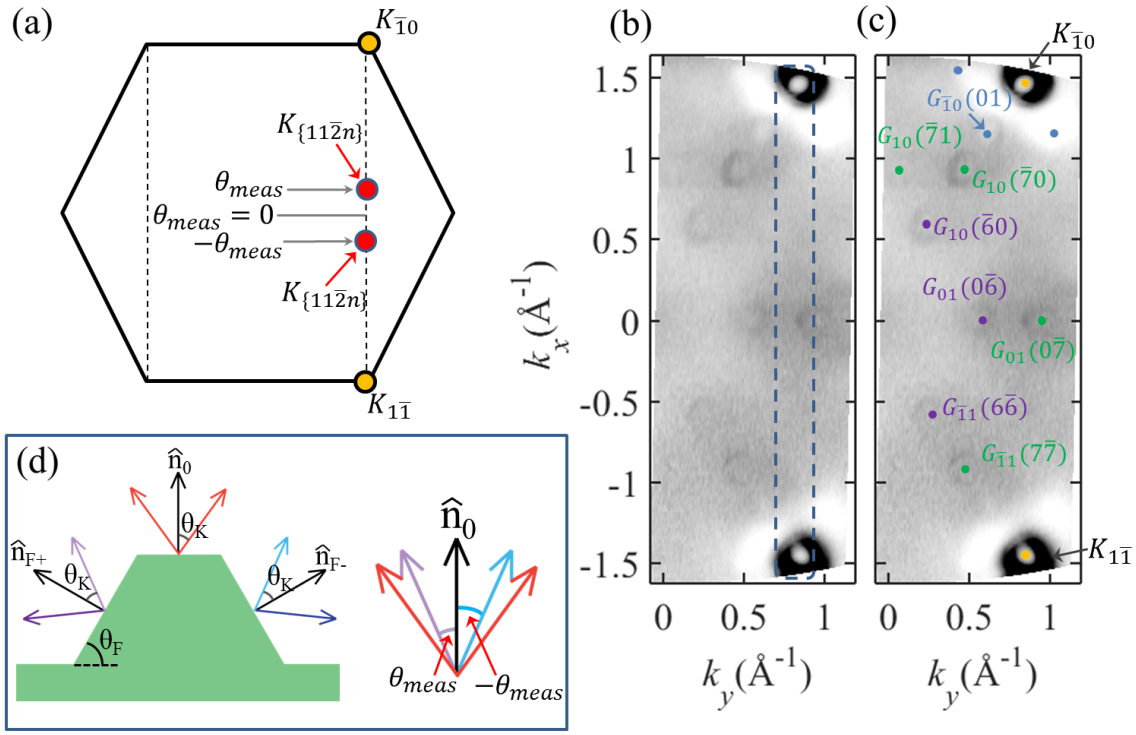

Figure 5.1: (a) Brillouin zone for a zigzag sidewall sample, with the expected locations for zigzag facet cones shown. The angle θ_{meas} where the facet cones would be measured is dependent on the facet angle θ_{F}. Because of the direction in which zigzag trenches are faceted relative to the Si-face graphene Brillouin zone, facet cones would be expected along the $K_{\bar{1}0}$-$K_{1\bar{1}}$ direction, as shown. The exact location of the facet cones along that direction would depend on the facet angle, θ_{F}. (b) Fermi surface of a zigzag sidewall nanoribbon sample ($E - E_F = -1.1$ eV, $h\nu = 36$ eV). In addition to two K points from the Si-face graphene, many replica cones are observed. The dashed box indicates where zigzag facet cones would be expected; there are none. The two cones observed partially inside the dashed box are 6×6 replica cones, as shown in (c), which labels all of the observed replica cones. Clearly, the monolayer graphene on the Si-face trench tops is very well ordered. (d) Diagram indicating where the zigzag facet cones would be expected to be measured. Here, $\theta_{\text{meas}} = \pm|\theta_{\text{K}}| \pm |\theta_{\text{F}}|$.

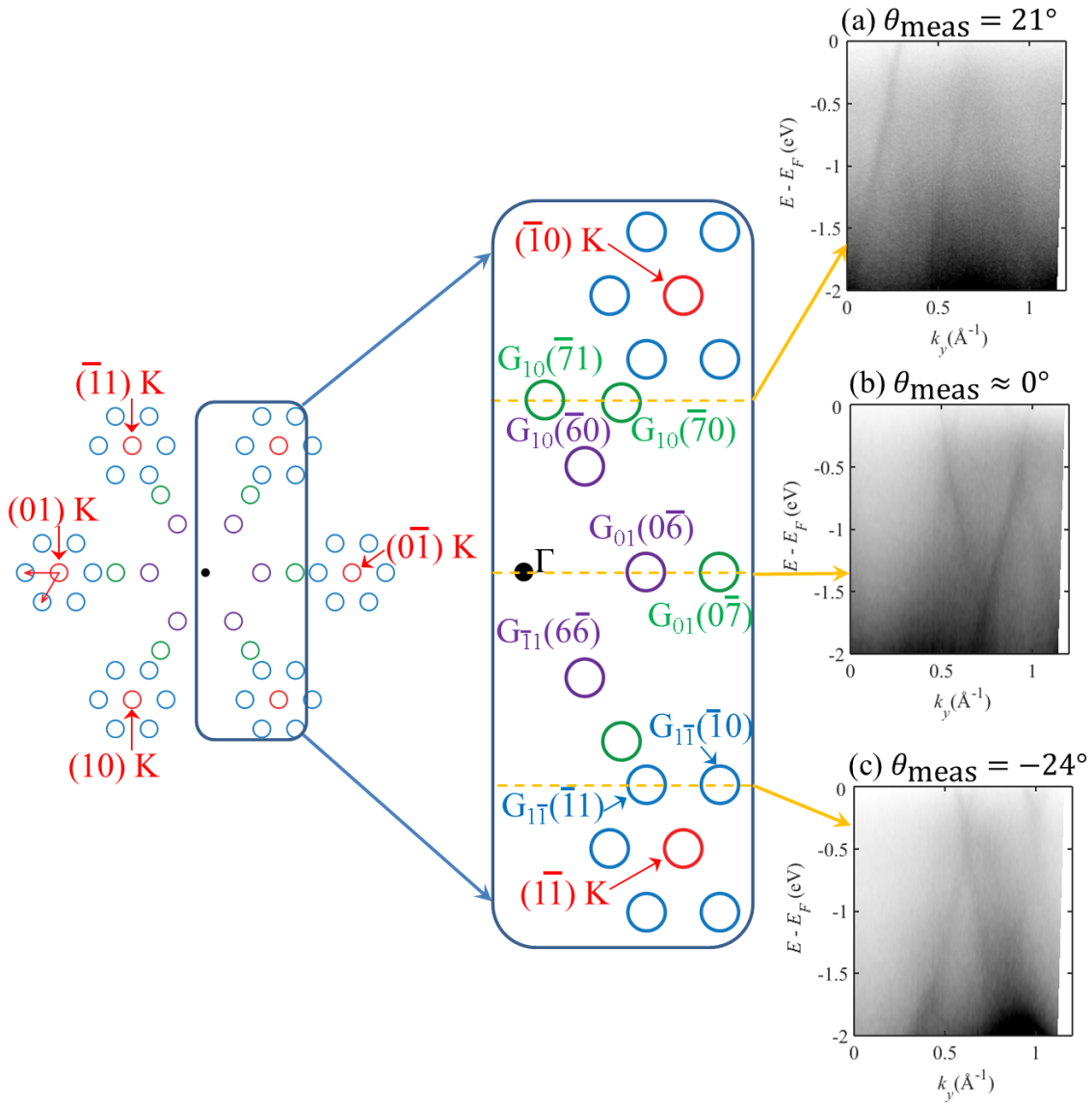

Figure 5.2: ARPES images of replica cones from monolayer on the zigzag sample trench tops. The cones are unquestionably replica cones because of their locations (indexed by SiC 6×6 unit vectors) and their doping level, which is identical to that of monolayer Si-face graphene, as expected. (a) ARPES cut showing replica cones $\mathbf{G}_{10}(\bar{7}1)$ and $\mathbf{G}_{10}(\bar{7}0)$. These cones are caused by multiple scattering, an indication of the high degree of order in the graphene film. (b) ARPES cut showing replica cones $\mathbf{G}_{01}(0\bar{6})$ and $\mathbf{G}_{01}(0\bar{7})$. While these cones happen to fall near the $(\bar{1}0)$K-$(1\bar{1})$K direction, this is only because of the length of the SiC reciprocal lattice vector from the (10)K point relative to the size of the graphene Brillouin zone. (c) ARPES images of the first-order 6×6 replica cones surrounding the $(1\bar{1})$K point. In all ARPES images of zigzag samples, a diffuse background is observed. This diffuse background is strongly indicative of disorder in the sample. However, it is known that the trench tops are very well-ordered due to the observation of many first- and second-order replica cones. Thus, it is possible that the disordered background intensity originates from other surfaces on the sample, such as the zigzag sidewalls. For all ARPES images, $h\nu = 36$ eV.

5.4 Additional Surface Characterization Techniques Used to Analyze Zigzag Sidewall Samples

ARPES is extremely informative for determining the electronic band structure of materials. However, if the structure of a topographically complex material is not already known, ARPES measurements should be used in conjunction with other characterization techniques to form a complete, well-informed picture of the structure of the samples being measured. As a result, additional surface characterization techniques have been used by several research groups in attempts to determine the structure of zigzag sidewall samples.

TEM performed by Baringhaus et al shows the structure of zigzag sidewalls prepared using growth methods dissimilar to Z_N and $Z_N^{(B)}$; see Ref. [112]. Figure 5.3(a) shows a TEM image of a zigzag sample (courtesy of Ref. [112]). For comparison, Fig. 5.3(b) shows a TEM image of an armchair sample (courtesy of Ref. [65]). It is evident that the two facets are structurally very dissimilar, as might be expected. While the TEM of armchair sidewalls shows a very well-resolved graphene monolayer on the sidewalls, TEM of the zigzag sample does not show any resolved carbon layers. Often, if there is disorder along the length of a sidewall (direction into the plane of the TEM image), blurring of the TEM image results. Thus, because no graphene sidewall layers have been resolved in any known TEM images of zigzag sidewall samples, TEM images support the idea that zigzag sidewalls are structurally more disordered than armchair sidewalls. The growth methods used in Ref. [112] are not identical to $Z_N^{(B)}$ or Z_N; however, the TEM image shown in Ref. [112] is currently the only known TEM image of a zigzag sidewall sample successfully completed.

Additional characterization techniques have been used to experimentally determine the structure of the zigzag sidewalls. Figures 5.5, 5.7, and 5.6 show experimental data concerning zigzag samples from techniques including μ-ARPES, LEEM, XPEEM, and μ-LEED. Before discussion of the structural information obtained from

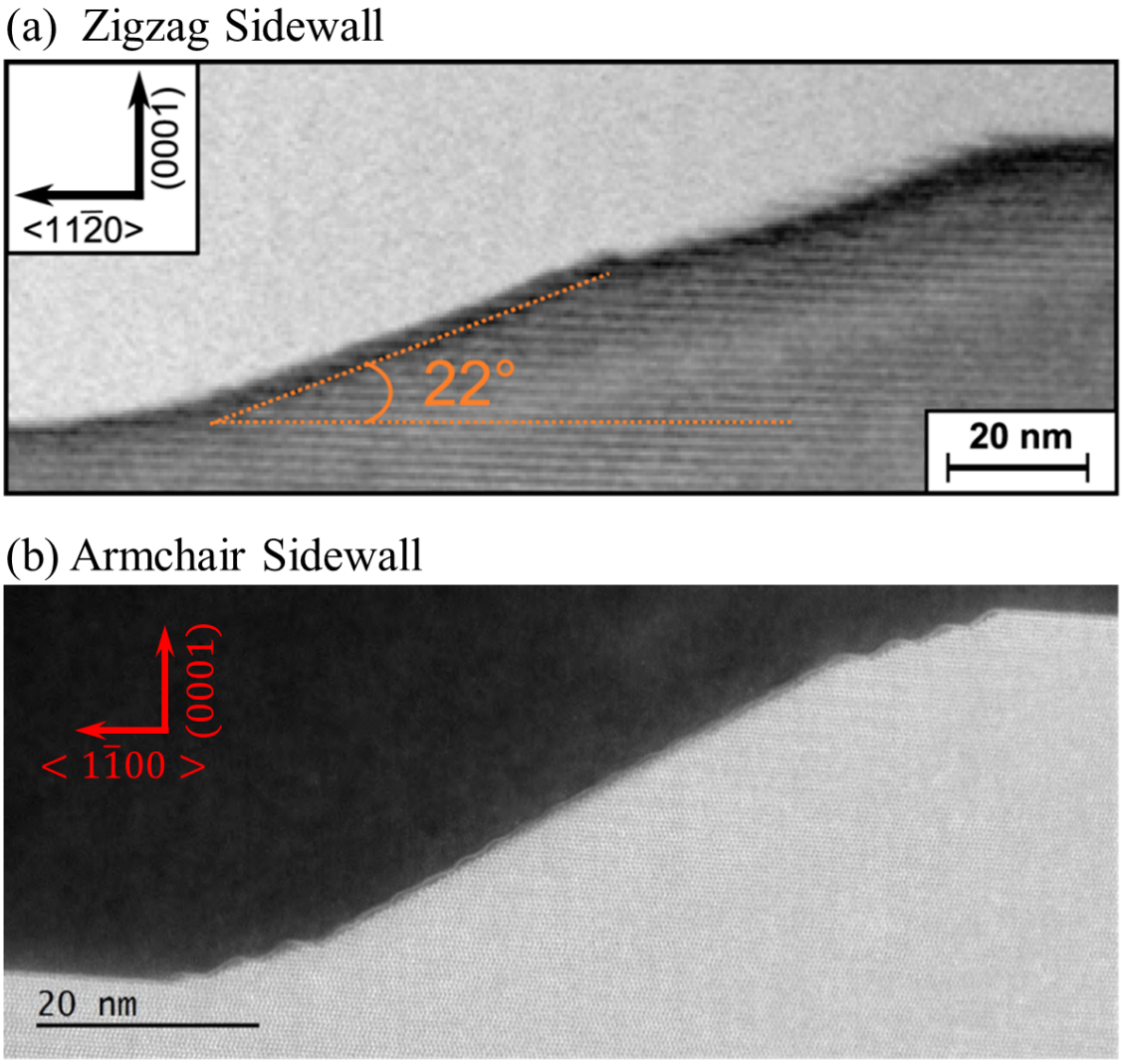

Figure 5.3: (a) TEM of a zigzag ribbon sample grown with a method described in Ref. [112]. The structure looks remarkably different from that of armchair sidewalls, as might be expected. The measured facet angle is 22°, which would be consistent with a (11$\bar{2}$ 16) facet, though it is not stated in Ref. [112] what the zigzag facet was determined to be. Unlike the armchair TEM image in (b), no graphene layers on the zigzag sidewall are able to be individually resolved, probably due to disorder along the trenches (direction into the plane of the image). Image used courtesy of Baringhaus et al [112]. (b) TEM of an armchair sidewall sample, for comparison with the zigzag sample. See Chapter 4 for more information about the structure of armchair sidewall samples. Monolayer sidewall graphene can be observed. Image courtesy of Palacio et al [65].

these characterization methods, it should be emphasized that the accurate crystallographic orientation of the zigzag trenches was confirmed through several independent techniques. Figures 5.4(a) and (b) show the real space graphene lattice and Brillouin zone orientation for the SiC directions indicated. Figure 5.4(c) shows μ-LEED taken on the zigzag sample, with the orientation of the graphene and SiC diffraction spots consistent with the lattice and Brillouin zone used in (a) and (b). μ-ARPES also shows a graphene Brillouin zone that is oriented correctly for the same crystallographic directions; a μ-ARPES Fermi surface taken from the sample is shown in Fig. 5.5(b), with the monolayer graphene K points consistent with the Brillouin zone in Fig. 5.4(b). The sample was then measured with BF-LEEM (indicating topography) while the sample was in the same LEEM system used to measure μ-LEED and μ-ARPES (the sample did not need to be removed to perform each subsequent characterization technique and, therefore, the orientation of the sample was not changed). Thus, it can be unequivocally stated that the patterned trenches are oriented along the zigzag edge direction (that is, the facets are SiC$(11\bar{2}n)$ facets).

5.4.1 μ-ARPES of Zigzag Sidewall Nanoribbons

μ-ARPES of zigzag nanoribbons grown with recipe Z_N is interesting and deserves discussion. Figures 5.5(a) and (c) show the reciprocal space directions along which zigzag and armchair facet cones would be expected to be measured in μ-ARPES. It can be seen that, due to the orientation of the facet surface normals with respect to the Si-face monolayer graphene Brillouin zone, zigzag facet cones would be expected along the K'_{0+}-K'_{0-} direction (as well as along its counterpart on the other side of Γ, indicated by both vertical lines in Fig. 5.5(a)), while armchair facet cones would be expected along the K_{0+}-Γ-K_{0-} direction (indicated by the horizontal line in Fig. 5.5(c)). Comparison of these directions with the μ-ARPES Fermi surface image in Fig. 5.5(b) reveals that there is no evidence of facet cones along the direction expected for zigzag

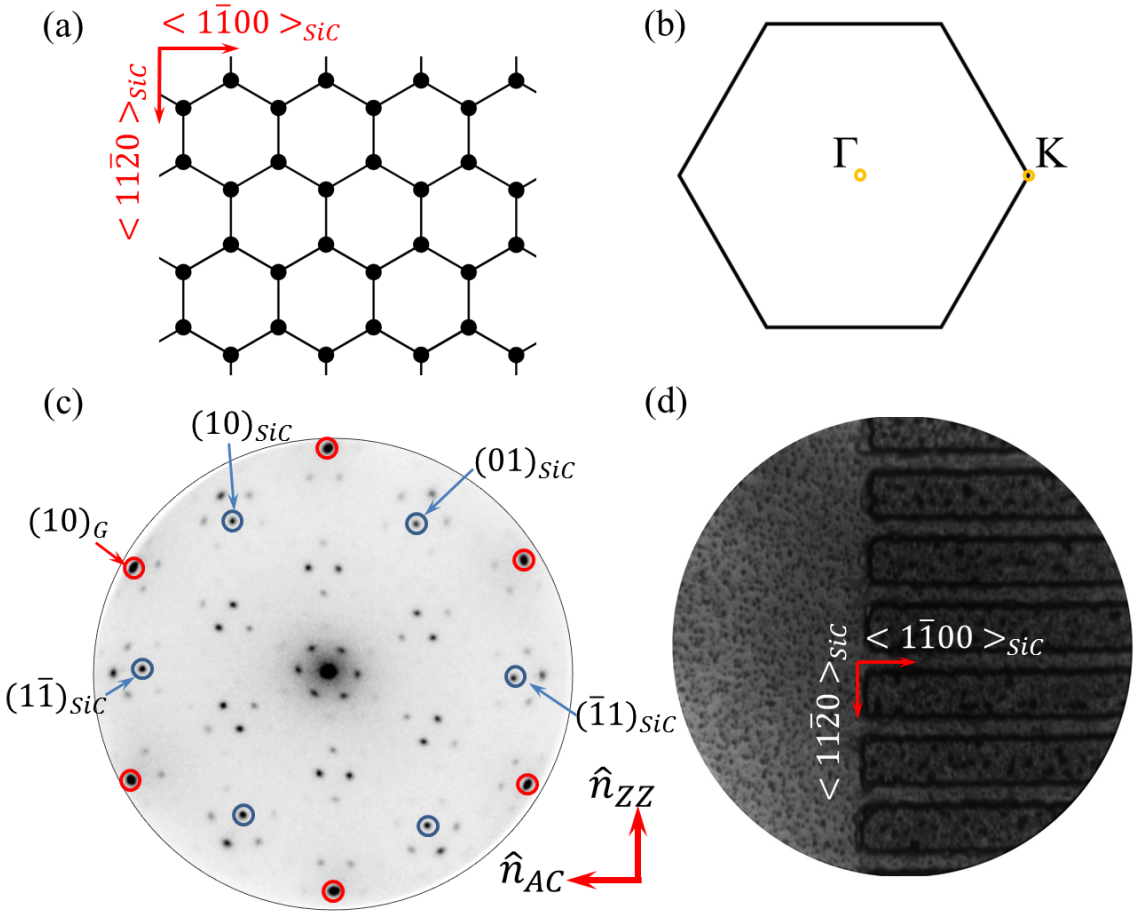

Figure 5.4: Confirmation that zigzag sidewall ribbon samples measured by μ-ARPES, μ-LEED, LEEM, and PEEM were, in fact, oriented along the appropriate direction for zigzag facets. (a) Graphene lattice, with directions shown for the orientation of epitaxial graphene on the Si-face. Zigzag edges are found along the $\langle 1\bar{1}00 \rangle$ direction. (b) Brillouin zone for graphene, with the correct orientation for the lattice in (a). (c) μ-LEED image taken at 38 eV, with the correct orientation to be consistent with (a) and (b). (d) BF-LEEM image of the zigzag sample, confirming that the orientation of the trenches run along the $\langle 1\bar{1}00 \rangle$ direction (perpendicular to the $\langle 1\bar{1}00 \rangle$ direction); thus, the etched trenches are $(11\bar{2}n)$ facets.

facets. Instead, intensity is seen along K_{0+}-Γ-K_{0-}, which is the direction expected for armchair facets. A cut through the K_{0+}-Γ-K_{0-} direction (shown in Fig. 5.5) reveals a weak Dirac cone, which necessarily must originate from armchair facets located somewhere along the length of the zigzag sidewalls.

Additional inspection of the monolayer graphene K points in the Fermi surface (Fig. 5.5(b)) reveals intensity from the buffer layer ε_2 band, originating from buffer layer on the trench tops. Lobes of intensity can be seen surrounding each K point, oriented along the Γ-K directions. This ε_2 intensity is in addition to the armchair facet cones observed along the K_{0+}-Γ-K_{0-} direction.

It is important to note that, because of the imaging abilities of techniques like μ-ARPES, any metallic graphene on the zigzag facets possessing a Dirac cone would be measured. Even extremely disordered, corrugated exfoliated graphene produces a Dirac cone measurable by μ-ARPES [102]. Thus, if there were any facet Dirac cone from graphene on the zigzag facets grown with these $Z_N^{(B)}$ and Z_N recipes, a weak zigzag facet cone would have been observed.

Many experiments show that armchair facets are energetically preferred: step bunching shows a preference for armchair facets [55, 103, 104]; circular pillars patterned on the Si-face show post-growth faceting into armchair facets [46]; and calculations show that armchair facets appear to be thermodynamically stable due to surface energy minimization [55, 105]. Thus, it is supported by experiment and theory that the zigzag sidewalls could create armchair facets during growth. Because such armchair facets are not macroscopically observed (e.g., patterned features have not been observed to melt and reform armchair facets), so it is likely that the armchair facet cone intensity observed with μ-ARPES originates from nanometer-scale armchair facets created somewhere along the length of the zigzag sidewalls.

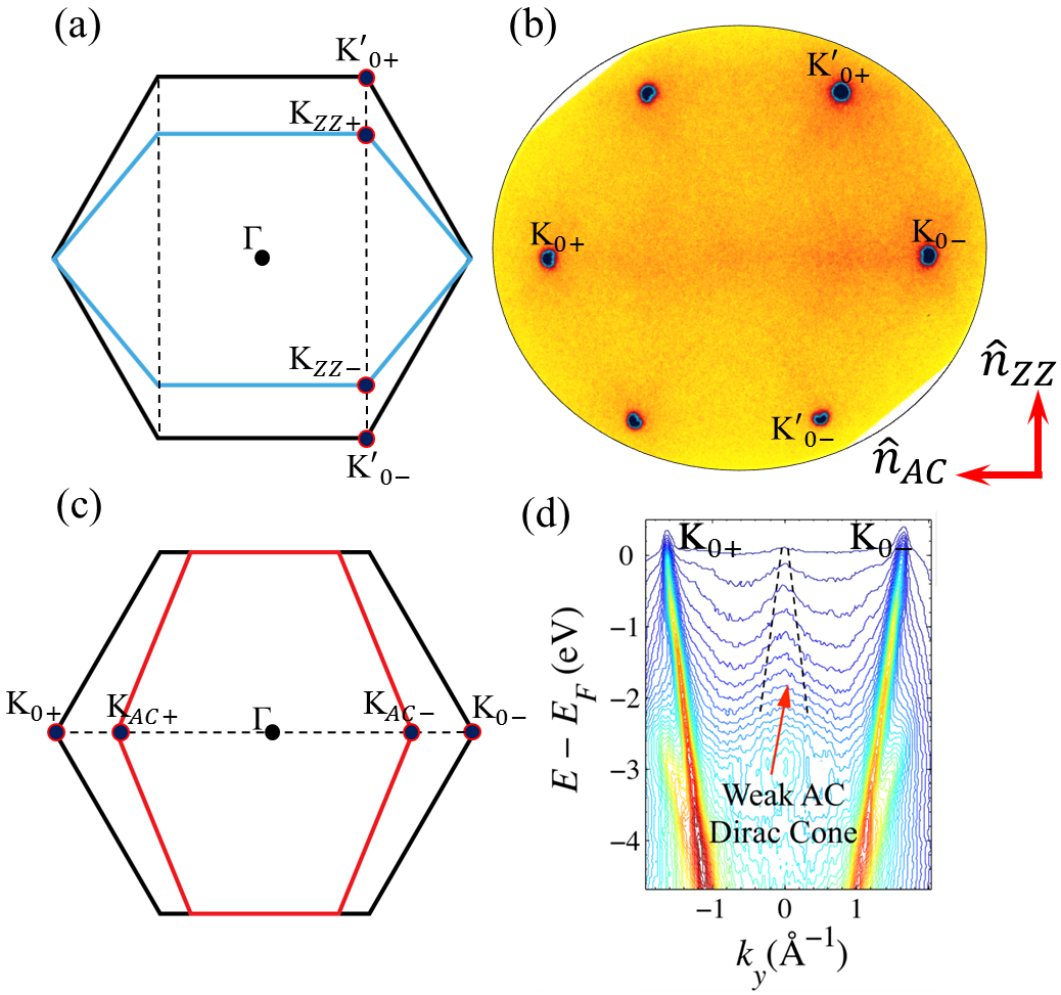

Figure 5.5: (a) Si-face monolayer graphene Brillouin zone (back) and tilted zigzag facet Brillouin zone (blue) for zigzag facets. Zigzag facet cones would be expected along the K'_{0+}-K'_{0-} direction, as shown. (b) μ-ARPES constant energy ($E = 36.75$ eV, $h\nu = 44$ eV) image of a zigzag nanoribbon sample grown with recipe Z_N. No ordered intensity is measured along the expected facet cone direction for zigzag facets (K'_{0+}-K'_{0-}). Instead, there is intensity along K_{0+}-Γ-K_{0-}, the direction expected for an armchair facet. Some of the intensity observed near the K points is due to ε_2 from buffer layer on the trench tops. The intensity surrounding each K point is oriented in three lobes along the Γ-K directions. (c) Si-face monolayer graphene Brillouin zone (back) and tilted Brillouin zone for armchair facets (red). Armchair facet cones would be expected along the K_{0+}-Γ-K_{0-} direction, as shown. This is, in fact, the direction along which the most intensity is observed in the μ-ARPES image in (b). (d) Binding energy versus k_y cut through the μ-ARPES image in, showing the Si-face monolayer Dirac cones K_{0+} and K_{+0}. A Dirac cone is weakly observed, as indicated. Because of the location of the cone, it must originate from armchair facets. Because μ-LEED and LEEM confirm the zigzag orientation of the etched trenches, it is concluded that the armchair facet cone intensity must originate from nano-armchair facets located along the zigzag trenches.

5.4.2 μ-LEED of Zigzag Sidewall Nanoribbons

μ-LEED of zigzag sidewall ribbons reveals diffraction spots from SiC and from graphene on the Si-face trench tops, as expected, shown in Figs. 5.4(c) and 5.6. Additionally, diffraction spots that move in energy are observed. μ-LEED images taken with a LEEM system produce diffraction rods that are independent of energy when the material's surface normal is parallel to the macroscopic surface normal. Therefore, any diffraction spots that appear to move with changing energy must originate from tilted surfaces. Consistent with the location of the facet cones observed in μ-ARPES, the tilted diffraction rods are oriented along two armchair directions. A $k_{\perp}$ versus $k_{\parallel}$ cut through a SiC diffraction rod where the tilted rods are observed reveals several well-ordered armchair facet rods. Because it was confirmed from both BF-LEEM and LEED that the trenches are oriented along the zigzag direction, the armchair diffraction rods must originate from nano-armchair facets located along the zigzag sidewalls. Also, it is important to note that because no zigzag facet diffraction rods are observed, we must assume that the zigzag facets' planes are more disordered than the 20 nm μ-LEED coherence length.

5.4.3 XPEEM of Zigzag Sidewall Nanoribbons

Evidence suggests that while there may not be metallic graphene on the zigzag sidewalls when grown within these parameters, there is most likely a graphene-like layer that forms on the sidewall. XPEEM images using the graphene C1s peak (Fig. 5.7(b)) for contrast show C1s intensity originating from the zigzag sidewalls. Because no corresponding Dirac cone is observed with μ-ARPES, it is likely that this C1s intensity originates from a functionalized graphene layer; analogous to the buffer layer on the SiC(0001), a graphene-like layer formed on the zigzag sidewalls must interact with the substrate in such a way that the π-bands are significantly altered.

Dark field-XPEEM (DF-XPEEM) images (Fig. 5.7(e)) show that the intensity

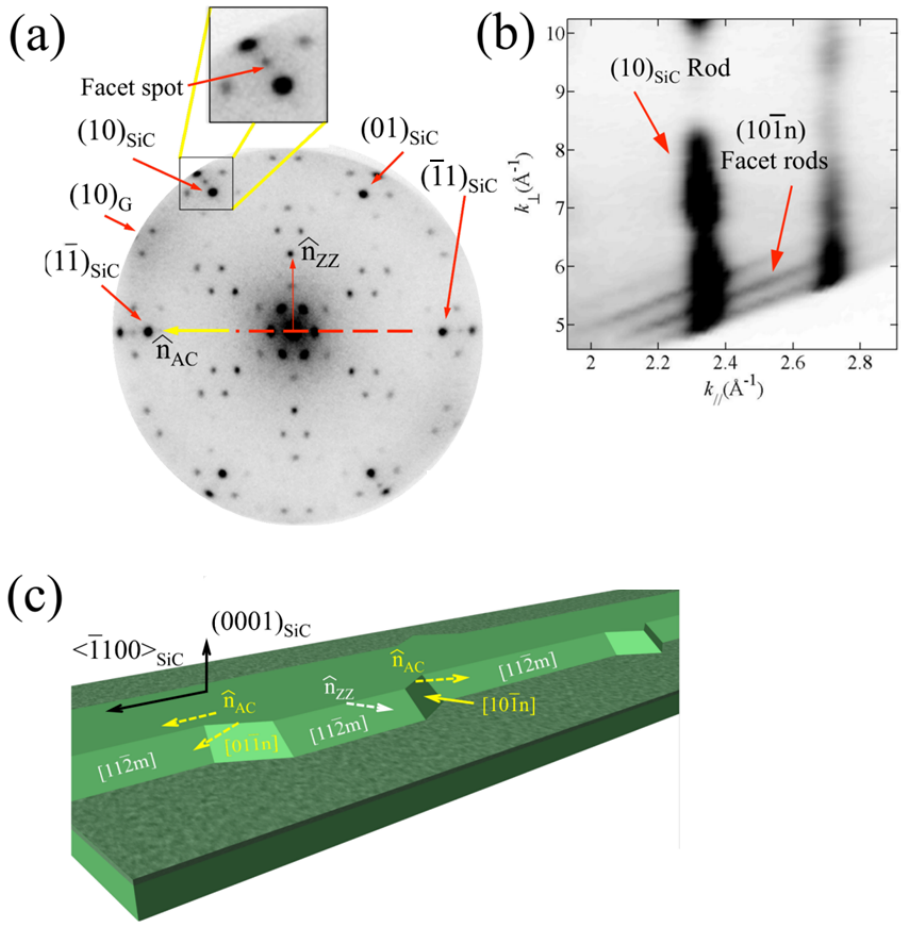

Figure 5.6: (a) μ-LEED image of a zigzag sidewall ribbon sample (E = 32 eV). Diffraction rods for SiC and Si-face epitaxial graphene are observed. Additionally, tilted diffraction rids are observed. However, the orientation of the diffraction rods is not consistent with zigzag facets. Instead, the tilted diffraction rods are observed to be tilted along two armchair facet directions. Facet spots can be seen near the $(10)_{\mathrm{SiC}}$, $(1\bar{1})_{\mathrm{SiC}}$, and $(\bar{1}1)_{\mathrm{SiC}}$ diffraction spots in the LEED image in (a). These directions correlate with armchair facet surface normals. (b) $k_{\perp}$ versus $k_{\parallel}$ cut through the $(10)_{\mathrm{SiC}}$ diffraction rod. Tilted facet rods from $(10\bar{1}n)$ armchair facets are observed. (c) Schematic depicting the representation of the structure of the zigzag sidewalls indicated by μ-ARPES, μ-LEED, and XPEEM. While the etched trenches are oriented along the intended zigzag direction, during growth portions of the sidewalls facet into armchair nano-facets. It is these armchair nano-facets that are well-ordered enough to produce facet cones in μ-ARPES and facet diffraction rods in μ-LEED. Clearly, the zigzag sidewalls contain a carbon-based material that is not structurally identical to graphene, or else the zigzag facets are extremely disordered.

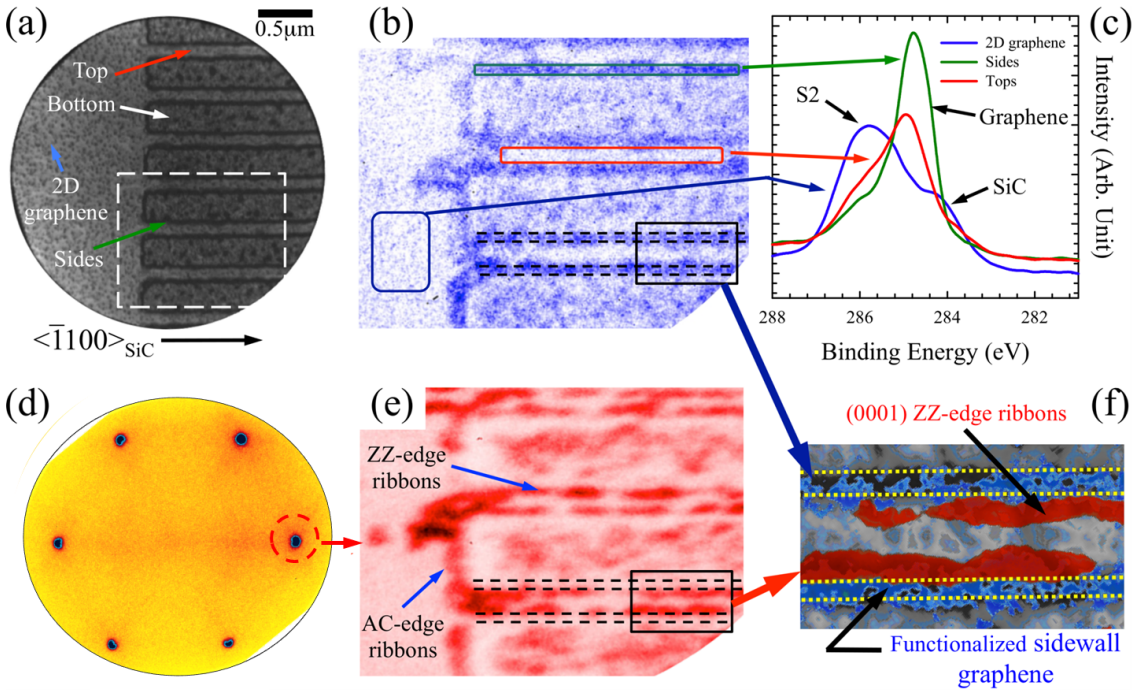

Figure 5.7: (a) BF-LEEM image of the zigzag nanoribbon sample, for comparison with images in the remainder of the figure. The tops and bottoms of the patterned features are indicated. The image was taken near the edge of the pattern, so an unpatterned area can also be seen. Field of view is 4 μn. (b) XPEEM image using the graphene C1s peak for contrast (BE = 284.6 eV, ΔE = 0.3 eV). Image area is the same as the white dashed region in (a). Horizontal dashed lines indicate the top and bottom edges of the sidewall facets, as determined by the LEEM image in (a). (c) XPEEM-derived spectra of the C1s peak, integrated over the three regions marked in (b). It is evident that the region off the pattern (blue box and spectrum) primarily possesses buffer layer and bare SiC. The trench tops (red box and spectrum) possess some buffer and monolayer graphene. The sidewalls possess a carbon-based material with a C1s peak similar to that of graphene. It is possible that the sidewalls contain a layer that is structurally like graphene. However, it can be seen from (e) and (f) that the carbon layer does not possess a Dirac cone. (d) μ-ARPES of the zigzag sample (E = 37 eV, $h\nu$ = 44 eV). Dirac cones from graphene on the Si-face are evident. Intensity along the direction for armchair facets are observed, despite the fact that the trenches are etched along the zigzag direction. (e) DF-XPEEM using the (0001) surface Dirac cone (red circle in (d)). Higher intensities are in red. Intensity is seen to originate from strips of monolayer graphene along the trench tops, near the step edges. The sidewall top and bottom edges are indicated by dashed black lines. (f) Composite image of BF-LEEM for topography (gray), XPEEM C1s intensity (blue) and DF-XPEEM intensity (blue). All characterization techniques are consistent with a structure that includes monolayer graphene in strips on the trench tops and a functionalized graphene layer (akin to the Si-face buffer layer) on the sidewalls, lacking a metallic Dirac cone.

from the monolayer Dirac cones observed with μ-ARPES originates from graphene grown in strips on the SiC(0001) trench tops near the step edges. These Si-face "nanoribbons" must begin to grow from Si-sublimation seeded near the trench step edges. Figure 5.7(f) shows an overlay that more clearly demonstrates the structural location of the intensities measured in Figs. 5.7(b) and (e). Correlation of topography from BF-LEEM (gray) indicates that DF-XPEEM intensity from the monolayer Dirac cone (red) exists on the Si-face near the step edges, while the XPEEM C1s intensity (blue) does, in fact, originate from functionalized graphene on the sidewalls.

5.5 Correlation of Structural Information with H-passivation Experiments

Because no zigzag facet Dirac cones are observed for samples grown with Z_N or $Z_N^{(B)}$, it is most probable that the SiC zigzag facet geometry causes the graphene-like layer, indicated to exist on the sidewall by XPEEM, to interact strongly and bond to the substrate. This functionalized graphene layer is analogous to the buffer layer on the Si-face. H-passivation experiments support this conclusion.

H-passivation of the Si-face buffer layer [91, 90] shows that the hydrogen atoms move between the buffer layer and the substrate, decoupling the buffer layer and allowing it to regain the Dirac cone expected for monolayer graphene; this layer is appropriately called quasi-free-standing monolayer [91, 90, 113]. Similarly, attempts were made to H-passivate zigzag samples in the hopes of revealing the functionalized graphene layer on the zigzag facets. While the only recipe that was successful required higher passivation temperatures and times than would otherwise be necessary for flat buffer layer samples, the H-passivated zigzag samples do, in fact, show bands along the expected zigzag facet direction. The Fermi surface in Fig. 5.8(a) shows two bands never before observed, measured at angles $\theta_{\text{meas}} \approx \pm 7^\circ$. The location of these bands is consistent with the zigzag facet geometry.

As previously discussed, for a facet with angle θ_{F}, facet cones are expected to

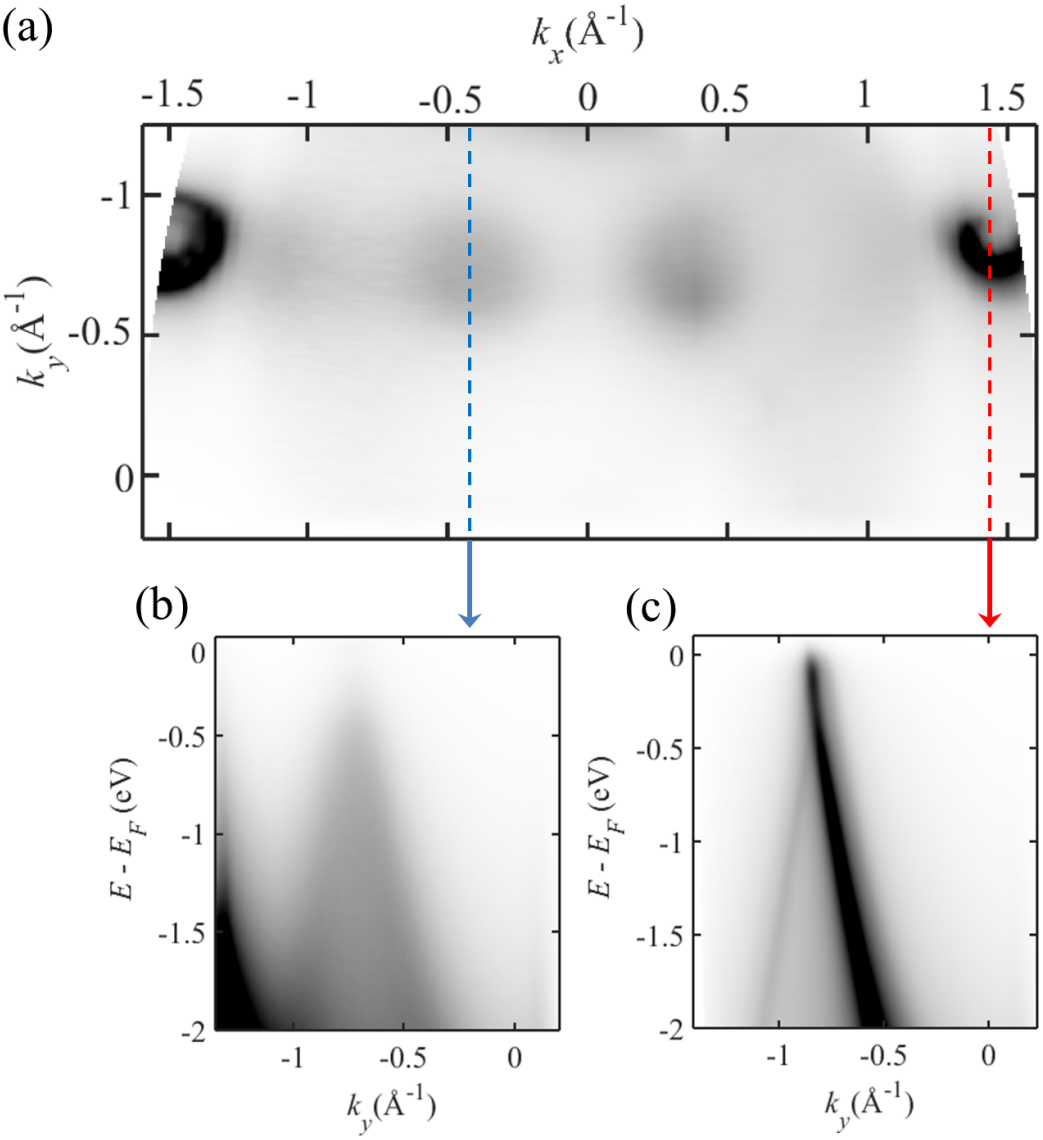

Figure 5.8: (a) ARPES Fermi surface of a H-passivated zigzag nanoribbon sample ($E - E_F = -0.9$ eV). The sample was passivated at 900 °C for 1 hour. Intensity can be seen for bands originating from zigzag facets at $k_x \approx \pm 0.4$ Å^{-1}, in units of the Si-face graphene Brillouin zone. This experiment was the first time a band from the zigzag facets had been measured. (b) Constant k_x cut through one of the facet bands, indicated by the dashed blue line in (a). (c) k_x cut through the Si-face graphene Dirac cone, originating from the trench tops; the cut location is indicated by the dashed red line in (a). The doping of the cone is consistent with quasi-free-standing monolayer, as expected for a H-passivated sample that primarily contained buffer layer on the trench tops. Weak secondary bands are partially visible, which could indicate the presence of some quasi-free-standing bilayer on the trench tops (monolayer graphene before H-passivation). For all ARPES images, $h\nu = 36$ eV.

be observed at $\theta_{\text{meas}} = \pm|\theta_{\text{K}}| \pm |\theta_{\text{F}}|$. It was experimentally determined for these H-passivated zigzag samples that $\theta_{\text{K}} \approx 29.75°$. So, it might seem trivial to determine θ_{F} from these measurements. However, a number of zigzag facets would be expected to produce bands at angle $\theta_{\text{meas}} \approx 7°$. See Table 5.1 for a list of zigzag $(11\bar{2}n)$ facets, their facet angles, and the angles where the facets would be measured, $\pm\theta_{\text{meas}}$. Knowing this, the location where the H-passivated zigzag bands are observed would be consistent with zigzag facets $(11\bar{2}n)$ with $n = 9, 15, 16$. Because of the angular resolution and Δk broadening in ARPES, it cannot be determined which of these is physically correct. AFM of zigzag samples measure approximate topographical angles of $\sim 30°$ (which would be roughly consistent with $n = 9$), while TEM of zigzag samples grown with different methods (see Ref. [112]) show $\theta_{\text{F}} = 22°$, which would be consistent with $n = 16$.

Table 5.1: Facet angle θ_F for each zigzag facet $(11\bar{2}n)$, relative to the SiC(0001) surface normal. θ_{meas} is the angle where a facet cone from each facet would be measured, assuming $h\nu = 36$ eV and, thus, $\theta_{\text{K}} \approx 29.75°$ (experimentally verified value). All θ_{meas} values can be positive or negative.

n	θ_{F}	$\pm\theta_{\text{meas,1}}$	$\pm\theta_{\text{meas,2}}$	n	θ_{F}	$\pm\theta_{\text{meas,1}}$	$\pm\theta_{\text{meas,2}}$
0	90°	60.3°	119.75°	11	30.8°	1.0°	60.5°
1	81.3°	51.6°	111.1°	12	28.6°	1.1°	58.4°
2	73.0°	43.3°	102.8°	13	26.7°	3.0°	56.5°
3	65.4°	35.6°	95.1°	14	25.1°	4.7°	54.8°
4	58.6°	28.8°	88.3°	15	23.6°	6.2°	53.3°
5	52.6°	22.9°	82.4°	16	22.3°	7.5°	52.0°
6	47.5°	17.8°	77.3°	17	21.1°	8.7°	50.8°
7	43.1°	13.3°	72.8°	18	20.0°	9.8°	49.7°
8	39.3°	9.6°	69.1°	19	19.0°	10.7°	48.8°
9	36.0°	6.3°	65.8°	20	18.1°	11.6°	47.9°
10	33.2°	3.5°	63.0°	21	°	°	°

It can be seen from ARPES images of H-passivated armchair sidewall samples

(Chapter 4, Section 4.8.4) that the H-passivation process tends to increase the Δk-widths of measured Dirac cones. However, the bands that are measured after H-passivation of zigzag ribbons are observed to be considerably broader and more disordered than cones for either quasi-free-standing monolayer or H-passivated armchair samples. Fitting the MDCs seen in Fig. 5.9 reveals Δk-widths varying between 0.106 ± 0.010 Å^{-1} and 0.148 ± 0.074 Å^{-1}. Also, it is noticeable from the ARPES k_x cuts as well as the EDCs in Fig. 5.9 that the zigzag facet bands show significantly reduced intensity above $E - E_F \approx -0.4$ eV. However, there are noticeable disparities between k_x cuts in how quickly intensity decreases near E_F. A graph of maximum MDC intensity verses measured angle is shown in Fig. 5.9(d). The centers of the peaks in intensity roughly correspond to the centers of the bands and, thus, indicate the facet angle. ARPES k_x cuts taken at the peaks in intensity are shown in Fig. 5.9(a)-(c). Despite the fact that these bands all originate from the centers of the measured facet bands and should, therefore, be relatively consistent with each other, a large difference is seen in how intensity falls off near E_F. Therefore, due to the large k-widths and overall inconsistency of the observed facet band intensity near E_F, it is currently unclear whether the bands are metallic or semiconducting ($E_{gap} \sim -0.1$ eV for Fig. 5.9(b), up to ~ -0.4 eV for Fig. 5.9(c)). Further experiments would be required to attempt to find an optimal growth recipe and H-passivation process, with better statistics for all ARPES images through the facet bands.

5.5.1 Future Direction for Experimental Attemps to Grow Zigzag Sidewall Graphene

Growth of graphene layers on the SiC(0001) face has been observed to be primarily activated by temperature. Large, flat areas without steps need temperatures ~ 1360 °C to grow buffer layer, while temperatures ~ 1520 °C are needed to grow monolayer. Similarly, it is possible (and, indeed, likely) that zigzag facets require higher growth

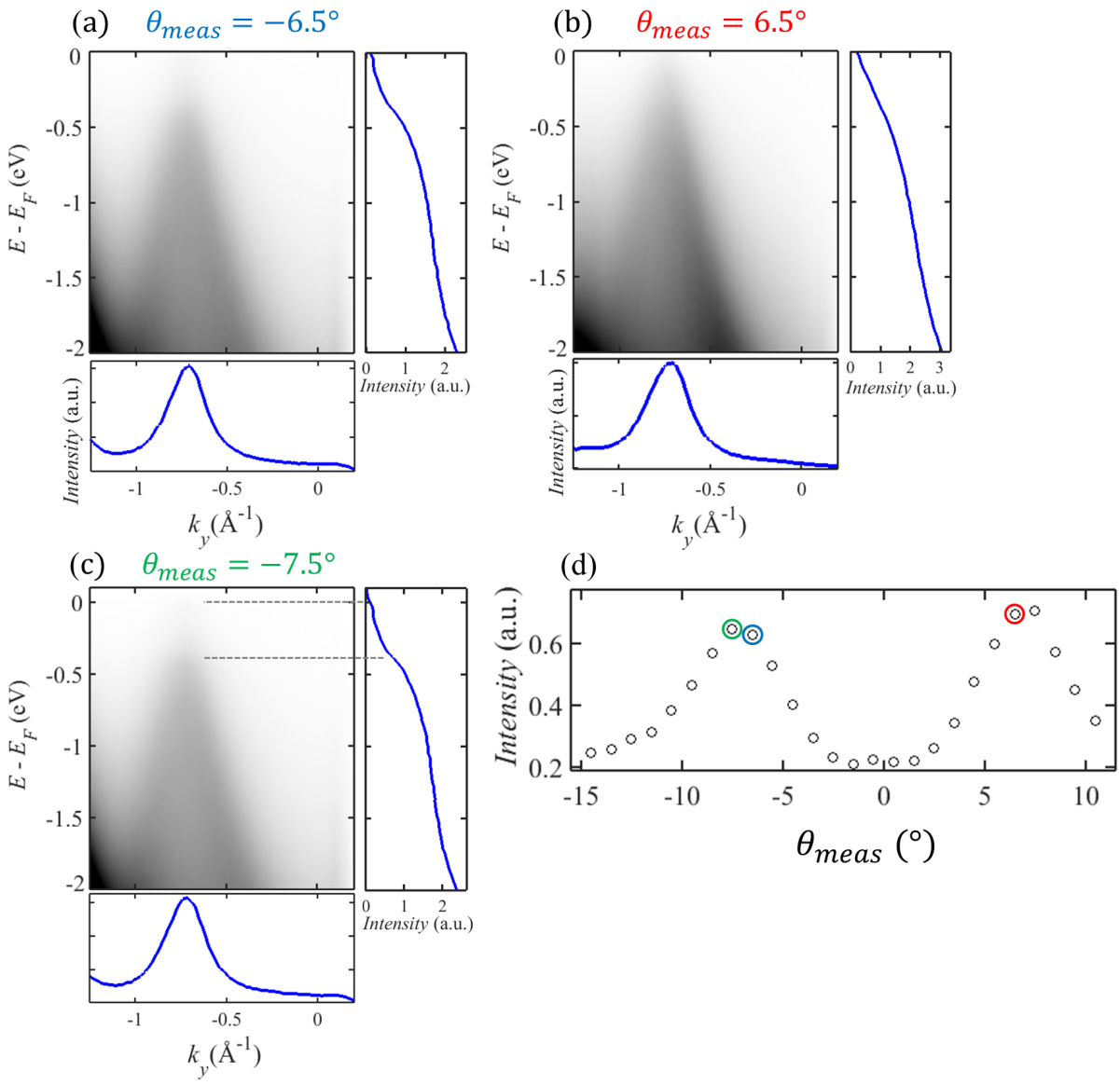

Figure 5.9: H-passivated zigzag sample. (a) k_x cut through one of the zigzag facet bands ($\theta_{\text{meas}} = -6.5°$). Bottom- MDC through $E - E_F = -0.4$ eV. Fits of this MDC find k-widths to be 0.106 ± 0.010 Å^{-1}. Right- EDC through the center of the band. Intensity does exist up to the Fermi level, though droping off quickly above $E - E_F = -0.4$ eV. (b) ARPES k_x cut through $\theta_{\text{meas}} = 6.5°$. Bottom- MDC through $E - E_F = -0.4$ eV. Fits of this MDC find k-widths to be 0.148 ± 0.074 Å^{-1}. Right- EDC through the center of the band. Intensity appears to go up to the Fermi level with greater intensity than the angle in (a). (c) k_x cut through $\theta_{\text{meas}} = -7.5°$. For this angle, there is very little band intensity above $E - E_F \approx -0.4$ eV. Bottom- MDC through $E - E_F = -0.4$ eV. Fits of this MDC find k-widths to be 0.112 ± 0.010 Å^{-1}. Right- EDC through the center of the band, which shows the quick drop off of intensity above $E - E_F = -0.4$ eV. (d) A graph of maximum MDC intensity as a function of measured angle θ. Two peaks in intensity are indicative of the facet angles. The maxima in intensities are located at $\theta_{\text{meas}} \approx 7°$. For all ARPES images, $h\nu = 36$ eV.

temperatures than armchair facets to induce growth of multiple sidewall layers. Because the first graphene-like layer to form on the zigzag facets has been shown to lack a Dirac cone, the formation of additional layers of sidewall graphene would be necessary to have metallic zigzag sidewall graphene exhibiting linear dispersion. Future research on zigzag ribbons should attempt to grow sidewall samples at higher growth temperatures than have thus far been used in Z_N and $Z_N^{(B)}$ recipes. It is also possible that longer growth times are needed, though samples that have been made with Z_N recipes using growth steps up to three times longer than growth steps for $C_N^{(d)}$ recipes have failed to produce metallic zigzag sidewall graphene.

5.6 Comparison of Zigzag Ribbons Grown with Various Methods

It has now been extensively discussed that zigzag sidewall samples, grown with CCS and parameters known to grow monolayer sidewall graphene on armchair facets, have failed to show metallic facet cones. However, transport measurements have been performed on zigzag sidewall samples (grown with other methods or higher temperature CCS recipes) that show ballistic transport [4, 112]. It is unlikely that the disordered "zigzag sidewall buffer" indicated to exist by various characterization methods is capable of such ballistic transport. Thus, an alternative explanation for the material origin of the observed transport properties is desired. As discussed below, the existence of a second sidewall graphene layer is the most likely explanation for the growth methods used in Refs. [4, 112]

Substrate interactions between a graphene layer and the underlying SiC are characteristic of the corresponding facet geometry and should not vary greatly different based on growth method. For example, on the SiC C-face, the first layer of graphene is metallic and shows linear dispersion whether the sample is grown in UHV or with CCS. The Si-face buffer layer is not metallic whether it is grown in UHV or with CCS. However, only buffer layer grown with CCS has been shown to be well-ordered

enough to produce coherent, dispersing semiconducting bands instead of the non-dispersing surface states observed for UHV grown samples [58, 114]. Therefore, it is most likely that the first layer of graphene grown on zigzag facets via other methods (Refs. [4, 112]) is still strongly bound to the substrate, as is indicated for CCS-grown samples. Considering the transport results, it is possible that the methods described are able grow both a zigzag sidewall buffer and a metallic graphene layer above it. Perhaps the growth conditions and temperatures achieved in Refs. [4, 112] were sufficient to stimulate the growth of a second, metallic sidewall layer. ARPES measurements on samples grown with those methods would be very enlightening. Otherwise, the discrepancy between structural characterization data for zigzag sidewalls and the results of transport measurements cannot currently be resolved.

CHAPTER VI

CONCLUSION AND FUTURE OUTLOOK

We have shown that graphene grown on SiC is a viable material for future electronic device development. EG does not require transfer to a secondary substrate because well-ordered graphene can be grown on SiC, a substrate that is compatible with lithography and capable of supporting devices. Therefore, all drawbacks of a transfer process are avoided. Confinement controlled sublimation growth methods for creating EG are ideal, because they produce highly ordered graphene films. As an additional benefit, the SiC substrate can actually be leveraged to tailor the properties of the graphene grown on its surfaces; this is demonstrated by the discovery of two forms of functionalized graphene, both of which appear to have room-temperature bandgaps of a reasonable size for graphene device development.

Chapter 2 revealed the semiconducting nature of the Si-face buffer layer. It was demonstrated that when growth is optimized, highly ordered substrate interactions produce two gapped graphene bands, located at and in lobes surrounding the K point. Both gapped buffer bands possess a reproducible room temperature bandgap ≥ 0.5 eV. Therefore, the buffer layer is a semiconducting form of graphene that should be further researched for use in graphene-based devices.

Because ARPES measures only filled states, the full size of the buffer layer bandgap is not currently known. However, the top of the ε_1 and ε_2 buffer bands are ~ 0.5 eV below the Fermi level, so the bandgaps are at least 0.5 eV. Further experiments are required to determine the full size of the gap by measuring the bottom of the conduction band; this could be accomplished either by utilizing a complementary technique (e.g. inverse photoemission spectroscopy) or by externally controlling the Fermi level

of the buffer samples (via deposition of charge donors like cesium, or by back-gating). Such efforts are currently being undertaken, in addition to further experiments aiming to determine the finer details of the buffer bands' dispersion.

Chapter 3 explained ARPES experimental procedures required for characterizing sidewall graphene nanoribbons. Details surrounding the ARPES experimental geometry and subsequent repercussions for data analysis were discussed. Because the ARPES spot size for the Cassiopée Beamline at the Synchrotron SOLEIL is $\sim 50\ \mu m$, acquired images represent the band structure averaged over several hundred sidewall ribbons. Therefore, experimental observations of sidewall graphene structures are promising because measured bands are consistent between dozens of samples, and Δk-widths approaching instrument resolution limits indicate well-ordered, structurally uniform features across all measured sidewalls.

Additionally, it was noted in Chapter 3 that ARPES measures $k_{\|}$ and that the Brillouin zone for each surface is parallel to the surface from which it originates. Therefore, any surfaces that are tilted with respected to the macroscopic surface normal possess Brillouin zones that are tilted by the same angle. As a result, bands originating from unrelated surfaces can be measured with the same (θ, ϕ) angular location, confounding proper data analysis. Correlation of band structure measurements with additional techniques that measure physical structure is extremely helpful for determining the source of newly measured bands.

Chapter 4 spoke at length about promising results for armchair-oriented sidewall nanoribbons. It has been consistently observed that well-ordered, metallic graphene nanoribbons form on SiC $\{1\bar{1}0n\}$ facets (so-called armchair facets). Specific processing and growth parameters probably determine the exact sidewall facet structure formed during the growth process. Nevertheless, all samples grown in this work were observed via ARPES and TEM to possess the same structure.

Initial ARPES results were re-analyzed in light of the discovery that initial growth

parameters used to create samples for Ref. [44] actually led to the formation of two sidewall layers. The individual sidewall bilayer bands from these earliest measurements were indistinguishable due to the fact that large Δk-widths prevented the bands from being individually resolved. Further improvements to processing and growth have since led to the direct observation of the sidewall bilayer band structure. It is evident that the band structure of the sidewall bilayer graphene is not identical to that of AB-stacked graphene, which is reasonable considering some amount of slip would be expected between the layers as they transition from the SiC(0001) trench top onto the sidewall facet. ARPES characterization experiments with increased statistics and larger Fermi surfaces would be needed, along with calculations, to further clarify the dispersion of the bilayer band structure.

Chapter 4 also included a discussion concerning the discovery that the bandgap reported in Ref. [44] actually originated from buffer layer films on the SiC(0001) trench tops near the sidewall step edges. A coincidental correlation of the k-space location of the gapped buffer layer ε_2 band with the idealized geometry of the bend region between the trench top and sidewall caused initial confusion. After independent measurement of the buffer layer band structure, the source of the gapped band in Ref. [44] was realized.

Improved processing and growth methods led to the discovery of a gapped graphene band different from those of the Si-face buffer layer. The newly measured band, $\varepsilon_{\mathrm{ter}}$, is robustly observed in samples that are known to possess monolayer graphene on the armchair sidewalls. Correlation of ARPES and TEM data led to the determination of the likely source of the gapped band. Nanometer-sized SiC(0001) terraces that exist between the nano-$(1\bar{1}05)$ facets were discovered to possess graphene that is bonded even more closely to the underlying SiC substrate than buffer layer on the SiC(0001) trench tops. It is reasonable to expect the substrate interaction between

the "nano-terrace" buffer layer and the underlying SiC to be different from the substrate interaction between a large buffer layer sheet and the SiC bilayers underneath, which have recently been shown to possess a mutual modulation with a fundamental period of ~ 1.9 nm, the approximate width of the average nano-terrace [60]. Thus, the band structure of the nano-terrace buffer layer would be expected to be different from that of a flat buffer layer.

ε_{ter} is shown to possess a bandgap ≥ 1.5 eV. Again, because ARPES does not measure unfilled states, the full size of the bandgap is currently unknown. Further experiments should aim to determine the full size of the bandgap through similar experiments as those mentioned above for flat buffer layer samples. If the conduction band minimum is found to be just above the Fermi level, the size of the terrace buffer bandgap would be ~ 1.5 eV, which is somewhat large compared to that of silicon (1.1 eV) or GaAs (1.4 eV). However, because it is likely that the exact processing and growth parameters used to fabricate the sidewall graphene directly affect the facet structure, it is possible that the size of the terrace buffer layer bandgap could be altered. It would be of interest to alter recipe conditions and measure samples with ARPES and TEM to determine if a different substrate interaction could be achieved on any nano-terraces that exist. Also, because the nano-terraces possess the same surface normal as the SiC(0001) trench tops, band structure features for the nano-terraces are convoluted with the monolayer trench top graphene in all measured samples thus far. Attempts to etch away any trench top graphene, post-growth, would hopefully reveal of any terrace buffer bands exist at the graphene K point.

Chapter 5 addressed the significant differences between armchair- and zigzag-oriented SiC facets, showing that while the first layer of graphene that grows on an armchair sidewall is metallic, graphene that grows on zigzag facets under similar conditions is bound to the substrate in some manner. When zigzag-oriented trenches are grown with conditions known to create monolayer metallic graphene on armchair

facets, ARPES measurements show that there are no Dirac cones from graphene on zigzag facets. LEEM and PEEM measurements also suggest that the zigzag facets are disordered and do not possess graphene with a Dirac cone. Instead, XPEEM images suggest that there exists a functionalized graphene layer on the zigzag sidewalls. H-passivation experiments confirmed this; upon H-intercalation of the sidewalls, zigzag facet bands were measured for the first time. Because graphene growth on the Si-face tends to be activated by temperature, it is possible that a graphene layer possessing a Dirac cone (not bound to the substrate) could be grown above the functionalized graphene layer on zigzag facets for samples grown at a higher temperature than would otherwise be required for armchair facets.

All of the results indicated in this work suggest that structured graphene is the most promising avenue for future graphene nano-electronics work. Epitaxial graphene and sidewall nanoribbons present an industry-compatible solution to manufacturing graphene of the highest quality. Also, the inherent two-dimensional nature of graphene sheets and one-dimensional nature of nanoribbons would be an attractive solution to the scalability problem currently being faced in silicon-based electronics development.

APPENDIX A

PROCESSING PARAMETERS

This Appendix contains the specific recipes for typical processing steps.

A.1 Plasma Etching

Plasma etching of SiC was performed in the Vision 2 Plasma Etching furnace in the GT IEN Cleanroom.

- Pressure (mTorr): 80
- RF1 (Platen, W): 200
- Ar (sccm): 10
- O_2 (sccm): 7
- SF_6 (sccm): 13

A.2 EBL Resist Processes

Polymethyl Methacrylate (PMMA):

1. Spin on Microchem® PMMA A4 at 4000 rpm with 2000 rpm/s ramp rate, for 60 sec total.
2. Bake for 90 sec at 180 °C (check hot plate temperature is accurate).
3. A typical base dose is about 1,000 $\mu C/cm^2$.
4. Develop for 30 sec in 1:2 MIBK:IPA and immediately rinse in gently-flowing IPA for 20 sec. Dry off sample gently with N_2.

5. To remove resist, submerge for 1 min in Microposit® Remover 1165.

6. Rinse briefly in acetone and then IPA, followed by an N_2 dry.

ZEONREX® ZEP520a:

1. Spin on 1:1 ZEP520a:anisole at 4000 rpm with 2000 rpm/s ramp rate, for 60 sec total.

2. Bake for 2 min at 180 °C (check hot plate temperature is accurate).

3. A typical base dose is about 170 $\mu C/cm^2$. For all ribbon features patterned in this work, base dose used was 170-210 $\mu C/cm^2$.

4. Develop for 2 min in Amyl acetate and immediately rinse in gently-flowing IPA for 20 sec. Dry off sample gently with N_2.

5. To remove resist, sonicate for 15 min in Microposit® Remover 1165 if no graphene has yet been grown. Otherwise, submerge in 1165 for 15 min on a hotplate heated slightly.

6. Rinse briefly in acetone and then IPA, followed by an N_2 dry.

APPENDIX B

SEASONING AND MAINTENANCE OF CCS GRAPHITE CRUCIBLES

When a new crucible is formed from a graphite rod, several steps need to be taken before it can be successfully used for growth of epitaxial graphene (and, in particular, sidewall nanoribbons).

1. Sonicate the new crucible, with the lid off, in IPA for at least 20 min or until the IPA is completely saturated with graphite particles.

2. Rinse crucible and repeat the sonication until there no longer appear to be graphite particles coming off the new crucible. Dry with N_2.

3. Bake the crucible at incrementally increasing temperatures (starting at $\sim 700\,^{\circ}\mathrm{C}$) for at least 15 min at each step, until pressures no longer spike unreasonably high during heating.

4. Once the crucible has been baked sufficiently, a few dummy samples will need to be grown before growth calibrations can begin.

5. If the crucible will be used for low temperature or flat graphene samples, heat the dummy samples $\sim 50 - 100\,^{\circ}\mathrm{C}$ higher than the growth temperature expected to be used.

6. If the crucible will be used for sidewall nanoribbons grown with high temperatures ($> 1500\,^{\circ}\mathrm{C}$), then a few ($\sim 3 - 5$) buffer layer/monolayer samples should be grown before ribbon samples are attempted.

7. After several dummy samples are made, attempts to grow the desired samples can begin. It is important to characterize the growth of each sample grown over time to calibrate recipes. If sample growth rates are increasing or decreasing significantly over time with the growth of each subsequent sample, additional dummy samples should be grown accordingly to adjust the silicon content in the crucible.

APPENDIX C

ARPES CALCULATIONS AND DETECTOR GEOMETRY

For ARPES experiments, it can be shown that for point detectors, k_x and k_y are related to θ and ϕ via the typical spherical coordinate relationships.

$$k_x = \frac{\sqrt{2m}}{\hbar}\sqrt{E_{KE}}\sin\theta\cos\phi \tag{C.1}$$

$$k_y = \frac{\sqrt{2m}}{\hbar}\sqrt{E_{KE}}\sin\theta\sin\phi \tag{C.2}$$

Otherwise, for slit detectors (as in the case of the experimental set-up at the Casiopée Beamline at the SOLEIL Synchrotron) eulerian coordinates are needed. So, the relationship between k_x, k_y and measured angles θ and ϕ can be shown to be

$$k_x = \frac{\sqrt{2m}}{\hbar}\sqrt{E_{KE}}\sin\theta\cos\phi \tag{C.3}$$

$$k_y = \frac{\sqrt{2m}}{\hbar}\sqrt{E_{KE}}\sin\phi \tag{C.4}$$

REFERENCES

[1] M. Sprinkle, D. Siegel, Y. Hu, J. Hicks, A. Tejeda, A. Taleb-Ibrahimi, P. Le Fevre, F. Bertran, S. Vizzini, H. Enriquez, S. Chiang, P. Soukiassian, C. Berger, W. A. de Heer, A. Lanzara, and E. H. Conrad, "First direct observation of a nearly ideal graphene band structure," *Physical Review Letters*, vol. 100, no. 22, p. 226803, 2009. [Online]. Available: http://journals.aps.org/prl/abstract/10.1103/PhysRevLett.103.226803

[2] C. Berger, Z. Song, T. Li, X. Li, A. Y. Ogbazghi, R. Feng, Z. Dai, A. N. Marchenkov, E. H. Conrad, P. N. First, , and W. A. de Heer, "Ultrathin epitaxial graphite: 2D electron gas properties and a route toward graphene-based nanoelectronics," *The Journal of Physical Chemistry B*, vol. 108, no. 52, pp. 19 912–19 916, 2004.

[3] A. S. Mayorov, R. V. Gorbachev, S. V. Morozov, L. Britnell, R. Jalil, L. A. Ponomarenko, P. Blake, K. S. Novoselov, K. Watanabe, T. Taniguchi *et al.*, "Micrometer-scale ballistic transport in encapsulated graphene at room temperature," *Nano Letters*, vol. 11, no. 6, pp. 2396–2399, 2011.

[4] J. Baringhaus, M. Ruan, F. Edler, A. Tejeda, M. Sicot, I. Taleb, A.-P. Li, Z. Jiang, E. H. Conrad, C. Berger, C. Tegenkamp, and W. A. de Heer, "Exceptional ballistic transport in epitaxial graphene nanoribbons," *Nature*, vol. 506, no. 7488, pp. 349–354, 2014. [Online]. Available: http://dx.doi.org/10.1038/nature12952

[5] C. Berger, Z. Song, X. Li, X. Wu, N. Brown, C. Naud, D. Mayou, T. Li, J. Hass, A. N. Marchenkov, E. H. Conrad, P. N. First, and W. A. de Heer, "Electronic

confinement and coherence in patterned epitaxial graphene," *Science*, vol. 312, no. 5777, pp. 1191–1196, 2006.

[6] F. Schedin, A. Geim, S. Morozov, E. Hill, P. Blake, M. Katsnelson, and K. Novoselov, "Detection of individual gas molecules adsorbed on graphene," *Nature Materials*, vol. 6, no. 9, pp. 652–655, 2007.

[7] J. D. Fowler, M. J. Allen, V. C. Tung, Y. Yang, R. B. Kaner, and B. H. Weiller, "Practical chemical sensors from chemically derived graphene," *ACS Nano*, vol. 3, no. 2, pp. 301–306, 2009.

[8] Y. Liu, X. Dong, and P. Chen, "Biological and chemical sensors based on graphene materials," *Chemical Society Reviews*, vol. 41, no. 6, pp. 2283–2307, 2012.

[9] X. Sun, Z. Liu, K. Welsher, J. T. Robinson, A. Goodwin, S. Zaric, and H. Dai, "Nano-graphene oxide for cellular imaging and drug delivery," *Nano Research*, vol. 1, no. 3, pp. 203–212, 2008.

[10] X. Wang, L. Zhi, and K. Müllen, "Transparent, conductive graphene electrodes for dye-sensitized solar cells," *Nano Letters*, vol. 8, no. 1, pp. 323–327, 2008.

[11] X. Li, H. Zhu, K. Wang, A. Cao, J. Wei, C. Li, Y. Jia, Z. Li, X. Li, and D. Wu, "Graphene-on-silicon Schottky junction solar cells," *Advanced Materials*, vol. 22, no. 25, pp. 2743–2748, 2010.

[12] X. Miao, S. Tongay, M. K. Petterson, K. Berke, A. G. Rinzler, B. R. Appleton, and A. F. Hebard, "High efficiency graphene solar cells by chemical doping," *Nano Letters*, vol. 12, no. 6, pp. 2745–2750, 2012.

[13] M. A. Rafiee, J. Rafiee, Z. Wang, H. Song, Z.-Z. Yu, and N. Koratkar, "Enhanced mechanical properties of nanocomposites at low graphene content," *ACS Nano*, vol. 3, no. 12, pp. 3884–3890, 2009.

[14] X. Zhao, Q. Zhang, D. Chen, and P. Lu, "Enhanced mechanical properties of graphene-based poly (vinyl alcohol) composites," *Macromolecules*, vol. 43, no. 5, pp. 2357–2363, 2010.

[15] M. Weinert, E. Wimmer, and A. J. Freeman, "Total-energy all-electron density functional method for bulk solids and surfaces," *Physical Review B*, vol. 26, pp. 4571–4578, Oct 1982. [Online]. Available: http://link.aps.org/doi/10.1103/PhysRevB.26.4571

[16] K. S. Novoselov, A. K. Geim, S. V. Morozov, D. Jiang, Y. Zhang, S. V. Dubonos, I. V. Grigorieva, and A. A. Firsov, "Electric field effect in atomically thin carbon films," *Science*, vol. 22, no. 5696, pp. 666–669, 2004. [Online]. Available: http://science.sciencemag.org/content/306/5696/666

[17] K. Novoselov, D. Jiang, F. Schedin, T. Booth, V. Khotkevich, S. Morozov, and A. Geim, "Two-dimensional atomic crystals," *Proceedings of the National Academy of Sciences*, vol. 102, no. 30, pp. 10 451–10 453, 2005.

[18] A. Locatelli, K. R. Knox, D. Cvetko, T. O. Mentes, M. A. Nin, S. Wang, M. B. Yilmaz, P. Kim, R. M. Osgood, Jr., and M. A, "Corrugation in exfoliated graphene: An electron microscopy and diffraction study," *ACS Nano*, vol. 4, pp. 4879–4889, 2010. [Online]. Available: http://pubs.acs.org/doi/abs/10.1021/nn101116n

[19] D. Goodman and J. Yates, "CO isotopic mixing measurements on nickel: Evidence for irreversibility of CO dissociation," *Journal of Catalysis*, vol. 82, no. 2, pp. 255–260, 1983.

[20] H. Madden, J. Küppers, and G. Ertl, "Interaction of carbon monoxide with (110) nickel surfaces," *The Journal of Chemical Physics*, vol. 58, no. 8, pp. 3401–3410, 1973.

[21] C. Mattevi, H. Kim, and M. Chhowalla, "A review of chemical vapour deposition of graphene on copper," *Journal of Materials Chemistry*, vol. 21, no. 10, pp. 3324–3334, 2011.

[22] K. S. Kim, Y. Zhao, H. Jang, S. Y. Lee, J. M. Kim, K. S. Kim, J.-H. Ahn, P. Kim, J.-Y. Choi, and B. H. Hong, "Large-scale pattern growth of graphene films for stretchable transparent electrodes," *Nature*, vol. 457, no. 7230, pp. 706–710, 2009.

[23] X. Li, W. Cai, J. An, S. Kim, J. Nah, D. Yang, R. Piner, A. Velamakanni, I. Jung, E. Tutuc *et al.*, "Large-area synthesis of high-quality and uniform graphene films on copper foils," *Science*, vol. 324, no. 5932, pp. 1312–1314, 2009.

[24] X. Li, C. W. Magnuson, A. Venugopal, R. M. Tromp, J. B. Hannon, E. M. Vogel, L. Colombo, and R. S. Ruoff, "Large-area graphene single crystals grown by low-pressure chemical vapor deposition of methane on copper," *Journal of the American Chemical Society*, vol. 133, no. 9, pp. 2816–2819, 2011.

[25] S. J. Chae, F. Güneş, K. K. Kim, E. S. Kim, G. H. Han, S. M. Kim, H.-J. Shin, S.-M. Yoon, J.-Y. Choi, M. H. Park *et al.*, "Synthesis of large-area graphene layers on poly-nickel substrate by chemical vapor deposition: Wrinkle formation," *Advanced Materials*, vol. 21, no. 22, pp. 2328–2333, 2009.

[26] A. N. Obraztsov, "Chemical vapour deposition: Making graphene on a large scale," *Nature Nanotechnology*, vol. 4, no. 4, pp. 212–213, 2009.

[27] M. Dresselhaus and G. Dresselhaus, "Intercalation compounds of graphite," *Advances in Physics*, vol. 30, no. 2, pp. 139–326, 1981.

[28] B. C. Brodie, "On the atomic weight of graphite," *Philosophical Transactions of the Royal Society of London*, vol. 149, pp. 249–259, 1859.

[29] S. Stankovich, D. A. Dikin, R. D. Piner, K. A. Kohlhaas, A. Kleinhammes, Y. Jia, Y. Wu, S. T. Nguyen, and R. S. Ruoff, "Synthesis of graphene-based nanosheets via chemical reduction of exfoliated graphite oxide," *Carbon*, vol. 45, no. 7, pp. 1558–1565, 2007.

[30] C. Mattevi, G. Eda, S. Agnoli, S. Miller, K. A. Mkhoyan, O. Celik, D. Mastrogiovanni, G. Granozzi, E. Garfunkel, and M. Chhowalla, "Evolution of electrical, chemical, and structural properties of transparent and conducting chemically derived graphene thin films," *Advanced Functional Materials*, vol. 19, no. 16, pp. 2577–2583, 2009.

[31] Z. Wei, D. Wang, S. Kim, S.-Y. Kim, Y. Hu, M. K. Yakes, A. R. Laracuente, Z. Dai, S. R. Marder, C. Berger *et al.*, "Nanoscale tunable reduction of graphene oxide for graphene electronics," *Science*, vol. 328, no. 5984, pp. 1373–1376, 2010.

[32] H. A. Becerril, J. Mao, Z. Liu, R. M. Stoltenberg, Z. Bao, and Y. Chen, "Evaluation of solution-processed reduced graphene oxide films as transparent conductors," *ACS Nano*, vol. 2, no. 3, pp. 463–470, 2008.

[33] C. Gómez-Navarro, R. T. Weitz, A. M. Bittner, M. Scolari, A. Mews, M. Burghard, and K. Kern, "Electronic transport properties of individual chemically reduced graphene oxide sheets," *Nano Letters*, vol. 7, no. 11, pp. 3499–3503, 2007.

[34] S. Pei, J. Zhao, J. Du, W. Ren, and H.-M. Cheng, "Direct reduction of graphene oxide films into highly conductive and flexible graphene films by hydrohalic acids," *Carbon*, vol. 48, no. 15, pp. 4466–4474, 2010.

[35] O. P. Hugh, "Handbook of carbon, graphite, diamond and fullerenes: Properties, processing and application," *USA Noyes Publication*, vol. 63, 1993.

[36] A. Buchsteiner, A. Lerf, and J. Pieper, "Water dynamics in graphite oxide investigated with neutron scattering," *The Journal of Physical Chemistry B*, vol. 110, no. 45, pp. 22 328–22 338, 2006.

[37] W. Chen, S. Li, C. Chen, and L. Yan, "Self-assembly and embedding of nanoparticles by in situ reduced graphene for preparation of a 3D graphene/nanoparticle aerogel," *Advanced Materials*, vol. 23, no. 47, pp. 5679–5683, 2011.

[38] A. J. Patil, J. L. Vickery, T. B. Scott, and S. Mann, "Aqueous stabilization and self-assembly of graphene sheets into layered bio-nanocomposites using DNA," *Advanced Materials*, vol. 21, no. 31, pp. 3159–3164, 2009.

[39] J. Cai, P. Ruffieux, R. Jaafar, M. Bieri, T. Braun, S. Blankenburg, M. Muoth, A. P. Seitsonen, M. Saleh, X. Feng *et al.*, "Atomically precise bottom-up fabrication of graphene nanoribbons," *Nature*, vol. 466, no. 7305, pp. 470–473, 2010.

[40] A. Van Bommel, J. Crombeen, and A. Van Tooren, "LEED and auger electron observations of the SiC (0001) surface," *Surface Science*, vol. 48, no. 2, pp. 463–472, 1975.

[41] I. Forbeaux, J.-M. Themlin, A. Charrier, F. Thibaudau, and J.-M. Debever, "Solid-state graphitization mechanisms of silicon carbide 6H-SiC polar faces," *Applied Surface Science*, vol. 162, pp. 406–412, 2000.

[42] J. Hass, F. Varchon, J. E. Millán-Otoya, M. Sprinkle, N. Sharma, W. A. de Heer, C. Berger, P. N. First, L. Magaud, and E. H. Conrad, "Why multilayer graphene on $4H$-SiC$(000\bar{1})$ behaves like a single sheet of graphene," *Physical Review Letters*, vol. 100, p. 125504, Mar 2008. [Online]. Available: http://link.aps.org/doi/10.1103/PhysRevLett.100.125504

[43] M. Sprinkle, M. Ruan, Y. Hu, J. Hankinson, M. Rubio-Roy, B. Zhang, X. Wu, C. Berger, and W. A. de Heer, "Scalable templated growth of graphene nanoribbons on SiC," *Nature Nano*, vol. 5, no. 10, pp. 727–731, 2010, 10.1038/nnano.2010.192. [Online]. Available: http://dx.doi.org/10.1038/nnano.2010.192

[44] J. Hicks, A. Tejeda, A. Taleb-Ibrahimi, M. S. Nevius, F. Wang, K. Shepperd, J. Palmer, F. Bertran, P. Le Fevre, J. Kunc, W. A. de Heer, C. Berger, and E. H. Conrad, "A wide-bandgap metal-semiconductor-metal nanostructure made entirely from graphene," *Nature Physics*, vol. 9, no. 1, pp. 49–54, 2013, 10.1038/nphys2487. [Online]. Available: http://dx.doi.org/10.1038/nphys2487

[45] I. Forbeaux, J.-M. Themlin, and J.-M. Debever, "Heteroepitaxial graphite on $6H-$SiC(0001) : interface formation through conduction-band electronic structure," *Physical Review B*, vol. 58, pp. 16 396–16 406, Dec 1998. [Online]. Available: http://link.aps.org/doi/10.1103/PhysRevB.58.16396

[46] W. A. de Heer, C. Berger, M. Ruan, M. Sprinkle, X. Li, Y. Hu, B. Zhang, J. Hankinson, and E. Conrad, "Large area and structured epitaxial graphene produced by confinement controlled sublimation of silicon carbide," *Proceedings of the National Academy of Sciences*, vol. 108, no. 41, pp. 16 900–16 905, 2011. [Online]. Available: http://www.pnas.org/content/108/41/16900.abstract

[47] J. Baringhaus, F. Edler, and C. Tegenkamp, "Edge-states in graphene nanoribbons: A combined spectroscopy and transport study," *Journal of Physics: Condensed Matter*, vol. 25, no. 39, p. 392001, 2013. [Online]. Available: http://stacks.iop.org/0953-8984/25/i=39/a=392001

[48] U. Starke and C. Riedl, "Epitaxial graphene on SiC (0001) and SiC(000$\bar{1}$): From surface reconstructions to carbon electronics," *Journal of Physics: Condensed Matter*, vol. 21, no. 13, p. 134016, 2009.

[49] K. V. Emtsev, A. Bostwick, K. Horn, J. Jobst, G. L. Kellogg, L. Ley, J. L. McChesney, T. Ohta, S. A. Reshanov, J. Rohrl, E. Rotenberg, A. K. Schmid, D. Waldmann, H. B. Weber, and T. Seyller, "Towards wafer-size graphene layers by atmospheric pressure graphitization of silicon carbide," *Nature Materials*, vol. 8, no. 3, pp. 203–207, 2009, 10.1038/nmat2382. [Online]. Available: http://dx.doi.org/10.1038/nmat2382

[50] J. Hass, R. Feng, T. Li, X. Li, Z. Zong, W. A. de Heer, P. N. First, E. H. Conrad, C. A. Jeffrey, and C. Berger, "Highly ordered graphene for two dimensional electronics," *Applied Physics Letters*, vol. 89, no. 14, p. 3, 2006. [Online]. Available: http://scitation.aip.org/content/aip/journal/apl/89/14/10.1063/1.2358299

[51] M. Sprinkle, J. Hicks, A. Tejeda, A. Taleb-Ibrahimi, P. L. Fvre, F. Bertran, H. Tinkey, M. C. Clark, P. Soukiassian, D. Martinotti, J. Hass, and E. H. Conrad, "Multilayer epitaxial graphene grown on the SiC (000$\bar{1}$) surface: Structure and electronic properties," *Journal of Physics D: Applied Physics*, vol. 43, no. 37, p. 374006, 2010. [Online]. Available: http://stacks.iop.org/0022-3727/43/i=37/a=374006

[52] J. M. Palmer, "Pre-growth structures for high quality epitaxial graphene nanoelectronics grown on silicon carbide," Ph.D. dissertation, Georgia Institute of

Technology, 12 2014.

[53] M. Oliveira Jr, T. Schumann, M. Ramsteiner, J. Lopes, and H. Riechert, "Influence of the silicon carbide surface morphology on the epitaxial graphene formation," *Applied Physics Letters*, vol. 99, no. 11, p. 111901, 2011.

[54] N. Srivastava, G. He, P. C. Mende, R. M. Feenstra, Y. Sun *et al.*, "Graphene formed on SiC under various environments: comparison of Si-face and C-face," *Journal of Physics D: Applied Physics*, vol. 45, no. 15, p. 154001, 2012.

[55] A. Nakajima, H. Yokoya, Y. Furukawa, and H. Yonezu, "Step control of vicinal 6H–SiC(0001) surface by H2 etching," *Journal of Applied Physics*, vol. 97, no. 10, p. 4919, 2005. [Online]. Available: http://scitation.aip.org/content/aip/journal/jap/97/10/10.1063/1.1901838

[56] J. Hass, R. Feng, J. Millan-Otoya, X. Li, M. Sprinkle, P. N. First, W. De Heer, E. Conrad, and C. Berger, "Structural properties of the multilayer graphene/4H-SiC($000\bar{1}$) system as determined by surface x-ray diffraction," *Physical Review B*, vol. 75, no. 21, p. 214109, 2007.

[57] X. Wu, X. Li, Z. Song, C. Berger, and W. A. de Heer, "Weak antilocalization in epitaxial graphene: Evidence for chiral electrons," *Physical Review Letters*, vol. 98, no. 13, p. 136801, 2007.

[58] K. V. Emtsev, F. Speck, T. Seyller, L. Ley, and J. D. Riley, "Interaction, growth, and ordering of epitaxial graphene on SiC{0001} surfaces: A comparative photoelectron spectroscopy study," *Physical Review B*, vol. 77, p. 155303, Apr 2008. [Online]. Available: http://link.aps.org/doi/10.1103/PhysRevB.77.155303

[59] J. Hicks, K. Shepperd, F. Wang, and E. Conrad, "The structure of graphene grown on the SiC($000\bar{1}$) surface," *Journal of Physics D: Applied Physics*, vol. 45, no. 15, p. 154002, 2012.

[60] M. Conrad, F. Wang, M. S. Nevius, K. Jinkins, A. Celis, M. N. Nair, A. Taleb-Ibrahimi, A. Tejeda, Y. Garreau, A. Vlad, A. Coati, P. F. Miceli, and E. H. Conrad, "The incommensurate SiC(0001) interface and its role in the formation of semiconducting graphene," *To Be Published*, pp. 1–7, 2016.

[61] J. Hass, W. A. de Heer, and E. H. Conrad, "The growth and morphology of epitaxial multilayer graphene," *Journal of Physics: Condensed Matter*, vol. 20, no. 32, p. 323202, 2008. [Online]. Available: http://stacks.iop.org/0953-8984/20/i=32/a=323202

[62] T. Ohta, A. Bostwick, J. L. McChesney, T. Seyller, K. Horn, and E. Rotenberg, "Interlayer interaction and electronic screening in multilayer graphene investigated with angle-resolved photoemission spectroscopy," *Physical Review Letters*, vol. 98, no. 20, p. 206802, 2007.

[63] J. Hass, J. E. Millán-Otoya, P. N. First, and E. H. Conrad, "Interface structure of epitaxial graphene grown on 4H-SiC(0001)," *Physical Review B*, vol. 78, p. 205424, Nov 2008. [Online]. Available: http://link.aps.org/doi/10.1103/PhysRevB.78.205424

[64] H. Hibino, S. Mizuno, H. Kageshima, M. Nagase, and H. Yamaguchi, "Stacking domains of epitaxial few-layer graphene on SiC (0001)," *Physical Review B*, vol. 80, no. 8, p. 085406, 2009.

[65] I. Palacio, A. Celis, M. N. Nair, A. Gloter, A. Zobelli, M. Sicot, D. Malterre, M. S. Nevius, W. A. de Heer, C. Berger, E. H. Conrad, A. Taleb-Ibrahimi, and A. Tejeda, "Atomic structure of epitaxial graphene sidewall nanoribbons: Flat graphene, miniribbons, and the confinement gap," *Nano Letters*, vol. 15, no. 1, pp. 182–189, 2015. [Online]. Available: http://dx.doi.org/10.1021/nl503352v

[66] T. Ohta, A. Bostwick, T. Seyller, K. Horn, and E. Rotenberg, "Controlling the electronic structure of bilayer graphene," *Science*, vol. 313, no. 5789, pp. 951–954, 2006.

[67] Y. Zhang, T.-T. Tang, C. Girit, Z. Hao, M. C. Martin, A. Zettl, M. F. Crommie, Y. R. Shen, and F. Wang, "Direct observation of a widely tunable bandgap in bilayer graphene," *Nature*, vol. 459, no. 7248, pp. 820–823, 2009.

[68] N. W. Ashcroft and N. D. Mermin, "Introduction to solid state physics," *Saunders, Philadelphia*, 1976.

[69] Z. H. Ni, T. Yu, Y. H. Lu, Y. Y. Wang, Y. P. Feng, and Z. X. Shen, "Uniaxial strain on graphene: Raman spectroscopy study and band-gap opening," *ACS Nano*, vol. 2, no. 11, pp. 2301–2305, 2008. [Online]. Available: http://dx.doi.org/10.1021/nn800459e

[70] V. M. Pereira, A. H. Castro Neto, and N. M. R. Peres, "Tight-binding approach to uniaxial strain in graphene," *Physical Review B*, vol. 80, p. 045401, Jul 2009. [Online]. Available: http://link.aps.org/doi/10.1103/PhysRevB.80.045401

[71] G. Cocco, E. Cadelano, and L. Colombo, "Gap opening in graphene by shear strain," *Physical Review B*, vol. 81, no. 24, p. 241412, 2010.

[72] J. Feng, W. Li, X. Qian, J. Qi, L. Qi, and J. Li, "Patterning of graphene," *Nanoscale*, vol. 4, no. 16, pp. 4883–4899, 2012.

[73] V. M. Pereira and A. C. Neto, "Strain engineering of graphenes electronic structure," *Physical Review Letters*, vol. 103, no. 4, p. 046801, 2009.

[74] K. Nakada, M. Fujita, G. Dresselhaus, and M. S. Dresselhaus, "Edge state in graphene ribbons: Nanometer size effect and edge shape dependence,"

Physical Review B, vol. 54, pp. 17 954–17 961, Dec 1996. [Online]. Available: http://link.aps.org/doi/10.1103/PhysRevB.54.17954

[75] K. Wakabayashi, M. Fujita, H. Ajiki, and M. Sigrist, "Electronic and magnetic properties of nanographite ribbons," *Physical Review B*, vol. 59, pp. 8271–8282, Mar 1999. [Online]. Available: http://link.aps.org/doi/10.1103/PhysRevB.59.8271

[76] Y.-W. Son, M. L. Cohen, and S. G. Louie, "Energy gaps in graphene nanoribbons," *Physical Review Letters*, vol. 97, p. 216803, Nov 2006. [Online]. Available: http://link.aps.org/doi/10.1103/PhysRevLett.97.216803

[77] L. Brey and H. A. Fertig, "Electronic states of graphene nanoribbons studied with the Dirac equation," *Physical Review B*, vol. 73, p. 235411, Jun 2006. [Online]. Available: http://link.aps.org/doi/10.1103/PhysRevB.73.235411

[78] V. Barone, O. Hod, and G. E. Scuseria, "Electronic structure and stability of semiconducting graphene nanoribbons," *Nano Letters*, vol. 6, no. 12, pp. 2748–2754, 2006.

[79] D. Elias, R. Nair, T. Mohiuddin, S. Morozov, P. Blake, M. Halsall, A. Ferrari, D. Boukhvalov, M. Katsnelson, A. Geim *et al.*, "Control of graphene's properties by reversible hydrogenation: Evidence for graphane," *Science*, vol. 323, no. 5914, pp. 610–613, 2009.

[80] R. Balog, B. Jørgensen, L. Nilsson, M. Andersen, E. Rienks, M. Bianchi, M. Fanetti, E. Lægsgaard, A. Baraldi, S. Lizzit *et al.*, "Bandgap opening in graphene induced by patterned hydrogen adsorption," *Nature Materials*, vol. 9, no. 4, pp. 315–319, 2010.

[81] S.-H. Cheng, K. Zou, F. Okino, H. R. Gutierrez, A. Gupta, N. Shen, P. Eklund, J. Sofo, and J. Zhu, "Reversible fluorination of graphene: Evidence of a two-dimensional wide bandgap semiconductor," *Physical Review B*, vol. 81, no. 20, p. 205435, 2010.

[82] J. T. Robinson, J. S. Burgess, C. E. Junkermeier, S. C. Badescu, T. L. Reinecke, F. K. Perkins, M. K. Zalalutdniov, J. W. Baldwin, J. C. Culbertson, P. E. Sheehan *et al.*, "Properties of fluorinated graphene films," *Nano Letters*, vol. 10, no. 8, pp. 3001–3005, 2010.

[83] E. L. Shirley, L. Terminello, A. Santoni, and F. Himpsel, "Brillouin-zone-selection effects in graphite photoelectron angular distributions," *Physical Review B*, vol. 51, no. 19, p. 13614, 1995.

[84] H. Hibino, H. Kageshima, F. Maeda, M. Nagase, Y. Kobayashi, and H. Yamaguchi, "Microscopic thickness determination of thin graphite films formed on SiC from quantized oscillation in reflectivity of low-energy electrons," *Physical Review B*, vol. 77, no. 7, p. 075413, 2008.

[85] E. Bekyarova, S. Sarkar, S. Niyogi, M. Itkis, and R. Haddon, "Advances in the chemical modification of epitaxial graphene," *Journal of Physics D: Applied Physics*, vol. 45, no. 15, p. 154009, 2012.

[86] S. Niyogi, E. Bekyarova, M. E. Itkis, H. Zhang, K. Shepperd, J. Hicks, M. Sprinkle, C. Berger, C. N. Lau, W. A. Deheer *et al.*, "Spectroscopy of covalently functionalized graphene," *Nano Letters*, vol. 10, no. 10, pp. 4061–4066, 2010.

[87] K. S. Novoselov, V. Fal, L. Colombo, P. Gellert, M. Schwab, K. Kim *et al.*, "A roadmap for graphene," *Nature*, vol. 490, no. 7419, pp. 192–200, 2012.

[88] C. Riedl, C. Coletti, T. Iwasaki, A. A. Zakharov, and U. Starke, "Quasi-free-standing epitaxial graphene on SiC obtained by hydrogen intercalation,"

Phys. Rev. Lett., vol. 103, p. 246804, Dec 2009. [Online]. Available: http://link.aps.org/doi/10.1103/PhysRevLett.103.246804

[89] A. Bostwick, T. Ohta, T. Seyller, K. Horn, and E. Rotenberg, "Quasiparticle dynamics in graphene," *Nature Physics*, vol. 3, no. 1, pp. 36–40, JAN 2007.

[90] C. Riedl, C. Coletti, T. Iwasaki, A. Zakharov, and U. Starke, "Quasi-free-standing epitaxial graphene on SiC obtained by hydrogen intercalation," *Physical Review Letters*, vol. 103, no. 24, p. 246804, 2009.

[91] F. Speck, J. Jobst, F. Fromm, M. Ostler, D. Waldmann, M. Hundhausen, H. B. Weber, and T. Seyller, "The quasi-free-standing nature of graphene on H-saturated SiC(0001)," *Applied Physics Letters*, vol. 99, no. 12, p. 122106, 2011. [Online]. Available: http://scitation.aip.org/content/aip/journal/apl/99/12/10.1063/1.3643034

[92] F. Varchon, R. Feng, J. Hass, X. Li, B. N. Nguyen, C. Naud, P. Mallet, J.-Y. Veuillen, C. Berger, E. H. Conrad, and L. Magaud, "Electronic structure of epitaxial graphene layers on SiC: Effect of the substrate," *Physical Review Letters*, vol. 99, p. 126805, Sep 2007. [Online]. Available: http://link.aps.org/doi/10.1103/PhysRevLett.99.126805

[93] A. Mattausch and O. Pankratov, "*Ab Initio* study of graphene on SiC," *Physical Review Letters*, vol. 99, p. 076802, Aug 2007. [Online]. Available: http://link.aps.org/doi/10.1103/PhysRevLett.99.076802

[94] S. Kim, J. Ihm, H. J. Choi, and Y.-W. Son, "Origin of anomalous electronic structures of epitaxial graphene on silicon carbide," *Physical Review Letters*, vol. 100, p. 176802, Apr 2008. [Online]. Available: http://link.aps.org/doi/10.1103/PhysRevLett.100.176802

[95] J. D. Emery, B. Detlefs, H. J. Karmel, L. O. Nyakiti, D. K. Gaskill, M. C. Hersam, J. Zegenhagen, and M. J. Bedzyk, "Chemically resolved interface structure of epitaxial graphene on SiC(0001)," *Physical Review Letters*, vol. 111, p. 215501, Nov 2013. [Online]. Available: http://link.aps.org/doi/10.1103/PhysRevLett.111.215501

[96] V. R. Manfrinato, L. Zhang, D. Su, H. Duan, R. G. Hobbs, E. A. Stach, and K. K. Berggren, "Resolution limits of electron-beam lithography toward the atomic scale," *Nano Letters*, vol. 13, no. 4, pp. 1555–1558, 2013.

[97] M. Y. Han, J. C. Brant, and P. Kim, "Electron transport in disordered graphene nanoribbons," *Physical Review Letters*, vol. 104, p. 056801, Feb 2010. [Online]. Available: http://link.aps.org/doi/10.1103/PhysRevLett.104.056801

[98] W. Norimatsu and M. Kusunoki, "Formation process of graphene on SiC(0001)," *Physica E: Low-dimensional Systems and Nanostructures*, vol. 42, no. 4, pp. 691 – 694, 2010, 18th International Conference on Electron Properties of Two-Dimensional Systems. [Online]. Available: http://www.sciencedirect.com/science/article/pii/S1386947709006432

[99] M. Hupalo, E. Conrad, and M. Tringides, "Growth mechanism for epitaxial graphene on vicinal 6H-SiC(0001) surfaces: A scanning tunneling microscopy study," *Physical Review B*, vol. 80, no. 4, p. 041401, 2009.

[100] W. Norimatsu and M. Kusunoki, "Growth of graphene from SiC(0001) surfaces and its mechanisms," *Semiconductor Science and Technology*, vol. 29, no. 6, p. 064009, 2014.

[101] S. Nie, C. Lee, R. M. Feenstra, Y. Ke, R. Devaty, W. Choyke, C. Inoki, T. Kuan, and G. Gu, "Step formation on hydrogen-etched 6H-SiC {0001} surfaces," *Surface Science*, vol. 602, no. 17, pp. 2936–2942, 2008.

[102] K. R. Knox, S. Wang, A. Morgante, D. Cvetko, A. Locatelli, T. O. Mentes, M. A. Niño, P. Kim, and R. M. Osgood, "Spectromicroscopy of single and multilayer graphene supported by a weakly interacting substrate," *Physical Review B*, vol. 78, p. 201408, Nov 2008. [Online]. Available: http://link.aps.org/doi/10.1103/PhysRevB.78.201408

[103] S. Nie, C. Lee, R. Feenstra, Y. Ke, R. Devaty, W. Choyke, C. Inoki, T. Kuan, and G. Gu, "Step formation on hydrogen-etched 6H-SiC{0001} surfaces," *Surface Science*, vol. 602, no. 17, pp. 2936 – 2942, 2008. [Online]. Available: http://www.sciencedirect.com/science/article/pii/S0039602808005049

[104] V. Borovikov and A. Zangwill, "Step bunching of vicinal 6H-SiC{0001} surfaces," *Physical Review B*, vol. 79, no. 24, p. 245413, 2009.

[105] H. Nakagawa, S. Tanaka, and I. Suemune, "Self-ordering of nanofacets on vicinal SiC surfaces," *Physical Review letters*, vol. 91, no. 22, p. 226107, 2003.

[106] M. S. Nevius, F. Wang, C. Mathieu, N. Barrett, A. Sala, T. O. Mentes, A. Locatelli, and E. H. Conrad, "The bottom-up growth of edge specific graphene nanoribbons," *Nano Letters*, vol. 14, no. 11, pp. 6080–6086, 2014. [Online]. Available: http://dx.doi.org/10.1021/nl502942z

[107] J. D. Hicks, "A combined top-down/bottom-up route to fabricating graphene devices," Ph.D. dissertation, Georgia Institute of Technology, 7 2013.

[108] M. S. Nevius, M. Conrad, F. Wang, A. Celis, M. N. Nair, A. Taleb-Ibrahimi, A. Tejeda, and E. H. Conrad, "Semiconducting graphene from highly ordered substrate interactions," *Physical Review Letters*, vol. 115, p. 136802, Sep 2015. [Online]. Available: http://link.aps.org/doi/10.1103/PhysRevLett.115.136802

[109] F. Ming and A. Zangwill, "Model and simulations of the epitaxial growth of graphene on non-planar 6HSiC surfaces," *Journal of Physics*

D: Applied Physics, vol. 45, no. 15, p. 154007, 2012. [Online]. Available: http://stacks.iop.org/0022-3727/45/i=15/a=154007

[110] Y.-W. Son, S.-M. Choi, Y. P. Hong, S. Woo, and S.-H. Jhi, "Electronic topological transition in sliding bilayer graphene," *Physical Review B*, vol. 84, no. 15, p. 155410, 2011.

[111] F. Ming and A. Zangwill, "Model for the epitaxial growth of graphene on 6H-SiC(0001)," *Physical Review B*, vol. 84, p. 115459, Sep 2011. [Online]. Available: http://link.aps.org/doi/10.1103/PhysRevB.84.115459

[112] J. Baringhaus, J. Aprojanz, J. Wiegand, D. Laube, M. Halbauer, J. Hübner, M. Oestreich, and C. Tegenkamp, "Growth and characterization of sidewall graphene nanoribbons," *Applied Physics Letters*, vol. 106, no. 4, p. 043109, 2015.

[113] S. Forti, K. Emtsev, C. Coletti, A. Zakharov, C. Riedl, and U. Starke, "Large-area homogeneous quasifree standing epitaxial graphene on SiC (0001): electronic and structural characterization," *Physical Review B*, vol. 84, no. 12, p. 125449, 2011.

[114] C. Riedl, C. Coletti, and U. Starke, "Structural and electronic properties of epitaxial graphene on SiC (0 0 0 1): a review of growth, characterization, transfer doping and hydrogen intercalation," *Journal of Physics D: Applied Physics*, vol. 43, no. 37, p. 374009, 2010.